Hochschule Aalen

Master Thesis

Photopolymer Layer Application and Structure curing on planar and non-planar Surfaces using a Laser Scanning Lithography Setup

Patrick Henreich

Date of submission: 12.01.2022

Thesis submitted in partial fulfillment of the
Requirements for the Degree of
Master of Science
at
Aalen University
Faculty of Optics and Mechatronics

Hochschule Aalen

Master Thesis

Photopolymer Layer Application and Structure curing on planar and non-planar Surfaces using a Laser Scanning Lithography Setup

Thesis submitted in partial fulfillment of the
Requirements for the Degree of
Master of Science

Author:	Patrick Henreich
Matriculation number:	57115
Completion period:	01.06.2021 - 12.01.2022
First supervisor:	Prof. Dr. Andreas Heinrich
Second supervisor:	Prof. Dr. Rainer Börret
University:	Hochschule Aalen
Major:	Advanced Systems Design (MSD)

Declaration of Originality

I affirm that I have produced the work independently and without the use of any aids other than those specified. All passages that are taken literally or in spirit from publications or other sources are marked as such. The paper has not yet been submitted to any examination office in the same or similar form and has not yet been published.

Aalen, den 12.01.2022
(Patrick Henreich)

Acknowledgements

First of all, I would like to thank my family, especially my parents who have always supported me and encouraged me in all my decisions. I would also like to thank Steffi for always believing in me and being an indispensable support in every situation.

I would like to thank Prof. Dr. Andreas Heinrich for the opportunity he gave me to complete this project in his research group and for always being available to support and advise me in the project. The time in the lab helped me a lot to develop personally and professionally.

I would like to thank the people from the lab who made this time not only one of the most educational times of my life but also one of the most enjoyable. In particular, I would like to thank Yannick Bauckhage, who, as my supervisor, always had an open ear and took a lot of time to support me in the implementation of the project and gave me many helpful comments and suggestions without which the project would not have been completed so successfully. Furthermore I would like to thAAnk Mike Dohmen who has been a great support, proof reader and friend throughout the last 2 years. Thank you to Christian Eder and Manuel Rank for always taking time to teach and explain me things, I have learned a lot from you. Thank you to Mr. Müller for your support in the manufacturing of the setup for the project. Finally I'd like to thank Martina Rosner, Lisa Batha, Hannes Suhr and Selina Burkert for the many constructive discussions and the harmonic teamwork.

Abstract

This thesis presents the development of a system and process to enable structure curing and surface functionalization in defined photopolymer layers on planar and convex surfaces using a galvanometer-based laser lithography setup. For this purpose, an investigation and characterization of the spin coating process for the application of defined and homogenous layers of the PR48 photopolymer to achieve layerheights between 5 and 30 µm on planar and convex glass surfaces is performed. A method and parameters to achieve repeatable layerheights on planar and convex substrates are presented. A modular lithography setup to be used as a stand-alone system and in combination with a 6 DOF hexapod to enable the orientation of substrates towards the lithography system and compensation of substrate surfaces is developed. Structure curing and surface functionalization, as well as correction of non-planar substrate geometries using the hexapod is presented and experimentally verified. The presented setup and process allows micronscale 2.5 D structure curing and surface functionalization in defined layers on planar and convex surfaces. Finally, further necessary steps for process automation and gray scale surface functionalization in multiple photopolymer layers are presented and discussed.

Table of Contents

List of Figures

List of Tables

List of Equations

Glossary

3D

Three dimensional

AM

Additive manufacturing

AOM

Acousto-optic modulator

CAD

Computer aided design

DAQ

Data Aquisition

DLW

Direct laser writing

DOE

Diffractive optical element

DOF

Degree(s) of freedom

EFL

Effective focal length

FDM

Fused deposition modelling

Galvo

Galvanometer mirror system

GUI

Graphical user interface

HOE

Holographic optical element

NA

Numerical aperture

oTter

G-Code To Cartesian Coordinates (python class)

PSU

Power supply unit

ROC

Radius of curvature

ROI

Region of interest

RPM

Revolutions per minute

SLA

Stereolithography (apparatus)

SLS

Selective laser sintering

TPP

Two-Photon Polymerization

USP

Ultra Short Pulse

UV

Ultra violett

voxel

Volume pixel

WLI

White light interferometer

List of Symbols

Symbol	Description	Unit
A	Area	m^2
C_D	Maximum curing depth	m
D_P	Penetration depth	m
E	Exposure energy	$\frac{J}{m^2}$
E_C	Gelation threshold	$\frac{J}{m^2}$
η	Dynamic viscosity	P
F	Force	N
f	Focal length	m
F_{ad}	Adhesion Force	N
g	Gravitational Force	$\frac{m}{s^2}$
γ	Surface energy	$\frac{J}{m^2}$
h_0	Initial height	m
I	Intensity	$\frac{W}{m^2}$
L_W	Maximum Linewidth	m
λ	Wavelength	m
M^2	Beam quality factor	-
n	Refractive index	-
ν	Kinematic viscosity	St
ω	Angular velocity	$\frac{1}{s}$
$P-V$	Peak-Valley Distance	m
P_L	Laser Power	W
r	Radial distance	m

Symbol	Description	Unit
ρ	Density	$\frac{kg}{m^3}$
S_a	Arithmetic meas height to surface	m
S_p	Maximum Surface Peak Height	m
S_v	Maximum Surface Valley Depth	m
S_z	Maximum Surface Height Deviation	m
t	Time	s
τ	Shear stress	Pa
V	Volume	m^3
v	Velocity	$\frac{m}{s}$
v_S	Scanning velocity	$\frac{m}{s}$
w_0	Beam waist radius	m
W_{ad}	Adhesion energy	$\frac{J}{m^2}$
x	Position in cartesian x-direction	m
y	Position in cartesian y-direction	m
z	Position in cartesian z-direction	m

1 Introduction

With the advancements and increased demand for micro-optical elements such as micro-lens arrays, diffractive optical elements (DOE), or holographic optical elements (HOE) in many industry fields such as, medicine, photography, illumination shaping, metrology, laser beam forming and optometry, much effort has been put into researching and developing precise and efficient processes for fabrication of those elements. [63, 22]

Traditionally functionalizing optical elements is done by combining a flat diffractive with a curved refractive surface [23]. The combination of both of these functions on a single surface allows a decrease in necessary space and adds additional degrees of freedom to the possible designs [22]. Typical applications for those so-called hybrid (diffractive-refractive) optical elements are the creation of spherical or aspherical lens arrays, beam shaping, corrections of spherical and chromatic aberrations and efficient grating fabrication [84]. For example, hybrid optical elements allow the functionalization of a single refractive optical element like a lens or a spectacle glass. The following figure 1.1 shows two examples for the application of functionalized curved surfaces. Here a computer-generated hologram for augmented light projection is shown in figure 1.1a as well as an array of micro-lenses on a convex lens substrate in figure 1.1b.

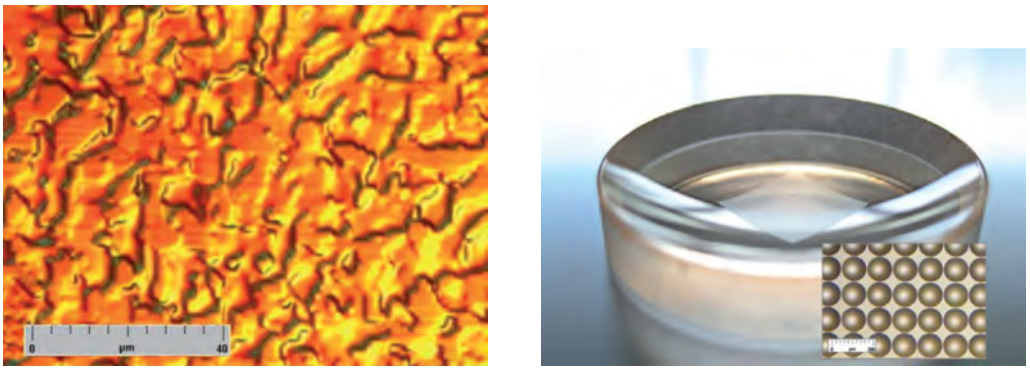

(a) (b)

Figure 1.1: Application examples for the creation of hybrid optical elements: a) Computer generated Hologram b) Array of Microlenses on concave surface [84]

With the possibilities of hybrid optical elements, traditionally employed lithographic methods for fabrication of micro-optical elements are becoming less desirable since they are limited to flat surfaces or curved surfaces with a very high radius of curvature and therefore low sag heights [23]. Existing systems for structuring on non-planar surfaces like nano imprint systems or electron beam writing suffer from low flexibility and relatively low throughput respectively [22], whereas other technologies such as diamond milling or turning suffer from a limitation in possible resolution [1] or deposition and etching which are only feasible for a limited number

of geometries [68]. With the advancements in additive manufacturing, laser stereolithography SLA has become an attractive technology. Laser stereolithography is a maskless, non-contact structuring technology that utilizes a focused laserbeam to directly structure patterns in a photopolymer film. The following figure 1.2 shows a basic setup for laser stereolithography using a UV laser in combination with a high speed galvanometer and a scan lens allowing precise positioning and focusing of a beam onto a plane surface. Combining the technology of SLA with a system setup that is not in itself limited to certain degrees of freedom theoretically allows the fabrication of structures without the limitation to a planar or even homogenous surfaces.

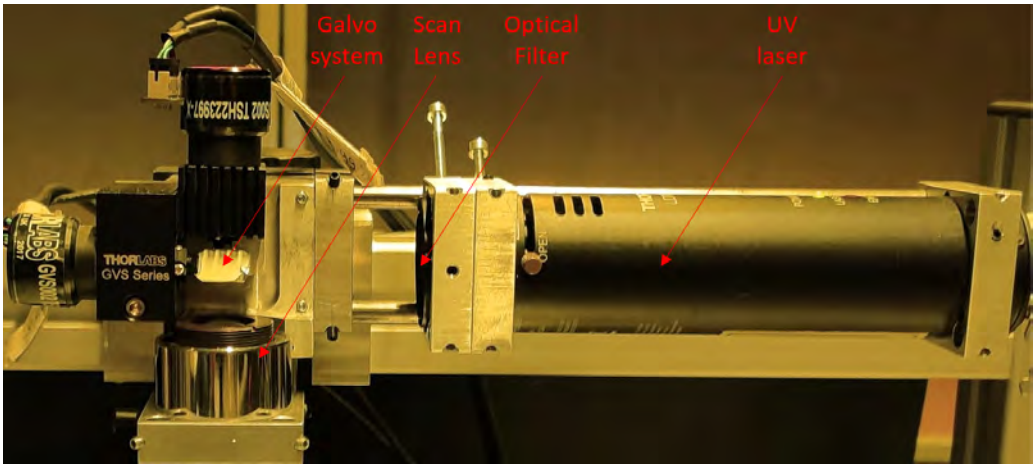

Figure 1.2: Current setup for laser scanning stereolithography functionality using a Galvo and a Scan lens

This work is part of a project with the overall goal to cure micron-scale structures in multiple defined photoresist layers on planar and non-planar surfaces, in this work specifically convex lenses. To achieve that goal, a setup using a 405 nm UV-laser in combination with a Galvanometer mirror system (Galvo) is utilized with a F-Theta scan lens to achieve laser scanning functionality. The previous reports on this project discuss the development of an initial test setup for planar surfaces, a control software for the Galvo system, as well as an analysis of the curing cross-section and polymer adhesion dependent on the exposure during the curing process. The results of the analysis led to boundary conditions for minimum and maximum exposure energy to achieve a parabolic curing shape of the photoresist adhering to glass (BK7) substrates. The goal of this work is the development of a layer application process for defined, repeatable, micron-scale layers on planar and convex surfaces using a spin coater and the functionalizing of planar and convex surfaces using the SLA setup with a hexapod system to enable 6 degrees of freedom for the incident beam on non-planar surfaces.

In an effort to achieve homogenous, repeatable layers on substrate surfaces, existing coating technologies shall be evaluated and a mathematical model for spin coating on planar, concave and convex substrates is used to calculate the expected layerheight on surfaces. Next the results of the coating process are to be evaluated and a measurement procedure for determining the layerheight of transparent photopolymer films on planar and convex surfaces shall be pre-

sented. Then, a substrate preparation process using plasma surface activation to improve the surface wettability, as well as the investigation of the photopolymer flow after coating on a convex lens needs to be performed. From this, the results for planar and convex surface coating shall be discussed regarding repeatability, layer stability and, in case of curved surfaces, time dependency. A rework of the curing setup with the implementation of the hexapod motion system and a setup for beam focusing will be necessary. Using the layer application parameters and the curing setup with hexapod integration, curing parameters for curing individual features and homogenous surfaces need to be determined. The geometry and repeatability of cured structures has to be evaluated and discussed. Finally, the hexapod shall be able to be used to cure structures on convex substrates with and without correction of the substrate geometry and curing results on convex surfaces will be discussed. An outlook will present the next steps in analyzing structures on convex surfaces, coating multiple layers on substrates and automating the layer application and curing process.

2 State of the Art

This chapter deals with an introduction in the process of Laser stereolithography and the advancements in processes to cure micron and sub-micron scale structures as well as the development of systems for the manufacturing of micron-scale hybrid optical elements on non-planar surfaces such as lenses. The focus of this chapter is on the setups used to achieve hybrid optical elements, the – mostly geometric – restrictions of the setups, the methods employed to achieve a defined layerheight on a substrate surface and the resulting curing geometry, in order to get an understanding of the current state of the art as well as to determine possible challenges and possibilities for the development of a laser stereolithography setup with 6 degrees of freedom and the structuring on non-planar surfaces.

The process of Laser stereolithography (SLA) is a process, where laser radiation is applied to selected areas of a photosensitive material [52, p. 2]. During the process of SLA an absorption of focused laser light in a small volume of photosensitive polymer occurs, causing this volume to polymerize. With respective beam movement introduced by moving the substrate or the laser beam for example with a Galvo system, 2.5D structures can be generated. Laser stereolithography is part of the laser additive manufacturing technology which is the oldest and still most precise additive manufacturing (AM) process. [17, p. 37] The technology as well as the documentation of this process has been extensively researched and improved since its invention.
Today the process of laser stereolithography is used to create small scale structures in photosensitve layers with dimensions typically ranging from a few hundred nanometers to a few micrometers being limited on the low end by the diffraction limit of the laser. [22] The technology can and has been used to manufacture diffractive optical elements. The following figure 2.1 shows a chart on the possibilities of manufacturing diffractive optical elements on a surface for with process of direct laser writing which is introduced in the next section, as well as a sub-micron scale structure with a structure width of around 600 nm which is on the lower limit of possible curing size cured by a one-photon absorption lithography setup. The manufacturing of DOEs as shown in figure 2.1a is done by curing binary or continuous structures which can be created using laser power modulation or using lithographic masks to modulate the exposure energy. The possibilities of creating DOEs with direct laser writing can be translated to laser stereolithography, except for curing 3D structures, which enhances the diffractive properties without compromising the lateral resolution as well as enhancing the freedom of design for the cured element, though those can only be achieved through layer-by-layer curing in traditional laser stereolithography.

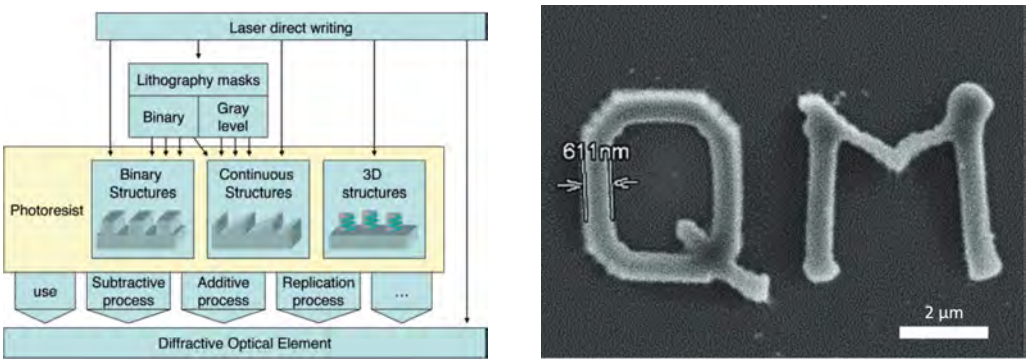

(a) (b)

Figure 2.1: The process and result of stereolithographic fabrication a) Methods for creating Diffractive optical elements using a DLW setup [22] b) Example for a submicron structure cured with a one photon stereolithography setup [49]

To achieve more sophisticated and precise structures, two-photon lithography can be used, which allows achieving structures below the diffraction limit of the laser by using a ultra-short pulse (USP) femtosecond laser. Using a femtosecond laser introduces a highly localized polymerization reaction using irradiation in the infra-red spectrum which is double the wavelength of the polymers absorption range, as long as the radiation is big enough to induce two-photon absorption. Since many photoresists are transparent in the infrared spectrum, this method not only significantly increases the possible spacial resolution to circa 100 nm, it also enables the curing of 3D structures since the polymerization can be induced at any given point in a photopolymer. [35, p. 430-433] The process of using the technology of two-photon polymerization to create sub-diffraction limit 3D freeform geometries is called direct laser writing DLW. It should be noted that even though commonly associated with two-photon polymerization, laser direct writing can also refer to a single-photon laser lithography process, which this work will refer to as laser (stereo)lithography or SLA. The following figure 2.2 shows a DLW setup with a femtosecond laser for two photon polymerization as well as a photonic crystal manufactured using two photon polymerization, which shows the fabrication possibilities of a resolution of 100 nm and the fabrication of a three dimensional structure.

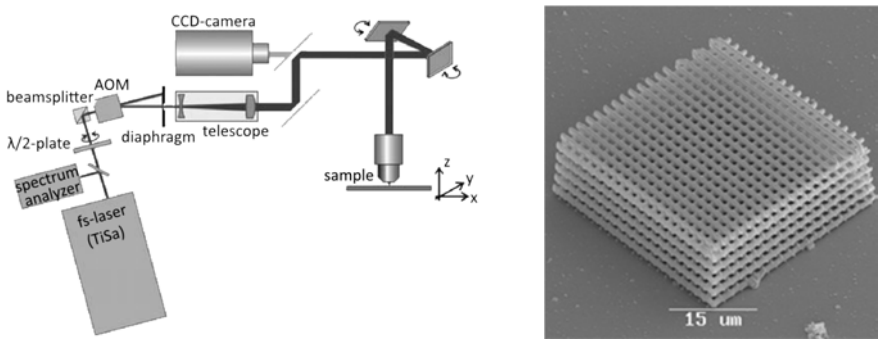

(a) (b)

Figure 2.2: Two photon polymerization setup and results a) Modified direct laser writing setup with femtosecond laser [35, p. 435] b) Photonic crystal manufactured with TPP [35, p. 438]

The following sections discuss the current advancements in the fabrication of hybrid optical elements on curved surfaces.
First efforts in utilizing stereolithography to manufacture large DOEs on curved surfaces are presented by Xie et al. [82, 81] using a substrate on an air-bearing spindle and 3-axis stage with an optical head assembly for beam manipulation to create rotationally symmetric structures on a convex lens. With their setup they are able to create a diffraction grating [82] as well as a large holographic element by deliberate over-/ double curing of defined sections of a lens [81]. Their curing results reach dimensions of 0.7 to 10 µm structure width at a thickness of 0.9 µm of a spin coated diluted positive photoresist, resulting in a structure height in the range of 250 nm. [82, 81] The following figure 2.3 shows a 3D measurement of a section of a circular grating manufactured with the setup proposed by Xie et al. Their setup however limits the surface geometry to large radii of curvature of the substrates in the range of hundreds of millimeters, where the beam needs to be refocused for a defined distance from the surface center, but the marginal change in curvature leads to negligible influence on the structure geometry relative to the lateral movement from the lens center.

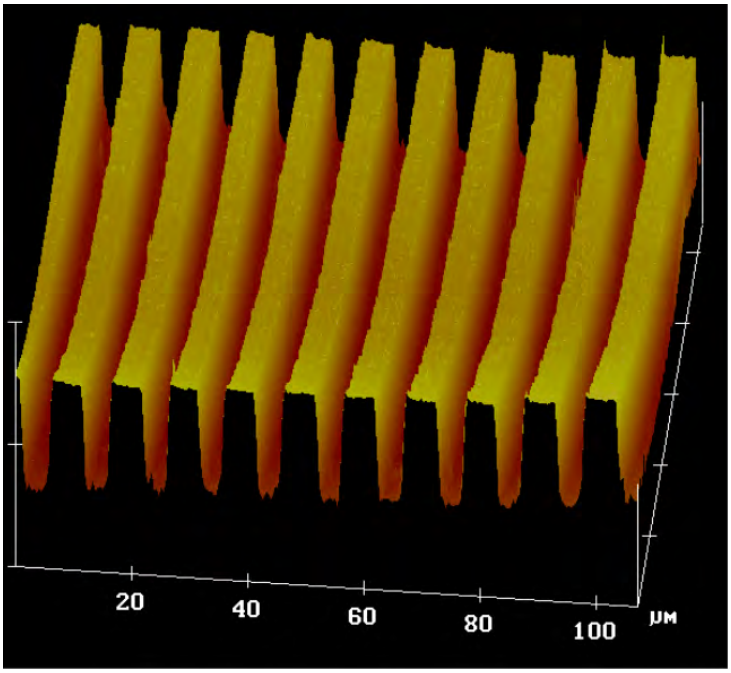

Figure 2.3: 3D measurement of a periodic circular grating segment with a structure width of 10 µm manufactured on a concave lens with a ROC of 504 mm [82]

Radtke et al. developed a SLA system to overcome these aforementioned restrictions [63]. By introducing a two-directional mechanical tilt of the substrate and one-directional tilt of an industrial lithography setup, the curvature of a substrate can be mitigated by positioning the incident beam perpendicular to the intermediate tangent plane of a small defined area of the surface. A sketch of the basic functionality and operating principle of this setup is shown in the following figure 2.4. This setup allows mechanical tilt of up to 10 degrees and therefore increases the viability of curing on curved surfaces down to a minimum radius of curvature (ROC) of around

10 mm and the ability to compensate sag heights of up to 30 mm. The positioning of the substrate is achieved using an optical auto-focus and a control software to adjust curing profiles and setup position. The beam is positioned using a mechanical stage in combination with an acusto-optical deflector.

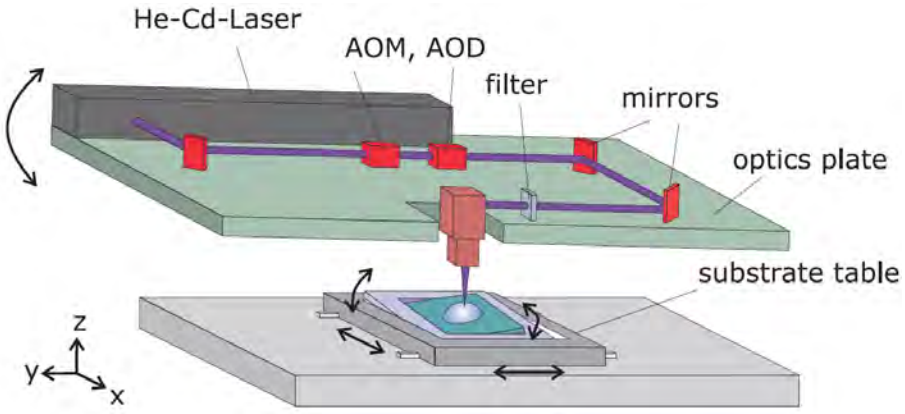

Figure 2.4: Operating principal of a laser stereolithography setup with a tilt correction for structure curing on curved surfaces with large sag heights [63]

Using an algorithm for pre-distorting surface data, geometry data is calculated and the surface is divided into 600 x 600 µm subfields which are exposed separately under a defined tilt angle. With this setup the creation of a DOE to reduce chromatic aberrations of a biconvex lens is achieved using a diffractiv lens geometry cured by emulating grey-scale lithography, scaling the laser power within a discrete number of steps to achieve a continuous structure on the lens. The following figure 2.5 shows a sketch of the diffractive element cross-section cured onto the biconvex lens and the resulting structure as seen under a microscope, where the separation of the individual subsections of the lens that are manufactured individually are clearly visible. This setup shows a comparable structure quality to planar surfaces.

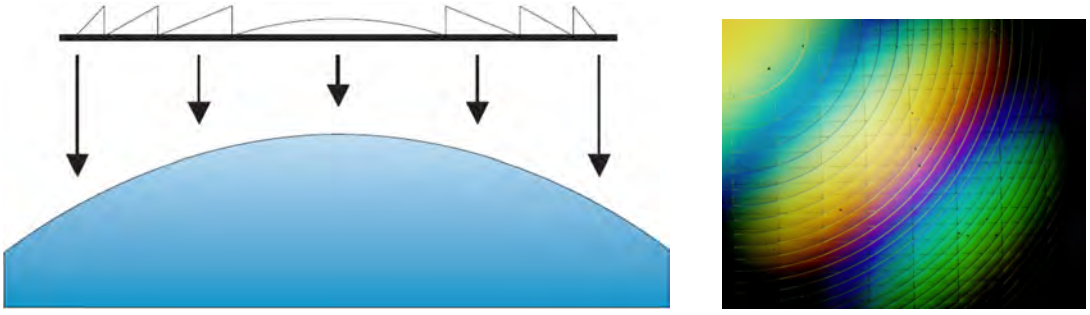

(a) (b)

Figure 2.5: Curing results of a laser lithography setup for a continuous zone plate structure on a biconvex lens [63] a) Sketch of pattern Design for quasi gray-scale curing on convex lens b) Picture of cured structure on convex surface

The results presented show the possibility of functional, high quality optical micron scale structures on curved surfaces with large sag heights up to 30 mm for surface deviations of up to 10 degrees using a complex highly modified industrial SLA setup. This basic idea has been

adopted and improved over the last years. The following sections discuss different approaches as well as the advancements of setups and utilized hardware and methods to show current approaches on the subject.

Häfner et al. [23] proposed and showed a different approach using a high precision auto-focus sensor in combination with a piezo actuator and polar coordinate modelling of structures to create continuous patterns as well as binary structures using laser stereolithography. The focus of their work was on the compensation of sag distance and surface irregularities rather than mitigating the incident angle of the beam. This setup allows the manufacturing of rotationally symmetric structures on curved surfaces up to an angle of 15° by in-situ adjusting the focus position in a range of up to 20 µm. All movements are performed using mechanical stages on the setup in combination with a rotation stage where the substrate is located.[23] The following figure 2.6 shows the schematics of the setup with the optical autofocus and the writing beam which is dynamically focused on the lens surface during the curing process, as well as the measurement of a resulting grey scale geometry at the maximum described surface angle of 15 degrees. This setup shows a comparable structure quality to structures cured with SLA on planar surfaces, however it is only viable when neglecting the shape deviation induced by the substrate curvature, which is only feasible for very small feature and layer sizes and might influence the achievable optical properties, especially for binary structures.

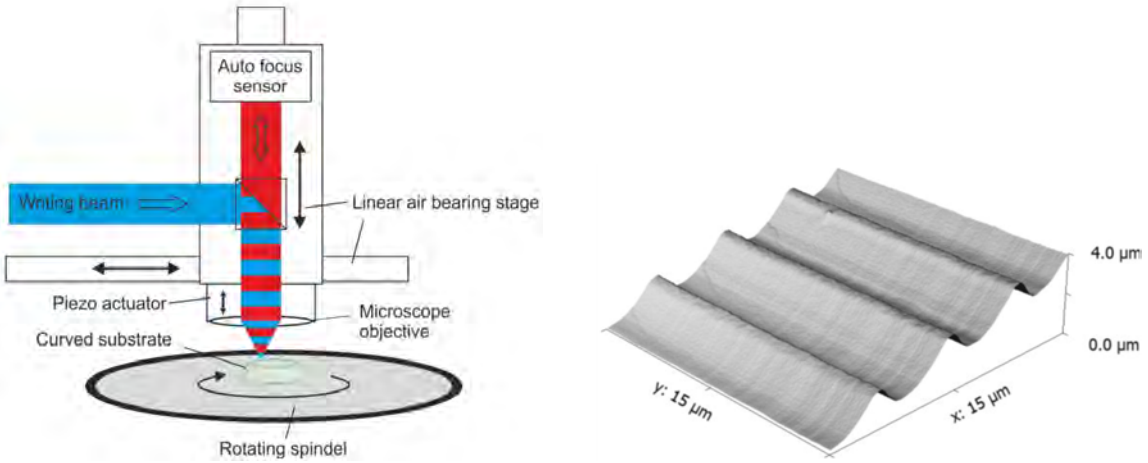

(a) (b)

Figure 2.6: Curing setup on curved surfaces up to 15° without tilt mitigation [23] a) Schematic representation of system functionality with optical auto-focus and piezo precision position control b) 3D measurement of a continuous gray scale structure at a surface angle of 15°

Ai et al. [1] propose a similar setup to Häfner et al. but with the advancement for rapid fabrication by using a voice coil actuator to achieve a more dynamic refocusing process and a high-speed Galvo scanner, achieving a fast process time. A schematic of the used setup is presented in the following figure 2.7. Their setup utilizes a nanosecond laser and by introducing an additional z-stage allow the fabrication of geometries with a sag height of up to 50 mm. The use of a high power nanosecond laser enables the use of very high scanning speeds with sufficient exposure to operate more dynamically. The presented setup operates at a scanning velocity of

1000 mm s^{-1} at a laser power of 20 mW. [1]

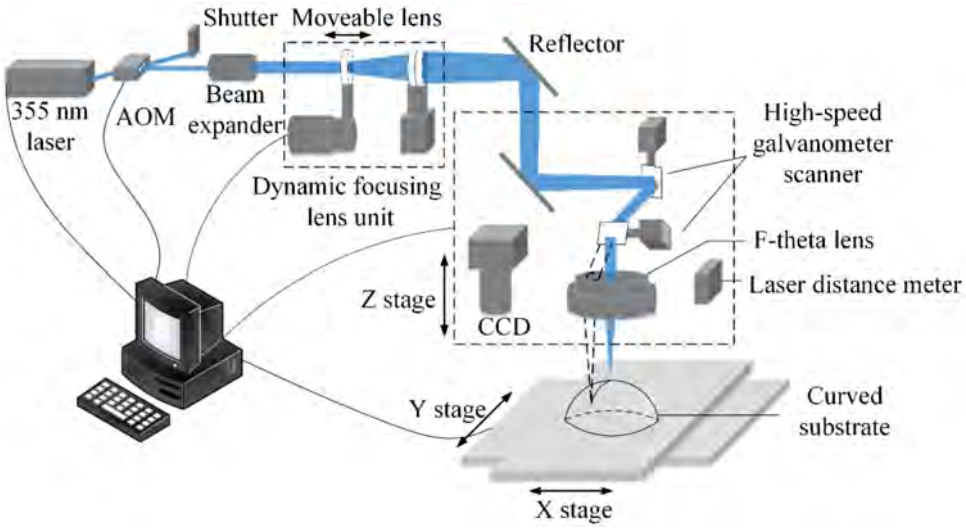

Figure 2.7: Setup for rapid structuring on curved surfaces without tilt mitigation using a voice coil actuator and a Galvo scanner [1]

In a clean room environment, to minimize substrate and resist contamination, they present the fabrication of a concentric circular grating with a width of 12.5 µm, a repeatable height of 1.6 µm and a spacing of 25 µm. By defining an acceptable error in focal spot diameter of 10% due to the curvature of the lens a sag height maximum needs to be individually determined for a substrate with a defined radius of curvature. Similar to Häfner et al. [23] this setup allows the fabrication of micron scale structures by defining an acceptable error due to substrate curvature for high quality structures without offering a compensation method for curvature induced shape deviation. However this setup due to the use of a Galvo system is able to manufacture free-form geometries rather than being limited to concentric structures.

Kim et al. [34] propose an optimization to the previously used in-situ focus abilities which utilizes a confocal sensor aligned with the curing beam measuring through the bottom of a transparent substrate. For their two-photon DLW setup this is a necessary step, because curing sub 100 nm structures requires a very precise focusing to achieve the best possible resolution. This allows the compensation of the issue, that when the beam path for curing is the same as for focusing, the polymerization occurring during the focus determination influences the measured result. Therefore the focus position is either slightly biased by the polymerization reaction, or the incident angle for the focusing beam needs to be adjusted so that the incident position is slightly different than for the curing beam. This is negligible for planar surfaces, however can play a role in the focus precision for curved surfaces with a small ROC. [34] This level of precision though is only required for sub-micrometer polymerization to mitigate as much error sources as possible due to the precision necessary to manufacture such small structures. Due to the structure sizes and small difference in the index of refraction between a cured and fluid photoresist this method is only applicable for a single layer. Using their setup they were able to create sub-micron scale structures with a high repeatability in structure height under 100 nm.

The result of a line pattern on a spherical surface with a cross section of the structure geometry is shown in the following figure 2.8.

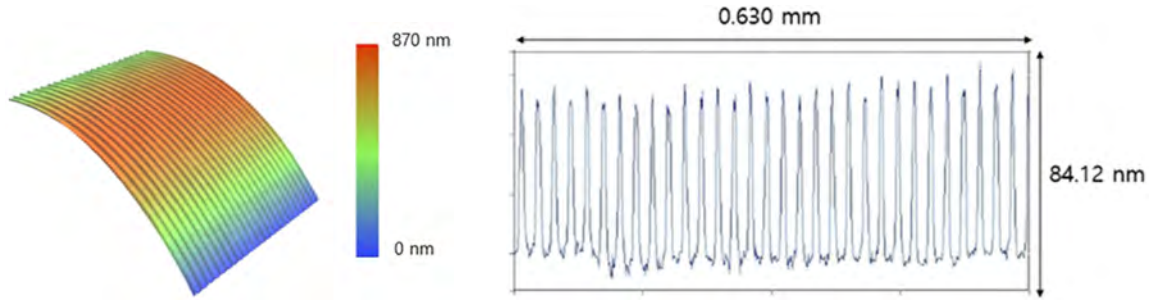

(a) (b)

Figure 2.8: Results of a TPP cured line pattern on a spherical substrate using a confocal autofocus method to mitigate error in conventional curing setups a) 3D measurement data of the line pattern on spherical surface b) cross-section of the mesaured line pattern

Setups like the ones presented have been used to manufacture micro- and nanophotonic structures and functionalize optical surfaces. For example, AlQattan et al. [2] manufactured two-dimensional holographic structures on a contact lens using two-photon absorption DLW ablation, increasing the diffraction efficiency of the lens by more than 10%. A result of their efforts is shown in the following figure 2.9, showing a holographic optical element on a contact lens in use and a photograph of the element in question, that is used as an optical transducer for diagnostic purposes of tear electrolytes using an optical fibre sensor.

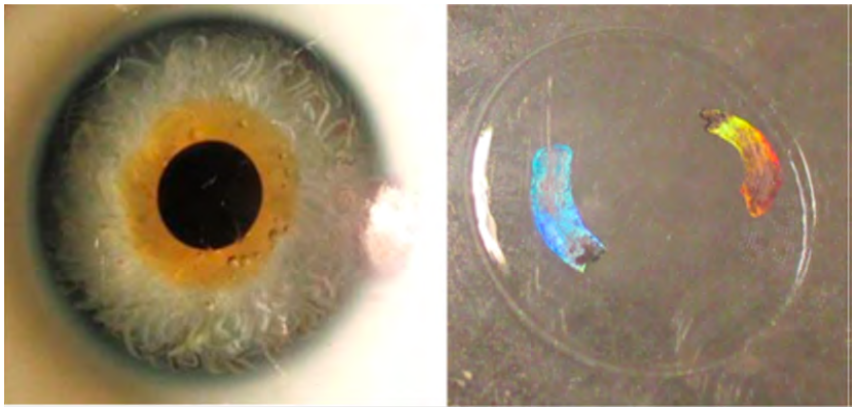

Figure 2.9: Picture of a functionalized contact lens for diagnostic purposes structured with DLW [2]

The current setups for SLA and DLW on curved surfaces show the possibilities for creating and curing hybrid optical elements on curved surfaces. The methods used to compensate the surface geometry employed are using a dynamic focus modulation with and without autofocus or even a dynamic focus in combination with a tilt correction of the incident beam to compensate the curvature influencing the relative focus shape at the point of incident. Utilizing the aforementioned methods, it is possible to compensate large sag heights in the range of tens of millimeters. Depending on the type of setup, quality of hard- and software as well as the polymerization principle (one or two photon) it is shown to be possible to cure structures with

dimensions in the range of hundreds of nanometers up to tens of millimeters even for highly curved substrates with heights below 100 nm. This means the achievable results for curing on curved surfaces are coming very close to the possible results achievable on planar surfaces.
Many of the presented setups however are limited to certain substrate geometries mostly the ROC of the substrates due to a lack of the possibility for precise positioning in a high z-range. Another common restriction is the limitation of the cured structures to be rotationally symmetric due to limitation of high-precision beam positioning systems, where the substrate rotates around its central axis and the beam position is modulated in one direction with a mechanical actuator. The last limitation of fabrication lies in the ability to compensate substrate curvature on the point of incident. Without correction for the angle on the incident beam, the cured shape will always deviate from its desired form, this influence is going to impact the results on large radial distance from the substrate center and for small - especially individually standing - features. Another thing to note is, that while the lithography setup and substrate intake are usually separated, the movement for beam positioning and focus is performed using a combination of moving both setups to achieve a displacement in certain degrees of freedom.
For the fabrication of the necessary defined layers on curved substrates the most commonly used technology is spin coating, which is utilized in all previously discussed setups and results. Most of the presented curing results are achieved using a positive photoresist, which is described in chapter 3.1. It is desirable to replicate structures after lithographic fabrication, this allows a more rapid production speed as well as - by varying material and replication process - an improvement of optical, mechanical or thermal properties of the functionalized structure. Such a replication process for example is UV molding, where a replica is produced by generating a master mold which can be easily transfered on many substrates allowing for a fast and repeatable replication.[62]. The use of positive photoresists instead of negative photoresists i.e photopolymers in spin coating has the advantage that those resists typically contain a high amount of solvent and dry during the evaporation step of the coating process, leaving a static layer if the process parameters are chosen correctly. For the fabrication of specialized structures such as microlens arrays, spin coating does not work due to the resulting curing geometry from laser induced polymerization, which is discussed in chapter 3.3. For special applications like this a different approach like a continuous reflow process, which exploits the surface tension of micro droplets needs to be used [62].

The following chapters deal with the development of a one-photon-polymerization laser stereolithography system. Due to the high cost and the necessary geometrically large and extensive setup, this system will not use a two-photon DLW setup and is used as a proof of concept and research object for laser scanning lithography on non-planar surfaces, eventually to be advanced. The setup will be using a high speed Galvo and a hexapod with 6 DOF to cure oriented structures on planar and convex surfaces and an investigation of the coating behaviour and coatability of substrates using the spin-coating technique and a negative photoresist are performed.

3 Fundamentals

This chapter deals with the fundamental processes, physical quantities, and principles as well as newly introduced hardware that are necessary to understand the setup. Observed phenomena and calculations performed in this report are described. The chapter focusses on the necessary fundamentals for especially the process of laser lithography, spin coating of planar and curved surfaces as well as an introduction into best practice for coating and preparing substrates.

3.1 Polymerization

Polymerization is a chemical process in which monomers or oligomers interconnect and form a three-dimensional network of highly cross-linked polymer to create a solid structure[35]. Figure 3.1 shows the base working principle of UV induced polymerization which is described in this section. There are two main types of polymerization, free-radical and cationic polymerization. The polymerization reaction in this setup is the free-radical polymerization and is presented in this section. The process of free-radical polymerization is founded on the curing of liquid monomers and oligomers. Exposing them to a light source with a specific wavelength causes them to form long polymer chains. The polymerization reaction consists of three key reactions. The start reaction, the chain reproduction reaction and lastly the termination reaction. [40] In the start reaction, photoinitiators will absorb the light and disintegrate due to the energy impact from the light source, providing active species with just one electron on the outer shell (radicals) that will cause the polymerization [69]. These extremely reactive radicals drive the chain growth. After the start reaction has taken place, the resulting radicals react with the double bound synthetic material (resin material) in the mono- / oligomer until a termination reaction occurs. This is called the chain reproduction reaction. The termination reaction describes the process of two polymer chains combining or one polymer reacting with an initiator, terminating the chain growth. [40]

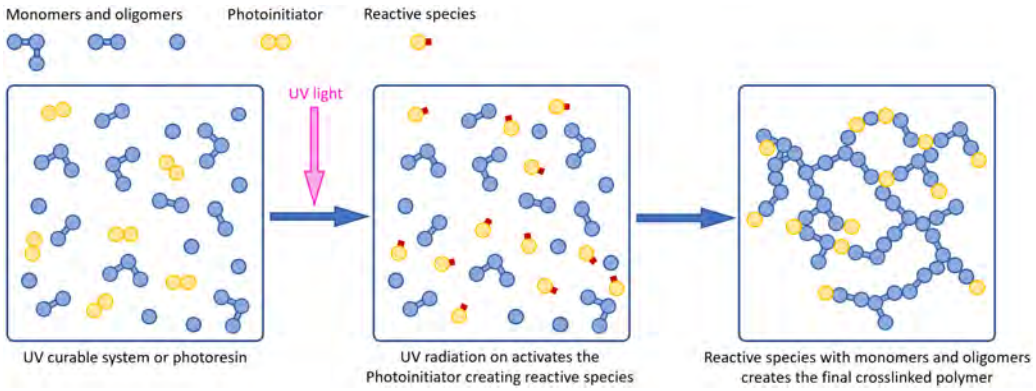

Figure 3.1: Schematic representation of the start, chain reproduction and termination reaction in a photopolymer upon exposure to UV irradiation [40]

Using highly localized radiation i.e. a focused laser beam. Polymerization can be induced only in a small volume of photosensitive material surrounding the impact of the beam. Materials that change properties when exposed to a light source of a defined wavelength are called photopolymers or photoresists. These materials can be divided into two categories, Photopolymeric (negative photoresists) and Photodecomposing (positive photoresists), the principle of both forms and the resulting geometry after exposure is shown in the following figure 3.2. Negative photoresists experience a polymerization of material upon contact with light radiation, leading them to form a solid cross-linked polymer. Positive photoresists form a solid layer on a surface after their application due to the evaporation of solvent in the resist. They experience photodissociation, which is a reaction that breaks their chemical compound upon exposure to a light source of a defined wavelength, which liquifies the exposed area. Positive photoresists typically allow a higher resolution for applications with structure sizes below 10 µm, however they mostly create a negative of the desired structure [73]. From this point forward, negative photoresists will be referred to by photopolymers, while positive photoresists will be referred to as photoresists.

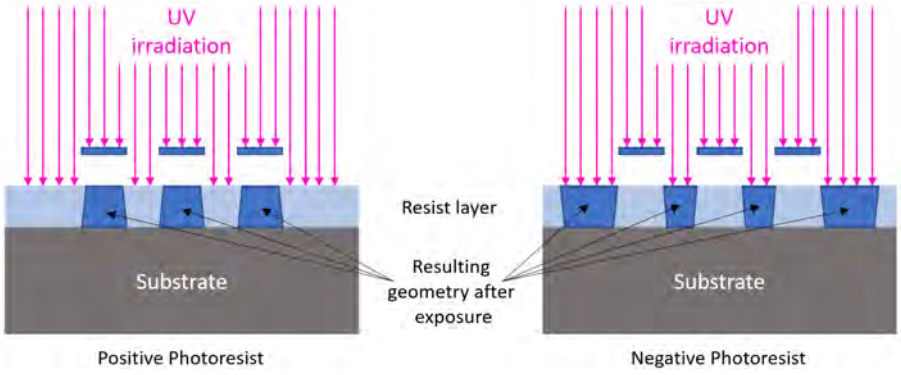

Figure 3.2: Schematic representation of the behavior for positive and negative photoresists reactive in the UV spectrum when partially exposed to a UV light source

For this setup a prototyping photopolymer (PR48) is chosen, which allows precise polymerization and therefore direct functionalizing by locally exposing the photopolymer with a SLA setup. The principle of a SLA setup is presented in the next subchaper 3.2.

3.2 Laser Stereolithography

Stereolithography (SLA) is not only the oldest, but till today also the AM process with the best resolution achievable. Laser stereolithography (SLA), direct laser writing (DLW) and selective laser sintering (SLS) belong to the class of laser-based AM techniques. SLA and DLW are used for example in manufacturing of micro-optics, microfluidics, biomedical implants or semiconductor technology. [69] The base working principle of SLA and DLW is to put a photosensitive polymer on a substrate and write 2.5D or respectively 3D structures in the photopolymer, by moving a focused laser spot in the resin. When a focused UV laser interacts with a UV absorbing molecule of the resin, a polymerization reaction occurs. In most cases the laser beam is

guided by a Galvo scanning system. [17, p. 37] Parts purely created by SLA are typically manufactured layer-by-layer in a resin vat. After scanning and solidifying a layer in a photopolymer the build platform is lowered by a defined distance which equals the desired layerheight into the resin vat. This recoats the top surface. Repeating this process from bottom to top generates the final geometry. Figure 3.3 shows the schematic of a standard SLA system setup. After the print is finished, the part has to be cleaned and fully cured. For post curing a UV chamber is used. This is a necessary post-processing step for the SLA procedure to fully harden the resin. [17, p. 38] This process can be used with filled and unfilled epoxy and acrylic resins only. [17, p. 39]

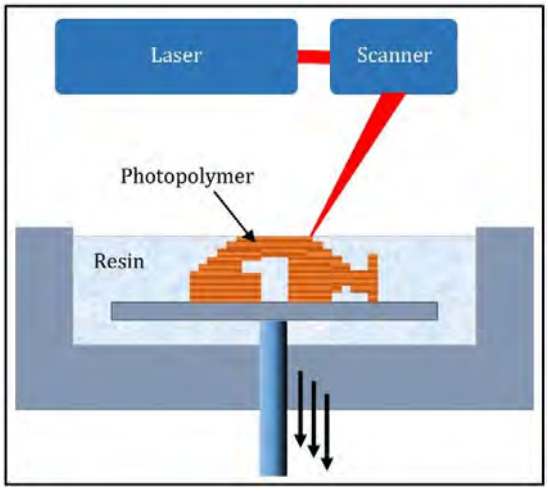

Figure 3.3: Schematic representation of a typical SLA setup for 3D part fabrication [16]

The basic setup shown in figure 3.3 above is for manufacturing entire parts using SLA. For creating hybrid optical elements with varying and especially non-planar substrate geometries the approach using a resin vat and submerging the substrate is no longer feasible. A different approach to achieve a homogenous layer and recoating on different substrates needs to be found. Creating HOEs using SLA or DLW therefore requires a modified setup as well as means to apply defined layers on a substrate, for example spin coating which is presented in section 3.6.

The active region of a focused laser beam has a spheroidal shape. This is the fundamental component of the procedure. When exposing a photopolymer with the focused laser beam it creates a so-called volume pixel (voxel), which describes the volume of material polymerizing by exposing it to a focused laser spot with a defined energy for a defined time. Contiguous geometries can be achieved by generating a defined voxel overlap using a precision positioning system like a Galvo mirror system. When the spacing of voxels is chosen correctly for a defined layerheight and exposure energy, the space between two neighboring voxels is filled by diffusion assisted polymerization. The principle of a voxel, the procedure of generating 2.5D geometries with DLW or SLA utilizing diffusion assisted polymerization and an example of a printed line with the setup used in this project is shown in figure 3.4. The size of an individual voxel is mainly determined by the used laser and the quality of the scan lens. A focus lens with a high

numerical aperture (NA) achieves a smaller focal diameter and therefore leads to the possibility of creating smaller voxels. [60]

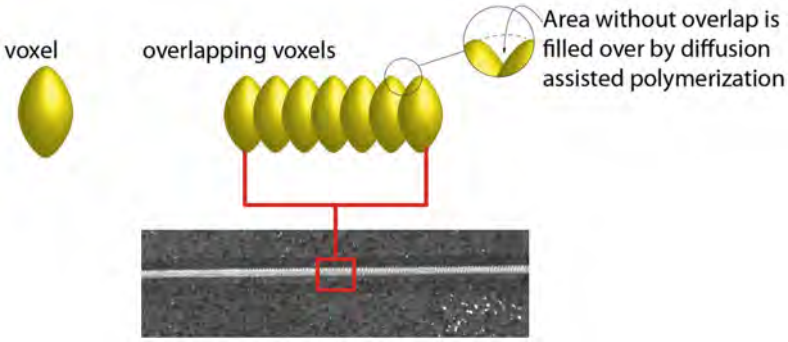

Figure 3.4: Schematic of voxels in laser lithographic processes and the creation of homogenous structures with diffusion assisted polymerization on the example of a cured line with the setup of this work [60]

The shape and the dependence of the shape of the resulting geometry from laser stereolithography has been mathematically described [29]. This work is presented in the next subchapter 3.3 and can be used to determine curing parameters for a desired curing shape in a photopolymer.

3.3 Fundamentals of Stereolithography

The following subchapter deals with the mathematical description of the curing results expected from laser lithographic processes as proposed by Jacobs in his Fundamentals of stereolithography [29]. This work has been extensively described in a previous report on this topic [26]. These next sections shall give an overview on the most important assumptions, relationships and results that are used to describe and predict the curing geometry for a defined setup and material. This mathematical description is mainly dependent on the scanning velocity and laser power (exposure) and will be used for the determination of curing parameters described in chapter 4.3.

The model of the stereolithography process as described by Jacobs is based on three key assumptions: the resin obeys the Beer-Lambert law of absorption, the intensity distribution of the focused beam has a gaussian shape and the transition of the resin from liquid to solid occurs exactly at the gel-point which is the point where the exposure energy is just high enough to start the polymerization process but not fully cure the resin.[29] Using these assumptions the maximum exposure energy at the center of the incident focused beam, which will be refered to as maximum curing energy going forward, which is proportional to the laser power and inversely proportional to the beam waist radius and scan velocity and can be calculated using the following equation 3.3.1.

$$E_{\max} = \sqrt{\frac{2}{\pi}} \cdot \frac{P_L}{v_S \cdot w_0} \tag{3.3.1}$$

With the laser power P_L, the beam waist radius w_0 and the scan velocity v_S. Following the Beer-Lambert law of absorption, the energy of the beam decreases from the center point outward.[29] Using the characteristic values for photopolymers, namely the penetration depth D_P describing the distance from the resin surface it takes for the intensity to reach $\frac{1}{e}$ of its original intensity and the gelation threshold E_C which is the minimum necessary exposure the Photopolymer needs to experience to start polymerization, the maximum curing depth can be calculated using equation 3.3.2.

$$C_D = D_P \cdot ln\left(\frac{E_{\max}}{E_C}\right) \tag{3.3.2}$$

With the penetration depth D_P, the maximum curing energy $E_{\max}$ and the gelation threshold E_C. This equation shows a logarithmic dependency of the curing depth C_D to the maximum curing energy. When plotted against a semilogarithmic scale on the x-axis, the working curve of the curing depth over the maximum curing energy is a linear curve with a slope of D_P. The corresponding expected linewidth for a specific curing depth can be calculated using the following equation 3.3.3.

$$L_W = w_0 \cdot \sqrt{\frac{2 \cdot C_D}{D_P}} \tag{3.3.3}$$

With the maximum curing depth C_D. The linewidth L_W is proportional to the beam waist radius w_0 and the square root of the curing depth over the penetration depth. This means that the ratio of curing depth to the penetration depth can be optimized to achieve a certain ratio of curing depth to line width by modifying the maximum curing energy (see chapter 4.3.2.1).
These previous equations 3.3.3 and 3.3.2 describe the maximum height and width of a polymerization reaction initiated by a focused laser beam in a photopolymer and leads to an understanding of the expected dimensions for defined curing parameters. To determine the actual expected geometry in a volume of photopolymer, the exposure energy at a given distance from the focal point of the laser in a cartesian coordinate system can be calulated, at any given point. Where the exposure energy $E(x,y,z)$ is greater than the gelation threshold of the photopolymer E_C a polymerization reaction will occur. By defining a coordinate system as shown in figure 3.5 and using the intensity distribution of a focused (gaussian) beam moving at a defined velocity v_S the exposure energy at a given point can be calculated [29].

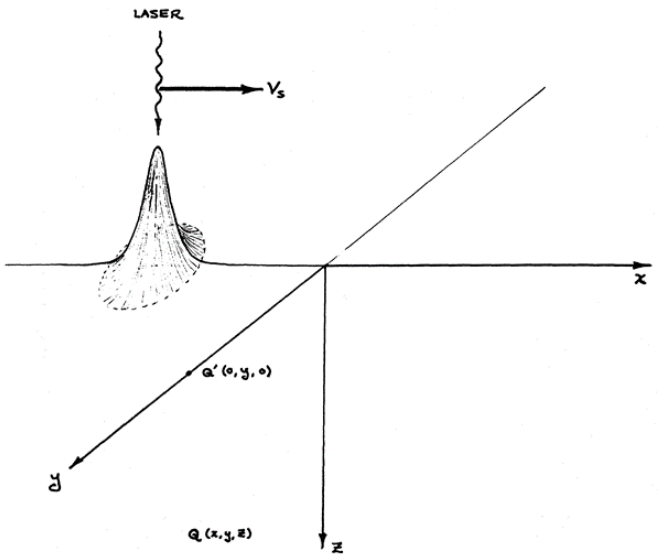

Figure 3.5: Intensity distribution on resin surface and definition of coordinate system for calculation of curing shape [29]

The intensity of a gaussian beam dependent on the radial and lateral distance from its respective focal point at a given point can be determined using the following equation 3.3.4.

$$I(r,z) = \frac{2 \cdot P_L}{\pi \cdot {w_0}^2} \cdot e^{-\frac{z}{D_P} - \frac{2 \cdot r^2}{{w_0}^2}} \tag{3.3.4}$$

With the radial distance from the center of the focal point r and the lateral distance z in curing direction . The radial distance from the focal point r can be translated to cartesian coordinates x and y using the pythagorean theorem and expressing r as $r^2 = x^2 + y^2$. Since the intensity distribution is rotationally symmetric. The cross-section geometry can be determined using just one variable x or y to determine the cross-section of a single voxel. The exposure energy is the intensity that the resin experiences over a certain amount of time, so it is the integral of the intensity over time. In other words, the amount of time the laser beams remains at a certain position x, dt = dx/vs [29]. With these dependencies established, the exposure energy a photopolymer experiences at a given point (y,z) from the center of the focal point can be expressed using the following equation 3.3.5.

$$\boxed{E(y,z) = \sqrt{\frac{2}{\pi}} \cdot \frac{P_L}{w_0 \cdot v_S} \cdot e^{-\left(\frac{z}{D_P} + \frac{2 \cdot y^2}{{w_0}^2}\right)}} \tag{3.3.5}$$

With the distance from the focus center on the polymer surface y. Using this equation, the geometry cross-section resulting from the exposure with a defined laser power and scanning

velocity of a defined photopolymer is determined as any point (y,z) where the exposure energy is higher than the gelation threshold of the photopolymer $(Y,Z) \in (E(Y,Z) > E_C)$. Using the equations presented, a model which is presented in chapter 4.3.2.1 can be created to optimize the curing parameters P_L and v_S to achieve a desired ratio of curing depth C_D to linewidth L_W and calculate the necessary exposure energy to achieve that ratio as well as describing the expected shape of the cured cross-section.

3.4 Material Shrinkage

The major limiting factor of the possible exposure energy and structure geometry for curing small scale structures in a photopolymer is polymerization induced shrinkage. It is observed that small structures cured with a high exposure energy are prone to detaching from a substrate and curling up. The curling effect observed suggests a force acting perpendicular to the adhesive force holding the structures on the substrate. Once this force exceeds the adhesive force the lines start detaching until an equilibrium is reached. If this equilibrium is reached before the line is completely detached, the structures do not fully detach from the substrate and a curling effect occurs. The phenomenon of polymer shrinkage in photopolymerization regarding structure adhesion and the influencing factors on shrinkage are described in the following sections.
Shrinkage is a phenomenon observed in photopolymerization that has a big influence on the final geometry [32]. Photopolymers experience shrinkage upon changing from a liquid to solid form. "As polymer chains form [...] during exposure, the density of the region is increased, [because of the change in the distance between monomers (van der Waals distance) [37]]. The individual monomer molecules polymerize in a chain formation and become tightly packed together, resulting in shrinkage of the photopolymer layer."[9] The total stress is dependent on the deformation due to shrinkage, that every volume element (voxel) experiences, since there is a timely separation between the start of the polymerization reaction for every single voxel. The following figure 3.6 illustrates the shrinkage force a voxel experiences upon polymerization. The adhesion force holding the structure on the substrate prevents material shrinkage at the adhesion point. The force of the shrinkage that cannot take place leads to an internal stress in the cured structure.[10]

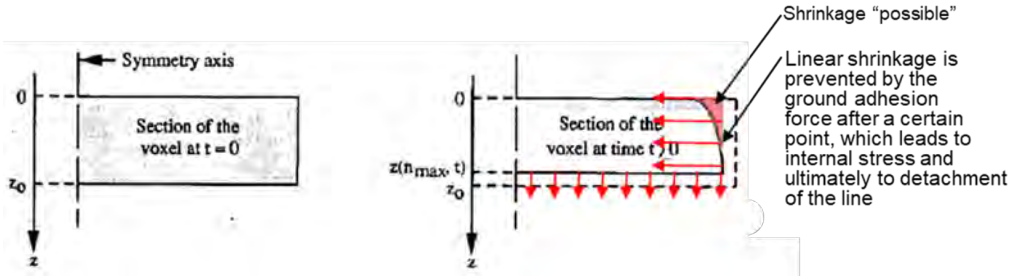

Figure 3.6: Schematic depiction of a voxel before and after the shrinkage effect with the resulting deformation. The adhesion force towards the substrate and shrinkage induced stress as red arrows [10]

"[The cured parts] experience shrinkage after they have been (post-) cured to complete the polymerization [...]. Shrinkage [...] can result in internally generated residual stresses and, subsequently, in strain deformations leading to considerable curl distortion and out-of-plane displacement (warpage) ".[31] "Residual stress generated during stereolithographic building and/or post-curing can be responsible for creep distortions, which can occur long after the structure is cured and may cause cracks and delamination within a geometry."[32] The main shrinkage occurs withing the first 30 s after the polymerization reaction and takes up to 15 minutes to be completed, depending on the resin [7]. Oxygen inhibition (see chapter 3.5), has been shown to delay the start of shrinkage occuring by approximately 20 s. [37]
The shrinkage occurring during and after a photopolymerization reaction is mainly dependent on the type of polymerization reaction and the curing parameters [61] as well as the overall degree of cure during the initial polymerization process. [32] The type of polymerization in this case using the PR48 prototyping photopolymer and a 405 nm UV laser is called free-radical polymerization. This form of polymerization reaction experiences the highest amount of shrinkage of up to 65% of its maximum dimensions. The curing parameters that play an important role in how much shrinkage occurs during photopolymerization are the curing energy, curing time (i.e. velocity) and geometry dimensions. Decreasing the exposure energy leads to a smaller absolute shrinkage since the cured volume per line drawn gets smaller. The geometry dimension and beam velocity are factors influencing the curing energy individually and can therefore influence the shrinkage rate. [80] The following Figure 3.7 shows the influence of the beam velocity and the line length on the rate of shrinkage occurring for two photopolymer prototyping resins with the capabilities of the setup used in this work highlighted.

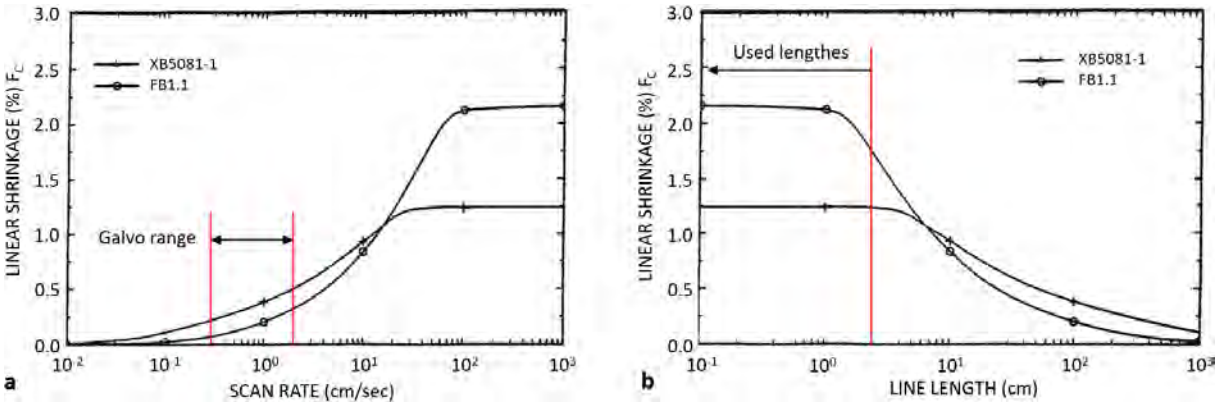

Figure 3.7: Investigation of the influence of velocity and linelength on the relative shrinkage.[80] a) Plot of the linear shrinkage over the scan rate (= scan velocity) for two prototyping resins with the velocity range for the current setup marked b) Plot of the linear shrinkage over the structure length for two prototyping resins with the possible range of curing length for the current setup

To conclude, the shrinkage during photopolymerization has a considerable impact on the resulting curing shape and can lead to a detachment of structures. Residual stress from shrinkage can lead to a detachment long after the curing process. The effects of shrinkage induced phenomena can be reduced by reducing the exposure energy and the scan rate (influencing the exposure

energy) or increasing structure sizes. Since the goal is to cure micron-scale structures, the exposure energy and the scanning velocity become the dominating factors in mitigating shrinkage effects. The information from this subchapter is used in an experiment presented in chapter 4.3.1 to determine threshold parameters for structures. These parameters reduce the influence of shrinkage to a point where the shrinkage induced effects no longer lead to detached or warped cured structures.

3.5 Oxygen Inhibition and mitigation Strategies

Oxygen inhibition is a phenomenon that occurs in photopolymer coatings that cure via free-radical polymerization which leads to uncured tacky surfaces and an incomplete cure after the polymerization process. It is a very undesirable process since it hinders the curing of desired heights in a layer especially in low-intensity processes e.g., a continuous laser source used for small-scale laser stereolithography like in the current project.[3] It also delays the shrinkage process (see chapter 3.4) leading to a more severe influence of shrinkage effects. This is because the shrinkage process takes place when the polymerization has already progressed further, leading to higher residual stress since the material is already more rigid. The phenomenon occurs when photopolymers are cured in an open-air environment. Here, oxygen present in the ambient air dissolves in the top portion of the liquid photopolymer layer. Oxygen present in a photopolymer may quench the excited state of photoinitiators. It can also react with propagating radicals that have already been excited, these reacted radicals are not energetically favorable for polymerization and rather tend to end the polymerization reaction by radical-radical recombination. Oxygen in the polymer can also abstract hydrogen from a molecule where a forming radical then has insufficient reactivity to instate the initiation process. This can lead to under- or even uncured structures, often requiring a much higher radiation dose to initiate a polymerization reaction. [39]
Since oxygen inhibition is an undesired phenomenon and the current setup operates under open-air conditions, these next sections will present some mitigation strategies to counter oxygen inhibition. Generally, there are two possible tactics to mitigate oxygen inhibition, first, by chemically modifying the polymer properties to prevent or interrupt the reaction cycle of oxygen with the photopolymer and second, using physical approaches to prevent the inhibition before it can even happen. Since chemical approaches like adding photoinitiators, molecular inerting or using hydrogen donors [39] all require special photopolymers or the modification of a standard photopolymer it is not desirable for this work since the goal is to provide a simple and efficient curing setup for standard photopolymers and will not be further discussed. The main physical strategies for preventing oxygen inhibition are inerting, lamination, temperature increase and the use of higher light intensity [39] which will be summarized in the next section.
The most widespread approach in preventing the diffusion of oxygen is inerting, which utilizes an inert gas like Nitrogen, Helium or Carbon Dioxide to displace ambient air and therefore oxygen from the polymer surface. By lowering the present oxygen below 1% this method allows

curing with low intensities and photopolymers with a low percentage of photoinitiators. Due to its simplicity and, in a small-scale laboratory environment, relatively low cost, this method is the most commonly used outside of large industrial scale applications. [39] However this method requires a special setup to create and maintain an atmosphere of inert gas. Another way of mitigating oxygen inhibition is the lamination of the photosensitive layer. Here a protective layer of e.g. wax or a UV transparent film is directly applied onto the surface and peeled off after curing, or the substrate itself is submerged into a UV transparent liquid. This method, though very effective, is only feasible for a number of materials, where it does not interfere with the structural integrity of the layer. Increasing the polymers temperature can be used to decrease oxygen inhibition, since oxygen solubility decreases for most liquids with rising temperature. The increase of temperature however leads to increased diffusion especially in acrylate-based resins which are therefore more affected by oxygen inhibition at high temperatures. An increase in temperature also influences the stability of the polymer layer, especially for fluid photopolymers on non-planar surfaces. The last method of preventing oxygen inhibition is to increase the intensity of the light-source which increases the number of radicals formed. It has been shown that the intensity is significantly more influential on reducing oxygen inhibition than the exposure energy. Therefore, using a short pulse of light rather than continuous exposure can create a much higher concentration of radicals whilst maintaining the overall same exposure energy. Since the laser used in the current setup is a continuous laser, this method is not feasible to use for this work.[39]

3.6 Spin Coating

The following subchapter deals with the introduction of the layer application process of spin coating to apply micrometer scale layers of photopolymer on planar and non-planar surfaces. Spin coating is one of the predominant processes to apply a defined, uniform layer of organic photosensitive material on substrates. [6, p. 85] It utilizes centrifugal forces which apply a radial force to a liquid on a rotating substrate to distribute the liquid evenly and create a homogenous film. The thickness of this film is influenced by the fluid flow and evaporation which comes from solvents with which some materials – especially for positive photoresists – are diluted. The following figure 3.8 shows the setup for coating material on the example of the spin coater used in this work. This device uses a chuck system for substrate intake and has a basic user interface to control the parameters necessary for a defined process: spin velocity and spin duration. It offers up to 10 custom process steps for one coating process, achieving rotational speeds from 100 to 6000 RPM.

Figure 3.8: The Ossila spin coater used in this project and its features

A good substrate wettability and the addition of solvents can counteract a layer collapse or the retraction of the layer to the smallest possible surface area due to surface tension [67]. The achievable thickness and properties highly depend on the nature of resin and its properties like viscosity, drying rate, percent solids and surface tension. [77] These following sections deal with the comparison of the spin coating method with alternative techniques for applying polymer films, the process of spin coating in detail, as well as influential parameters on the curing results and error sources. Finally mathematical models will be presented to calculate and optimize the process of spin coating on planar, concave, and convex surfaces.

3.6.1 Comparison of Layer Application Methods

Spin coating uses a dispensed amount of photopolymer on a substrate centered on the rotation axis. By spinning with a defined angular velocity the resin expands on the substrate leading to thickness reduction. [54] It is a fast and simple and readily available process that is mainly coupled to two process variables, the angular velocity i.e. revolutions per minute (RPM) and the viscosity of the applied liquid. This makes the process easy to control, because the film thickness can be changed by only modifying the spin speed. It also allows the film to get progressively more uniform as it forms, allowing it to form very uniform layers in a range from tens of nanometers up to hundreds of micrometers. [67, 6, p. 86] It has been extensively researched, documented and mathematically described. Its application ranges from the fabrication of circuits, optical mirrors, detectors, sensors to nano scale devices and photo resist application for patterning wafers in microcircuit production [67]. In photolithography it is extensively used to deposit layers of photoresist and photopolymer in the micrometer range [77]. Its main disadvantages are the relatively low material efficiency (up to 98% of liquid is spun off) and the difficulty in coating high topography geometries [67, 45, 5]. It also poses a difficulty for coat-

ing multiple layers especially on structures with a difficult topography or small features, as well as for creating very thin layers in the range of sub 10 nm [6, p. 86]. The substrate shape can also influence the achievable coating quality (see chapter 3.6.4). For non-drying liquids, it also shows a propagating influence of gravity in the possibility of achieving defined homogenous layers, especially on non-planar surfaces.
Other common techniques for the preparation of thin polymer films include Dip- and Flow-coating, Spray-coating, as well as more sophisticated and niche technologies which require an extensive setup and technology like plasma polymerization or pulsed laser deposition and chemical methods such as grafting. [50] The most common layer application methods other than spin coating are Dip-Coating and Spray-Coating which will be presented in the next sections.
Dip-coating is a relatively crude method of layer deposition. Here the substrate is simply submerged into a polymer or polymer solution. By controlling the variables of viscosity (solvent addition) and removal speed a uniform layer can be formed by dipping and removing a substrate into the polymer. If the substrate is planar, very homogenous, well-defined films can be created. [50] Like spin coating, dip-coating also allows the fabrication of very thin layers. It is also feasible for various shapes and shows some multilayer possibility. It poses a low surface roughness and – given the polymer well can be easily reused – is very efficient regarding material consumption. However, this technology suffers from the wedge effect, which means the thickness of the layers varies from top to bottom. It is relatively time-consuming and coating substrates only on one side is almost impossible. Furthermore, it offers very poor results for coating curved or flexible structures. [38, 51]
Spray-coating is a method which is often used in industrial scale applications. Here a solution of a material is applied to a surface by creating an aerosol of the material-solvent solution and spraying it onto a substrate. The solvent evaporates during spraying and after deposition, creating a relatively uniform film. The uniformity depends on the controllability of the aerosol particle size of the process.[50] Spray coating is a very fast process, that offers little material consumption and a good reproducibility. It shows very uniform deposition over cavities and free-form geometries and is less dependent the substrate shape. However, to achieve a smooth and homogenous coating, a highly viscous and diluted material and extensive optimization process is necessary. Compared to Dip- and Spin coating it requires the most complex system and has many influence and system parameters, making it hard to effectively optimize. The high aerosol concentration also necessitates an exhaust system and can be hazardous. [78, 33, 45]
Due to its simplicity, repeatability and the fact that a spin coating system is readily available for this work, spin coating is chosen as the desired way of layer application for this project. This coating process is already well described, especially for the layer application on planar, convex and concave surfaces, which allows for a predictable and easily optimizable process. Since the ROI for curing structures is way smaller than the substrate surface area the edge-bead effect is negligible. The range of feasible thicknesses is more than sufficient for the desired layer thickness in the micrometer range. However, the influence of gravity on the coating homogeneity and layer stability will need to be evaluated (see chapter 5.4.4.1). The ability to coat multiple

defined layers is yet to be investigated, however some efforts have been made in describing and coating on topographies and free form substrate geometries [79, 56].

3.6.2 Method

The following section describes the process steps and functionality of spin coating. The process of spin coating consists of four basic stages: Deposition, spin-up, spin-off and evaporation. Whereby the spin-off and evaporation stage contribute the most to the final layer thickness. The viscous flow of the photopolymer dominates early in the spin-off process, whereas the evaporation dominates later. [67] However, the influence of the evaporation on the final layer thickness as well as the drying effect the layer experiences depends massively on the type of resin and the amount of solvent. For example the photopolymer used in this work has almost no solvent by default and is not diluted for the application, making the influence of evaporation almost negligible. The following figure 3.9 shows the process steps of the spin coating process schematically from dispensing a), to spin-up b), spin-off c) and finally evaporation d). These steps are discussed in the following sections.

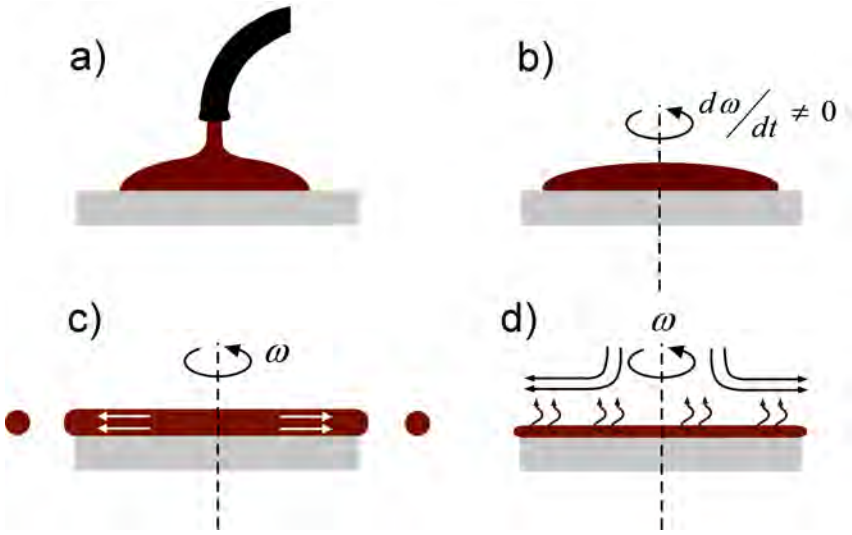

Figure 3.9: The four steps of the spin coating method for homogenous layer generation a) Deposition, b) Spin-up, c) Spin-off, d) evaporation [25]

The first stage in the spin coating process is the deposition stage, where a volume - typically in the range of a few micro- up to 10 millilitre - of an organic material, optionally in solution, is dispensed onto a substrate, usually with a pipette, syringe or specialized dispensing unit [6, 67, p. 85]. There are two variations in the dispensing step, static dispense and dynamic dispense. Static dispense is the deposition of a volume of material on or near the center of the substrate before spinning. Dynamic dispense is the process of applying the material whilst the substrate is turning at low RPM. [77] The ideal dispensing method hereby is dependent on the material and wettability of the substrate as well as the spin speed and the viscosity of the photopolymer. For very viscous photopolymers i.e. PR48 as well as for low spin speed, static dispense is recommended to avoid uncovered substrate areas and layer collapse. [54]

The second stage in the spin coating process is the spin-up stage. In this stage the substrate is gradually accelerated to its final velocity. During this stage the material expands over the substrate. This stage experiences aggressive material expulsion from the substrate by the rotational motion. [67]
The third and defining step of the spin coating process is the spin-off stage, which generates stable fluid outflow on the substrate edges. The viscous fluid forces triggered by the rotational motion dominate the material thinning, leading to a gradual fluid thinning by material removal – spin-off. This step is typically done at a range of 1000-12000 RPM for 30 - 120 s [54]. Here the amount of solvent present in the material defines the behavior of thinning. The less solvent present, the more the fluid behaves like a Newtonian fluid and the more uniform the fluid expands. This is important for the mathematical modelling of the process (see chapter 3.6.5). The edges of any substrate, especially for non-round substrates, are critical for the layer homogeneity. The fluid uniformly flows outward to an edge, however, due to surface tension and viscosity the material may form beads on the edges. The centrifugal force needs to overcome a certain point to fling these beads from the edges. Still the edge-bead effect is a common error influencing the layer homogeneity on substrate corners (see chapter 3.6.4).
When the spin-off stage is finished, i.e. when the rotation motion comes to an end, the evaporation of leftover solvent begins - the evaporation stage. Though the evaporation already leads to layer thinning during the spin-off stage, it now becomes the domination and only factor in layer thinning and, dependent on the material, drying. The effect and impact of this stage again depends on the composition of the material.

3.6.3 Influence of Material Viscosity on Spin Coating

Viscosity is the dominating physical quantity that influences the expansion and distribution of material during the spin coating process. Though other quantities like drying rate, percent solids and surface tension [77] have an influence on the process, their influence on layer thickness and uniformity become negligible compared to the viscosity [24]. Viscosity describes a materials resistance to flow. The higher the viscosity, the higher the resistance to a shear force applied to the liquid. There are two types of viscosity, dynamic and kinematic viscosity. Dynamic viscosity is the internal resistance when a liquid changes shape, i.e., is subjected to shear forces. "The viscosity of a material is defined as the ratio of the shearing stress ($\frac{F}{A}$) to the velocity gradient in a fluid." [19] Newton's equation describes this relationship using Newton's second law as follows. The shear a fluid experiences is proportional to the force applied and inversely proportional to the viscosity for a Newtonian fluid. The following equation 3.6.1 shows this relationship. [19]

$$\tau = \frac{F}{A} = \eta \cdot \frac{dv_x}{dz} \tag{3.6.1}$$

With the shear stress τ, dynamic viscosity η, force F, area A and the velocity gradient over distance from substrate $\frac{dv_x}{dz}$. The kinematic viscosity is the ratio of a fluids viscosity to its density and is a measure of the flow resistance under gravitational influence, as shown in equation 3.6.2. [19]

$$\nu = \frac{\eta}{\rho} \tag{3.6.2}$$

The viscosity is, except for material composition, mainly dependent on the temperature of the material. Typically, viscosity decreases with increasing temperature. [19]

3.6.4 Error sources in Spin Coating Technology

"A defect-free, uniform coating of photoresist film is critical to produce accurate and consistent [...] geometries."[24] In order to achieve good coating results, this section deals with the most predominant errors that are documented for the spin coating process. Typical errors in the process or process results are edge bead effects, comet errors, striations and pinholes and will be discussed in the next sections. [77]

Substrate edges are problematic for the spin coating process. Due to surface tension effects it becomes difficult for the material to detach from the substrate. Therefore, the first error that can occur is the edge bead effect, which is the formation of a droplet or bead on the substrate edge. This problem becomes even worse for square or rectangular substrates, where the laminar airflow that assists the material spreading (see figure 3.9 d)) can be perturbed, leading to non-uniformities on the edges. [77] The following figure 3.10 shows the process of a bead formation on substrate edges. Here, a volume of resin cannot be flung off during the spin process, which leads to residual volume of material after the flow-assisted thinning has taken place. Due to Laplace pressure, a phenomenon of surface tension, the liquid contracts from the substrate edge to the substrate surface. This leads to one or multiple non-uniform beads on the edge of the coating. Depending on the wettability of the substrate surface and the surface tension of the material this effect can lead to a propagation of the bead phenomenon far onto the substrate and influence the layerstability as a whole.

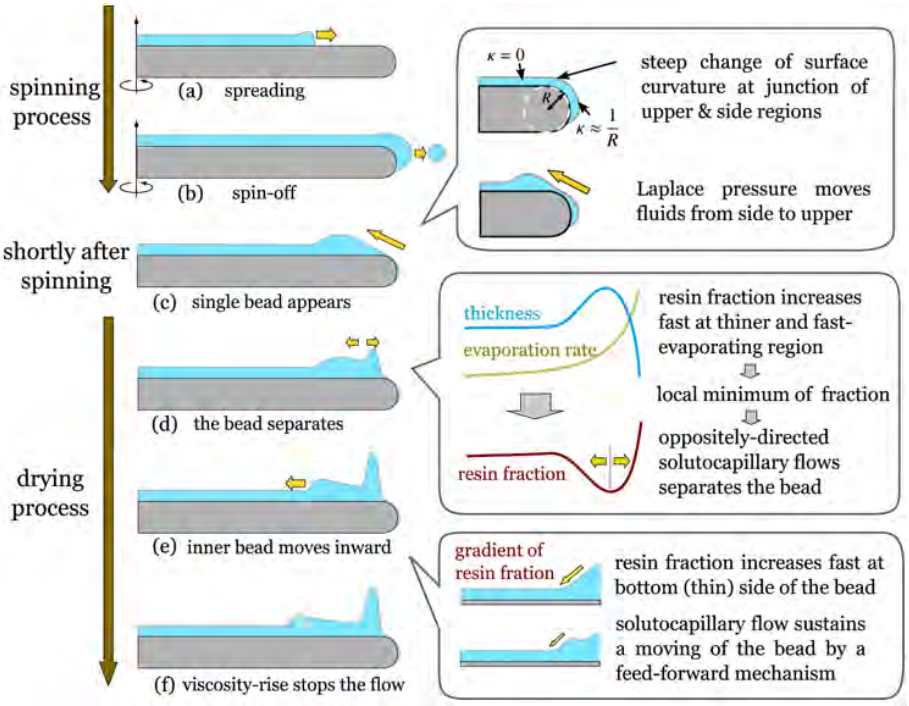

Figure 3.10: Schematic depiction of the formation of Edge Beads during the spin coating process [70]

The edge bead effect can be mitigated by using less viscous materials, increasing the RPM during the spin-off stage (therefore decreasing the spin time) or mechanically removing the material during the spin process using a wiping blade of kinds. Nonetheless especially for non-drying layers it is still good practice to avoid structure edges when processing the coated substrate if possible.

Another common error in the coating process are comet errors. They are called comet errors, due to the characteristic shape of resin flow around the defect location, which looks like a comet and its tail. These errors occur when relatively large particles either in the coating material or on the substrate impede the flow of the expanding material. Figure 3.11 shows a typical comet error on a coated surface. Here the particle that interfered with the resin flow is clearly visible and the influence of this particle creating the tail of resin behind it is shown.

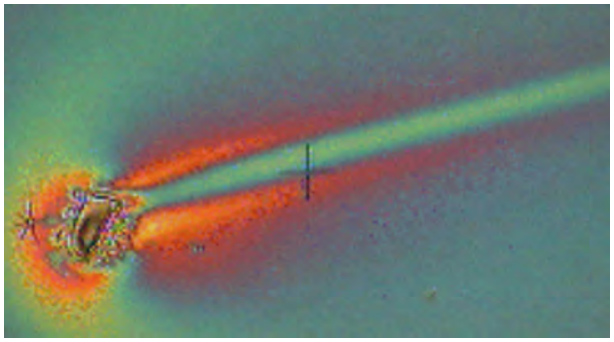

Figure 3.11: Picture of a comet error formed during while spin coating a photoresist [8]

This error can be prevented by working in clean environments – in some cases it may be advisable to work in a clean room environment – ensuring substrate cleanliness and, in case of

contamination or prolonged use, filtering the coating solution. [77]
An error that is rather prone to solvent heavy spin coating solutions i.e. photoresists, are striations. This type of error manifests itself by creating a pattern of radially parallel lines varying in thickness on the coating surface like shown in the following figure 3.12. This effect is founded on the Maragoni effect and comes from the fast evaporation of light solvents in the early stages of the coating process. This can lead to an enrichment of less volatile elements in the surface layer, which influences the surface tension of this layer. If this surface tension is larger than the coating solution, an instability is created where the higher surface tension draws in material in intervals, leading to higher evaporation in the spaces inbetween. A surface relief forms. [77]

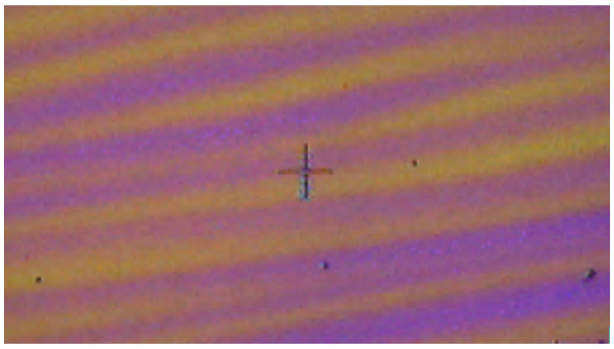

Figure 3.12: Picture of a striation formed during while spin coating a photoresist [8]

The mitigation strategy for this effect is using a gradient increase in velocity during the spin-up process, therefore allowing for a more controlled evaporation of solvents. [8] Since this phenomenon only occurs in very solvent heavy solutions, it is not relevant for the coating of undiluted photopolymer materials.
The last common error in the spin coating process is the formation of pinholes. Pinholes are a phenomenon, where small holes form in the layer due to relatively small particles or gas bubbles in the resin. These layer impurities break the layer integrity locally, leading to a material contraction around the particle, forming a hole. The most common reason for the formation of pinholes is an insufficiently clean substrate or the inhibition of bubbles in the liquid. Bubbles can come from moving or shaking the material vile, nitrogen which has dissolved into the liquid, especially for photopolymers that have been stored for a long time - and air bubbles that can form in the pipetting process. Very thin layers can lead to an increase in pinhole density. [24] Since very small layers have a lower series resistance, the influence of even small particles becomes more significant. [83] Furthermore when coating with a high velocity, air turbulence forms right above the resin surface [59] and even smallest particles in the liquid can act as nucleation sites. This problem becomes even more significant when coating on a topography, here the surface roughness of the topography can act as a nucleation site as well. The following figure 3.13 shows a measurement of a layer coated on top of a square topography cured with the laser lithography setup in this work. Here the pinholes that have formed are clearly visible, this has a significant impact on the quality of structures cured in that layer.

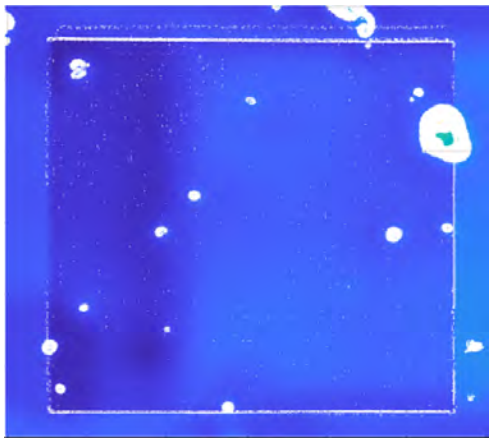

Figure 3.13: Top-down view of a WLI measurement of a recoated topography with pinhole formation

Mitigating the formation of pinholes can be achieved by developing a good substrate cleaning process. For small layers (high RPM) and coating on topographies it is also advisable to handle the liquid container with care, let the material decompress by opening the container and letting it sit for a while before coating and using the correct pipetting technique (see chapter 3.8). When the formation of bubbles on nucleation sites in the photopolymer or on top of topographies is observed it is also good practice to introduce nitrogen purging to the coating process. Here a continuous stream of nitrogen gas is introduced perpendicular to the spinning substrate with the purpose that this flow breaks turbulences disturbing the laminar air flow and to mitigate the effect of bubbles forming on nucleation sites. [21]

3.6.5 Mathematical Models

The following subchapter presents mathematical models and their corresponding approaches in modeling the process of spin coating for a non-diluted photopolymer on planar, concave, and convex surfaces. For many photopolymers, including the PR48 photopolymer used in this work, the relative amount of solvent is negligible. This means the behavior of the expansion during the coating process is that of a Newtonian-fluid. For other resists, especially photoresists, which show a much higher concentration of solvent, the influence of the evaporation during the spin-up and spin-off stage of the coating process creates non-Newtonian behavior which cannot be neglected [67]. Therefore, the models presented in this subchapter are only viable for solvent-free photopolymers or materials that only contain a very small amount of solvent, hence the radial force is the dominating factor in layer thinning. These next sections will discuss the spin coating model for planar surfaces as presented by Emsli et al. [13], the model of spin coating on concave surfaces by Feng et al. [14] as well as a derivation of Feng's model approach to be able to coat on convex surfaces.

3.6.5.1 Planar Substrates

This section presents the model of spin coating on planar surfaces as presented by Emsli et al. [13]. This model assumes a homogenous flow of a Newtonian fluid without solvent addition

and initially uniform distribution (equal radius droplet), that is spun on an infinite horizontal surface at constant radial velocity, neglecting the acceleration time and the Coriolis force. The acceleration time can be neglected if the spin-off time is greater than the acceleration time by a magnitude, the Coriolis force can be neglected for layerheights smaller 1 mm.
The mathematical description is founded on the force-motion equilibrium. This means the fluid expands where the centrifugal force through the rotation is equal or greater the viscous force per unit volume. This can be expressed as shown in the following equation 3.6.3.

$$-\eta \cdot \frac{\delta^2 v}{\delta z^2} = \rho \cdot \omega^2 \cdot r \tag{3.6.3}$$

With the dynamic viscosity η, the velocity v, the material density ρ, the angular velocity ω and the expansion distance from the point of rotation r. By integrating the previous equation twice, the velocity experienced at a given height and distance from the center can be calculated. Using the boundary conditions that the velocity on the substrate surface is zero (v(z=0) = 0) and that the shear force on the surface of the liquid must be zero $\frac{dv}{dz}(z = h) = 0$. This leads to the following expression 3.6.4.

$$v = \frac{1}{\eta} \cdot \left(-\frac{1}{2} \cdot \rho \cdot \omega^2 \cdot r \cdot z^2 + \rho \cdot \omega^2 \cdot r \cdot h \cdot z \right) \tag{3.6.4}$$

With the z-position in the material z and the absolute height of the resin h. Using the radial flow per unit length and applying the continuity condition for an incompressible fluid $\frac{\delta h}{\delta t} + \frac{1}{r} \cdot \frac{\delta}{\delta r} \cdot \left(r \cdot \int_0^h v \quad dz \right) = 0$ for the absolute decrease of the layerheight h, a differential equation for the change of layerheight can be obtained (see equation 3.6.5)

$$\frac{\delta h}{\delta t} = -\left(\frac{\rho \cdot \omega^2}{3 \cdot \eta} \right) \cdot \frac{1}{r} \cdot \frac{\delta}{\delta r} \cdot r^2 \cdot h^3 \tag{3.6.5}$$

This differential equation has a specific solution when the liquid is distributed beyond the substrate edges, i.e. coating of a non-infinite substrate. Here the height of the substrate can be expressed dependent on the coating time t and the angular velocity (spin speed) ω. This is shown in the following equation 3.6.6.

$$h(\omega,t) = \frac{h_0}{\sqrt{1+4\cdot\frac{\rho\cdot\omega^2}{3\cdot\eta}\cdot {h_0}^2\cdot t}} \tag{3.6.6}$$

With the height over angular velocity and time h(ω,t), the initial height of liquid on the substrate h_0 and the time t after starting the spinning motion. Using this equation, a model to determine the desired coating parameters for planar surfaces can be derived (see chapter 5.3).

3.6.5.2 Concave Substrates

Based on the model of Emsli et al. presented in the previous section, Feng et al. [14] expanded the model by accounting for a force equilibrium on a concave substrate, where the tangential force coming from the centrifugal force on a point along the substrates curvature as well as the influence of the gravitational force is taken into account. Their model is valid for concave substrates with the center of rotation at the center of the substrate and will be discussed in the following sections. The following figure 3.14 shows the geometric model of the substrate with a volume of liquid on a given distance from center. Using this geometric approach the influence of the centrifugal force and the gravity can be expressed for a given point on the substrate with the distance r from the center of rotation, if the substrates radius of curvature (R) is known.

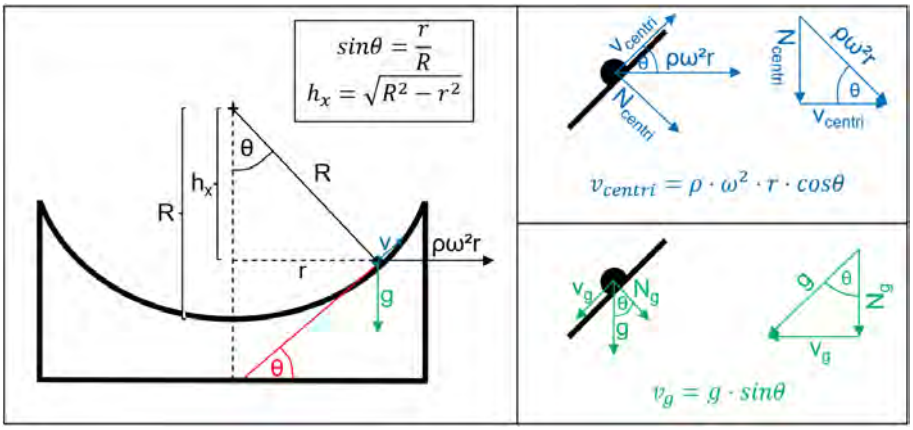

Figure 3.14: Geometric model of a concave substrate for spin coating and derivation of tangential forces influence to derive a force equilibrium (cf. [14])

Using this geometric model, the steps in calculating the expected height can be performed analogous to Emsli et al.s approach. Therefore the force-motion equilibrium on a concave surface for spin coating can be expressed using the following equation 3.6.7.

$$-\eta\cdot\frac{\delta^2 v}{\delta^2 z} = \rho\cdot\omega^2\cdot r\cdot cos\theta - g\cdot sin\theta \tag{3.6.7}$$

With the angle θ of a point at distance r to the center of roation and the gravitational force g. Using the geometric model and applying $cos\theta = \frac{h_x}{R}$ and $h_x = \sqrt{R^2 - r^2}$ this equation can be simplified and expressed only dependent of the radius of curvature of the substrate R and the radial distance from center r. This leads to the following substituted force motion equilibrium in equation 3.6.8.

$$-\eta \cdot \frac{\delta^2 v}{\delta^2 z} = \frac{r}{R} \cdot \left(\rho \cdot \omega^2 \cdot \sqrt{R^2 - r^2} - g\right) \tag{3.6.8}$$

With the substrates radius of curvature R. Double integration and applying the mass continuity equation for incompressible fluids gives the following differential equation 3.6.9.

$$\frac{\delta h}{\delta t} = \frac{h^3}{3 \cdot \eta \cdot R} \cdot \left(2 \cdot g - 2 \cdot \rho \cdot \omega^2 \cdot \sqrt{R^2 - r^2} - \frac{\rho \cdot \omega \cdot r^2}{\sqrt{R^2 - r^2}}\right) \tag{3.6.9}$$

The specific solution to this equation, again, gives the height dependent on the rotation speed and time spun, see the following equation 3.6.10. This time however dependent on the radial distance r. This dependency means the film thickness will be non-uniform forever, however the influence of the distance can be minimized to achieve quasi homogenous layerheights in a defined distance around the rotation center.

$$\boxed{h(\omega, t, r) = h_0 \cdot \sqrt{1 + \frac{2 \cdot {h_0}^2 \cdot t}{3 \cdot \eta \cdot R} \cdot \left(2 \cdot \rho \cdot \omega^2 \cdot \sqrt{R^2 - r^2} - 2 \cdot g - \frac{\rho \cdot \omega^2 \cdot r^2}{\sqrt{R^2 - r^2}}\right)}} \tag{3.6.10}$$

Using this equation, the expected height at a defined point on a substrate with the distance r from the center of rotation can be determined for a Newtonian fluid on a concave substrate with known radius of curvature. The height distribution over a defined distance from center can be calculated and optimized for a desired layerheight (as done for convex surfaces in chapter 5.4). It should be noted here, that Feng et al.s work also proposed an equation to account for non-Newtonian behavior when the liquid is diluted or naturally contains a certain amount of solvent. Since irrelevant for the current use case this adaption will not be further discussed here.
In the case of coating on concave surfaces Feng et al. point out a geometric boundary condition which limits the geometry of the substrate to a geometric constraint. By defining the condition for coating as the influence of the centrifugal force along the curvature exceeding the influence of the gravitational force and solving equation 3.6.10 for that condition, there is equation

3.6.11 describing the maximum substrate radius in relation to its radius of curvature for gradual substrate thinning in the coating process to be valid.

$$0 \leq r_{max} \leq \sqrt{\frac{2}{3}}R \tag{3.6.11}$$

With the (maximum) substrate radius r_{max}. This boundary is only necessary for concave substrates, where the influence of gravity counteracts the centrifugal force.

3.6.5.3 Convex Substrates

Using Feng et al.s approach from the previous sections, the same relationships can be established for the behavior of a Newtonian-liquid on a convex substrate while spin coating. The following figure 3.15 shows the geometrical model for a convex surface derived from the one presented for concave surfaces (figure 3.14).

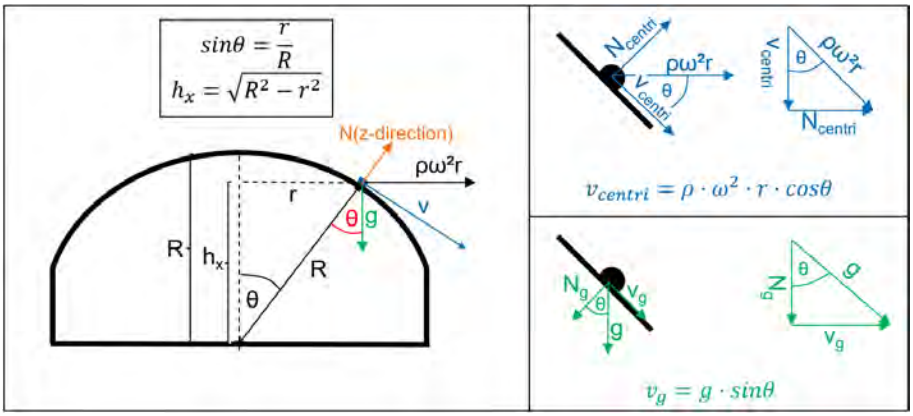

Figure 3.15: Geometric model of a convex substrate for spin coating and derivation of tangential forces influence to derive a force equilibrium (compare [14])

The geometric relationships for angle θ and h_x stay the same, so do the relative forces a volume of resin experiences. The only difference therefore is the direction in which the gravitation force interacts with the liquid. Due to the shape of the surface, it is now perpendicular to the influence of the centrifugal force, which increases layer thinning instead of counteracting it. Therefore the geometrically simplified force-motion equilibrium only switches sign to form equation 3.6.12.

$$-\eta \cdot \frac{\delta^2 v}{\delta^2 z} = \frac{r}{R} \cdot \left(\rho \cdot \omega^2 \cdot \sqrt{R^2 - r^2} + g\right) \tag{3.6.12}$$

This leads to a very similar differential equation 3.6.13 for the change of layerheight over time.

$$\frac{\delta h}{\delta t} = \frac{h^3}{3 \cdot \eta \cdot R} \cdot \left(2 \cdot g + 2 \cdot \rho \cdot \omega^2 \cdot \sqrt{R^2 - r^2} - \frac{\rho \cdot \omega \cdot r^2}{\sqrt{R^2 - r^2}} \right) \tag{3.6.13}$$

The respective solution for this differential equation is also very similar to the solution of the differential equation for concave substrates. The following equation 3.6.14 shows the solution of the differential equation 3.6.13 to give the expected layerheight h at a given time, angular velocity and radial distance from the center of rotation.

$$\boxed{h(\omega, t, r) = h_0 \cdot \sqrt{1 + \frac{2 \cdot {h_0}^2 \cdot t}{3 \cdot \eta \cdot R} \cdot \left(2 \cdot \rho \cdot \omega^2 \cdot \sqrt{R^2 - r^2} + 2 \cdot g - \frac{\rho \cdot \omega^2 \cdot r^2}{\sqrt{R^2 - r^2}} \right)}} \tag{3.6.14}$$

This equation shall be used in chapter 5.4 to calculate an expected layerheight for a defined convex substrate and optimize the curing parameters to achieve best homogeneity in layerheight over a defined region of interest on the substrate surface.

3.7 Adhesion and Surface Activation

When two surfaces of different materials get in contact, the force needed to separate them is called adhesion. If the two surfaces are the same material, then the separating force is called cohesion. This Adhesion force (F_{ad}) describes the minimum force required for the detachment of two surfaces and is dependent on the interactions between the molecules on the two surfaces, the number density of the molecules, and the contact area [20].
The free-energy change during the process of adhesion is denoted as the adhesion energy W_{ad}. [85] The surface energy γ has become one of the most fundamental and important parameters in polymer science and is formulated in equation 3.7.1. [20]

$$\gamma = \frac{dW}{dA} \tag{3.7.1}$$

The surface energy γ is defined as the energy change dW with the surface area A increasing by dA in vacuum.
For a contact of two different surface materials (1,2) in a medium (3), the combination of the interfacial energies γ dependent on their influence on the adhesion results in the adhesion energy. The adhesion energy is calculated with the following equation 3.7.2.

$$W_{ab} = \gamma_{13} + \gamma_{23} - \gamma_{12} \tag{3.7.2}$$

The interfacial energies γ_{12}, γ_{13} and γ_{23} which are the surface energies between the media surfaces involved in the adhesion, namely, the surface energy of each medium (polymer, glass) as well as the medium in which the bond occurs (air). These surface energies are generally dependent on the composition of the two surfaces. The composition of a surface is considered to be a combination of polar and apolar components. This leads to adhesion due to a combination of van der Waals forces and electrostatic or covalent interactions between the two materials. These are the predominant adhesion forces and in combination with the coherent forces inside the polymer describe the whole adhesion force of a polymer on a substrate (adsorption). [44] The strength of these forces strongly depends on material parameters of the polymer and substrate used, i.e. on molecular weight of the polymer, segment polarity, chain mobility, surface roughness, temperature and contact time [85]. The following figure 3.16 shows the adhesion influence processes and parameters established in this chapter as an example for a droplet of fluid on a surface. The surface roughness (indicated in red) plays a big role in adhesion, because it increases the adhesion area and therefore the total adhesion force. For smooth surfaces adhesion force is lower than on rough or textured surfaces.

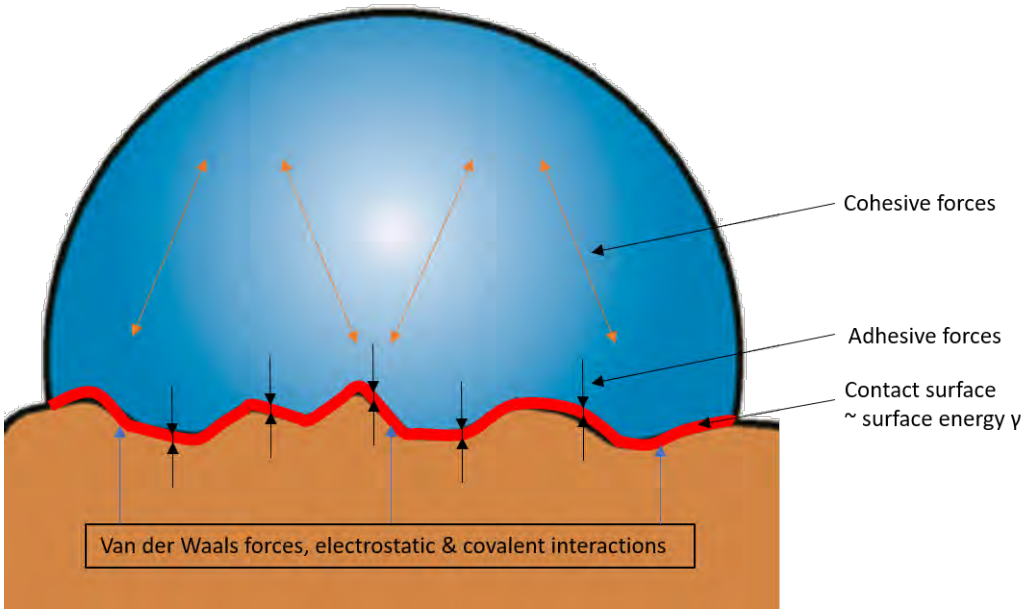

Figure 3.16: Influence factors on material adhesion on a surface presented on the example of a droplet on a surface [20]

In case of photopolymerization, the adhesion forces of the polymer on the substrate combine with the cohesive forces inside the cured polymer. During the curing process the cohesive forces increase significantly leading to overall better adhesion of the geometry as a whole on

the substrate, which is relevant in mitigating the influence of polymerization induced shrinkage (see chapter 3.4). To ensure a good adhesion on a substrate a clean substrate surface is necessary, every contaminant present interferes with the adhesion between the two materials.
In case of surface coating, it is important to create a stable layer with sufficient adhesion between a substrate and the applied material. This is especially relevant for substrate materials like glass, which due to its low surface roughness shows a very weak adhesion strength, making it a difficult substrate to use, compared to for example plastic substrates.[64] If the surface energies enabling the adhesion of a coated film are smaller than the surface tension of the film, the substrate wettability and layer stability after coating become insufficient. In this case the modification or activation of its surface becomes necessary. The activation of a surface means to increase the surface energy. This can be done by using chemical groups or charges like adhesion promoters or plasma techniques, or by physically changing the surface and increasing the roughness using processes like etching or ablation.[42, 11, 71] Physical surface roughening is no option for this work since this would interfere severely with the optical properties of the used substrates. Adhesion promoters and other chemical primers have to be individually selected for a defined material. Therefore, plasma surface treatments have become an attractive technology. The following subchapter 3.7.1 deals with the process of surface activation using (oxygen) plasma and the hardware used in this work to promote layer adhesion using oxygen plasma.

3.7.1 Plasma Surface Activation

Plasma surface activation generates an ionized gas which, when applied to a surface, polarizes this surface, increasing the surface energy, leading to a better wettability and adhesion. One of the most common gases for plasma surface treatment is oxygen, because it creates quickly and easily, forming hydroxyl (OH) groups on the substrate surface. This changes the chemical composition of the substrate surface temporarily. These OH groups react with other chemical bonds in the surface and applied film, creating a covalent bond between the surface and the applied film.[71] The effect of surface activation with oxygen plasma is shown in the following figure 3.17, which shows the effect of activating the surface with plasma on the contact angle (i.e. wettability) and a schematic of how the activation creates OH groups on the surface allowing covalent bonding of materials.

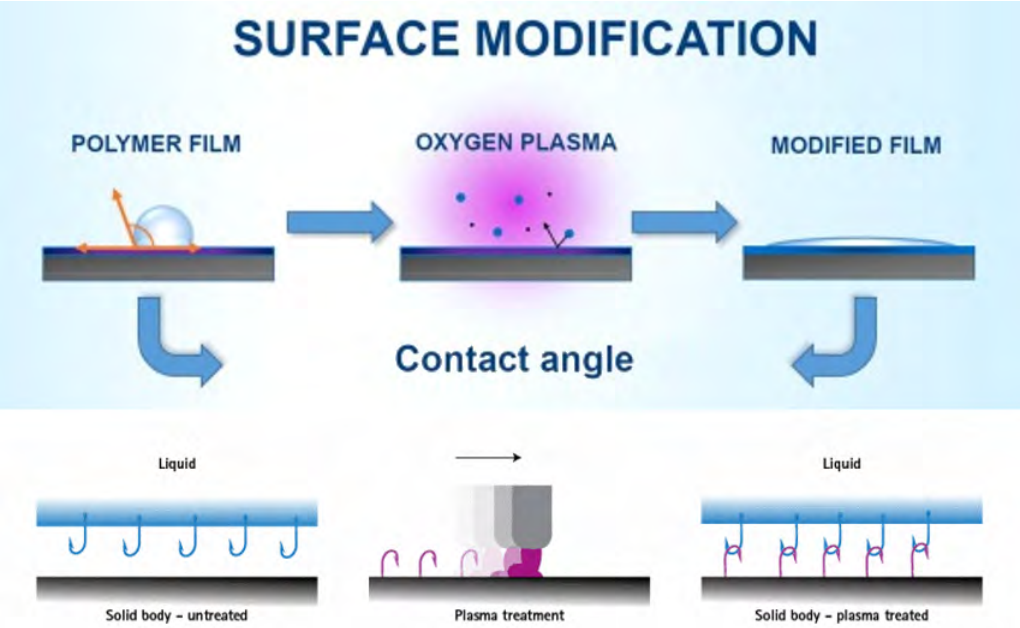

Figure 3.17: Schematic of the effect on plasma surface activation on contact angle and formation of covalent bonds [65, 43]

The bond created by plasma activation however is not time stable since it offers no permanent chemical connection of materials. For the coating and processing of substrates this means the whole process is time-dependent and needs to be completed before the surface activation wears off. [71, 64, 44] For this work a hand-held atmospheric-pressure plasma device creating oxygen plasma is used and will be presented in the next section. Using this activation method and hardware typically leads to surface activation of around 20 minutes [36]. A positive side effect of the plasma surface activation method is that during the exposure process it removes contaminants and cleans the surface [36].

The device used for this work is the piezobrush PZ3, a hand held device which creates cold active plasma at a temperature of less than 50° C using a piezoelectric transformer which allows for the dissociation and ionization of the ambient process gas. The change in temperature due to the surface activation needs to be accounted for in the calculation model for coating. However, due to the relatively low process temperature the temperature change does not interfere with the layer formation or subsequent stability due to cooling off after treatment. It offers an efficient and safe process with a high-power density. With a treatment rate of a few square centimeters (2-5 cm^2 for its predecessor) per minute it is sufficiently fast for a laboratory setup with small substrates like in this work. The following figure 3.18 shows a picture of the device next to a CAD assembly with the components of the device labeled. The device operates using a 24 V PSU and creates the plasma with the CeraPlas module (piezoelectric transformer). It comes with two nozzles, one for conductive and one for non-conductive materials. The status of the device is shown on the LCD display and it is operated using the start (and stop) button, which will release a continues plasma stream at a set power (0-100%). Slowly moving the nozzle at a distance of 1 – 7 mm from the substrate will lead to an activation of the surface. [36]

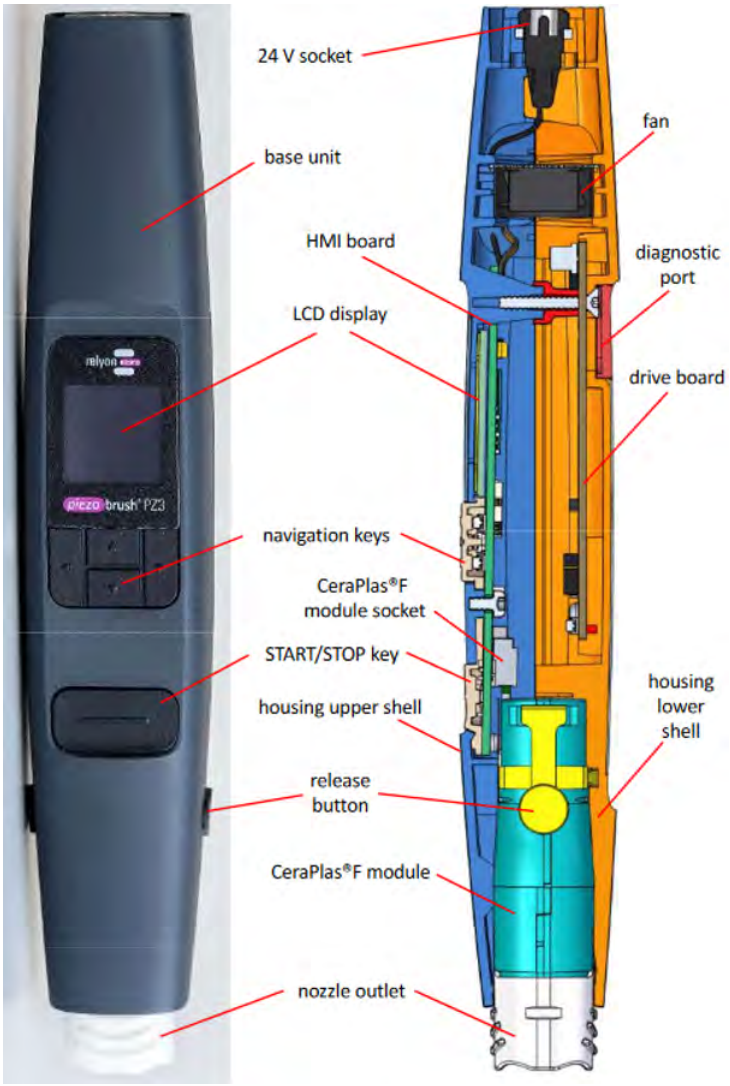

Figure 3.18: Picture of the piezobrush PZ3 and a CAD assembly of it with labeled components [36]

3.8 Pipetting

The mathematical calculation models for the layerheight of a spin coated polymer film require the initial layerheight h_0. Therefore, it is important to be able to apply a repeatable volume of material on a substrate. Even though it shall be established that the influence of the dispensed volume has little influence on the expected layerheight (see chapter 5.3.2 and chapter 5.4.3), it is important to establish a reliable dispense process for photopolymers on a substrate and minimizing the inhibition of bubbles in the photopolymer during the material deposition. An available way of dispensing a precise amount of liquid for this work is an air-displacement pipette with a volume range of 10 – 100 µL. The following figure 3.19 shows a schematic of an air-replacement pipette. This form of pipette uses disposable plastic tips for volume intake. Using the push button, with which a desired volume can be set by rotating the button, a defined volume of air is displaced in the disposable tip, using a piston inside the pipette's shaft. The push button can be pushed to two levels, the first level displaces the volume set with the rotation of

the push button and displayed on the volumeter display, the second level displaces the maximum amount of volume and can be used to purge the volume left in the pipette tip.

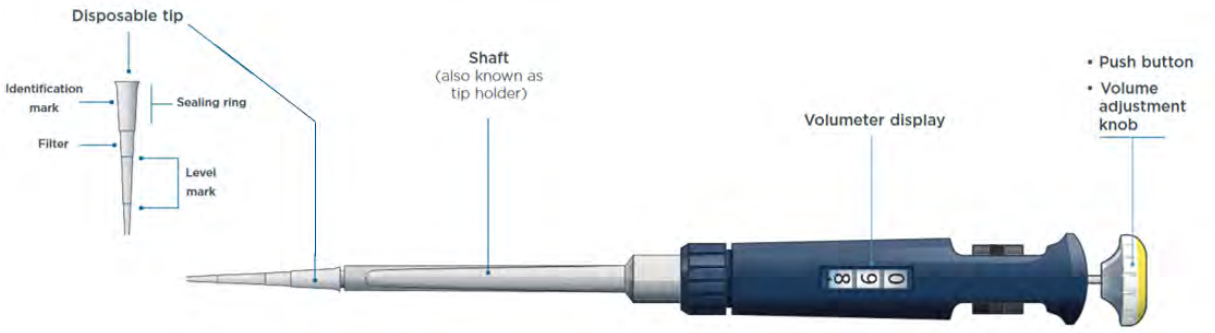

Figure 3.19: Schematic of an air-displacement pipette and its components [18]

This type of pipette is more suited for aqueous solutions with a relatively low viscosity [18]. The photopolymer used in this work has a relatively high viscosity (400 cP at 20° C), therefore the choice of the correct pipetting technique is important to ensure the deposition of the correct amount of the photopolymer while making sure no bubbles form during the filling of the pipette tip or during the pipetting itself. Normally pipetting a defined volume is done by setting said value, pushing the button to the first stop, submerging the tip about 1 cm into a liquid and slowly releasing the push button to suck the desired volume up. The dispensing is then done by pushing the push button to the second stop, releasing a defined volume. However, for viscous liquids this process leads to an amount of resin that will remain in the tip of the pipette after dispensing, or when forced out by repeatedly pushing the button to the second stop will generate air bubbles in the dispensed liquid. Therefore, dispensing the photopolymer in this work is performed using the reverse pipetting technique.[58] The following figure 3.20 shows the principle of the reverse pipetting technique. Here the push button of the pipette is pushed to the second stop before submerging into liquid and then slowly released. The dispensing is done by pushing the button to the first stop. Since this technique does not force the complete volume out of the tip, even for viscous solutions, the desired volume is dispensed. The remaining liquid can then be redeposited in its container by pushing the push button to the second level.

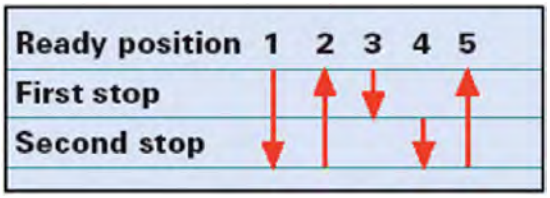

Figure 3.20: Push button position chart for the reverse pipetting technique [58]

Using an air-displacement pipette and the reverse pipetting technique are used in this work to dispense a defined and repeatable volume of photopolymer onto a substrate.

3.9 Hexapod Motion Control System

This subchapter will discuss the specifications of a hexapod and its use case for the current setup. Newports hexapod motion control system HXP100P-MECA is newly introduced hardware in this work. Hardware used in previous works will be presented in short in the next chapter 4, where the basic setup used in this work is reiterated. Hexapods are kinematic devices that provide motion in 6 degrees of freedom (x,y,z, pitch u (θ_x), roll v (θ_y) and yaw w (θ_z)). These systems allow highly precise positioning and movement profiles for high loads in a limited range of motion. The hexapod used in this work is driven by 6 high-precision piston actuators oriented at an angle, which allows for a submicron accuracy and repeatability in movement in 6 DOF. The following table 3.1 shows the main specifications of the HXP100P-MECA used in this work.

Table 3.1: Specifications for Newports HXP100P-MECA hexapod motion system [48]

Parameter	**Specification**
Max. load	60 N
Travel range (x,y,z)	$\pm$ 27.5, $\pm$ 25, $\pm$ 14 mm
Rotation range (θ_x,θ_y,θ_z)	$\pm$ 11.5, $\pm$ 10.5, $\pm$ 19 $^\circ$
One-directional Travel repeatability (x,y,z)	$\pm$ 0.1, $\pm$ 0.1, $\pm$ 0.05 μm
One-directional Rotation repeatability (θ_x,θ_y,θ_z)	$\pm$ 0.05, $\pm$ 0.05, $\pm$ 0.1 mdeg
Bi-directional Travel repeatability (x,y,z)	$\pm$ 0.25, $\pm$ 0.25, $\pm$ 0.125 μm
Bi-directional Rotation repeatability (θ_x,θ_y,θ_z)	$\pm$ 0.125, $\pm$ 0.12, 0.25 mdeg
Max. Travelspeed (x,y,z)	12, 10, 5 $\frac{mm}{s}$
Max Rotationspeed (θ_x,θ_y,θ_z)	8, 8, 16 $\frac{^\circ}{s}$
Origin Repeatability	x,y,z: $\pm$ 5, 5, 2.5 µm u,v,w: $\pm$ 2.5, $\pm$ 2.5, $\pm$ 5 mdeg

Using a simple Web-GUI, a Newport software package or implementing the motion control in a programming environment using the .NET framework (see chapter 6.3), the movement in a single direction or movement profiles can be created to precisely position a load with the hexapod. The position of the hexapod platform is expressed using three coordinate systems, the base

coordinate system, the work coordinate system and the tool coordinate system. A visualization of these coordinate systems is shown in the following figure 3.21. The base coordinate system is a fixed cartesian coordinate system that is located on the center of the hexapod platform but has its origin in z-direction on top of the base of the hexapod (a custom position can be chosen though), it is used as a reference for the other two systems. The work coordinate system acts as a world-coordinate system for movement. Translation and rotation can be performed relative to this fixed reference. The work coordinate system can be manually shifted relative to the base coordinate system to create a custom point of reference for motion and rotation. It is normally located in the center of the hexapod platform with the z-origin on the top of the platform. The third coordinate system is the tool coordinate system, which is a dynamic coordinate system that is always positioned relative to the current hexapod position. The tool coordinate system is defined relative to the top plate and can be shifted individually from the work coordinate system. The tool coordinate system can be useful for perfoming a motion relative to the current hexapod position and allows for more freedom in the definition of movement profiles and allows for two individually defined centers of motion (work- and tool coordinate system).[47]

Figure 3.21: Illustration of the coordinate systems used for hexapod motion control [47]

The correct definition of the coordinate systems relative to a substrate on the hexapod platform is necessary to achieve the correct relative motion. This will be important for defining the center of rotation when compensating the geometry of a convex lens for laser stereolithography in chapter 7.3.

4 Previous Setup and Results

This chapter will give a short overview of the previous setup and the control software used for the experiments to determine the working parameters of the setup. In the end, the important results of the previous work, necessary to understand the outcome of this work are summarized.

4.1 Basic Setup

To develop a reliable control software as well as characterizing and analyzing the curing process a temporary hardware setup mounted to an optical plate is used. This setup is in large parts FDM printed,which allows a quick and easy adjustment of the setup to determine the necessary components and their alignment. Figure 4.1 shows the CAD assembly of the test setup and its individual components. The system has three main components. The fixation and orientation of the UV laser, the Galvo system with scan lens and the substrate mount. The Galvo System is used for positioning the beam on the subtrate whereas the focus of the beam can be adjusted with the movable subtrate mount. Using the FDM printed intake, the UV laser can be mounted and oriented relative to the Galvo mirrors using screws to manipulate position, height and tilt of the laser relative to the mirror(s) of the Galvo system. The Galvo system is mounted externally and deflects the beam onto a scan lens which is permanently mounted to the Galvo system and can focus the deflected beam in a 10 x 10 mm area on a flat image plane. The substrates in these initial experiments are microscopic slides which are positioned in a FDM printed intake. The substrate can be manually focused using a target by adjusting the intake position using a precision lift table and guiding the intake with linos rods.

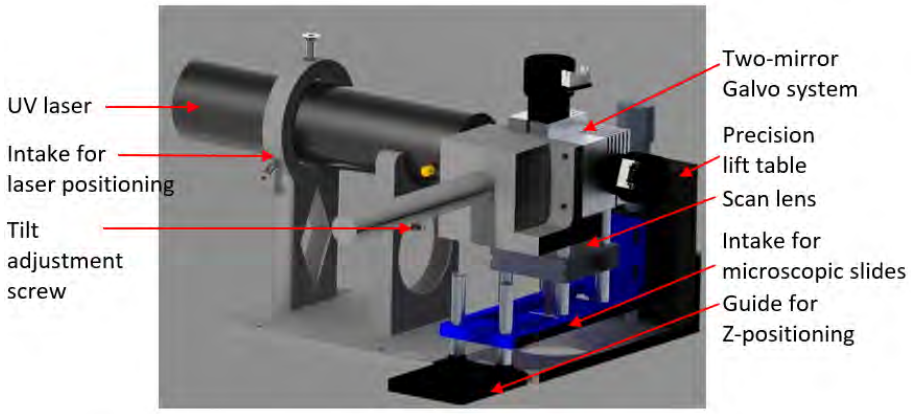

Figure 4.1: CAD rendering of the assembled and labeled lithography setup from previous reports [27, 26]

During the experiments the implementation of an optical filter for reducing the laser power beyond its normal reliable capability showed necessary. Therefore, a mount for a polarizing filter

is added externally, to adjust the laser power. The following sections summarize the relevant specification for the used UV laser, Galvo system and scan lens used in this work.
The laser used in this project is Thorlabs LDM405 compact diode laser with a wavelength of 405 nm (min 395 – max 415 nm). It has a built-in (manual) mechanical shutter, and the laser power can be manually adjusted from 0.1 to 4 mW using a potentiometer. However, it is shown in an experiment that the power increase is only linear above 0.45 mW. Above 2.75 mW the slope of the laser power curve is relatively low. The laser power in the range above 2.75 mW can be set more precisely. Therefore the laser power is decreased by a filter to operate in the flat part of the working curve and then fine tuned using the potentiometer.
The Galvo system used in this work is a Thorlabs GSM002-EC/M, a high speed scanning system for laser beams of up to 5 mm diameter. It uses two high-precision stepper motors to achieve a rotation range of $\pm$ 12.5° for two silver coated mirrors (wavelengths between 400 and 750 nm) at an angular resolution of 15 µrad. Each individual mirror rotation is controlled using an analog voltage input signal of up to $\pm$ 6.25 V. In this setup the analog voltage is supplied using National Instruments NI USB-6001 digital-analog converter (DAQ) card with a 14-bit resolution at a sample rate of up to 5 kS/s for dual analog output of up to $\pm$ 10 V with an accuracy of 6 mV.
The scan lens used in the setup is a Thorlabs LSM03-VIS telecentric scanning lens system. This lens system produces a flat image plane in an area of 10.3 x 10.3 mm^2. The scan lens is optimized for wavelengths between 400 and 700 nm. Its effective focal length (EFL) is 39 mm and it has a parfocal distance of 50.7 mm. These two parameters are relevant for calculating the desired mirror rotation for the control software (see chapter 4.2.1).

4.2 Software

This subchapter presents the calculation approach for the analog mirror voltages necessary to achieve a defined beam displacement on the image plane of the scan lens and introduces the python control software created to generate an output signal for the Galvo motor drivers. Using the calculation approach and control software a laser path with a defined voxel resolution and scan velocity can be calculated to create laser scanning functionality of the presented setup.

4.2.1 Mirror Voltage Calculation

To be able to scan paths with defined dimensions on a substrate, the corresponding mirror voltages for a defined beam displacement to a given position in x- and y-direction on the image plane need to be calculated. Using the dimensions of the Galvo system and the scan lens, a geometric model of the beam displacement relative to the mirror rotation can be derived. Figure 4.2 shows a sketch of that model. The displacement on the image plane is equal the displacement on the imaginary plane of the effective focal length from where the beam is focused perpendicular to the image plane. Using the scanning distance for a two-mirror system, which is the path

marked in red, the necessary deflection angle of both mirrors θ can be determined.

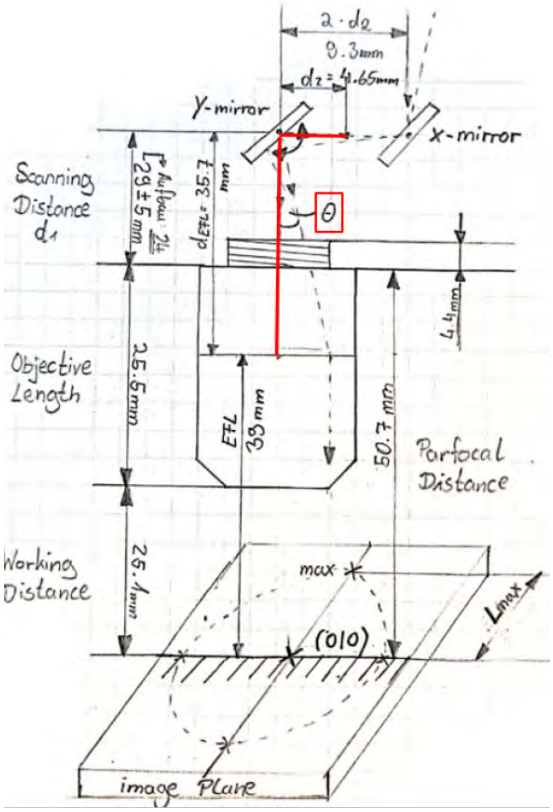

Figure 4.2: Schematic of the geometric relationships in laser scanning for the calculation of mirror voltages for beam deflection

The scanning distance (red path) to calculate the deflection angle based on the dimension shown in the model can be calculated using the following equation 4.2.1.

$$d_{scanning} = d_{parfocal} - EFL + d_1 + \frac{d_2}{2} \tag{4.2.1}$$

With the parfocal distance $d_{parfocal}$, the effective focal length of the lens EFL, the distance from the point of the effective focal length to the y-mirror d_1 and the mirror distance d_2. The angle θ is the resulting angle through the rotation of both Galvo mirrors. From there the necessary rotation of the individual mirrors can be calculated. It is important to consider the influence of the rotation of the y-mirror on the necessary displacement of the x-mirror due to the mirror distance d_2. Using the voltage to rotation scaling factor of the Galvo motor drivers, the necessary voltage input signal for a beam displacement to a given point (x,y) on the image plane can be calculated using the following equations 4.2.2.

$$V_x = \frac{1}{4} \cdot tan^{-1}\left(\frac{x}{d_2 + \sqrt{d_{scanning}^2 + y^2}}\right) \quad ; \quad V_y = \frac{1}{4} \cdot tan^{-1}\left(\frac{y}{d_{scanning}}\right) \tag{4.2.2}$$

The mirror voltage of the y-mirror V_y is dependent on the desired y-distance from the center and the scanning distance $d_{scanning}$. The voltage for the x-mirror V_x is dependent on both the x- and y-distance (i.e. y-mirror rotation) from the center, as well as the mirror distance d_2 (= 9.3 mm for current setup) and the scanning distance $d_{scanning}$. Using this equation, the necessary mirror voltages for a desired beam displacement can be calculated. The following section 4.2.2 introduces a python control software that is developed to create movement profiles for the beam deflection with a defined voxel resolution and velocity.

4.2.2 Python control Software

These following sections describe the functionality of the python control software introduced in previous works to generate movement paths as coordinate arrays for laser scanning with a defined line resolution and velocity. The presented software can read G-code files from a standard FDM slicing tool (Cura) or a user defined array of coordinates, and transform them into an analog voltage output signal for the Galvo. The working principle of the software is shown in the following figure 4.3. When a G-Code file is the input of the software, the G-Code to Cartesian Coordinates class (oTter) returns an object in the form of a list, where each element of the list contains relevant coordinates (x,y,z) and information (tool, layer number) about a single layer (figure 4.3 - 1). This offers the possibility of designing structures with multiple layers in a CAD system and curing them by outputting the path for each individual layer using the control software. The user can also manually create scanning paths by entering the desired x- and y- coordinates of a movement profile as individual vectors and defining if a vector pair is for scanning (curing) or positioning (moving to a point without curing) by defining the third input vector (tool) of ones (scanning) and zeros (positioning)(figure 4.3 - 2). This coordinate input is very useful for testing and creating simple and easily modifiable structures like line- or circle patterns because these coordinates can be easily calculated and adjusted. The output from the oTter class or the user coordinate vectors are then processed by the CoordinatesToGalvo class. This class returns an object in form of a list with the calculated output voltages for each voxel (figure 4.3 - 3). This is done by calculating the corresponding mirror voltages for a given input using equations 4.2.2 for each pair of XY coordinates in every layer of the list. Using the experimentally determined value for the resolution (voxel distance - see chapter 7.2.1) to achieve homogenous lines, the individual coordinates for each voxel in a line are calculated (figure 4.3 - 4). This results in a list of arrays with homogenously spaced points to create the desired movement profile with the Galvo system. Finally, every positioning coordinate (i.e. tool = 0) is deleted from the list (optional) to directly skip to the next desired scanning point (figure

4.3 - 5). The calculated coordinates are then uploaded in the flash memory of the DAQ card to minimize latency when outputting the signal (figure 4.3 - 6). Using the determined resolution and desired scanning velocity, the corresponding sample rate for the DAQ card analog output can be calculated and the signal can be put out.

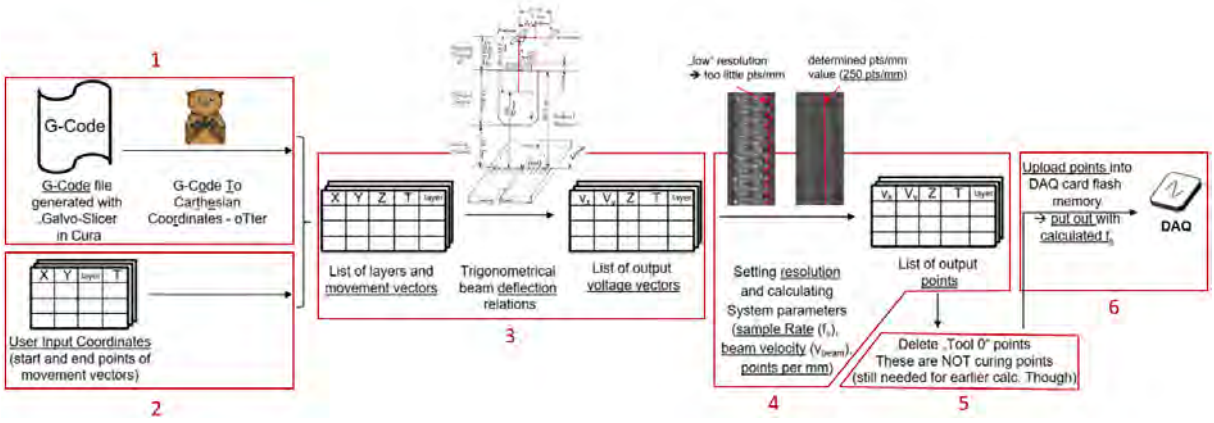

Figure 4.3: Process visualization of the slicing and coordinate handling process with the python control software

Using this software, the voltage output signal for any G-Code file or coordinate input can be calculated using only the signal and desired scanning velocity as an input. The user can also define a custom scale factor to the input coordinates. This is especially useful for G-Code input since it allows the CAD design and slicing process to be done in millimeter scale for which most CAD and slicing programs are better suited.

For better usability and for verifying the output signal, a graphical user interface (GUI) is created to easily load, process, preview and output data. The following figure 4.4 shows the GUI. In the top right frame, the user can select the input data type (G-code, coordinate vectors). After selection, the interface shown in the figure appears, here the user can select a file, which contains the data to process. In the top right frame, the user can now select a file and enter the desired parameters (resolution (pts/mm) and velocity). In this frame, the user can also optionally change the effective focal length to adjust the calculation of the mirror voltages if the scanning process is performed with a defocused beam or a different scan lens. The user can enter a scaling factor for the input data which is verified by the software to fit the maximum field of view of the setup. Finally, the user can select if the positioning coordinates in the tool vector shall be removed. Not removing these coordinates allows for an eventual implementation of an external shut-off mechanism. The calculations necessary to create the output voltage signal are performed by clicking the “Get Coordinates from Gcode/Coordinates” button. After the calculation a preview of the shape calculated will appear in the top right frame. When all parameters are set and verified, the user can now select the device type, the device number and the used output ports for a given DAQ card by clicking the “Start Galvo Settings” button in the top left frame. This allows for the change of DAQ card or DAQ card configuration. Pressing the “Start Galvo Movement” button uploads the signal into the DAQ card memory and starts the signal

output process. Information (grey), status updates (black), warnings (orange) and errors (red) during the slicing and output process are displayed in the console in the bottom right frame.

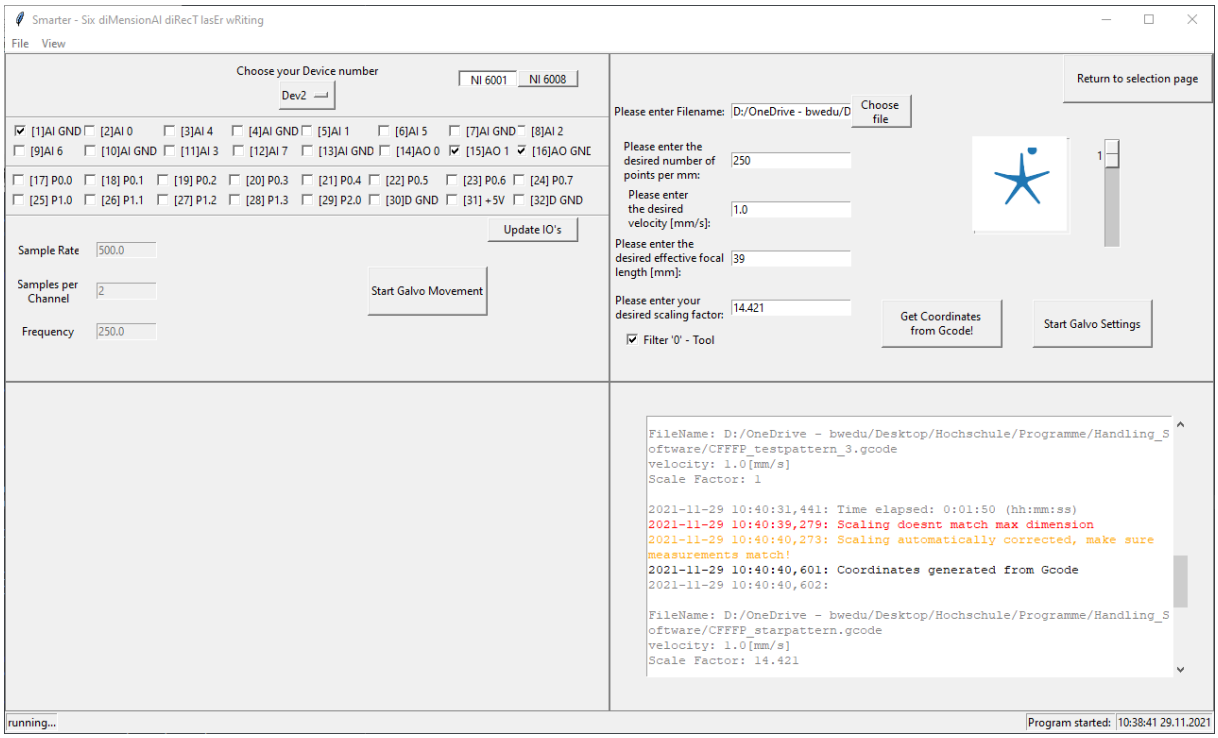

Figure 4.4: Screenshot of the graphical user interface GUI for the python control software with an example G-code file to preview and process

The control software allows the generation of an output voltage signal optimized for the setup shown in chapter 4.1. This combination of hard- and software creates laser stereolithographic functionality of the setup. The next subchapter 4.3 presents the initial experiments and their results to characterize and optimize the achievable curing results of this setup to create predictable, homogenous structures on a glass slide while ensuring substrate adhesion.

4.3 Experimental Results

This subchapter presents the experimental results for an investigation of the influence, the exposure energy has on substrate adhesion and the determination and modeling of the curing geometry cross-section. These results are used to limit the viable parameter range for the process and use these parameters in combination with the cross-section model, to optimize curing parameters for a defined layerheight.

To achieve maximum adhesion area and allow for the structure to fully polymerize, the following experiments are performed by curing through a glass slide in an enclosed photopolymer volume. This allows the evaluation of the cross-section as a whole and mitigates the influence of oxygen inhibition since it creates an enclosed, air-free environment. The substrate setup for the following experiments is shown in figure 4.5. Here a resin volume between to glass slides is created by using a FDM printed brim on the bottom glass slide and filling the brim with

photopolymer, creating a meniscus. By placing the second glass slide on top of the brim, this slide displaces the extra photopolymer and adheres to the brim due to co- and adhesive forces between the photopolymer and the top glass slide (see chapter 3.7). Designing the brim to be significantly higher than the expected curing depth allows for the structures to fully polymerize. Focusing the laser beam on the adhesion area on the top glass slide leads to maximum exposure on the point of adhesion (glass slide surface), creating maximum adhesion area for the structures. In comparison to curing structures directly through the photopolymer onto the glass slide as shown in the figure, this leads to a better-defined adhesion area independent of the brim- or layer height and allows measuring the curing geometry to determine the cross-section using a White Light Interferometer (WLI).

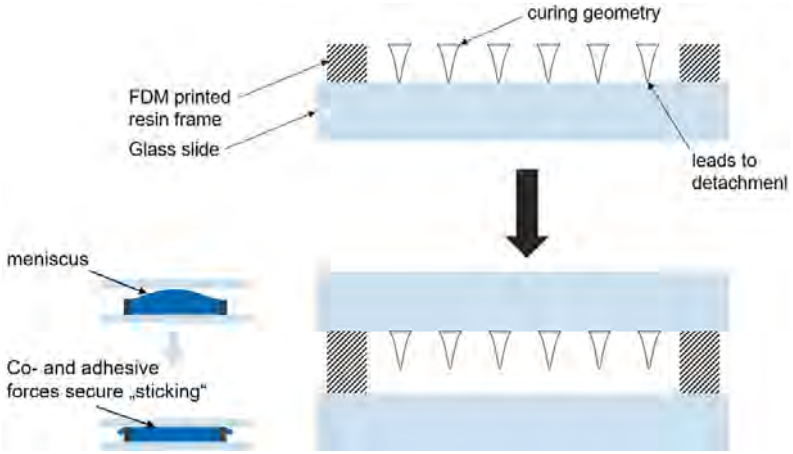

Figure 4.5: Schmematic of the substrate preparation for curing through a glass slide using two microscopic slide and a brim filled with photopolymer to achieve an enclosed material well

To ensure better adhesion on the glass slide in general, a standardized cleaning process of the glass slide is used to provide a clean surface. Having grease residuals and small particles on top of the surface interrupts the direct adhesion between the polymer and the glass surface (see chapter 3.7). This cleaning process also decreases the risk for the formation of pinholes (see chapter 3.6.4) after the curing process. This procedure is a standard in the laboratory and can be split into two basic steps which are presented in the following list.

1. Base cleaning
   (a) Cleaning off coarse impurities and fat residuals with Helarin
   (b) Using an ultrasonic bath with Helarin and water for in depth cleaning for 60 minutes
   (c) Drying off the slides in an oven at 200° C for 10 minutes
2. Residual contaminant removal
   (a) Remove smears, residuals of the cleaning agent and small particles with methanol and a dust free cloth
   (b) Remove evaporation residuals by wiping the glass slide with a dust free cloth

With the substrate preparation and the cleaning procedure in place, the error influences of the process are minimized. The next sections present the determination of a threshold exposure energy for the adhesion of small structures and measurement of the cross-section geometry.

4.3.1 Material Shrinkage and Polymer Adhesion

First structures cured with the setup and software with an arbitrary exposure energy (400-500 mJ/cm^2) show curling and detachment effects. This happens for structures cured directly onto a substrate through the resin in a 200 µm brim as well as for the modified setup by curing through a glass slide. The following figure 4.6 shows a picture of two line triplets that have detached from their substrate. The dimensions of these lines are relatively big with height and width in the range of 300 µm and a length of 10 mm. The detachment of structures is observed to happen between directly after the curing up to 72 hours after the process.

Figure 4.6: Fotograph of two detached line triplets with cured with an exposure energy of 474.24 mJ/cm^2

The hypothesis is, that residual stress from polymerization induced shrinkage eventually leads to a detachment of the structures from the substrate. Looking at the theory of shrinkage in photopolymerization, the main influence factors are determined to be the exposure energy, scan rate (scanning velocity), the structure size and polymerization type (see chapter 3.4). The structure size cannot be influenced since they are dependent on the desired structures dimensions. Neither can the type of polymerization process be changed. The change of velocity is possible but curing with a low velocity would lead to a less dynamic process. The first test is therefore to reduce the laser power to decrease the exposure energy for better adhesion. If a threshold for the exposure energy can be determined, where the structures stay attached to the substrate, the process stays dynamic whilst solving the detachment problem. To test if the reduction of exposure energy is sufficient, the laser power is gradually reduced, and a new set of test structures is defined. Since smaller structures are more strongly influenced by shrinkage related detachment effects, a new pattern of a line triplet with ascending lengths of 0.2, 1 and 3 mm is created. A star pattern with three tips is created to see if shrinkage in an area influences the attachment of small features on the structure edge, like the tips.
The exposure energy is gradually lowered from 200 down to 85 mJ/cm^2. The following figure 4.7 shows the results of decreasing the exposure energy for line patterns and verification with free form geometries. First attempts cured with an exposure energy between 150 and 200 mJ/cm^2 show significant curl distortion and all structures detach from the substrate (see figure 4.7a). Since the structure lengths are now significantly smaller than in the first experiments, the

detachment effect is expected to be more significant than with bigger structures. After lowering the exposure energy below 150 mJ/cm^2 the larger lines stayed attached to the substrate. Reliable adhesion for all tested structures is achieved at exposure energies below 93 mJ/cm^2 (see figure 4.7b). The threshold for reliable substrate adhesion is set at an exposure energy of 90 mJ/cm^2. This threshold also holds for the adhesion of the star pattern (figure 4.7c) and arbitrary structures like text (figure 4.7d).

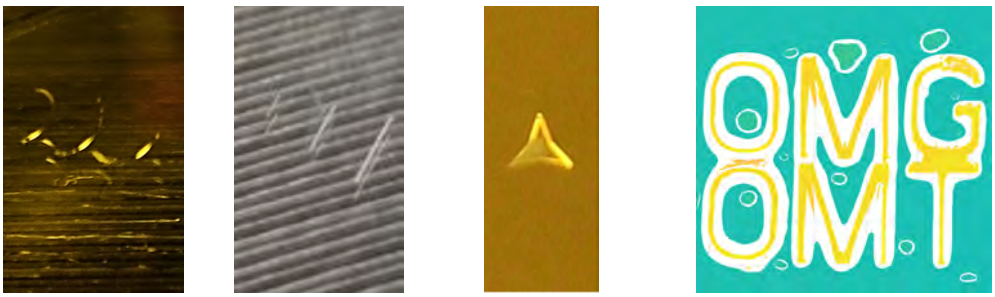

(a) (b) (c) (d)

Figure 4.7: Expermental results for decreased exposure energy on structure adhesion a) Line triplet cured with 162.17 mJ/cm^2 experiencing great curl distortion, b) Line triplet cured with 92.67 mJ/cm^2 attached to the substrate, c) Star structure cured below exposure threshold adhering to the substrate, d) WLI measurement of cured text on a substrate

The determined threshold limits the range of feasible exposure energies E to E_C < E < 90 mJ/cm^2. This range is used to cure and evaluate structures. The next sections deal with the investigation of the structure geometry on a substrate and present an optimization approach for the curing cross-section in defined layerheights.

4.3.2 Determination of the cross-section Geometry

To determine and optimize parameters for curing structures, the cross-section of the curing geometry needs to be evaluated. The model for calculating the curing cross-section proposed by Jacobs (see chapter 3.3) suggests a parabolic curing cross-section that can be calculated using the following equation 4.3.1, which can be derived from equations 3.3.1, 3.3.2 and 3.3.5.

$$C_D(y) = -D_P \cdot \left(\left| ln \left(\frac{E_C \cdot w_0 \cdot v_S}{\sqrt{\frac{2}{\pi}} \cdot P_L} \right) \right| + \frac{2 \cdot y}{{w_0}^2} \right) \tag{4.3.1}$$

With the penetration depth D_P, the gelation threshold E_C, the beam waist radius w_0, the scanning speed v_S and the laser power P_L. This equation is valid for a range of y within the linewidth L_W ranging from $\left\{ -\frac{L_W}{2}; +\frac{L_W}{2} \right\}$. The resulting shape of the curing geometry describes the intersection of the exposure distribution around the focal point with the gelation threshold as shown in the following figure 4.8 as a dotted line.

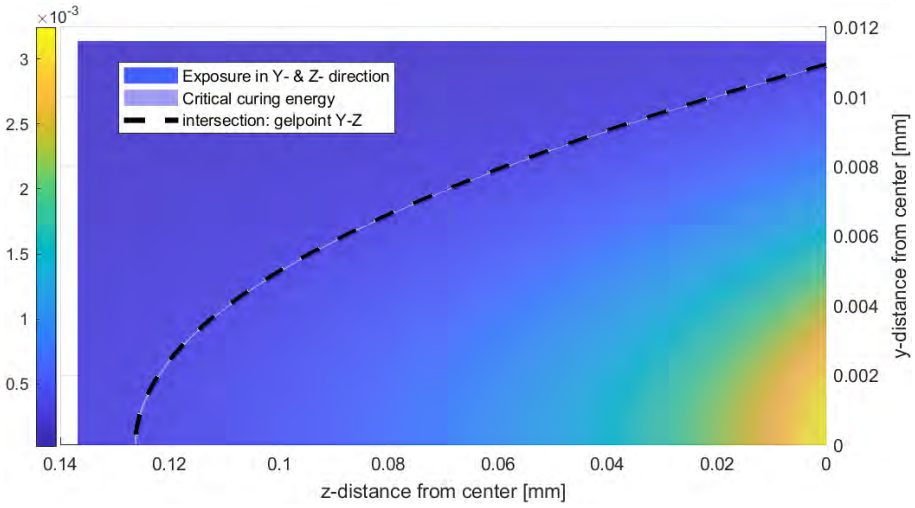

Figure 4.8: Top-down view of plot of the energy distribution around the focal point with the expected curing cross-section highlighted as dotted line

To verify this cross-section shape, the flank geometry of a structure needs to be measured and compared to the theoretical results. Since the cured structures have very steep flanks, the flank geometry cannot simply be measured using top-down WLI measurement since this measurement cannot measure steep flanks. The following figure 4.9 shows an averaged WLI measurement of such a line. Here data points are only available on top of the cured line and on the edge of structure on the structure. With so few data points, it is difficult to make a statement about the actual cross-section geometry. Although the parabolic shape as described by Jacobs would fit, no definite statement can be made. The cross-section could for example also have a gaussian shape like shown in the figure.

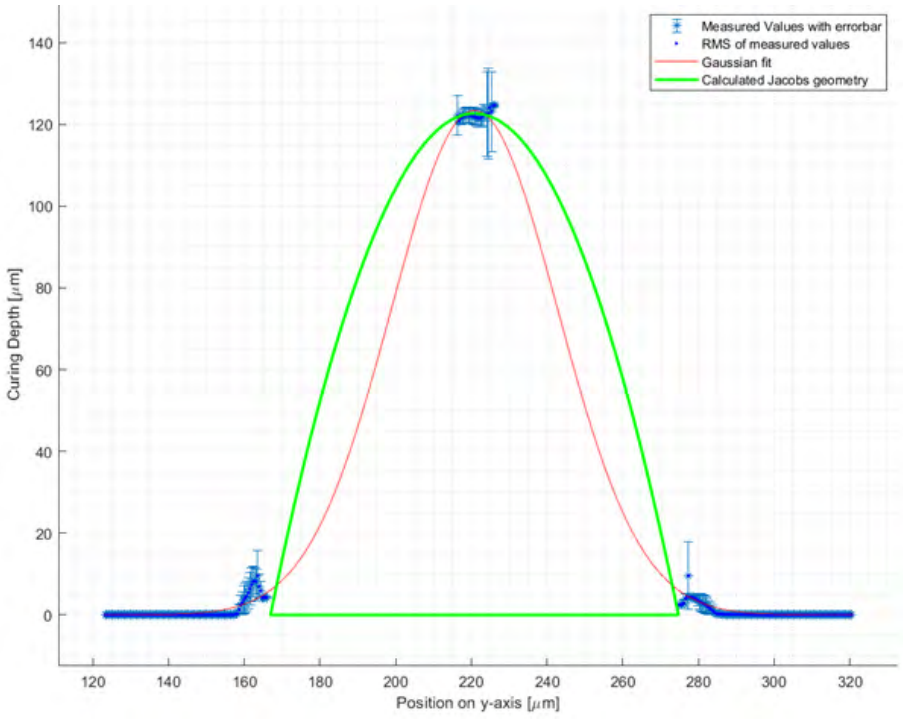

Figure 4.9: Plot of averaged height of a geometry measurement with a fit of a possible gaussian flank shape in red and the calculated parabolic flank geometry in green

To determine the actual cross section shape, a method to measure the flank geometry of the cured lines is necessary. The flanks of a cured line are measured by curing the structure at the edge of the substrate and then measuring it with the WLI under different tilt angles. If the flanks are measured at sufficiently small intervals, the complete flank geometry can be determined by stitching the measurements together. The following figure 4.10 shows the measurement configuration for this purpose.

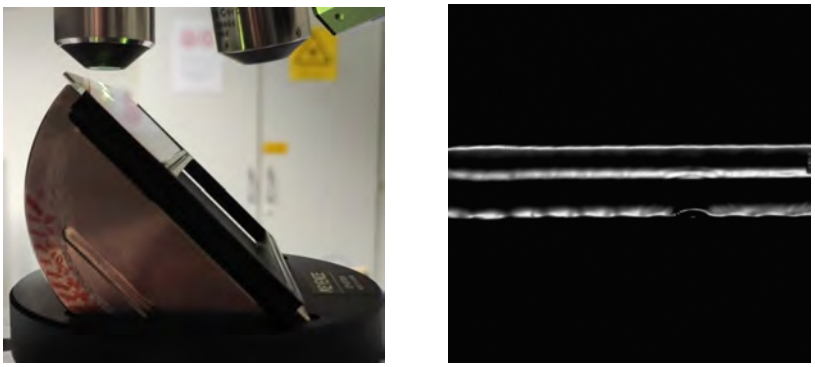

(a) (b)

Figure 4.10: Setup for determining the flank geometry of a cured line using tilted measurements a) Tilt stage at 45° tilt on the WLI, measured with 20x magnification b) WLI picture of line section that was measured at 45° tilt

Removing the tilt and stitching the measurements together, the shape of the curing geometry is fully determinable. Through changing the exposure energy, the behavior of the cured cross-section can be analyzed and compared with the theoretically expected shape. The following figure 4.11 shows the behavior of the cross section when the energy is reduced gradually. These measurements show that the cross section initially has a triangular shape for exposure energies that are much larger than the adhesion threshold (figure 4.11a). When the energy is reduced within the adhesion threshold, a parabolic shape is seen, but a shoulder phenomenon is observed for a certain range of exposure energy. The observed shoulder leads to a deviation from the expected shape at the substrate and shows an unfavorable flank geometry (figure 4.11b). Only at curing energies below around 48 mJ/cm^2 the shoulder phenomenon disappears and the expected parabolic shape is observed (figure 4.11c).

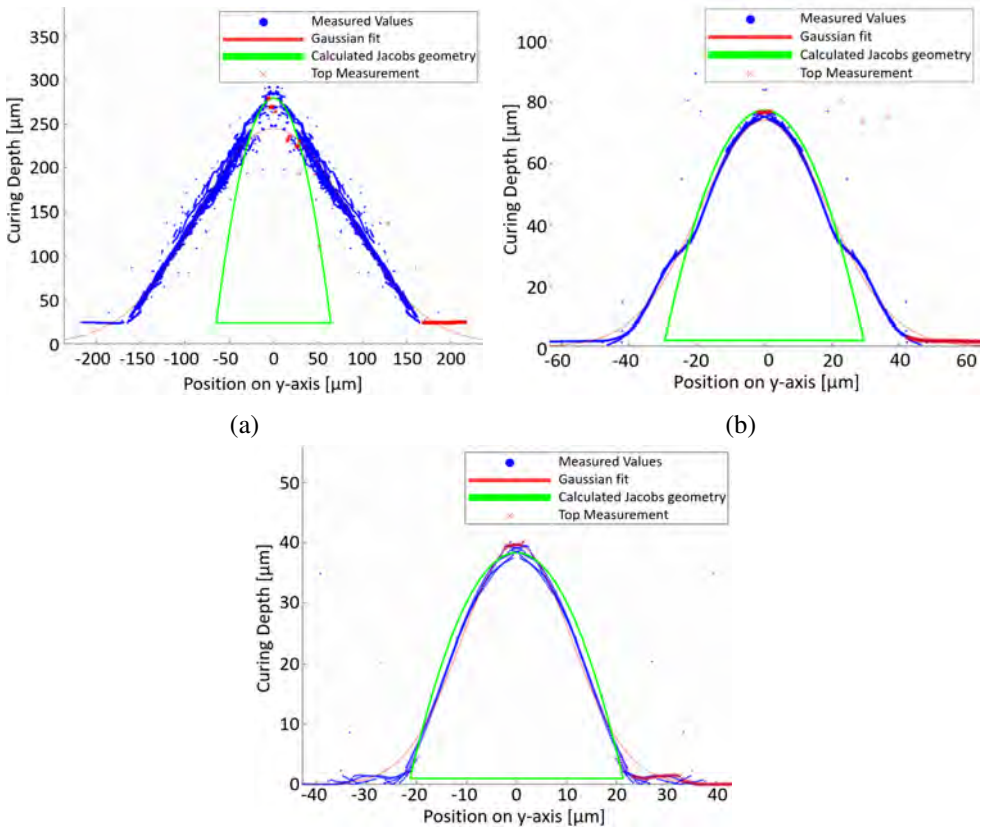

Figure 4.11: Comparison of cross section geometries with calculation model for decreasing exposure energy a) Triangular cross section shape for high exposure energy (here: 950 mJ/cm^2), b) Shoulder phenomenon on cross section for exposure energy in adhesion threshold range (here: 85 mJ/cm^2), c) Parabolic cross section shape for exposure energy below 48 mJ/cm^2 (here: 47.3 mJ/cm^2)

Since the goal is to achieve homogeneous and predictable flank geometries to allow calculation and optimization of the curing parameters, the parabolic shape is desirable. Therefore, the range of exposure energy is further limited to below 40 mJ/cm^2 to safely ensure a parabolic cross-section shape and structure adhesion. At this point the width and height of the structures are in a range below 50 µm and the resulting geometry can be reliably predicted with equation 4.3.1. Since the focus procedure is performed manually using a target and mechanical positioning table, the beam waist radius must be approximated (avg. 38 µm - from stitch measurements). To check the feasibility of this assumption, the measured cross sections cured with the same exposure energy can be compared with the expected cross section geometry. The following figure 4.12 shows the measurements of the cross section for three individual lines cured with the same exposure energy of 40.67 mJ/cm^2 and the expected curing shape from the calculation. Though there are still deviations of up to 18% within the individual geometries due to for example stability of the laser power, deviation in substrate height, inaccuracy of the measurement stitching and difference in focal position, the calculation model represents the expected geometry with sufficient accuracy.

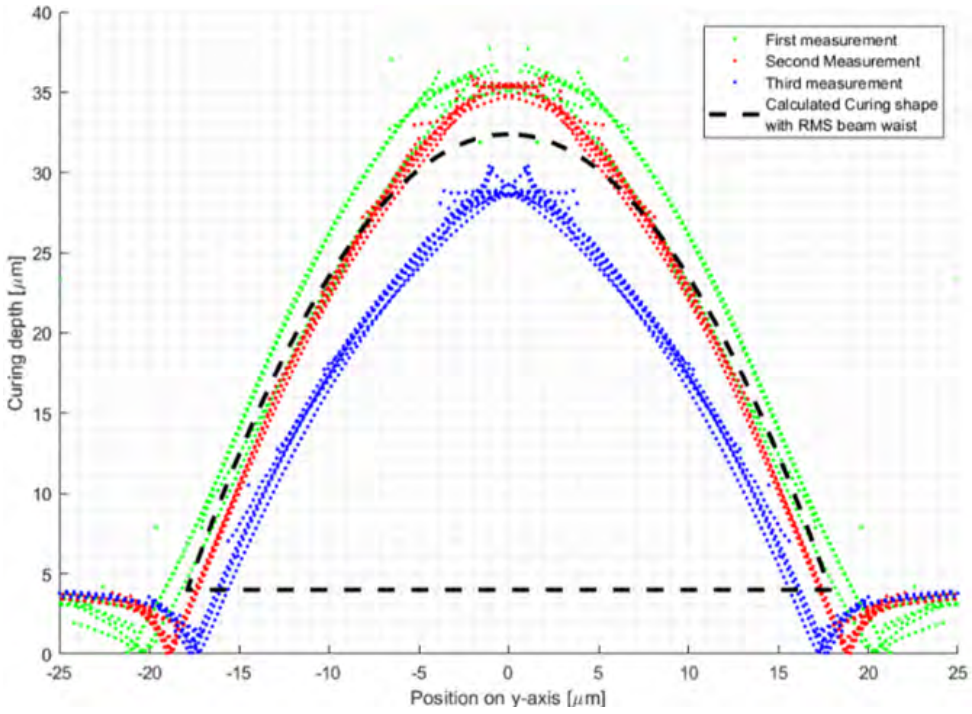

Figure 4.12: Comparison of cross section geometries cured with an exposure energy of 40.67 mJ/cm^2 with the corresponding expected shape by approximating a beam waist diameter of 38 µm

Now that the cross section shape is verified in an exposure energy range of $E_C < E < 40$ mJ/cm^2, the calculation model can be used to optimize curing parameters for a desired structure geometry. This optimization approach is presented in the following section 4.3.2.1.

4.3.2.1 Parameter Calculation for a defined Layerheight

To determine the optimal curing parameters for a structure in a defined layerheight, a condition for what is considered an ideal structure cross-section is necessary. The ideal cross-section is defined to be square, leading to an equal lateral resolution in y- and z-direction. Since the curing cross section is established to be parabolic, the curing cross-section can never be square. To determine the quality of a cured line two conditions are defined. The idea of the first condition is shown in figure 4.13. Here a cross-section of a curing geometry that is cut off at the defined layerheight is depicted with a square as an indicator for the ideal curing cross-section. The line width at the top of the geometry is smaller than the squares width and bigger at the bottom of the geometry. The first condition is therefore, that the area that is cured over the square geometry shall be equal to the area that is cured less than the square shape. This leads to the cured area of the cross-section being the same as the squares area. Depending on the desired layerheight and curing parameters, this results in more than one feasible curing energy setting. Therefore, the second condition defines that the sum of the areas that are cured above and below the desired curing width shall be as small as possible. The second condition demands an overall smaller deviation of the geometry to the ideal square shape. Combining the two conditions leads to the least geometry deviation from the ideal square while maintaining the area integrity as good as possible.

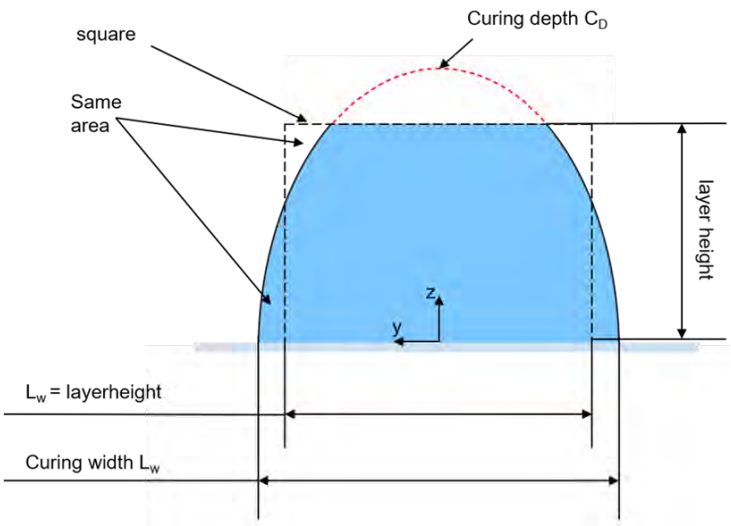

Figure 4.13: Visualization of the curing geometry capped by a layerheight with the ideal square curing geometry indicated as a dashed line

To put the defined conditions in mathematical terms, the first condition defines that the result of the integral of the function for the curing depth (eq. 4.3.1) in the bounds between the cured line width and half the layerheight (= edge of the ideal square) shall be equal its integral between half the layerheight and the width of the curing geometry at the layerheight. To just get the missing area between the calculated geometry the function needs to be subtracted from the layerheight. This leads to the following equation 4.3.2

$$\int_{-L_W}^{\frac{L_H}{2}} C_D(y) \quad dy - \int_{\frac{L_H}{2}}^{y(C_D(y)=L_H))} L_H - C_D(y) \quad dy = 0 \tag{4.3.2}$$

With the layerheigh L_H, the equation for the curing depth C_D (eq. 4.3.1) and the linewidth L_W. Analogous the second condition is formulated in the following equation 4.3.3:

$$\int_{-L_W}^{\frac{L_H}{2}} C_D(y) \quad dy + \int_{\frac{L_H}{2}}^{y(C_D(y)=L_H))} L_H - C_D(y) \quad dy = MIN \tag{4.3.3}$$

Using the quality conditions and corresponding equations, ideal curing parameters can be empirically determined. Based on the established conditions and restrictions, a Matlab optimization script is created. This script optimizes curing parameters by iteration to find the most viable cross section geometry using the quality conditions. The following figure 4.14 shows the example of the curing parameter determination for the calculated beam waist radius 37.96 µm for the current curing setup, optimized for a layerheight of 30 µm.

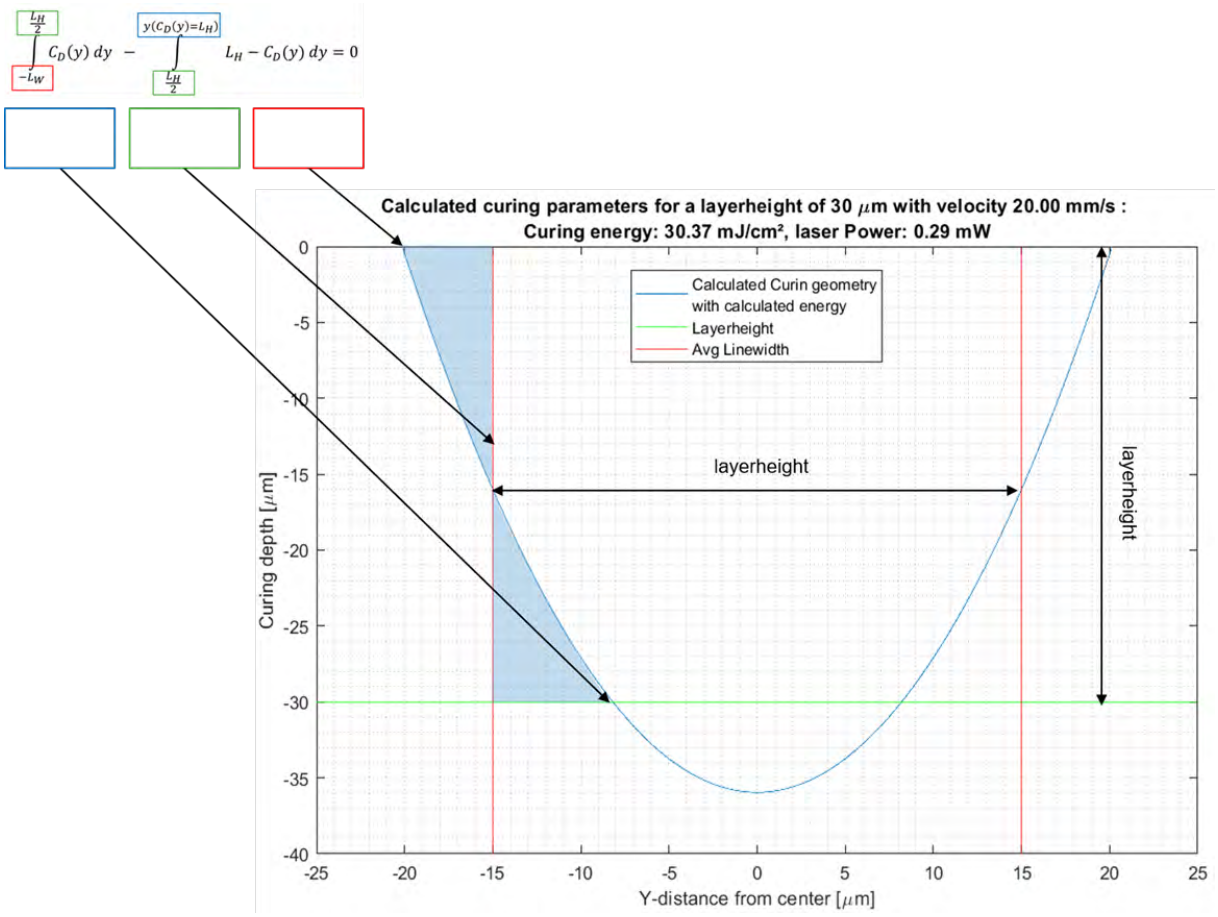

Figure 4.14: Plot of the curing cross-section optimized for a layerheight of 30 µm with the calculated mean beam waist radius 37.96 µm. The integral borders are colorcoded for better understanding

The ideal exposure energy for the example shown in the figure calculated by the script is 30.37 mJ/cm^2, which can be achieved by curing with a velocity of 20 mm/s and a laser power of 0.29 mW. The light blue areas in the figure show the deviation of the curing geometry over and under the ideal square geometry, which is represented by the red and green lines. For a better understanding of the integral borders, the individual borders are color coded in blue, green and red. The corresponding blue, green and red squares point to the placement of the borders. Blue is the maximum linewidth of the geometry, green is the edge of the ideal square and red is the calculated linewidth at the layerheight.

To accomodate small layerheights (< 20 µm) this calculation model needs to be expanded in this work to allow setting a minimum adhesion length (see chapter 7.1). This is neccessary, since for a layerheight of less than 20 µm, the ratio of the structure thickness to its height can no longer be determined solely on the basis of the deviation from an ideal square. This is because of the aspect ratio mismatch of the height and width of structures in this case not allowing the cross section to fit within a square geometry. The optimization for the minimum deviation of the cross section to an ideal square would lead to a very small adhesion area on the substrate. This is shown in the following figure 4.15a. The figure 4.15b shows the approach to solve this problem, which is to set another boundary condition for the determination of the laser power, here a minimum necessary adhesion length of the cross section can be set by the user, this allows

for determining curing parameters with a sufficient adhesion area. Here a minimum adhesion length of 4 µm in a 5 µm layer is chosen.

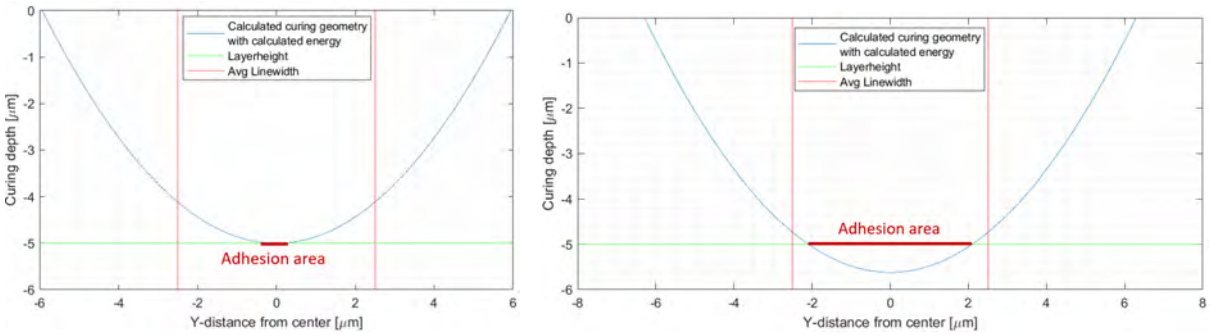

(a) (b)

Figure 4.15: Calculated curing shape with optimized parameters for structure curing in 5 µm layer a) Without correction of minimum adhesion length, b) With a user defined minimum adhesion length of 4 µm

Using the optimization script in compliance with the exposure energy threshold the curing parameters (laser power and scanning velocity) can be optimized for a desired layerheight. The next chapter 5 presents the coating of defined layerheights on planar and convex surfaces.

5 Spin Coating of defined Layers

This chapter deals with the application of a defined photopolymer layer on planar and convex surfaces using the PR48 prototyping photopolymer and a commercially available spin coater. For this purpose, measurement methods for transparent films on glass substrates are compared and tested. After being able to determine the layerheight and surface quality, approaches for predicting the layerheight are presented and the coating process is investigated and improved experimentally. The goal is to achieve homogenous films of photopolymer within the range of one micrometer up to several tens of micrometers on planar and convex surfaces.

5.1 Measuring Layerheights on planar Substrates

To be able to determine the height and characterize the quality of a spin coated transparent film, a way of measuring the height and surface of a coated photopolymer over a defined area is necessary. Using the available hardware there are two options: using a chromatic confocal sensor or using white light interferometry. The following sections discuss these approaches and their benefits as well as challenges for the current application.

5.1.1 Thickness Measurements with chromatic confocal Sensor

A chromatic confocal sensor works by focusing white (polychromatic) light onto a surface. The principle of a confocal measurement is shown in the following figure 5.1. Each wavelength of the light source is focused on an individual image plane due to chromatic aberration. The reflected light from the surface is collected by the objective lens, deflected using a beam splitter and analyzed using a spectrometer. Using a confocal pinhole ensures the light that is in focus reaches the spectrometer at a much higher illumination density leading to a peak for that specific wavelength, since only this wavelength is exactly in focus. Using this peak, the distance to the measured surface point can be determined precisely and contactless. [15, 30, 53]

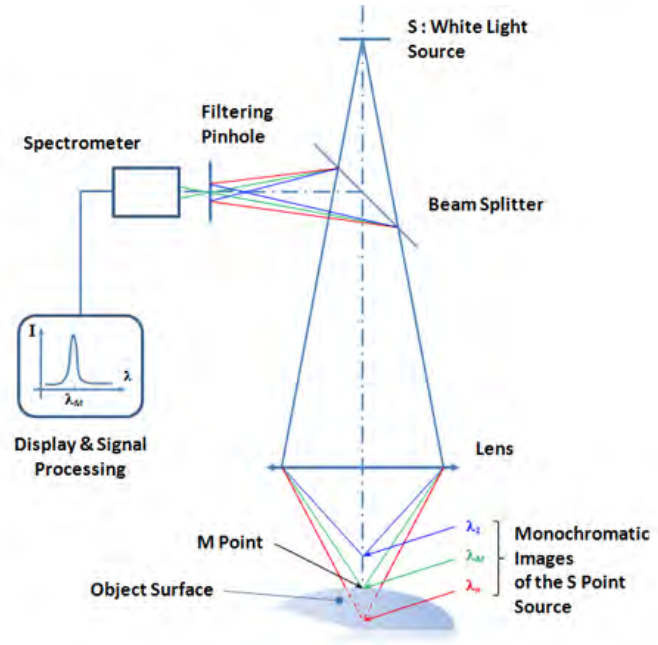

Figure 5.1: Schematic representation of the measurement principle of a chromatic confocal sensor [57]

These sensors are capable of measuring layer thickness even for multiple layers if the individual layers are transparent and have different refractive indices. In this case every surface reflects a wavelength which is focused on the layer, resulting in multiple recorded peaks on the spectrometer. From these peaks, the thickness of a layer can be calculated from the peak distances, if the refractive index of the materials is known. The refractive index of the coating leads to a parallel shift of the focal point in the material, which influences the measured distance leading to an underestimation of the actual thickness. This influence on the thickness measurement can be corrected using the following equation 5.1.1.

$$d = d_{meas} \cdot n \tag{5.1.1}$$

With the thickness d, the thickness measured with the sensor d_{meas} and the refractive index of the layer n. Confocal metrology offers a submicron resolution which makes it ideal for topography measurements. For topography measurements it is almost independent of the material. For thickness measurements however, it is limited to transparent materials. The measurement speed is relatively high (up to 70 kHz measurement rate [72]) but requires an external positioning setup for measuring surfaces since the topography or thickness can only be measured one point at a time. The measurement is however limited to a specific distance between the sensor and the surface. [30]
While the resolution of the measurement is very high, leading to a precise determination of distance or thickness, the minimum layer thickness showed to be critical for the desired application. The following figure 5.2 shows a measurement of the thickness for a PR48 droplet on a

microscope slide. The measurement shows a thickness of 507 µm, the correction for the refractive index is performed by the measurement software automatically when given the materials refractive index (PR48: 1.4761) and abbe number (PR48: 40). The figure also shows the issue that arises when using the specific sensor, namely Micro Epsilons IFS2405-1, that is readily available. Here, even at the highest peak amplification and best lateral resolution setting, the second peak in the material is very low and very close to the main peak of the photopolymer surface. When the layerheight is further reduced the peak becomes even smaller and moves closer to the main peak, eventually becoming indistinguishable from signal noise.

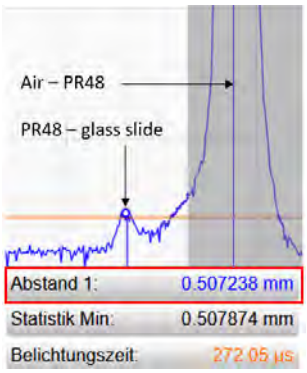

Figure 5.2: Measurement of layerthickness for a PR48 droplet on a microscope slide using Micro Epsilons IFS2405-1 confocal sensor

Since the goal is to coat photopolymer layers in the range of 10 µm, the current sensor configuration is insufficient for thickness measurement. Eventhough the available sensor head has a sufficient measurement range of 1 mm and a dynamic resolution of 52 nm, making it very desirable for the topography measurement of the coated surface, the minimum measurable layerheight is 50 µm. Using the sensor in the middle of its measurement range allows the measurement of thinner layers, but not down to the micron scale range necessary for the desired coating height in this work.[41] Not only would the thickness and topography measurement of a spin coated layer using this confocal sensor require the development of a positioning and evaluation system to measure over a surface area of coated substrate, but it would also be necessary to purchase a more precise and expensive sensor head. Therefore, in the next section another readily available approach of determining the layerheight and surface topography is investigated - white light interferometry.

5.1.2 Thickness Measurement using a White Light Interferometer

The functionality of a White Light Interferometer (WLI) is based on the Michelson interferometric principle and offers non-contact 3D measurement of surfaces. The following figure 5.3 shows the principle of the interferometric measurement process. The measurement works by splitting the light of the white light source into two beams. These beams are reflected by a reference mirror and the surface of the measurement object. Superimposing these reflections on a camera chip leads to an interference pattern. The surface geometry within the same optical

path length of the reference beam creates a phase pattern (fringes). Scanning along the z-axis leads to a shift of the fringe pattern. Thereby, each pixel samples a different point on the surface whereas the intensity of the fringes is used to decode the height. The interference signal is strongest at a point on the measured surface when the optical path length is exactly the same as for the reference beam. Correlating the interference signal with the position of the WLI stage allows for precise topography measurement in an area. The size of this area depends on the objective lens. [4] This measurement method only works for reflective surfaces. For measurements of less reflective or thin transparent materials a small coherence length (i.e. white light) is necessary to achieve a high resolution and prevent the superposition of reflections on multiple surfaces.

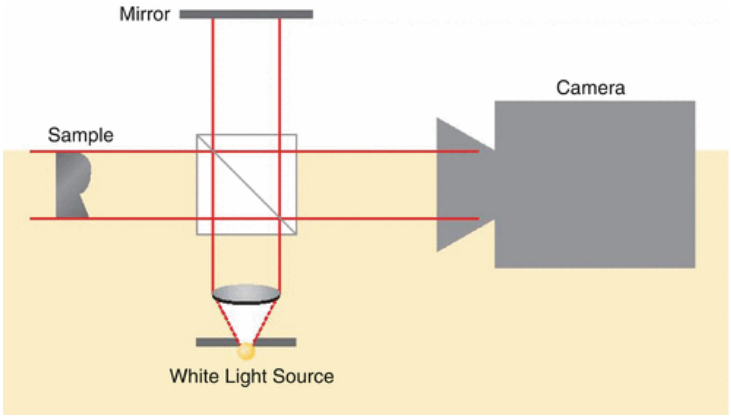

Figure 5.3: Interferometric measurement principle on the example of a Michelson interferometer [4]

The WLI used in this work is the Zygo NewView 8000. It comes with four objectives allowing a magnification of 5x, 10x, 20x and 50x and allows a digital zoom of 0.5x, 1x or 2x. It has a vertical scan range of 150 µm using a precision piezo drive and up to 20 mm using a motorized z-stage. It shows a 0.12 nm topography repeatability and a submicron optical lateral resolution (depending on the objective). The device is equipped with an XY positioning stage, which allows measurements in a lateral measuring area of up to 150 x 150 mm. This is possible because the associated software allows individual measurements to be combined by overlapping part of the measurement area. A movement profile is created with the positioning stage and the measured profiles are stitched together by the software. [86]
Since the available device does not allow direct thickness measurement there are two options for determining the height of a spin coated layer: stitch measurement and measuring the substrate surface through the transparent coating and calculating the layerheight. The first option is to use a substrate, that is big enough that a part of the substrate remains uncoated. This is schematically shown in the following figure 5.4. The idea is to use the uncoated substrate surface as a reference and use the XY stage and stitch option of the WLI to measure the topography over an area large enough to cover uncoated parts of the substrate. This adds a reference to the measured surface topography and enables to determine the layer thickness of the coating.

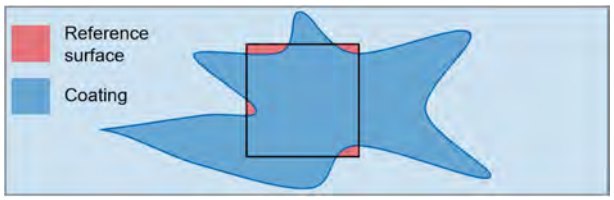

Figure 5.4: Schematic of layerheight determination using WLI stitch measurement

However, this method has two major flaws. Firstly, due to the stage movement, the stitch measurement loses accuracy and the precise z-position is compromised. The stitch measurement is achieved by combining individual measurements using an overlap in the XY position between measurements. Even a slight tilt of the substrate or deviation in z-position due to movement results can lead to an offset in the measurement, this is shown in the following figure 5.5. The software tries to compensate these influences. However, these positioning and orientation errors can lead to creases in the measured surface and a distorted measurement which cannot be compensated by the software anymore. The bigger a stitched area is, the more severe are the influences on the quality of the stitch.

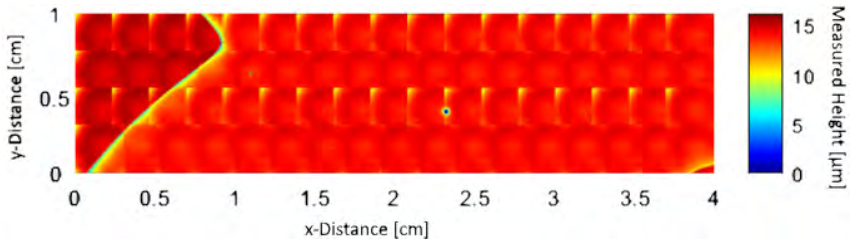

Figure 5.5: WLI stitch measurement of a photopolymer film

The second problem with the stitch measurement is, that it is a time-consuming process, a stitch measurement as shown in the figure above takes tens of minutes. This is problematic, as surface stability may decrease during this period, leading to contraction of the layer and increasing the risk of contamination by ambient particles, resulting in damage to the film (see chapter 3.6.4). This method of measurement allowed for an initial measurement of the layerheight to verify the plausibility of the calculation model (see chapter 5.3.4). However, this method is insufficient for determining an exact layerheight. Therefore, the next sections present another approach for determining the layerheight of a transparent coating using the WLI.

The following sections present the approach of determining the layerheight on a planar substrate by measuring the substrate surface through the transparent layer. Since the coated photopolymer is a different material than the substrate and the coated layerheights are greater than the coherence length of the white light source, the transition area (i.e. substrate surface) can be measured individually with the WLI for transparent materials. If a common z-reference for the measurement of the layer and substrate surface is found, these measurements can be used to determine the layer thickness in the field of view of the objective lens of the WLI by subtracting the measured position of the substrate topography from the position of the layer topography. In

order to determine the layer thickness with this method and to establish a common reference point, three things need to be considered. The first is the influence of measuring through a material other than air on the measurement results. Other than for the confocal sensor, the deviation that arises by measuring through a material is not influenced by the parallel shift of the focus but by the increase of the optical path length inside a material with a refractive index greater than 1. This leads to an overestimation of a measured distance and therefore to a reverse correction of the thickness measurement compared to equation 5.1.1. The influence of a materials index of refraction in a WLI measurement can therefore be corrected using the following equation 5.1.2.

$$d = \frac{d_{meas}}{n} \tag{5.1.2}$$

The second thing that needs to be established to allow the measurement is the internal reference the WLI uses to determine the z-coordinate of a point. The system does not apply its global coordinate reference to a measurement. A single measurement is always referenced to the lowest point that is approached during the scanning. The third important thing to consider is the fact that the surface that is used in a measurement is always the first surface that is found during the measurement. Using this information, a measurement method is developed as shown in the following figure 5.6. The thickness of a layer is determined by using the same scan origin point for both the measurement of the layer and the substrate underneath with a different scan length. This is possible because the position of the origin point is centered in the motion profile of the scanning process and the device returns to the origin point after the scanning process. To measure the substrate- or layer surface, the scan length can be adjusted. Since the scanning movement is performed with the high precision piezo drive which has nanometer repeatability, the origin of both measurements can be considered equal.

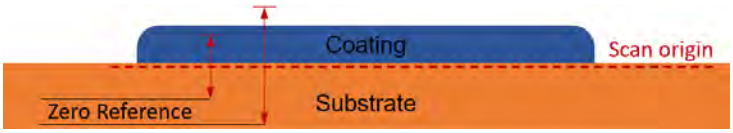

Figure 5.6: Principle of through resin measurement using the WLI

Using the measurements of the substrate and coating surface, the height of a coated layer at a given point XY can be determined using the following equation 5.1.3.

$$h_{layer}(x,y) = \frac{z_{coat}(x,y) - z_{substrate}(x,y) + 0.5 \cdot l_{scan_{coat}} - 0.5 \cdot l_{scan_{substrate}}}{n} \tag{5.1.3}$$

With the measured z coordinates on the coating surface z_{coat}, the z-coordinates of the substrate surface $z_{substrate}$, the scan length of the coating measurement $l_{scan_{coat}}$ and the scan length of the substrate measurement $l_{scan_{substrate}}$. This measurement method allows for a reliable determination of the layerheight in the field of view of the measurement. Since the layerheight is determined relative to the substrate surface, this method also compensates of small tilts in the substrate. The feasibility and accuracy of this measurement method can be determined by measuring on the edge of a coating using a part of uncoated substrate as a reference. The following figure 7.2 shows a measurement of the edge of a 20 µm photopolymer layer with (5.7b) and without (5.7a) the correction of the of the error due to the materials index of refraction.

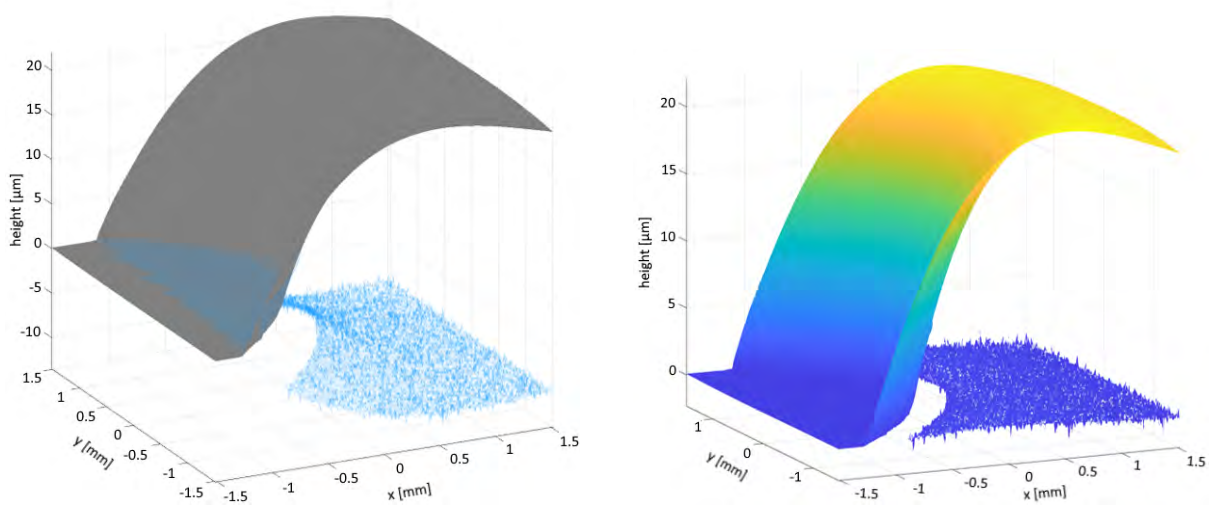

(a) (b)

Figure 5.7: WLI measurement of layer thickness on the edge of a transparent coating a) Without correction b) With correction

Using the uncoated substrate as a reference and fitting a plane to its surface allows analyzing the measurement as shown in the figure 7.2 above. By subtracting the measured surface from this fitted plane, the accuracy of the measurement method can be determined. The following figure 5.8 shows the fitted plane in the refraction corrected measurement and the result of the subtraction. The analysis of the subtraction shows that the average deviation of the measured surface to the plane fit is 269 nm, but the surface quality of the measurement through the coating is really poor. However, the sub micrometer deviation in height is acceptable and the surface quality is negligible since the topography of a coated surface can be analyzed using the measurement of the coating surface only.

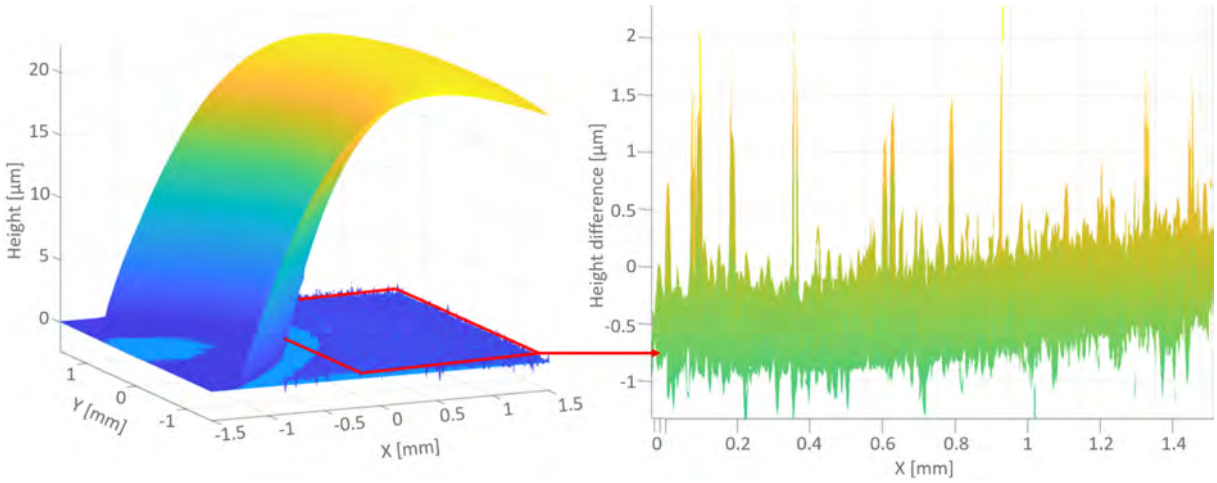

Figure 5.8: Analysis of the deviation of a measurement through a transparent film to the expected substrate geometry using a WLI measurement on the edge of the coating

A Matlab script to calculate the layerheight and surface quality is developed allowing the measurement data to be evaluated automatically. The following figure 5.9 shows the measurement and evaluation of a spin coated surface on glass slide with a height of 17.22 µm and the determined surface parameters, which are the arithmetic mean of surface deviation S_a, the maximum peak height S_p, the maximum valley depth S_v and the maximum peak-valley $(P-V)$ distance S_z.

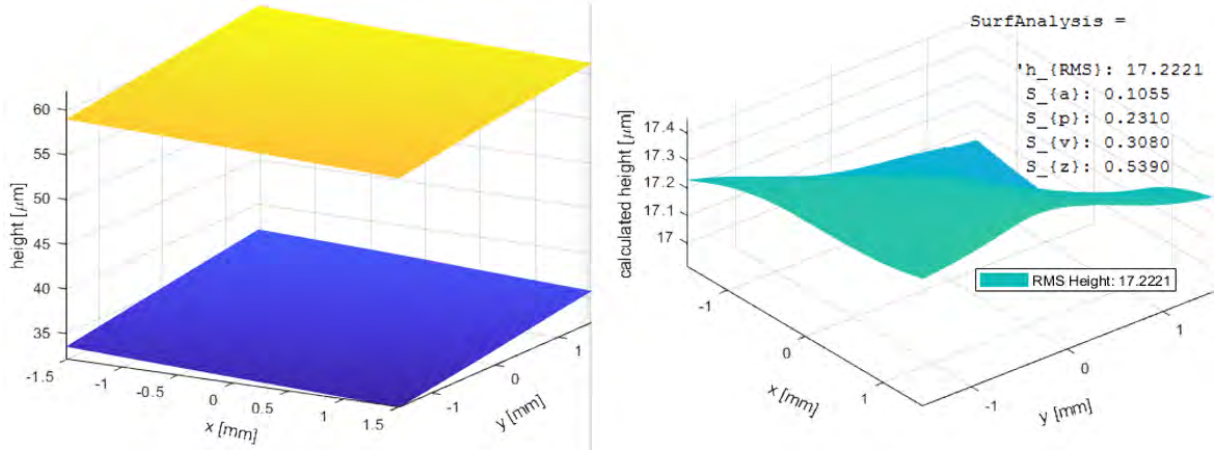

Figure 5.9: Combined surfaces from through resin measurement of planar layerheight and layerheight evaluation with surface analysis for spin coated PR48 film

This measurement method allows for a fast and simple way of determining the layerheight of a transparent coating on a substrate. It shows sub micrometer accuracy in determining the layerheight. The area in which the layerheight can be determined is limited by the field of view of the WLI, for the device used in this work this means a maximum of 3.03 x 3.03 mm. To verify homogeneity over a bigger area, multiple measurements of the layerheight can be performed in different positions and analyzed individually. The next section 5.2 presents the adaptation of this measurement method to determine the layerheight and analyze the topography of transparent coatings on convex surfaces.

5.2 Measuring Layerheight on convex Substrates

This subchapter deals with the development of a measurement method for layerheights on convex surfaces perpendicular to the surface geometry using the same principle of measuring through a transparent coating presented in the previous section. Due to the surface geometry of a convex surface, the measurement through the coated film does not require the correction of the scan length since both measurements measure the film surface outside of the measurement center and can be combined using this surface as reference. The following figure 5.10 shows the measurement principle and examples for resulting measurements. The movement profile of the scan is changed to measuring downwards. This setup allows for a much higher z-range of the scanning motion up to 20 mm, which means even for small radii of curvature, the whole surface geometry can be determined in the WLIs field of view. The measurements of the substrate reference and layer geometry are performed with different origins and can be combined by using a point on the coated surface that is seen by both measurements. Using this setup, the coating surface and a partial measurement of the substrate surface as a reference point is obtained.

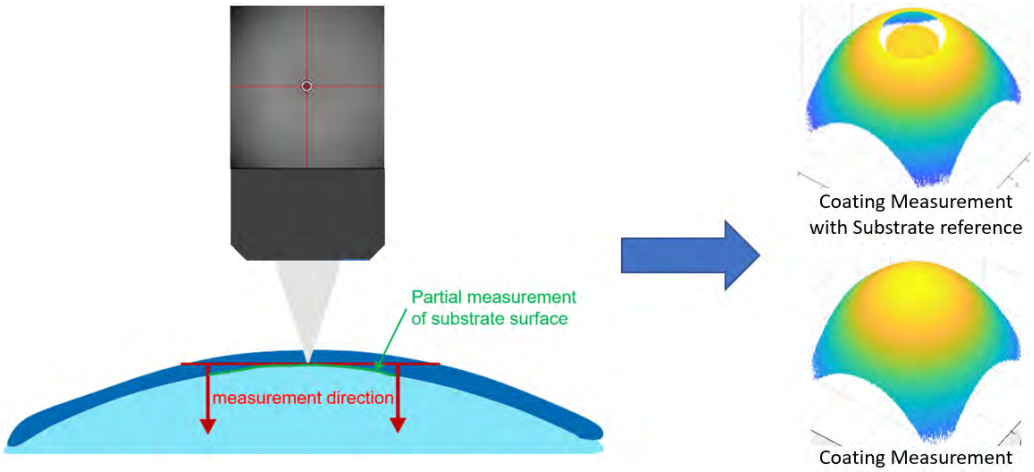

Figure 5.10: Measurement principle and resulting surface measurements for determination of layerheight on convex surfaces

To determine the layerheight on a convex substrate using this measurement method, the following calculation method is developed. The following figure 5.11 shows the approach using a geometrical model of the substrate to determine the layerheight perpendicular to the substrate surface. The idea of this approach is to use the center of the substrate surface as a reference to determine the center point of the substrates radius of curvature. This is done by calculating the normal vector on the peak of the measured substrate reference and using the known radius of curvature of the substrate to determine the center point. Before doing this it is important to compensate the influence of the material on the measurement using equation 5.1.2.

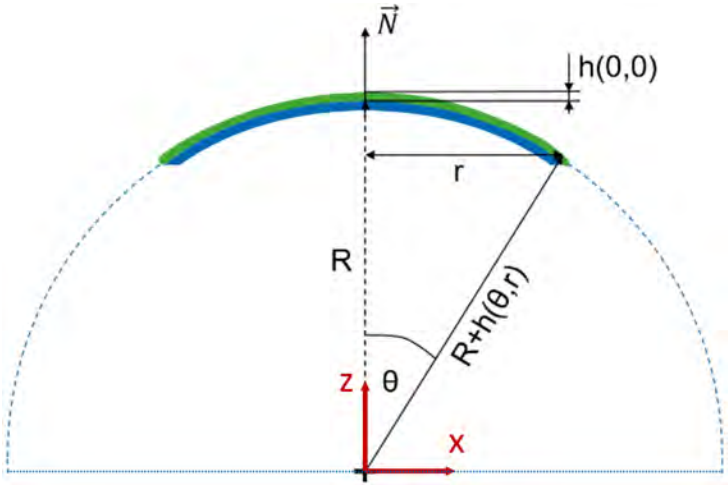

Figure 5.11: Geometric model of a coating on a convex surface with known radius of curvature for calculating the film thickness

Using the relative height of the measurement to the center point and the radial distance r from the center point to determine θ and substituting the distance r for $\sqrt{x^2+y^2}$ using their trigonometrical relationship, the height of a coated film on a given point XY using the geometric model can be determined using the following equation 5.2.1.

$$h(\theta,x,y) = \frac{\sqrt{x^2+y^2}}{sin\theta} - R \tag{5.2.1}$$

With the cartesian x- and y- coordinate to a point of the coating surface, the angle to the point on the coating surface θ and the radius of curvature of the substrate R. Using this equation, the layerheight of the film can be determined. The viability of using the normal vector do determine the center reference point for the measurement can be verified by measuring multiple surface segments using the WLI and comparing these measurements with the theoretically expected shape using the calculated center point. The following figure 5.12 shows this comparison for a slice through the y-axis of a measurement. Here the measured surface segments are shown on the left side of the measurement overlapping the calculated geometry completely, which is shown on the right side as the orange curve. Here a sub-micrometer deviation from the measured to the calculated lens geometry is seen. This shows that the determination of the center point from the measured segment is sufficiently accurate.

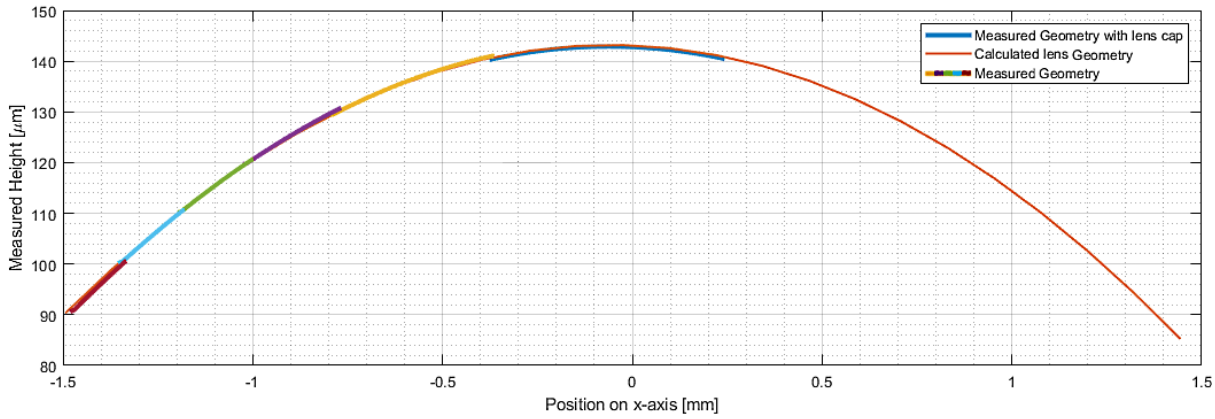

Figure 5.12: Measurement of substrate surface segments in comparison to calculated surface geometry

Using the determined measurement and calculation method an evaluation script is developed which calculates the layerheight and displays the calculated surface of the layer as well as a slice through the measurements in x- and y- direction. The following figure 5.13 shows those slices and the correspondingly calculated layerheight.

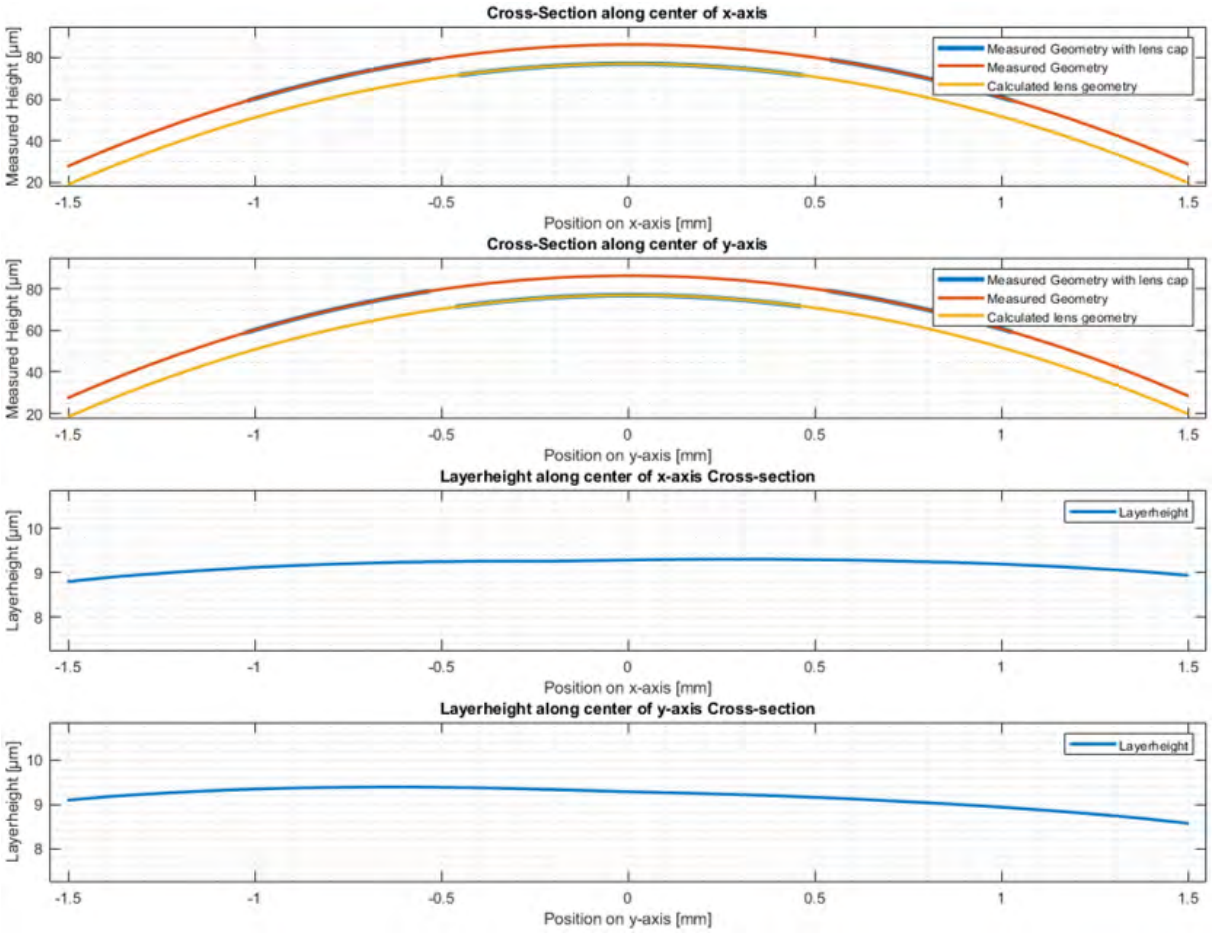

Figure 5.13: Slices in x- and y- direction through the measurement of 9.05 µm photopolymer layer with the respective slices through the calculated layerheight

Using the established measurement methods for layerheights on planar and convex surfaces, the spin coating quality, results and parameter determination can be evaluated and optimized. The

next subchapters present the development of a reliable and predictable spin coating process to achieve layerheights between 5 and 30 µm on planar and convex substrates.

5.3 Defined Layer Application on planar Surfaces

This subchapter presents the experiments for spin coating a photopolymer layer with a defined height onto a planar substrate and necessary improvements of the coating process. To achieve this goal, a calculation model is presented to determine spin coating parameters for a desired layerheight. The expected influence of the initial height, which needs to be approximated, on the layerheight is evaluated. Finally, experiments and improvements of the coating process are presented, and their results are discussed.

5.3.1 Calculation Model for Spin Coating Parameters

This section describes the implementation of the mathematical spin coating model on planar surfaces presented in chapter 3.6.5.1 and the development of an optimization script to calculate feasible parameters for a desired layerheight. To be able to use equation 3.6.6 to determine the layerheight of a spin coated film on a planar surface, the initial height of a volume of fluid on the substrate is needed. This height can be approximated as the height of a sphere cap. Using the equation for the volume of a sphere cap and solving for the height h, the initial height can be approximated using the following equation 5.3.1.

$$h_0 = \frac{\left(\sqrt{\pi^2 \cdot a^6 + 9 \cdot V^2} + 3 \cdot V\right)^{\frac{2}{3}} - \pi^{\frac{2}{3}} \cdot a^2}{\sqrt[3]{\pi} \cdot \sqrt[3]{\sqrt{\pi^2 \cdot a^6 + 9 \cdot V^2} + 3 \cdot V}} \tag{5.3.1}$$

With the base radius of a sphere cap a, and the drop volume V. This gives an approximation of the initial layerheight. If the initial height needs to be predicted more precisely more sophisticated methods, like the sessile drop technique need to be used to determine the initial height. The influence and therefore importance of the initial height for this model is evaluated in the next section 5.3.2. By measuring the radius of a droplet with a defined volume that is pipetted on a substrate, the initial height can be approximated. The following figure 5.14 shows these measurements for a PR48 volume between 50 - 250 µl. In that range an almost linear behavior of the radius over volume is seen.

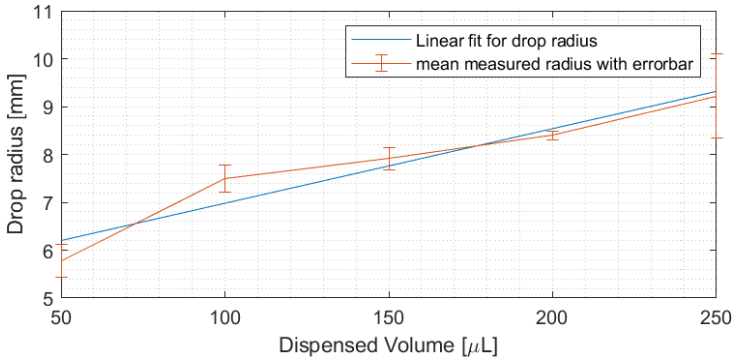

Figure 5.14: Measurement of PR48 drop radius over material volume on a plasma activated glass surface

Using the linear fit in the figure above, the radius of a 50 - 250 µl drop of PR48 on plasma activated surfaces can be approximated using the following equation 5.3.2.

$$r_{PR48}(V) = 0.0156 \cdot V + 5.422 \tag{5.3.2}$$

With the Volume of the droplet V in µl. Using this approximation for the initial height of a PR48 droplet in combination with the temperature dependent viscosity of the material, the height of a layer over time and angular velocity as described in equation 3.6.6 can be calculated. Since the velocity of the used spin coater is set in revolutions per minute, the angular velocity is converted to RPM using the following equation 5.3.3.

$$\frac{1}{min} = \frac{60}{2\pi} \cdot \omega \tag{5.3.3}$$

With the angular velocity ω. By substituting the angular velocity and solving equation 3.6.6 for the revolutions per minute, the desired RPM can be calculated using the following equation 5.3.4.

$$\boxed{RPM(h,t) = \frac{60}{2\pi} \cdot \frac{\sqrt{3} \cdot \sqrt{\eta \cdot \left(h_0^2 - h^2\right)}}{2 \cdot h \cdot h_0 \cdot \sqrt{\rho} \cdot \sqrt{t}}} \tag{5.3.4}$$

With the initial height h_0, the desired height h, the viscosity η, the material density ρ and the coating time t. Using the coating time as a variable, any combination of RPM and spin time that leads to a defined layerheight can be calculated. This is used in a Matlab script to calculate RPM over coating time for a set of desired layerheights. The following figure 5.15 shows the RPM over time for layerheights between 5 and 30 µm. Here, a volume of 100 µl and a temperature of 28.7° C, which is an experimentally determined temperature of the PR48 photopolymer on a substrate after plasma activation, is used. This figure can be used to determine parameter pairs for the coating process. It is advisable to use parameter pairs where the curve has a low slope, this makes the result less error-prone.

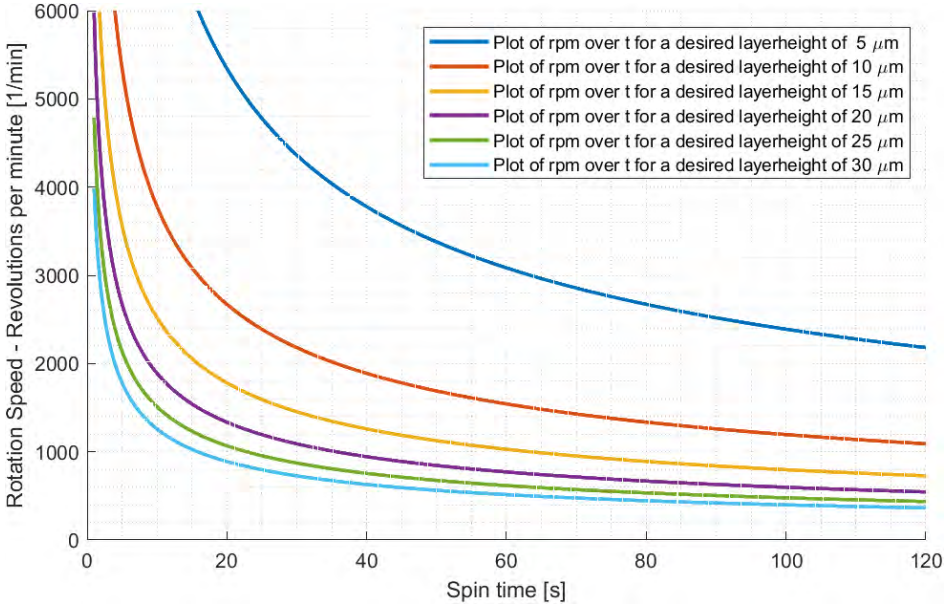

Figure 5.15: RPM over coating time for desired layerheights between 5 and 30 µm on a planar surface on a planar surface for a volume of 100 µl PR48

Using the model established in this section, the coating parameters for a defined layerheight on a planar substrate can be predicted, the next section describes the calculation of the influence of a change in the initial height on the layerheight to determine if the approximation of the initital height is usable.

5.3.2 Determination of Deviation in Coating

This section presents an error calculation for the influence of a deviation in initial layerheight on the expected coating results. This allows to determine, if a deviation due to the approximation of the initial height or a deviation from the pipetted volume has a significant influence on the expected height. Using the following equation 5.3.5 for error propagation, the influence of an error on another parameter can be determined.

$$\Delta z = \sum_{1}^{j} \left(\frac{\delta f}{\delta x_j} \cdot \Delta x_j \right) = \left| \frac{\delta f}{\delta x_1} \cdot \Delta x_1 \right| \left(+ \left| \frac{\delta f}{\delta x_2} \cdot \Delta x_2 \right| + \ldots + \left| \frac{\delta f}{\delta x_j} \cdot \Delta x_j \right| \right) \tag{5.3.5}$$

With the function of the influenced parameter f, an influencing parameter x_j and the change of the influence parameter Δx_j. By deriving a function by one of its influencing parameters and inserting the deviation of the influencing parameter, equation can be used to determine the expected deviation. Using this equation, the influence of the initial height on the expected layerheight after spin coating can be determined using the following equation 5.3.6.

$$\Delta h_{h_0} = \frac{3 \cdot \sqrt{3}}{\left(\frac{4 \cdot h_0^2 \cdot \rho \cdot t \cdot \omega^2 + 3 \cdot \eta}{\eta}\right)^{\frac{2}{3}}} \cdot \Delta h_0 \tag{5.3.6}$$

When evaluating the results of this function for arbitrary spin coating parameters, it is shown, that the influence of the initial height on the height after coating is very low. For example, a change of 5% in pipetted Volume (for an initial Volume of 100 µl at 20° C) would result in a deviation of 0.018 nm in height. For a deviation of 50% in volume this deviation only increases to 0.236 nm. With an influence that small, the approximation of the initial height and eventual errors in pipetted volume become negligible. The calculation model in combination with the initial height approximation can be used. The next section 5.3.3 presents experimental results for coating with the determined calculation model in this chapter.

5.3.3 Coating Results and Measurements

Based on the spin coating parameters determined with the calculation model, this section presents experimental results, measurements, and improvements of the coating procedure to generate homogenous films with a defined layerheight on planar surfaces. First the application method of the photopolymer is investigated. This is done by applying 100 µl of the PR48 photopolymer prior to the spinning motion (static application) and during the spin up process (dynamic application). In both methods the (unactivated) substrates are then spun at the calculated RPM for a defined time. The material is applied centrally on the substrate using a FDM printed adapter. Figure 5.16 shows the photopolymer application using an air-displacement pipette (figure 5.16a) as well as the results of a spin coating process with each application method. To achieve a layerheight of 20 µm, the substrate is spun at 1400 RPM for 30 s, for static (figure 5.16b) and dynamic (figure 5.16c) application of the photopolymer. Here, the coatings with static material application show an intact layer. However, for repeated measurements with the same parameters, the expansion form and is seen to vary significantly and measurements of the surface topography show bead formation on the edges of the coating, which influence the surface shape throughout the whole layer. The coatings with dynamic material application show an inconsistent coverage of the substrate with spotty areas and holes in the surface. The high

viscosity of the resin leads to scattering upon impact on the surface making this application method unusable for the current process. The static material application method is chosen for further experiments.

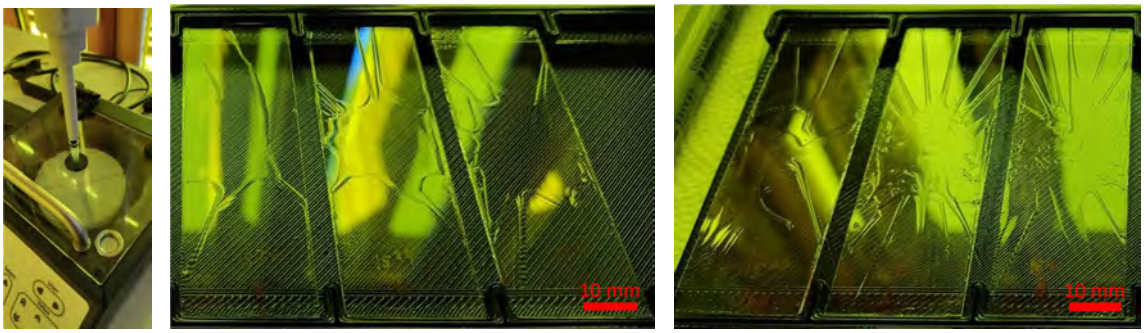

(a) (b) (c)

Figure 5.16: Material application comparison for spin coating a) Pipetting with FDM printed intake for central dispense, b) Coatings with static material application, c) Coatings with dynamic material application

When investigating the distribution of the layer during the coating process on a clean, unactivated surface, poor surface wettability and a non-uniform distribution of material is observed. The following figure 5.17 shows images of a spin coating process at 3000 RPM of 100 µl PR48 taken with a high speed camera. Even before the coating process begins, the droplet is highly contracted and not distributed in a completely symmetric form. During the spin coating process, a non-uniform distribution around the center is observed. This is undesirable since it limits the reliably coatable area and repeatability of the process.

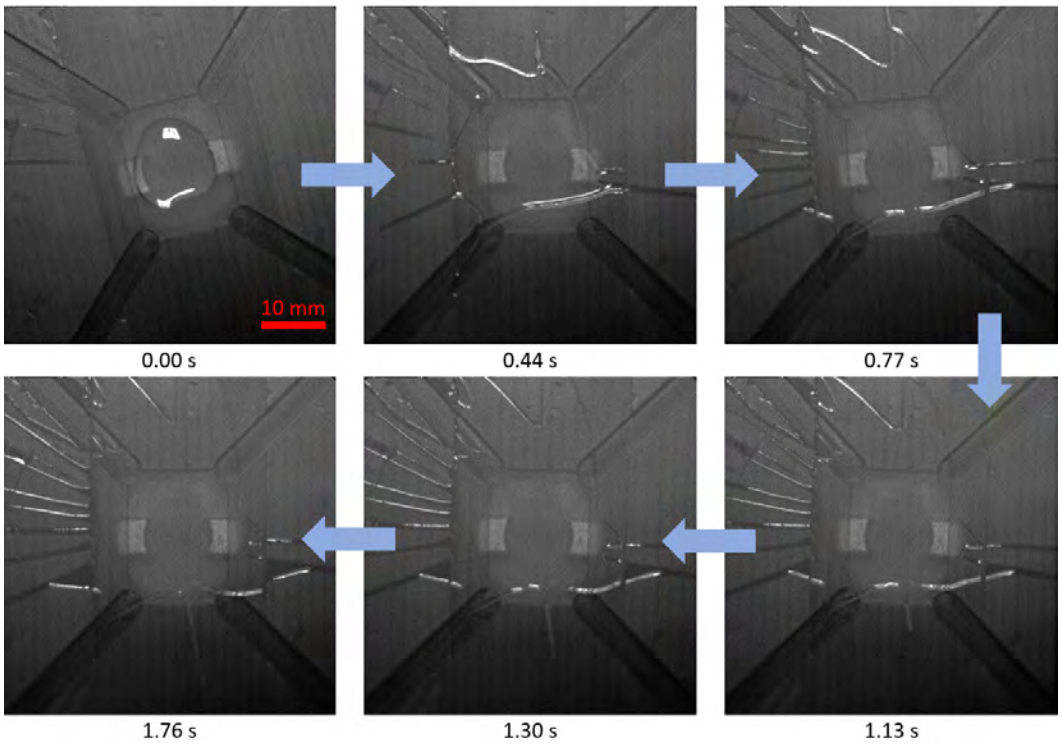

Figure 5.17: High-speed camera pictures of the spin-up process without surface activation

Another observation with these coatings is the lack of layer stability. During the first 30 minutes after the coating process, the film contracts strongly. The following figure 5.18 shows the WLI stitch measurement in an area of 15 x 15 mm around the substrate center of a spin coated layer directly after the coating process (figure 5.18a) and 30 minutes after the coating (figure 5.18b). This shows two things: first, the previously observed bead formation on the edge of the layer in figure 5.18a and second, the highly contracted layer (figure 5.18b), which almost forms a drop again.

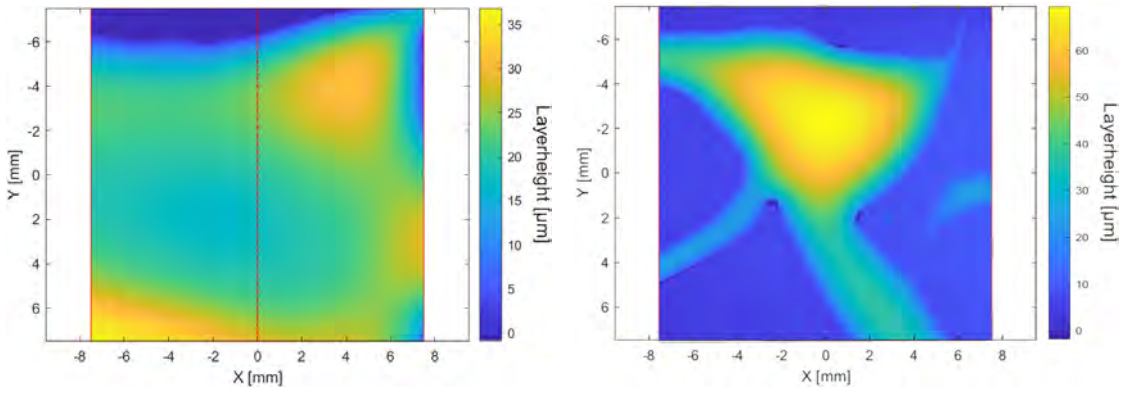

(a) (b)

Figure 5.18: Layer stability on unactivated surfaces a) Stich measurement directly after spin coating b) Stich measurement 25 minutes after spin coating

When analyzing the overall height of a coated layer, these Measurements show, that right after the coating process, the layerheight at the center of the substrate is close to the expected value from the calculation model. The following figure 5.19 shows a slice at x=0 of the measurement in the previous figure 5.18a. This coating is created by spinning at 1400 RPM for 30 s, which results in an expected height of 20 µm. In the center of the layer the height of the film is around 20 µm which supports the calculation approach.

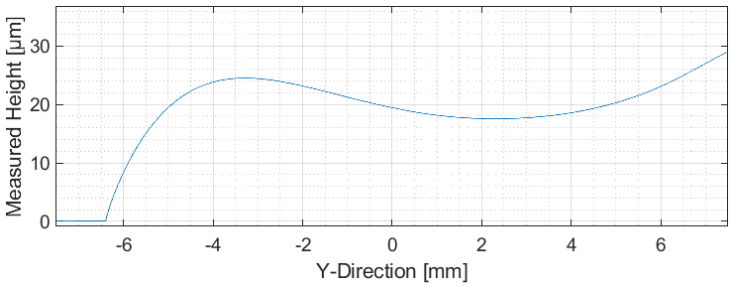

Figure 5.19: Slice through a stitch measurement of a coating on an unactivated surface

The results of these initial experiments show that the static material application is better suited than the dynamic application for the spin coating of PR48 films. Due to the observed inhomogeneity, bead formation and layer contraction the activation of the substrate surface prior to the spin coating process becomes necessary. Further experiments are performed using the static layer application method and using oxygen plasma to activate the substrate surface. These results are presented in the next section.

5.3.4 Improvement of Coating Results through Surface Activation

This section describes spin coating experiments with plasma activated surfaces and the improvement of the results by considering the influence of the process temperature. For this purpose, the surface is manually treated with the Piezobrush PZ3 plasma pen (see chapter 3.7.1). The surface of a substrate is activated by moving the nozzle of the plasma pen over the surface for 180 s. The following figure 5.20 shows the initial expulsion of a PR48 drop on a glass surface during a spin coating process with the same parameters as the figure 5.17 in the previous section (3000 RPM, 100 µl) for a plasma activated surface. Here, the initial state of the material on the substrate shows a radially uniform distribution of material and a significantly lower contact angle on the substrate, compared to the previous coating without surface activation (see figure 5.17). The distribution of material during the spin-up stage, shown in the figure, is seen to be significantly more uniform. This allows for better surface coverage and repeatable coating results.

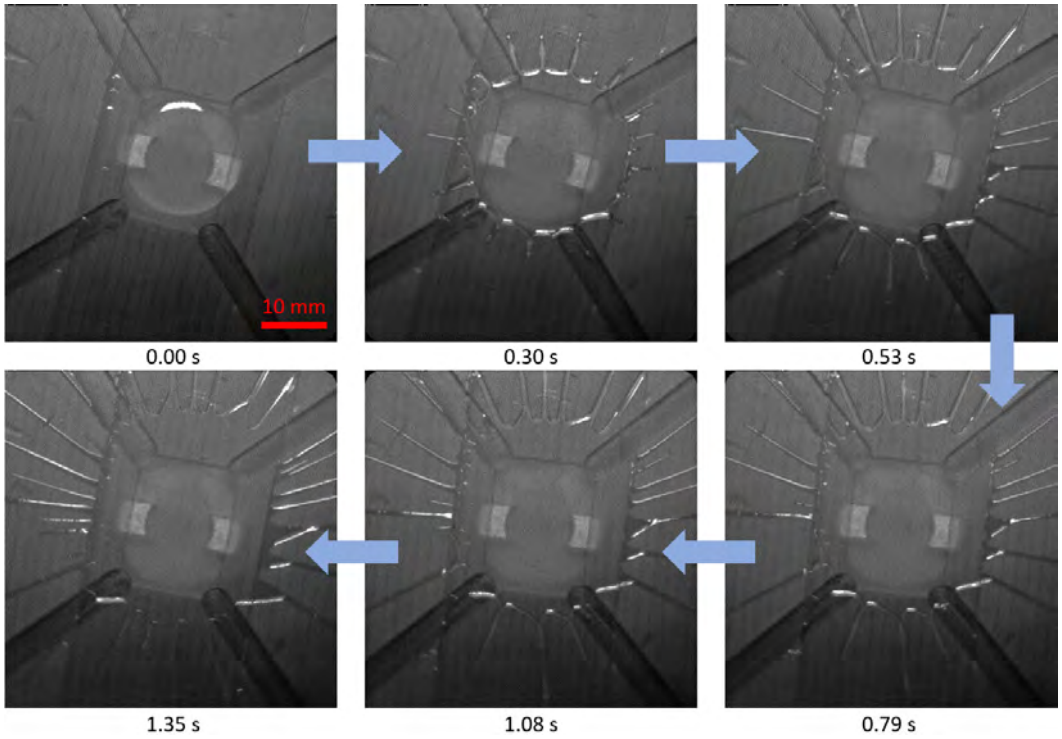

Figure 5.20: High-speed camera pictures of the spin-up process with surface activation

Measurements of coatings on plasma activated surfaces show a complete coverage in the center of the substrate. The following figure 5.21 shows a WLI stitch measurement of a PR48 film coated with parameters for a 20 µm layheight (figure 5.21a) and a surface plot of the measured layerheight in the substrate center (figure 5.21b). The bead formation of the layer is significantly smaller than for coatings without the surface activation and is only seen at the long edges of the substrate, where the material is not spun off the substrate. The surface, especially in the substrate center, is homogeneously coated and the coating spreads uniformly across a large area of the substrate compared to previous results without surface activation. This shows that

the coating results greatly improve with plasma activated surfaces, especially in the substrate center, which is the important area for the desired curing process.

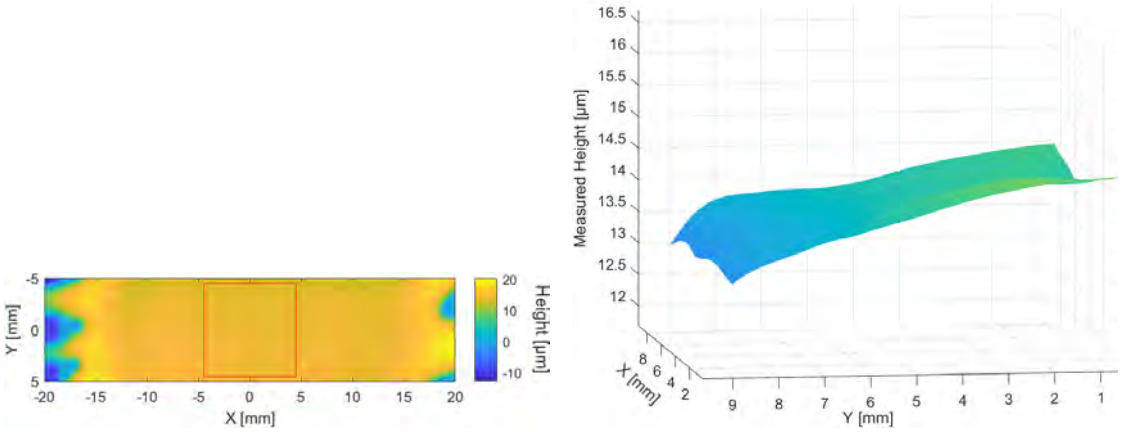

(a) (b)

Figure 5.21: Stitch measurement and surface analysis of coating on an activated surface a) 40 x 10 mm stitch measurement of coating b) Surface geometry in region of interest around the substrate center

Looking at the layerstability, the measurements of the layers show a way better stability than in the unactivated state. The following figure 5.22 shows the stitch measurement of a coating directly after the spin coating process (figure 5.22a) and 25 minutes later (figure 5.22b). Here, an influx in layerheight of circa 1 µm due to contraction can be observed. The shape and integrity of the coating stays intact. A deviation of 1 µm is acceptable, however, limiting the time between coating and processing leads to more repeatable results. Therefore, when curing structures, the curing is performed directly after the coating process to minimize layer contraction.

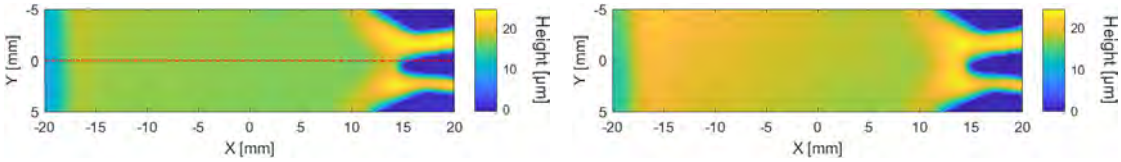

(a) (b)

Figure 5.22: Determination of layer stability using WLI stitch measurement a) 40 x 10 mm stitch measurement directly after coating b) 40 x 10 mm stitch measurement 25 minutes after coating

When the layer distribution and evenness for these experiments are compared with the coating results without plasma activation, the layer distribution on the substrate is seen to be significantly more uniform. Only at the edge of the coating are there still slight bead formations. The following figure 5.23 shows a slice through the middle of the layer from the previous figure 5.22a. Comparing this with the slice through a layer without plasma activation (see figure 5.19), the improvement in layer homogeneity and uniformity becomes apparent. The slice through the measurement shows an even layerheight throughout the coating without the big deviations and waviness observed for unactivated surfaces. This shows that the surface activation using oxygen plasma is very effective and needs to be used to ensure a homogenous and even material distribution on the substrate.

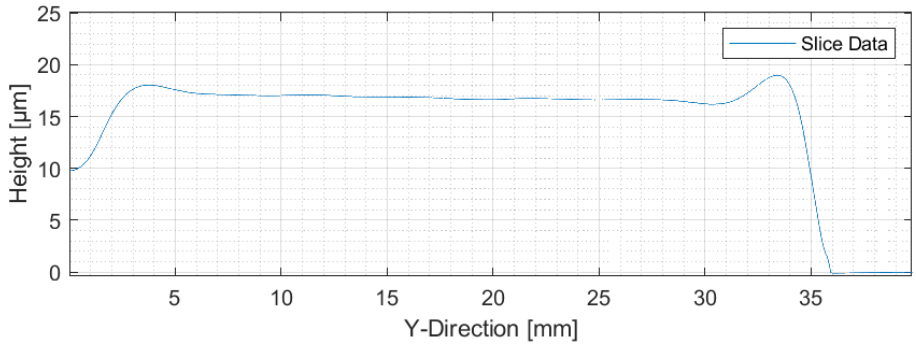

Figure 5.23: Slice through a WLI stitch measurement for a coating on an plasma activated surface

When analyzing these measurements however, two observations are made, firstly some measurements show a significant tilt throughout the whole measurement and secondly, the layerheight of the coating is significantly lower than the expected 20 µm in the region of interest (red square) and varies greatly between measurements. The measured layerheights for experiments perfomed with plasma activated surfaces are shown in the following figure 5.24. Here the results for coating with parameters for an expected layerheight of 10, 20 and 30 µm are shown in a boxplot. Each boxplot contains the determined layerheight using WLI stitch measurement for four individual coatings. These measurements show, that the measured layerheight falls below the expected value of the calculated layerheight. It also shows a great deviation in the height of individual coatings with the same coating parameters. The asymmetric position of the median in the measurement for 10 µm layers can be attributed to the small amount of data. For each desired layerheight, the measured height varies up to 5 µm. Fifty percent of the measurements are within a 4 µm range. This great variation in repeatability is assumed to be an error coming from the tilt observed in the previous measurements. The measured layerheight is greatly influenced by the degree of tilt of a measurement.

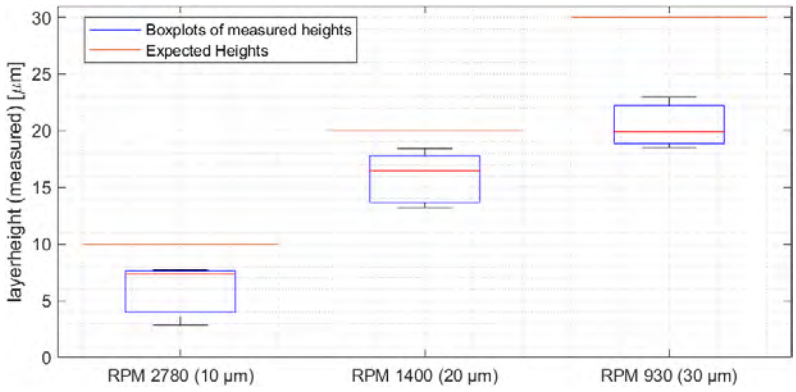

Figure 5.24: Boxplot of measured layerheight with the WLI stitch measurement

Since the observed tilt differs in severity and orientation for different measurements, it is assumed that it is either the result of a substrate tilt that cannot be compensated by the stitch measurement or an error propagation in the orientation of the individual measurements of the stitch. Both of these factors can be compensated by employing the measurement through the coatings surface. The deviation in coating height is assumed to be due to the temperature- and therefore

viscosity change of the photopolymer upon contact with the substrate surface that is heated during the activation process. The next sections present the investigation of the layerheight using the measurement method through the coating (see chapter 5.1.2) with the compensation of the temperature change in substrate and material due to surface activation.
To compensate the change in resin temperature due to ambient and substrate temperature, the temperature change of the substrate and the applied photopolymer is measured after the surface activation. The following figure 5.25 shows the measurement of the substrate and PR48 temperature over time after plasma activating the surface of the substrate for 180 s. The photopolymer is applied approximately 60 s after the surface activation. The graph in the figure shows an exponential decline in temperature over time slowly approaching the ambient temperature (23.8 ° C). Upon application the temperature of the photopolymer drop (100 µl) heats up to the temperature of the substrate within 30 s.

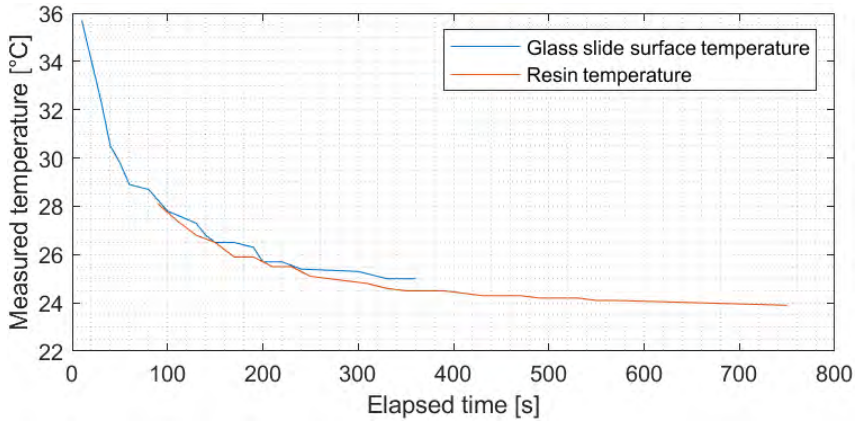

Figure 5.25: Temperature measurement of substrate surface and photopolymer after surface activation with plasma pen

Using this measurement the change in the material viscosity due to the increased temperature can be taken into account. The value for the viscosity in the calculation model to fit the measured layerheights is experimentally determined to be the viscosity at 28.7 ° C for spin coating directly after the surface activation, which fits with the temperature measurement.
When measuring the film thickness through the coated film in a 3.03 x 3.03 mm area, the tilt in the measurement is no longer observed. The following figure 5.26 shows segments of measured layerheights (5, 10, 20 and 30 µm) and their corresponding surface parameters. These results are obtained using the temperature adjusted calculation model. The measured coatings show a good surface homogeneity with a variation in the height over the measured area below 1.2 µm (P-V) and an arithmetic mean deviation (S_a) of below 200 nm for every measurement.

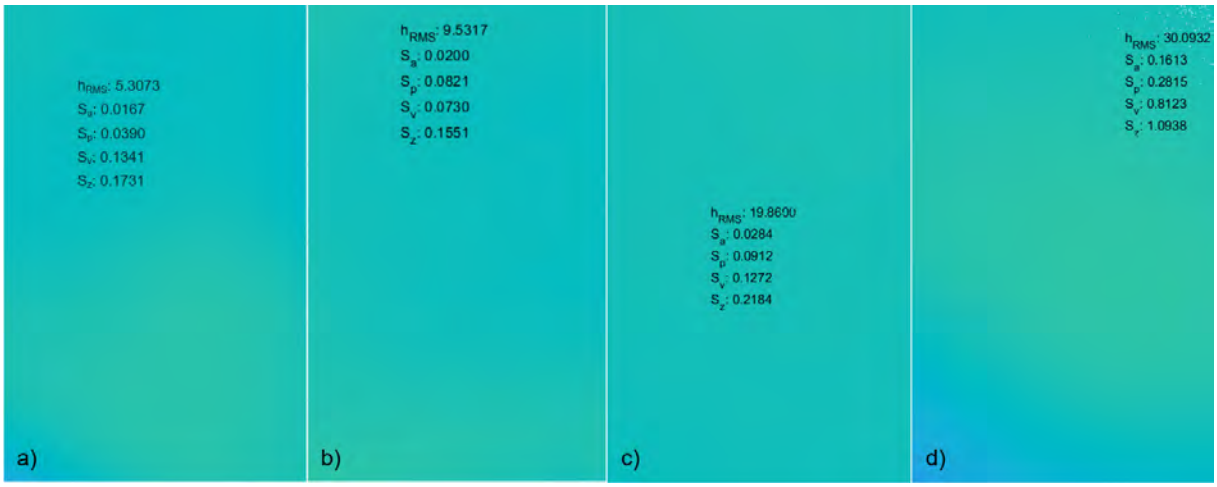

Figure 5.26: Layerheight and surface parameter measurements for layerheights of 5, 10, 20 and 30 µm on activated surfaces with through-resin WLI measurement

With this calculation as well as coating- and measurement process, spin coating of PR48 layerheights between 5 - 30 µm are experimentally shown to be possible. The following figure 5.27 shows the results for coatings with the temperature corrected model and the through resin measurement as a boxplot, with a sample size between 3 and 7 measurements per layerheight. The coatings with the temperature corrected calculation show a very good repeatability below 700 nm, supporting the hypothesis that the lack of repeatability in earlier measurements (figure 5.24) was due to an insufficiently precise measurement method. The measured layerheight deviates from the desired layerheight by less than 650 nm. By measuring at multiple points with an offset from the center, the layerheight and surface quality is shown to be homogenous within a 9 x 9 mm region around the substrate center.

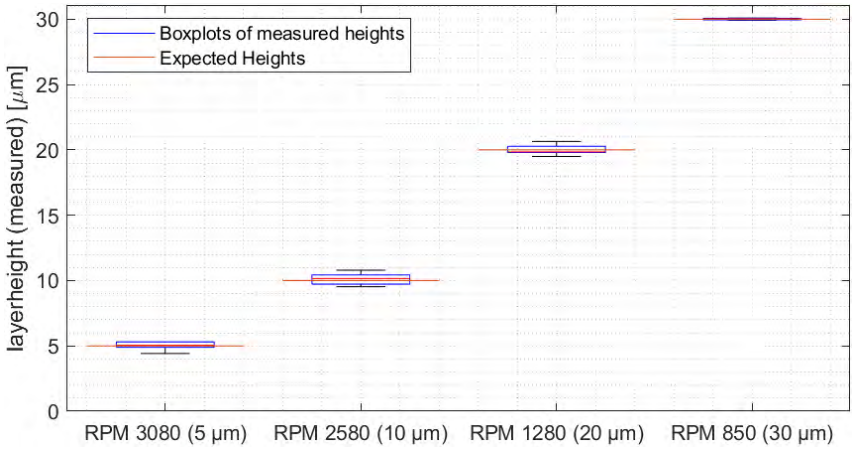

Figure 5.27: Boxplot of the measured layerheight of spin coated layers with activated substrate surfaces and through-resin measurement for layerheights of 5, 10, 20 and 30 µm

Below a layerheight of 10 µm, defects in the surface occur more frequently. Especially pinhole formation is seen. The defect rate increases very strongly with decreasing layer thickness. Below a layerheight of 5 µm, further measures would need to be taken to ensure a homogeneous surface. The results presented in this section show a predictable and repeatable way of spin

coating PR48 photopolymer layers on planar surfaces as well as a measurement method to determine the layerheight and surface quality. The following section 5.3.5 summarizes the results of this subchapter.

5.3.5 Results and Conclusion

This subchapter presented the development of a calculation model and parameter determination script to calculate spin coating parameters for a defined layerheight on planar surfaces. Experimental results show that a surface activation of the glass substrates is necessary to achieve homogenous material distribution. The measurement method using WLI stitch measurements is shown to be insufficiently precise to determine the layerheight reliably. Measuring the layer thickness directly through the coating offers a fast and precise way of determining the layerheight and surface quality of a coating. The temperature influx due to the surface activation needs to be accounted for in the calculation model. The photopolymer temperature can be assumed to be 28.7° C for plasma activated surfaces in the calculation model. These calculation-, coating- and measurement methods show coatings with an accuracy in layerheight below 600 nm and a repeatability within 700 nm within a 9 x 9 mm area around the substrate center. The surface of the coatings shows a good surface homogeneity with a variation in height over the measured area below 1.2 µm ($P-V$) and an arithmetic mean deviation (Sa) of below 200 nm for every measurement. The substrate cleanliness is very important to mitigate coating errors. The following list summarizes the coating process step-by-step.

0. Determine Curing Parameters using the Matlab script (see chapter 5.1.2)
1. Clean Substrates (see chapter 4.3)
    (a) Re-clean substrates after 24 h by wiping with methanol cloth
2. Activate the whole substrate surface using the plasma pen
    (a) For microscope slides: 180 s
3. Centrally apply photopolymer (PR48) directly after surface activation
4. Directly start spin coating with the calculated parameters

5.4 Defined Layer Application on convex Surfaces

This subchapter describes the development and testing of spin coating on convex surfaces analogous to the previous subchapter 5.3. In the next sections, the development of an optimization model based on the mathematical model from chapter 3.6.5.3 is described. The expected error in the optimization model due to the initial drop height and temperature induced viscosity change is evaluated. Finally experiments and optimizations for the defined layer application are presented and the results are discussed.

5.4.1 Calculation Model for Spin Coating Parameters

Since the film thickness of spin coated layers according to the model presented in chapter 3.6.5.3 depends on the distance to the substrate center, the parameter determination model introduced in this section is developed depending on the substrate diameter or a user defined circular region of interest. For this purpose, equation 3.6.14 is used to calculate the expected average coating thickness in the region of interest within the parameter range of the spin coating process. To achieve this, the script iterates through RPMs between 500 and 6000 (see chapter 3.6) for coating times between 30 and 120 s. For each iteration the average expected coating thickness is calculated. Then the calculated thicknesses are compared with the desired layerheight and the parameters with the smallest deviation are determined. The script outputs the corresponding spin coating parameters (RPM and spin time) and plots the cross section of the expected coating thickness within the region of interest. The following Figure 5.28 shows the result of the calculation of spin coating parameters for a coating thickness of 5 µm in an 8 mm region of interest.

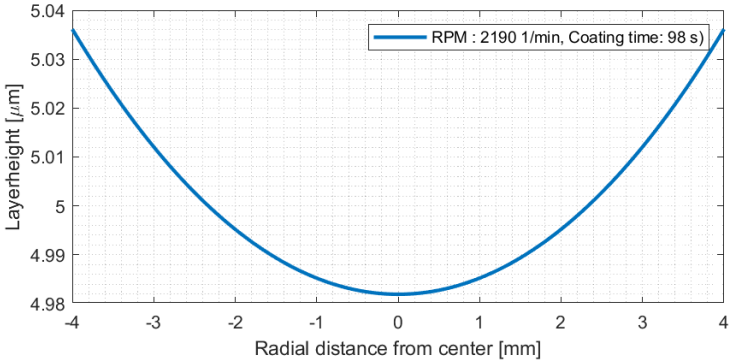

Figure 5.28: Resulting plot of the expected layer cross-section for optimized spin coating parameters for a 5 µm layerheight

The next section presents initial experimental results, using the calculated parameters with this model.

5.4.2 Coating Results and Measurements

This section presents experimental results of spin coating on meniscus lenses (BK7) with a diameter of 26.1 mm and a radius of curvature of 19.5 mm. These initial experminents are performed with calculated coating parameters for 20 and 30 µm layerheights. The spin coating is perfomed using a FDM printed custom chuck for the lenses. The lens surface is cleaned and manually activated with the plasma pen for 60 s directly before the material application. The resulting coatings are measured using the method presented in chapter 5.2. The following figure 5.29 shows the resulting layerheights from this initial test. Here a central slice through the calculated layer surface is shown for each individual measurement with the calculated parameters.

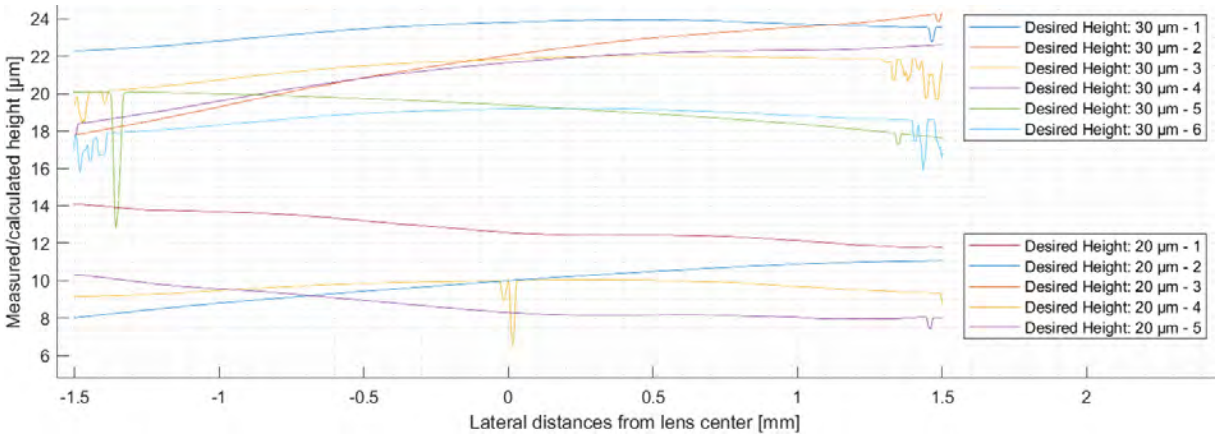

Figure 5.29: Cross Section of initial layheight measurements on convex surfaces with desired layerheights of 20 and 30 µm

These initial experiments show that the measured film thickness is much lower than the expected layerheight. Furthermore, there is a strong deviation within the measured film thicknesses, which were produced with the same spin coating parameters. This suggests that the temperature change on these substrates needs to be re-measured for the substrates and that an inaccuracy in the spin coating process affects the repeatability of the measurement. Another observation from these measurements is that some measurements show a tilt. Since no planar reference surface is available in the WLI measurement, the substrate holder must be tilt corrected prior to the measurement. Each measurement needs to be checked for a tilt in the calculated layerheight and tilted measurements need to be repeated to ensure a sufficiently precise determination of the layer thickness. This is done for all further measurements.
During these measurements on convex substrates, it is also noticed that the photopolymer is still in motion at the time of measurement (directly after coating). A flow behavior along the substrate geometry is suspected from an observed movement of the WLI fringes. The following figure 5.30 shows an evaluation of the coating height over time for four measurements that are coated with parameters for a desired layerheight of 20 µm. This measurement shows that due to the substrate shape the material height declines exponentially over time. This means that time deviations in the measurement process have a major influence on the measured layerheight. Furthermore, this phenomenon shows that the processing of the layer directly after the coating process can lead to large deviations in the thickness of the coating when curing structures. Another observation is that the height profile of the layer thickness of individual measurements has an offset in the x-direction and the initial measured height deviates within the measurements. After about 12 minutes, all measurements show a quasi-linear course with a small slope parallel to each other. The measured layerheights show a deviation in measured height of up to 1.5 µm. This observation leads to the hypothesis, that the deviation in temperature due to the manual surface activation impacts the fluid viscosity and therefore leads to a deviation in the flow behavior, resulting in the offset seen in the measurements.

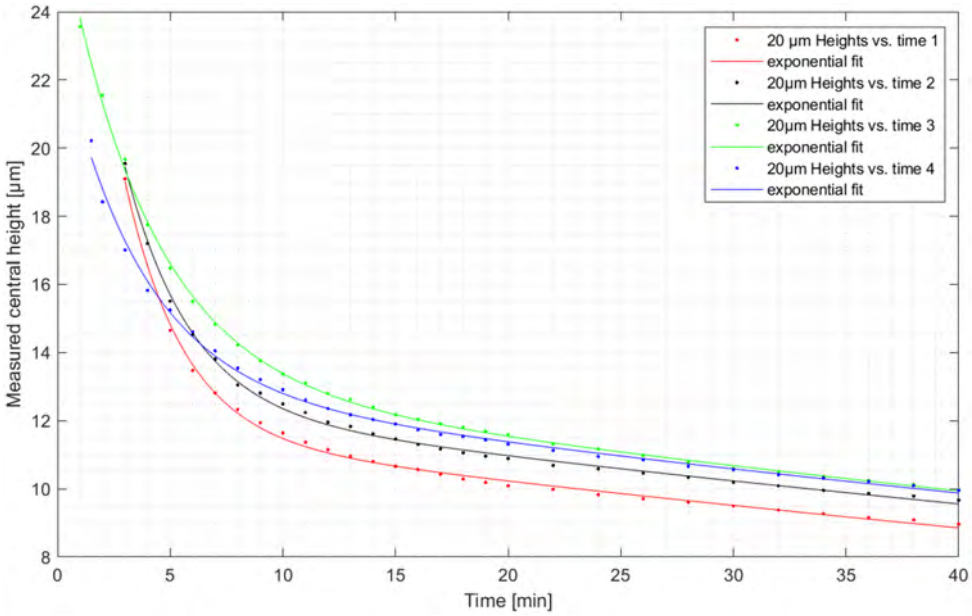

Figure 5.30: Determination of layerheight over time on convex substrates with manual surface activation

To determine what influences the repeatability of the coatings the next section presents an evaluation of the influence of the initial material height as well as the influence of a deviation in material temperature on the expected coating height.

5.4.3 Determination of Deviation in Coating

This section presents an error calculation for the influence of a deviation in initial height and change of viscosity due to temperature on the expected coating results to determine if the temperature change leads to the observed deviation in coated heights. Analog to the determination of the influence of the initial height on planar surfaces, the error influence can be determined using equation 5.3.5. Therefore the influence of the deviation in initial height can be determined using the following equation 5.4.1.

$$\Delta h_{h_0} = \left(\frac{1}{\sqrt{\frac{2 \cdot h_0^2 \cdot t \cdot a}{3 \cdot \eta \cdot R} + 1}} - \frac{2 \cdot h_0^2 \cdot t \cdot a}{3 \cdot \eta \cdot R \cdot \left(\frac{2 \cdot h_0^2 \cdot t \cdot a}{3 \cdot \eta \cdot R} + 1 \right)^{\frac{2}{3}}} \right) \cdot \Delta h_0 \tag{5.4.1}$$

$$with: a = \left(2 \cdot g + 2 \cdot \rho \cdot \omega^2 \cdot \sqrt{R^2 - r^2} - \frac{\rho \cdot \omega^2 \cdot r^2}{\sqrt{R^2 - r^2}} \right)$$

With the gravitational force g, the radius of curvature R and the radial distance from the substrate center r. The deviation due to a viscosity change can be determined respectively using the following equation 5.4.2.

$$\Delta h_\eta = \left(\frac{h_0^3 \cdot t \cdot a}{3 \cdot \eta^2 \cdot R \cdot \left(\frac{2 \cdot h_0^2 \cdot t \cdot a}{3 \cdot \eta \cdot R} + 1 \right)^{\frac{3}{2}}} \right) \cdot \Delta\eta \tag{5.4.2}$$

The overall expected error therefore is determined using the following equation 5.4.3.

$$\Delta h = \Delta h_{h_0} + \Delta h_\eta \tag{5.4.3}$$

With the error influence from the initial height deviation Δh_{h_0} and the error influence of a viscosity deviation Δh_η. When evaluating the error influence, it shows that, as for the planar surfaces, the initial height has an insignificant influence on the coating results. For a deviation in applied volume of 5% (Δ_{h_0} : 0.036 mm) at 3000 RPM with a spin time of 30 s, a sub-nanometer influence (0.07 nm) is determined, which only increases to 0.09 nm for a 50% (Δ_{h_0} : 0.469 mm) deviation, since the thinning is mostly RPM dependent and not on the initial drop height for a sufficiently long spin time. However, the influence of a change in material temperature of just one degree (28 to 29° C) at the same coating parameters results in a deviation of 0.26 µm. Since the initial temperature of the substrate is highly dependent on the distance of the plasma nozzle and duration of the plasma treatment on a given point on the substrate surface, this can lead to significant deviations in the expected layerheight. Therefore, the process of substrate activation needs to be standardized to minimize deviations initial substrate temperature. The substrate temperature decreases exponentially after surface activation (see figure 5.25), so the timing of material application has a large effect on the temperature and therefore expected height. The application of material after a certain waiting time, when the substrate has already cooled down, reduces this influence significantly. The next section discusses the development of a standardized surface activation process and coating with material application after a waiting period.

5.4.4 Improvement of Coating Results

In order to mitigate the influence of temperature deviations on the flow behavior of the photopolymer on convex substrates seen in the previous section 5.4.2, this section presents the development of a repeatable activation process of convex substrates using the spin coater. The following figure 5.31 shows the activation setup using the spin coater and a mount for the plasma pen. Here, the spin coater is used at its lowest angular velocity (100 RPM) to rotate the substrate for a defined amount of time. By mounting the plasma pen at an angle, the stream of oxygen plasma can be positioned perpendicular to the substrate shape within a 5 mm distance to the

substrate. Using a magnet to trigger the safety switch, the spin coater can be used without the lid. This setup provides a repeatable way of activating the surface of a convex substrate. For this purpose the substrates are spun at 100 RPM for 90 s under the plasma pens nozzle.

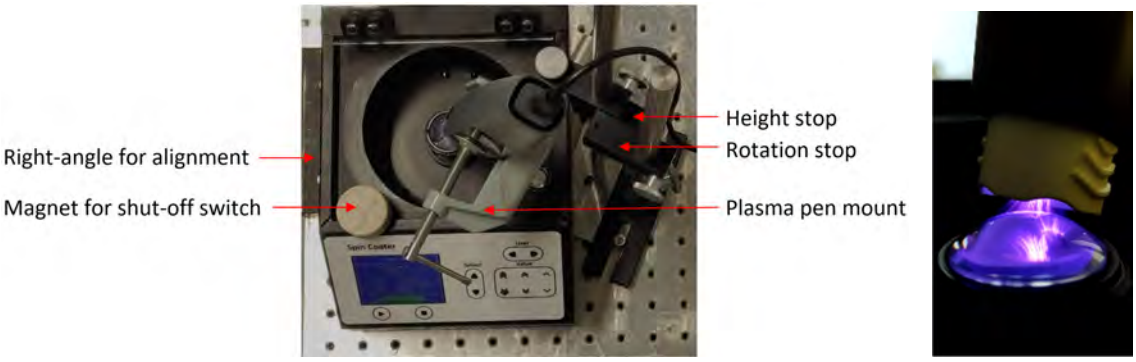

(a) (b)

Figure 5.31: Setup for standardized surface activation on convex surfaces a) Setup with spin coater and plasma pen mount for repeatable surface activation, b) Alignment of plasma nozzle to substrate surface

Using this setup, the substrate surface is repeatably and homogenously activated. During this activation process the substrate heats up to 39.5° C. To decrease the influence of the temperature deviations further, the substrate coating is performed 10 minutes after the surface activation, when the substrate has cooled off significantly and the temperature gradient experienced by the material during and after the spin coating process is reduced. In order to further mitigate the temperature influence, the layerheight on the substrate is measured in a temperature-controlled room, ensuring a highly repeatable ambient temperature to test the repeatability of the flow behavior with reduced influence factors and a repeatable surface activation method. The next section presents the evaluation of the flow and repeatability of a spin coated PR48 film on convex surfaces with the new setup and presents the results for a parameter definition to coat layers, where the desired layerheight is achieved within a timeframe in the more stable part of the flow progression.

5.4.4.1 Determination of Material flow on convex Substrates

When evaluating the flow of a layer on a convex substrate it is shown that the flow leads to a thinning of the layerheight over time. The following figure 5.32 shows the progression of the layerheight over time with the substrate surface as a reference (blue line). Here, the progression of the film thickness of a layer with an expected height of 20 µm is measured repeatedly within two hours after the coating process. This measurement shows a homogenous layer shape over time, however, the decline due to material flow is still significant. The layerheight decreases from 25.54 µm (3 minutes after coating) down to 7.25 µm over two hours.

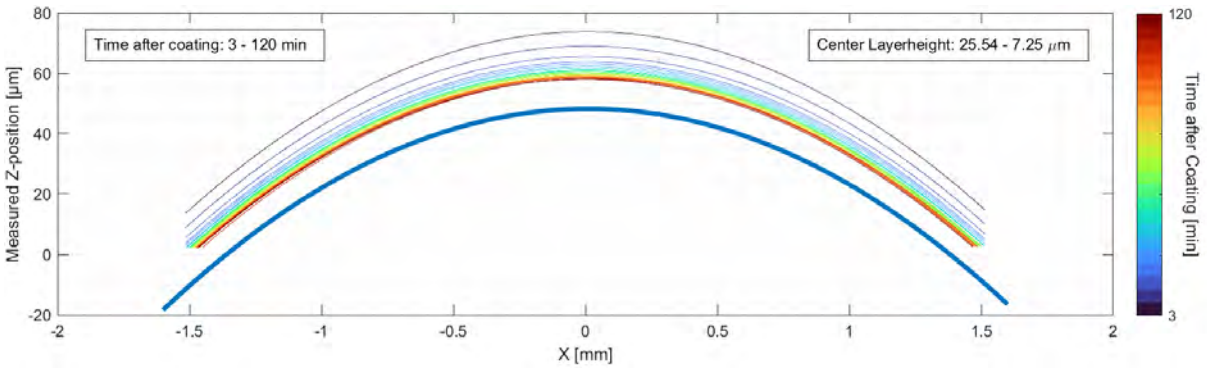

Figure 5.32: Cross-section of layerheight measurement with a desired height of 20 µm for a time after spin coating between 3 to 120 min

When comparing the repeatability of the material flow using the new activation setup in a temperature-controlled environment to the previous results (see figure 5.30), the measurements still show an exponential decline in layerheight, however, the repeatability of the measured height at any given time is below 500 nm and becomes even less influential when the flow has slowed down. The following figure 5.33 shows the layerheight progression on three substrates coated with the same spin coating parameters over time. Here, the expected layerheight from the calculation model is 20 µm. The measurement shows the good repeatability of the coating height over time. However, the calculated layerheight does not fit the measured initial height, nor the height, the film thickness settles towards. Another observation with these measurements is, that the layerheight, independent of the coating parameters, always decreases rapidly below a height of 15 µm before the slope decreases significantly.

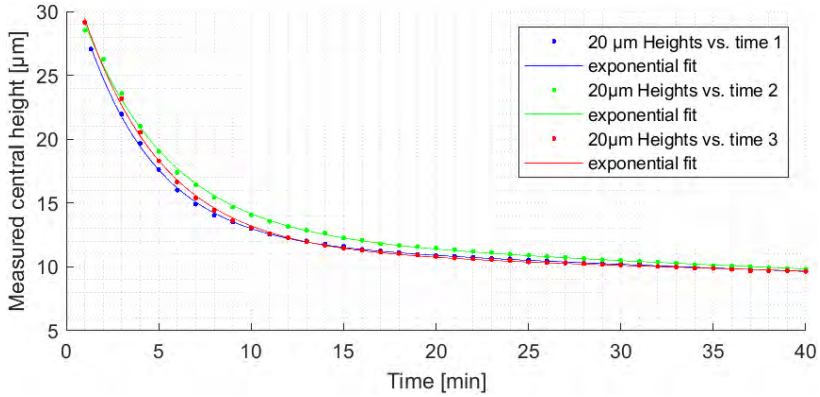

Figure 5.33: Determination of layerheight over time on convex substrates with standardized surface activation

The observations from the investigation of material flow on convex surfaces show that the flow on the substrate needs to be accounted for in order to achieve a homogenous repeatable layer-height. The layer must be allowed to settle for at least 10 minutes before processing it. Ideally the layer is processed in a time range in which the change in layerheight due to the material flow is in a linear range with a low slope. The achievable layerheight in this range is below 15 µm. The coating parameters to achieve a defined height after >10 minutes need to be determined, and a time range for an acceptable change in layerheight needs to be established. The

viability for the calculation model needs to be tested in the range of layerheights below 15 µm. The parameters for a desired height after a defined time need to be determined empirically with the calculated parameters as a reference. The next section presents the determination of spin coating parameters with these informations from the analysis of the material flow.

5.4.5 Determination of Spin Coating Parameters

Since the determination of the material flow showed that the spin coated layers need to be thinner than 15 µm and the formation of pinholes for layers below 5 µm is also seen for convex surfaces, this section presents the determination of spin coating parameters for a layerheight of 5 and 10 µm on convex surfaces.
When coating layers with a desired layerheight of 5 µm it is observed that the layerheight still declines initially, however, after 10 minutes the height settles and stabilizes. The measured layerheight is smaller than the calculated layerheight using the ambient temperature. For a calculated height of 5 µm (at 21.3° C), a final height of 3.5 µm is achieved. This shows that while the calculation model can give an estimate of parameter pairs for a desired height, the actual parameters to achieve a precise layerheight need to be determined experimentally. This is done by reversing the calculation model and using the measured layerheight. Since the layerheight deviation is close to the desired layerheight, the measured layerheight can be used to determined an equilibrium viscosity to achieve the correct layerheight. The spin coating parameters for the desired layerheight are then calculated using this equilibrium viscosity. The following Figure 5.34 shows the result of this process using a 5 µm film thickness. Here, based on the previously measured film thickness of 3.5 µm, an equilibrium viscosity of 244 cP is determined (corresponding to 29° C material temperature, cf. 430 cP for 21.3° C). With this approach, spin coating parameters for individual layerheights can be determined quickly and easily by experiment. The figure shows that the coating thickness has leveled off at a time of 10 minutes after the coating process. Repeatable layerheights of 5 µm can be produced. These show a maximum deviation of 500 nm from the measured coating thickness and are very stable over time from this point on.

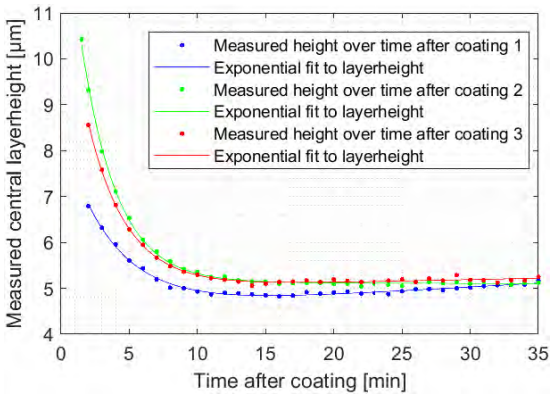

Figure 5.34: Layerheight over time for experimentally determined spin coating parameters for a layerheight of 5 µm on convex surfaces

This method results in spin coating parameters of 2190 RPM and 98 s for a non-temperature controlled room at 24° C for the spin coating of 5 µm layers. The following figure 5.35 shows a boxplot with a sample size of 3 measurements of the measured layerheights after a time of 10, 15 and 20 minutes. The evaluation of the boxplot shows that after a period of 10 minutes after the coating process, the coating thickness has settled in a range of 500 nm around the expected height. The individual layer thicknesses show a repeatability of less than 400 nm. Within a 5 minute time window, the layerheight decreases to an average of 5.03 µm and remains stable from this point on. The maximum deviation of the film thickness for a processing time of 10 - 20 minutes after coating is 520 nm. This allows repeatable spin coating of 5 µm layers on the used substrates.

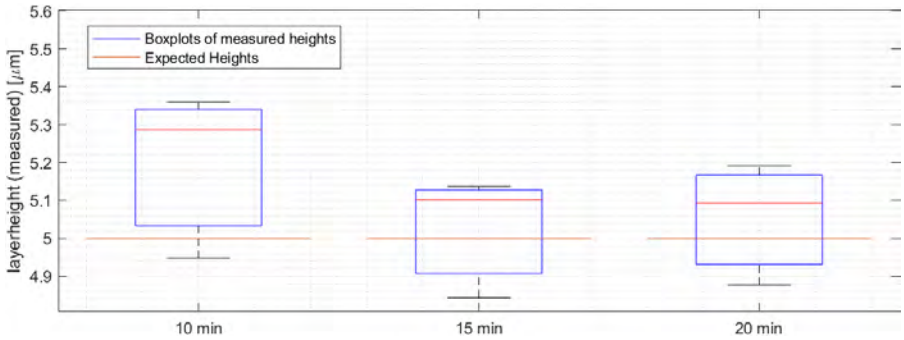

Figure 5.35: Boxplot representation of the layerheight for 5 µm spin coating parameters on convex surfaces within 10, 15 and 20 minutes after spin coating

Analog to the 5 µm layer application, the parameter determination method is used to achieve 10 µm layers. The results are shown in the following figure 5.36. However, since the layer thickness does not level off here, the corresponding time window for the desired layerheight is smaller. According to the experimental results, an equilibrium viscosity of 158 cP (1720 RPM, 31 s) is determined for this layerheight. The desired film thickness is achieved in a time period between 15 and 17 minutes after the coating process. Because the film experiences greater material flow, there is a greater deviation in the repeatability of the thickness for this layerheight. The measurements show a repeatability of 750 nm with a precision of ± 500 nm around the desired film thickness.

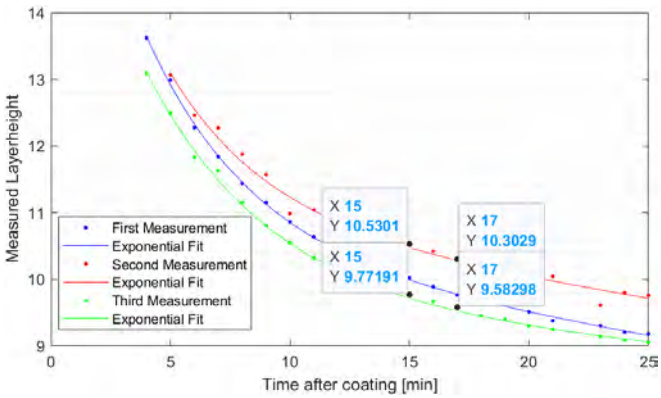

Figure 5.36: Layerheight over time for experimentally determined spin coating parameters for a layerheight of 10 µm on convex surfaces

This deviation is also shown in the statistical analysis of the spin coated 10 µm layer with a boxplot. This analysis is shown in the following figure 5.37. Here the measured layerheights are evaluated in a temperature controlled and laboratory environment to determine the influence of temperature stability. Because the ambient temperature in the laboratory fluctuates, greater deviations from the expected coating thickness and poorer repeatability are observed. Due to the lower ambient temperature, the coating in the temperature-controlled room reaches the expected thickness later. The measurements in the temperature-controlled environment show a repeatability of 300 nm and a deviation from the expected coating thickness ± 300 nm in a period of 17 to 21 minutes after the coating process. The measurements in the laboratory show a repeatability below 800 nm and a deviation from the expected film thickness of ± 500 nm in a period of 15 to 17 minutes after coating. In this time period, the measured layerheights are centrally distributed around the desired height. These results are very close to the determined repeatability and accuracy on planar substrates and show a sufficiently accurate deposition of a 10 µm layer on the convex substrates.

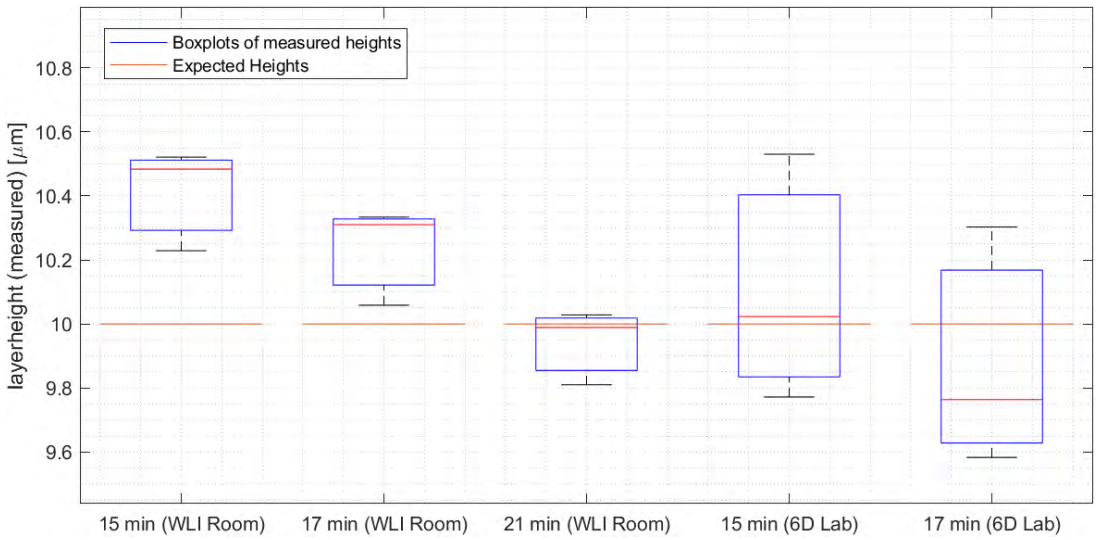

Figure 5.37: Boxplot representation of the layerheight for 10 µm spin coating parameters on convex surfaces in a temperature-controlled and laboratory environment 15, 17 and 21 minutes after spin coating

When looking at the surface quality of the coated layers on planar surfaces, it is seen that the absolute $P-V$ deviation in the layer thickness is similar to the coatings on planar surfaces in the range of up to 1.5 µm. However, the average deviation of the coating thickness (S_a) is amplified by the substrate shape, which leads to an S_a within a range below 400 nm. One thing to keep in mind when determining surface quality is that the area in which it is determined must be manually selected to exclude the influence of measurement artifacts caused by a lack of data points due to the curvature on the edge of the substrate. The following figure 5.38 shows a surface plot of the measured height of a layer with an expected film thickness of 10 µm 15 minutes after the coating process, as shown in figure 5.37 above. Here, the measurement artifacts at the edge of the measurement are clearly visible. For this reason, the surface parameters S_a, S_p, S_v and S_z

for this measurement are determined in a circular area with a radius of 1 mm around the center, mitigating the artifact influence.

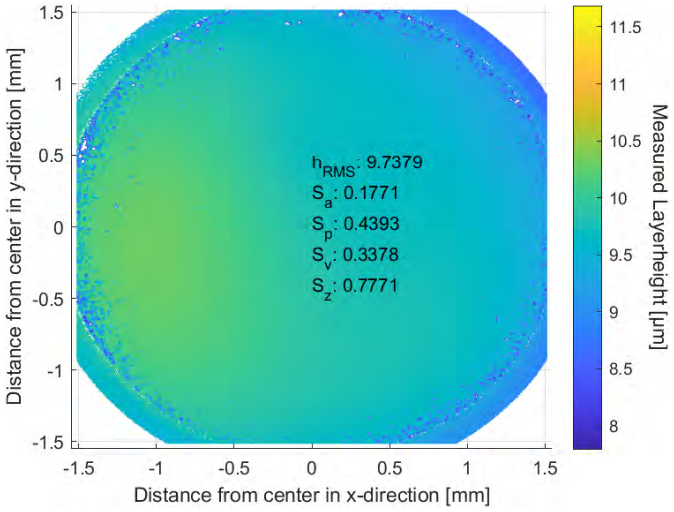

Figure 5.38: Surface of a calculated layerheight for spin coating parameters for a layerheight of 10 µm with surface quality parameters, 15 minutes after spin coating

5.4.6 Results and Conclusion

This subchapter presented a development of a Matlab optimization script to determine the spin coating parameters on convex surfaces. The surface activation process using oxygen plasma is standardized and the substrates are allowed to cool down after the activation to mitigate the influence of the material temperature gradient on the coating results. It is seen that PR48 exhibits flow on the used substrates during and after the coating process. The investigation of the flow shows that the maximum achievable layerheight on the used substrates is below 15 µm. The change of layerheight over time is seen to be almost linear after 10 minutes. The calculation model is shown to be inaccurate to precisely predict a layerheight within the linear portion of the layerheight flow. The calculation model can be used to experimentally determine coating parameters for a defined layerheight by approximating initial coating parameters and determining an equilibrium viscosity. Using this information, spin coating parameters for a layerheight of 5 and 10 µm are determined. The resulting parameters allow the coating of a PR48 film with a defined layerheight on convex substrates with a radius of curvature of 19.5 µm. The coating parameters need to be individually and experimentally determined for each desired layerheight, surface geometry and material. Since the layerheight on convex surfaces is time dependent, the structure curing on the substrates needs to be performed within a time span (typically ca. 2 min) after a defined waiting time (10 min for 5 µm, 15 min for 10 µm). Using this coating method 5 and 10 µm layers with an accuracy of $\pm$ 500 nm around the desired layerheight and a repeability below 800 nm can be fabricated. These layers show a maximum $P-V$ distance of 1 µm and an average surface deviation (S_a) below 400 nm.

5.5 Conclusion

This chapter presented the development and optimization of a measurement and spin coating process to apply defined, homogenous, and repeatable films on planar and convex surfaces using the PR48 prototyping photopolymer and a commercially available spin coater. A measurement process by measuring through a transparent film using a White Light Interferometer and calculating the respective layerheight is presented and adapted for the determination of a layerheight on planar and convex surfaces. This method allows the precise and fast measurement of a layerheight within a 3.03 x 3.03 mm field of view. A way of activating the substrate surface using oxygen plasma to improve surface wettability and distribution homogeneity is presented. The spin coating parameters are determined using a Matlab optimization script based on the mathematical models presented in chapter 3.6.5 for both surface shapes. It is shown that the calculation of the coating parameters on a convex surface is insufficient to directly optimize for a defined layerheight. The calculation script can however be used to approximate and experimentally optimize the coating parameters. The determination for coating parameters to achieve a layerheight of 5 and 10 µm is presented. Due to material flow the layerheight on convex surfaces is time dependent, this needs to be accounted for when coating and curing on these substrates. The model for coating on planar substrates allows for the determination of parameters for a variety of layerheights. The model is verified for layerheights between 5 and 30 µm. Due to pinhole error formation for layerheights below 5 µm, the viable range of layerheights needs to be above 5 µm without the introduction of further optimization steps, e.g. nitrogen purging to mitigate the formation of pinholes. Using the determined models, measurement methods and parameters it is possible to coat layers with an accuracy below 650 nm and a repeatability of below 800 nm on planar surfaces. Respectively the layers on convex surfaces show an accuracy below 750 nm and a repeatability of 800 nm within a two-minute timeframe that needs to be individually determined for a desired layerheight. The presented methods offer a sufficiently precise method of measuring and applying photopolymer films with a defined thickness on planar and convex surfaces. These layer application methods can be used to fabricate and process photopolymer layers for laser stereolithography to cure micron-scale structures and functionalize planar and convex surfaces.

6 Curing Setup

In order to increase the precision and repeatability of the curing results with the laser stereolithography setup and to achieve the best possible results with the available hardware, this chapter presents the further development of the lithography setup. For this purpose, the previous setup (see chapter 4.1) is rebuilt to increase the rigidity and fix the component position. The new setup is integrated into a frame of item profiles, intending to enable structure curing with the use of the hexapod as well as stand-alone. The design of a substrate holder with inert gas chamber to mitigate oxygen inhibition is presented. Finally, the development of a system for beam focusing is presented.

6.1 Curing Setup Modification

The previous test setup (see chapter 4.1) showed that the correct orientation of the UV laser to the Galvo mirrors is very important for precise beam positioning. Furthermore, during the investigation of the curing geometry (see chapter 4.3.2.1) it became clear that a way to reduce the laser power is needed to achieve the desired structure dimensions. In addition, FDM printed parts show susceptibility to vibration and deformation under load, which reduces the precision of the curing process. To meet the requirements and mitigate error influences, this subchapter presents the further development of the lithography setup to increase component robustness and provide means to reduce laser power. The following figure 6.1 shows an exploded view of the resulting setup. Here the correct orientation of the components is achieved by mounting the UV laser directly to the Galvo system. For this, LINOS mounts and rods are used, allowing a stable and precise orientation of components to each other. In addition, optical filter mounts (ND filter and polarizer) are integrated to be able to reduce the laser power. The whole system is mounted on a precision positioning table to adjust the z-position relative to the substrate position. With an adapter, the system can be mounted to a standard 40 x 40 mm item profile.

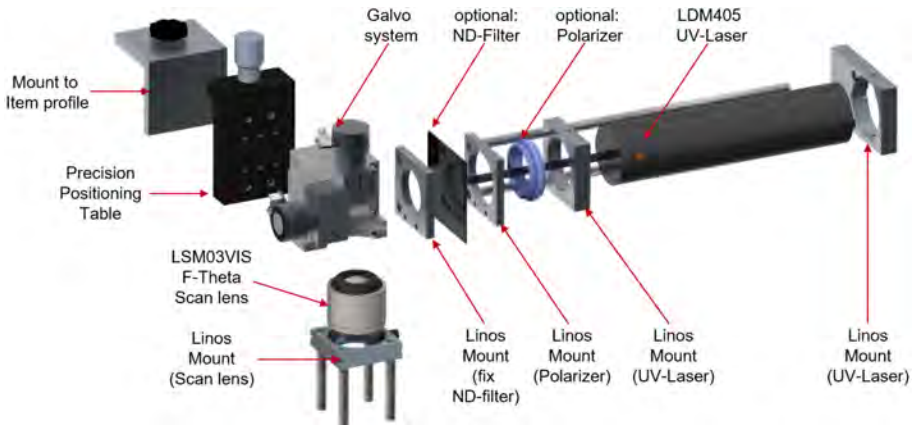

Figure 6.1: Exploded view of the revised lithography setup

This setup allows robust and precise mounting of the laser and filters to the Galvo system. For modular application with and without hexapod, a frame of item profiles is developed for this setup. The following figure 6.2 shows a CAD rendering of the complete setup in combination with the hexapod (figure 6.2a) and the setup as a stand-alone system without hexapod (figure 6.2b). To use the setup without the Hexapod, an aluminum plate with two linear bearings is mounted on the frame. With the linear guided aluminum plate and the precision lift table, the z-position of the setup relative to the substrate can be changed and the laser beam can be focused on the substrate. The substrate holder must be aligned relative to the scan lens, for this purpose the LINOS rods on the scan lens mount can be used (see the following chapter 6.2). To use the frame in combination with the Hexapod, both components are mounted and aligned on an optical table. The lithography setup can be aligned to the substrate using the adapter for mounting on the item profile, the precision lift table and the movement of the hexapod. By incorporating the hexapod, a possiblity for high-precision positioning of the substrate with six degrees of freedom is created.

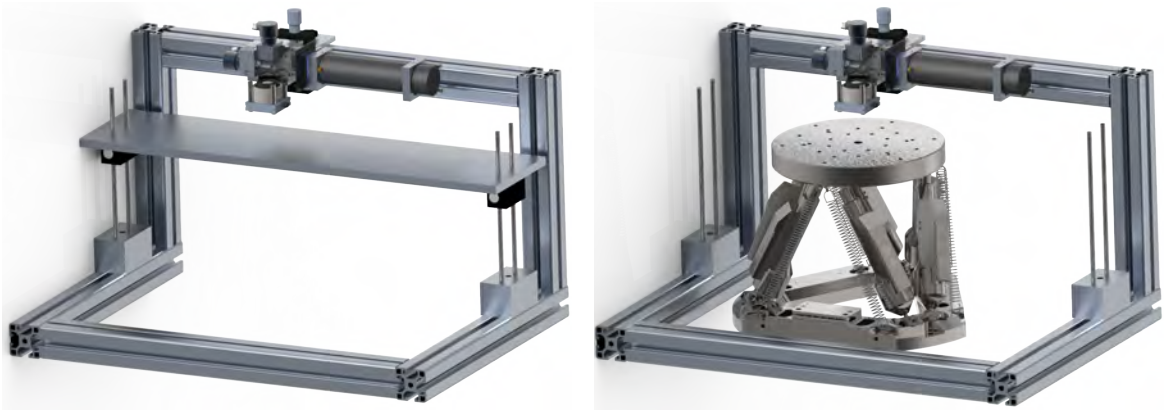

(a) (b)

Figure 6.2: CAD Render of modular lithography setup with Item-frame a) Stand-alone setup, b) Setup with hexapod integration

The modular design allows the lithography setup to be used independently, however, compensation of the substrate geometry is not possible in that case. The following subchapter deals with the development and construction of a hybrid substrate holder for planar and convex surfaces, as well as a possibility to determine the focus position.

6.2 Substrate Setup

This section introduces a substrate holder that can be positioned and mounted on the hexapod or aluminum plate. This holder shall allow the orientation of the lithography setup to the substrate, provide the possibility to use planar and convex substrates and be used for beam focusing (see following chapter 6.3). Since first tests of the lithography setup show that structures in a photopolymer layer only cure with very high laser power, which indicates oxygen inhibition, a

cavity for an inert gas chamber is integrated into the substrate holder to counteract oxygen inhibition (see following chapter 6.2.1). The following figure 6.3 shows a CAD rendering of this substrate holder with its components for functionalization and structure curing. FDM printed components are shown in blue in the figure. The basic setup for focusing and curing consists of the substrate holder and the nitrogen chamber. The nitrogen chamber allows to create a closed volume of gas around the substrate. A ND filter seals the chamber and still allows the laser light to pass through. Since the refractive index of the filter leads to a beam shift, the nitrogen chamber must be used for the focusing process. To position the lithography system, the nitrogen chamber is mounted on the substrate holder. Now the lithography setup can be positioned perpendicular and centered to the substrate using the LINOS rods of the scan lens holder and the holes in the nitrogen chamber. The substrate holder allows direct mounting of glass slides. To ensure repeatable orientation, convex substrates are positioned by mounting them in the substrate holder with their chuck for spin coating. Focusing (see following chapter 6.3) is performed with a photodiode sensor for an optical power meter and a precision pinhole. Both of these components can be mounted in the substrate holder.

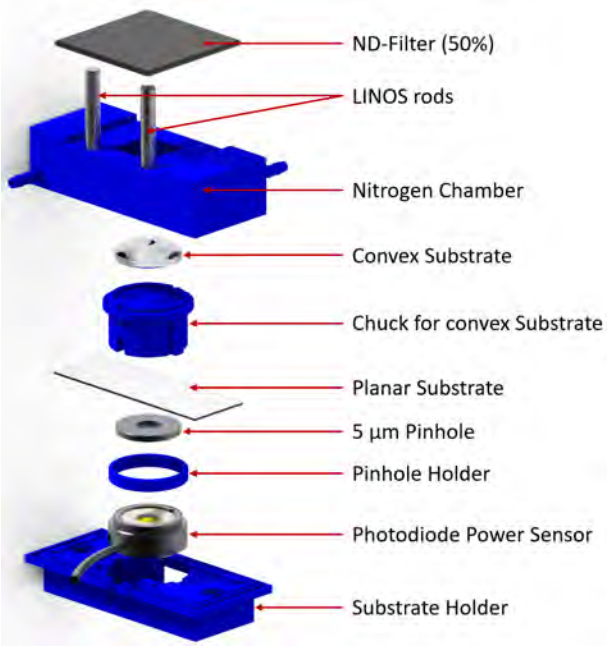

Figure 6.3: Exploded view of CAD assembly for the substrate intake, focusing and inerting functionality

This substrate setup combines three functionalities: inerting to prevent oxygen inhibition, substrate mounting for structure curing on planar and convex substrates and mounting of the components for the determination of the focus position. This setup enables all necessary steps for reliable and defined structure curing to be carried out in a repeatable manner with one permanently mounted substrate holder. The following section presents the investigation of the feasibility of the nitrogen chamber for inerting to mitigate oxygen inhibition during the structure curing.

6.2.1 Mitigation of Oxygen Inhibition with Nitrogen Chamber

Since initial curing experiments showed that, by curing in a thin layer of photopolymer on a substrate, structures would only cure with significantly higher laser power than determined in chapter 4.3.2.1 and the resulting structures showed a tacky uncured top surface, the nitrogen chamber presented in the previous section 6.2 is developed to allow inerting with nitrogen in a volume around the substrate to mitigate the effect of oxygen inhibition. In order to determine the viability of this setup and to specify the necessary time for the nitrogen flow, the efficiency of the setup with the nitrogen chamber needs to be evaluated. The following figure 6.4a shows a schematic of the approach to determine the oxygen concentration when nitrogen is introduced in the chamber. For this an oxygen sensor is mounted to the outlet of the chamber. The chamber is sealed using the ND-Filter. This allows for a simple and easy way of determining the oxygen concentration. Using this setup, the oxygen concentration is measured over time for a continuous stream of Nitrogen on the input of the chamber. Figure 6.4b shows the progression of the oxygen concentration in a period of 260 s after the start of the introduction of a nitrogen flow. Here, an exponential decrease in the oxygen concentration over time is seen. The concentration drops below 1% after around 110 s and settles on 0.4 % by 180 s.

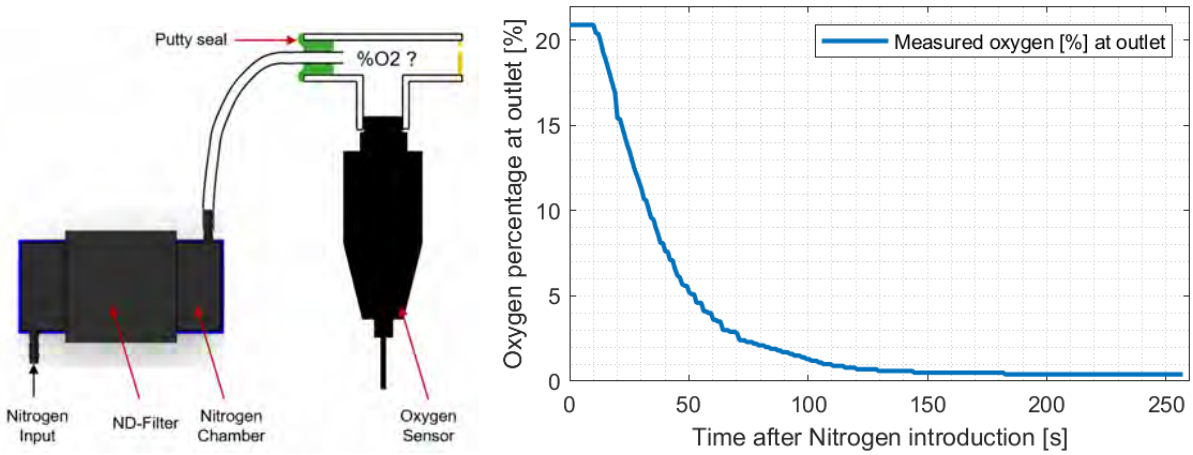

(a) (b)

Figure 6.4: Evaluation of the effectiveness of the nitrogen chamber for oxygen displacement a) Schematic setup of the oxygen concentration measurement, b) Oxygen concentration over time for continous nitrogen flow in chamber

The literature on oxygen inhibition suggests a decrease in oxygen below 1 % allows for sufficient mitigation of the influences of oxygen inhibition [39]. To ensure the best efficiency and to give the inerting sufficient time to take effect, a nitrogen flow time of 180 s is selected before structures are cured. This must be taken into account especially when curing on convex surfaces in order to use the correct time window for a defined layerheight (see chapter 5.4.5). This experiment demonstrates the usability of the nitrogen chamber for structure curing. The setup is viable. The following figure 6.5 shows the final setup of the lithography system on the item frame with the substrate holder mounted on the hexapod and the nitrogen chamber.

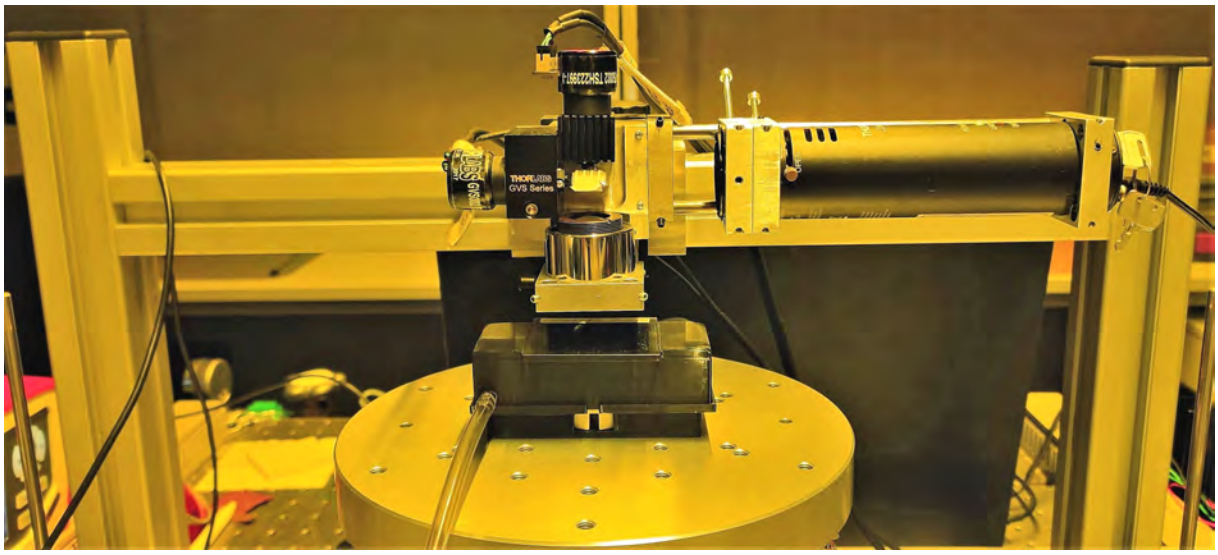

Figure 6.5: Picture of the Lithography setup in combination with the hexapod und substrate setup

With the curing and inerting setup in place, the following section 6.3 introduces the basic idea and the implementation of an automatic focus process using the hexapod and an optical power meter.

6.3 Focus Determination

In order to determine the focus point of the beam relative to the hexapod z-coordinate, this section presents an approach using the photodiode sensor of an optical powermeter in combination with a precision pinhole. The approach is to use a pinhole that is smaller than the focused laser beam. This way, the maximum power is measured at the power meter when the pinhole is positioned directly at the focal point of the laser. With the following equation 6.3.1 the focused beam diameter can be determined.

$$d_f = \frac{4 \cdot M^2 \cdot \lambda \cdot f}{\pi \cdot d_0} \tag{6.3.1}$$

With the beam quality factor M^2, the wavelength λ, the focal length f and the initial beam diameter d_0. For an ideal Gaussian beam with a wavelength of 405 nm, a beam diameter of 4 mm and the effective focal length of the scan lens of 39 mm, the minimum diameter of the focused laser beam is calculated to be 5.03 µm. Since the laser used is not an ideal Gaussian beam, the expected minimum diameter is correspondingly larger. For this reason, a readily available pinhole with a diameter of 5 µm is chosen. The following figure 6.6 shows the schematic setup for determining the focus position. For this purpose, the photodiode sensor of a powermeter is positioned in the substrate holder. A 5 µm pinhole is placed in a FDM printed adapter above the

sensor. The position of the pinhole is chosen to be at the same location as the surface of the planar substrate. By positioning the laser beam directly into the pinhole and moving the substrate assembly in the z-direction using the hexapod (or positioning table for stand-alone operation), the focus point on the pinhole can be determined depending on the hexapod z-coordinate.

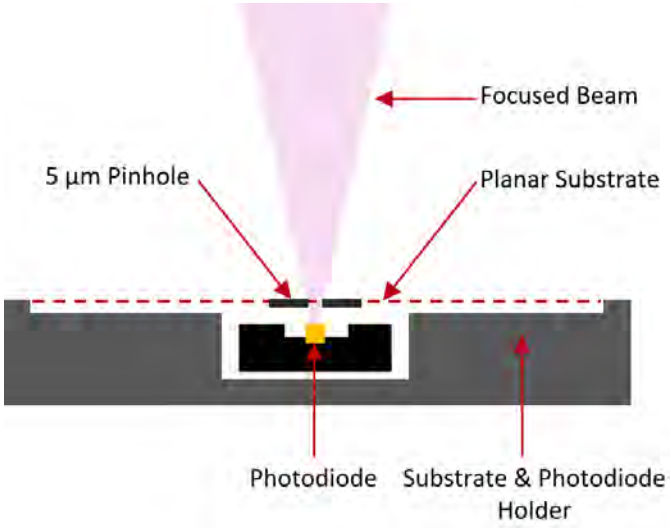

Figure 6.6: Schematic representation of the focusing principle using a pinhole and a photodiode sensor

The focal point determined with this method is theoretically exactly on the surface of the planar substrate. However, it must be taken into account that the positioning is done manually in a FDM printed adapter and the distance to the substrate surface is determined based on the CAD model. Therefore, both the positioning of the pinhole in the adapter and tolerance deviations of the FDM printed components (substrate holder and pinhole adapter) play a role in the accuracy of the focus determination on substrates. Since the surface of the convex substrates is located at a different z-coordinate anyway, it is advisable to experimentally determine the offset of the substrate surface to the determined focus position for each substrate (see chapter 7.1.2). With this, the focus position on known substrates can be determined with the focus method for an arbitrary placement of the hexapod coordinate systems (see chapter 3.9).
In order to achieve repeatable results with the focusing method, the incident beam must centrally enter the pinhole. Since the mechanical setup does not allow for micrometer precision when aligning the substrate and lithography setup, a way of determining the correct beam position is needed. This allows for precise focus determination and at the same time gives the offset for the position of the Galvo mirrors to be exactly in the substrate center. The beam positioning and determination of the focal position is performed using a Matlab script. The script controls the output voltage of the DAQ card to the Galvo mirror and uses that to meander the beam position in small incremental movements around the expected center of the substrate. At the same time the measured laser power from the powermeter is read out using the .NET wrapper driver to integrate the powermeter read-out in Matlab. Using this setup, the measured laser power is determined for each position of the Galvo mirrors. By finding the maximum laser power and determining the corresponding mirror voltages, a voltage pair for the beam to be

perfectly positioned in the pinhole center is determined. By repeating this process with smaller voltage increments, a precise position for the beam to be positioned centrally on the pinhole is determined. The following figure 6.7 shows the result of this position determination. When the best position is found, the script calculates and returns the corresponding mirror offset voltages.

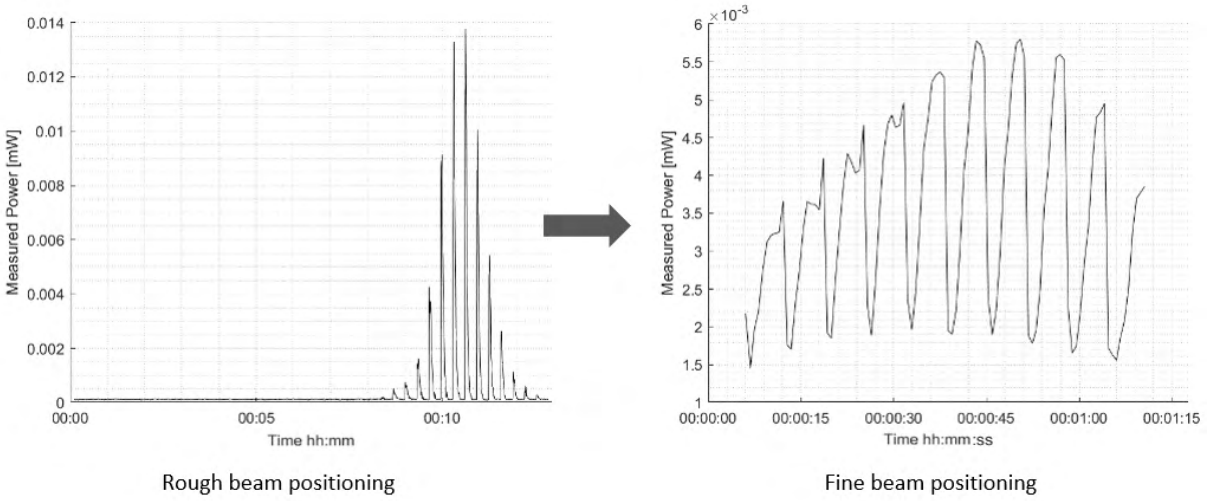

Figure 6.7: Live-Plot of measured laser power for the determination of mirror voltages and live-plot of repeated measurement with smaller voltage increments

When the correct beam position is determined and set, the script uses Newports HXP API to allow hexpod movement using Matlab. By moving the hexpod z-axis around the expected focal point (from the effective focal length of the scan lens), the hexapod z-coordinate, where the focal point of the beam is at the pinhole can be determined, once again by measuring the laser power. After the measurement is performed, the maximum laser power and the corresponding position of the hexapod is returned. The following figure 6.8 shows the measurement of the laser power over time for the movement of the hexapods z-axis and a boxplot of the determined focal positions for repeated focusing attempts. For the focus experiments, the photodiode sensor and pinhole are removed from the setup and reinserted, this allows the repeatability of the process to be determined. The boxplot of 7 individual focus point determinations shows the determined z-coordinate of the focal point in work coordinate system of the hexapod. This analysis that the z-coordinate of the focal point is determined repeatably within a range of 160 µm. Half of the measured focal positions are within a range of 80 µm. There is an outlier which comes from a slightly tilted positioning of the pinhole adapter.

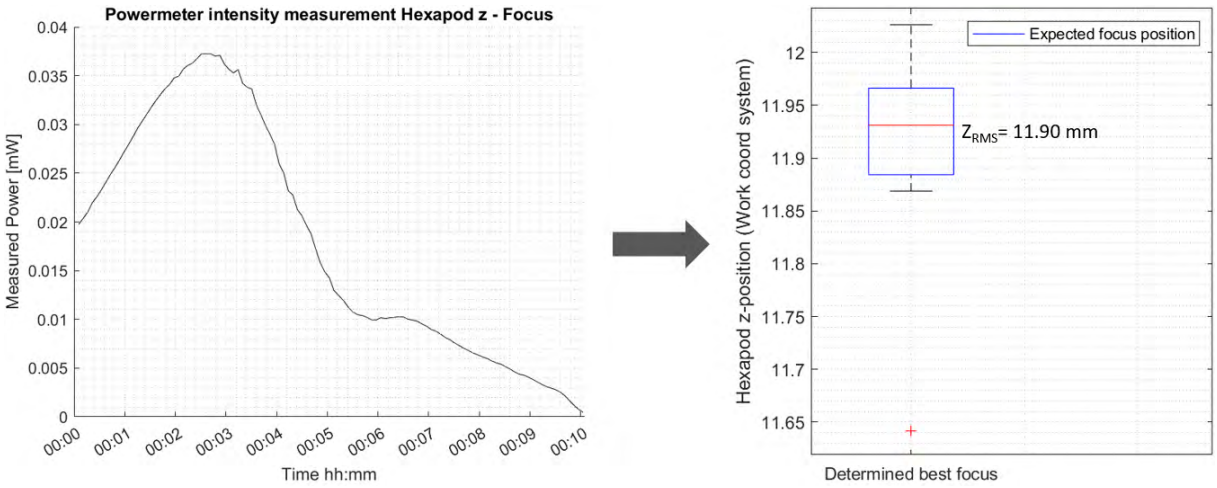

Figure 6.8: Live-Plot of the measured laser power over time for the movement of the hexapods z-axis and boxplot of the determined focal position for repeated focusing attempts

The setup presented in this chapter allows curing in layers on planar and convex substrates. The lithography setup is robustized and modularized for use with the hexapod and as a stand-alone system. An inert gas chamber for mitigation of oxygen inhibition is constructed and tested. The determination of the focal point from this section is sufficient to be used for testing of precise structure curing. The next chapter 7 presents experimental results for structure curing and surface functionalization on planar and convex surfaces using the layer application methods presented in chapter 5 and the setup from this chapter.

7 Structure Curing in defined Layers

This chapter presents the determination of curing parameters and experimental results for structures cured on planar and convex substrates using the layer application methods presented in chapter 5 and the lithography setup with the hexapod presented in the previous chapter 6. Initially parameters to achieve homogeneous structures with the smallest possible size are determined. Experimental results and the optimization of lithographically curing structures on planar surfaces followed by convex surfaces are presented. To achieve comparable results for planar and convex substrates this chapter focusses on structures cured in layers with heights of of 5 and 10 µm, since these are shown to be possible on both planar and convex substrates.

7.1 Determination of Curing Parameters

This subchapter presents the experimental determination of curing parameters using the method for calculating the laser power in chapter 4.3.2.1 and observations made from initial curing tests. The hexapod position is experimentally determined and compared to the results from the focusing method presented in the previous chapter 6.3. The minimum necessary laser power for fully cured structures in a defined photopolymer layer is determined. The next section 7.1.1 presents the determination of the voxel distance and the resulting parameter range for the scanning speed of the Galvo mirrors to create a homogeneous structure cross section.

7.1.1 Resolution for homogenous Structures

With the new setup for inerting to mitigate the effects of oxygen inhibition in the curing process, structures are now observed to cure with the determined laser power from the calculation presented in section 4.3.2.1. However, a non-homogenous cross section geometry is observed. The following figure 7.1 shows a WLI measurement of a line segment which was cured in a 5 µm layer of PR48 on a glass slide. Undercuring can be observed at some points. This is manifested by a reduced height and width of the line at these points. This effect occurs periodically at intervals of 40 µm. There are two hypotheses for the development of undecuring. First, that due to an insufficient number of voxels, not enough discrete points are approached to fully cure the structure by diffusion assisted polymerization. It is suspected, that the voxel resolution of 250 points per millimeter, that was determined in chapter 4.2, is no longer sufficient for thin photopolymer layers between 5 and 30 µm. However, the period (40 µm) in which this phenomenon occurs is significantly larger than the set voxel spacing (4 µm). This leads to the second hypothesis, that the error may be due to a periodic overflow of the DAQ cards output data for the maximum update rate. This would mean that individual points are skipped or be approached for too briefly.

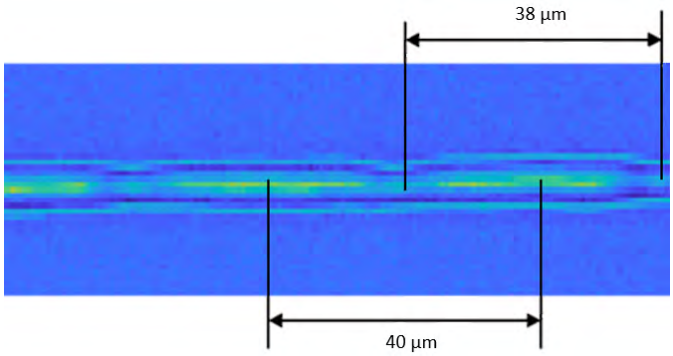

Figure 7.1: WLI measurement of a line cure with 250 pts/mm at 20 mm/s with periodically narrow cross section

Both the hypotheses of the insufficient voxel resolution and update rate overflow can be resolved by increasing the number of points per millimeter. This leads to a better voxel resolution and decreases the maximum possible scanning velocity, leading to a decrease in the necessary update rate of the DAQ card at maximum scanning velocity. The following figure 7.2 shows the measured line geometry for structures cured with a voxel resolution of 284 (figure 7.2a) and 333 (figure 7.2b) points per millimeter. These parameters limit the maximum scanning velocity to 17.5 and 15 mm/s respectively. Figure 7.2a still shows a periodic undercuring of the structure, however, the distance of the phenomenon occurring is increased to 120 µm, supporting the update rate hypothesis. When the maximum velocity is further decreased to 15 mm/s, the measurement in figure 7.2b shows a homogenous structure cross section.

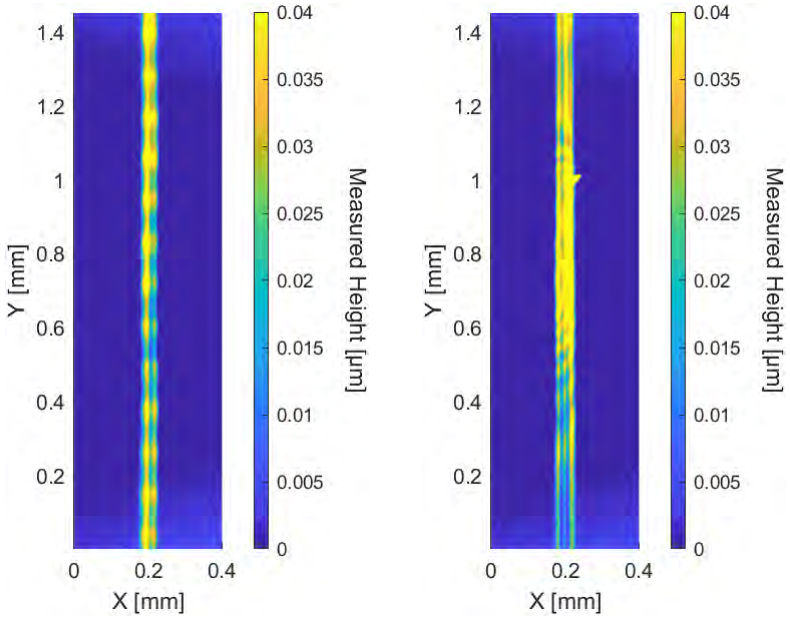

Figure 7.2: Determination of minimum voxel resolution and maximum scanning velocity a) WLI measurement of a line cured with 284 pts/mm at 17.5 mm/s scanning velocity, b) WLI measurement of a line cured with 333 pts/mm at 15 mm/s scanning velocity

Using this information leads to a determination of a maximum scanning velocity of 15 mm/s for

lithographic fabrication of homogenous structures in photopolymer layers down to 5 µm using the available NI 6001 USB DAQ card. With this scanning velocity, the structures can be cured up to a voxel resolution of 333 points per millimeter when operating the setup at maximum velocity. Since a dynamic process for rapid fabrication is desirable, it may be necessary to look at alternative digital to analog converters with better resolution and higher output rate to increase the possible scanning speed and fully utilize the Galvo systems capabilities in the future. For this work the operation at 15 mm/s at 333 pts/mm is chosen to achieve the maximum possible system dynamic. Since these initial measurements show that the structure height of the cured lines is very low, the following sections 7.1.2 and 7.1.3 describe the experimental determination of the correct focal position and laser power respectively, to achieve the smallest possible linewidth for fully cured structures in a defined layerheight.

7.1.2 Determination of optimal focus Position

This section describes the experimental determination of the ideal focus position on planar substrates to achieve the smallest possible structure aspect ratio while fully curing the layer and the comparison with the determined focal position from the focusing method described in chapter 6.3. For this, planar substrates with a 5 and 10 µm photopolymer layers are used with a fixed laser power (here: 220 µW for an approximated beam waist diameter of 37.96 µm in chapter 4.3.2.1) and the maximum velocity and voxel resolution determined in the previous section 7.1.1. Using the hexapod, the z-position of the substrate is moved within a range around the determined focal position from the previous chapter 6.3. The following figure 7.3 shows, that for z-coordinates of the hexapod coordinate system in the range between 10.8 and 12.5 mm around the previously determined coordinate (11.9 mm - see figure 6.8), the measured structure height increases steadily. This suggests that the ideal focal position for fully cured structures on planar surfaces is not reached within this range. Therefore, an offset of the substrate surface to the pinhole position is suspected.

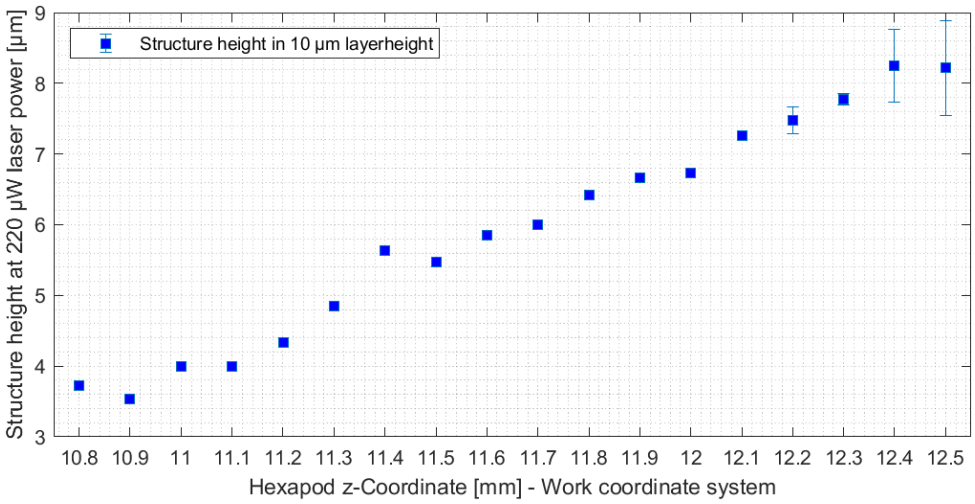

Figure 7.3: Measured structure height in a 10 µm layer over hexapod z-position around the determined focus position (11.9 mm)

To determine the correct focal position and corresponding offset to the position determined with the focusing method, the z-position of the substrate is increased further. The following figure 7.4 shows the results for a hexapod z-position of between 11.9 and 13.8 mm in photopolymer layers with a height of 5 and 10 µm for three measurements with the corresponding standard deviation. This shows that the maximum achievable structure height with the used curing parameters is achieved at a z-position of 12.9 mm in the hexapod work coordinate system. Therefore an offset of 1 mm of the pinhole position to the substrate surface is determined, which can be used from now on to determine the focal position with an arbitrary coordinate system position of the hexapod, a realignment of the setup, or for stand-alone use of the system. The analysis also shows that the final structure height achieved is significantly lower than the applied layerheight with an average structure height of 8.48 µm in a 10 µm photopolymer layer and 3.44 µm in a 5 µm layer. This observation can either mean, that the used laser power is too low to achieve a fully cured structure in these layerheights, or that the structures still don't fully cure due to oxygen that has diffused into the material during storage or layer application, which cannot be fully mitigated by the inerting process. Another reason for the deviation of the height of cured structures from the layerheight could be the polymerization-induced material shrinkage (see chapter 3.4). Another observation with these measurements is that the measured structures show a variation in height for the same hexapod position of up to 1.5 µm. This observation supports the hypothesis that the deviation in height is due to diffused oxygen in the material, since a different concentration of oxygen that has diffused in the material for each test would result in a variation of of the amount of uncured material.

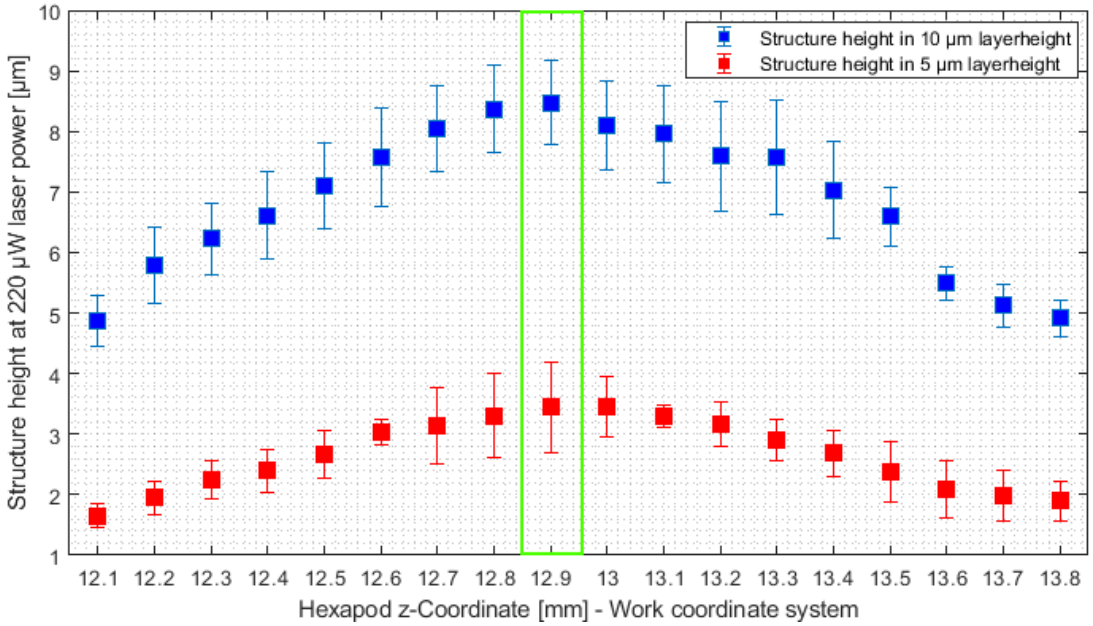

Figure 7.4: Measured structure heights and standard deviation over hexapod z-Position to determine the best focus position for maximum cured structures in a 5 and 10 µm layer

With the measurements presented in this section, the offset to the determined focal position in chapter 6.3 is determined to be 1 mm for the used planar substrates. Analog to that, the offset

for convex substrates is determined to be 15.45 mm. Using this information, the ideal focus position for planar and convex substrates is determined, and the focusing method from chapter 6.3 can be used to calibrate the setup with the hexapod and determine the ideal focal position in stand-alone operation. In order to test the hypothesis that the structures do not fully cure due to insufficient laser power and to determine the minimum necessary laser power for maximum cured structures with the smallest possible structure width, the following section 7.1.2 presents the experimental determination of the necessary laser power for reliable structure curing.

7.1.3 Determination of necessary Laser Power

This section presents an approach similar to the one used in the previous section 7.1.2 to determine the minimum laser power necessary for fully curing structures while achieving the smallest possible structure width. For this, the substrates are positioned at the previously determined z-position to achieve the maximum structure height and the laser power is varied around the previously used value of 220 µW for the laser power. This parameter is determined using the calculation method to determine curing parameters introduced in chapter 4.3.2.1. To be able to use the calculation method with the revised setup, the transmittance (here: 50%) of the ND-filter used to seal the nitrogen chamber presented in chapter 6.2.1 needs to be accounted for in the model. Since this method was developed for a process where the substrate was positioned on top of a photopolymer volume, the intensity distribution in the photopolymer is different for the current setup. In addition, the ideal z-position of the substrate was determined experimentally, thus the exact focal position relative to the layer surface is unknown, which further affects the model. For these reasons, the model can only be used to estimate the necessary laser power, the actual laser power for the best structure resolution is determined experimentally in this section. To determine the minimum necessary laser power for a fully cured layer, individual lines are cured with a laser power between 50 and 370 µW. The following figure 7.5 shows an excerpt of the measured structure heights on three substrates over the laser power between 50 and 250 µW with their corresponding standard deviation. In this analysis it is seen that the maximum structure height is achieved at a point around 75 µW laser power. To safely ensure a maximum structure height, the minimum laser power for curing in 5 and 10 µm layers is set to 100 µW. These measurements show that the hypothesis of height deviation due to insufficient laser power must be rejected. The measured heights do not significantly increase for laser powers above 100 µm. The measurements still show deviations of up to 1.6 µm within measurements performed at the same laser power. Since there is no discernible trend that the curing height continues to increase with higher laser power, the minimum laser power for reliable and full structure curing in 5 and 10 µm layers is set at 100 µW to ensure fully cured structures.

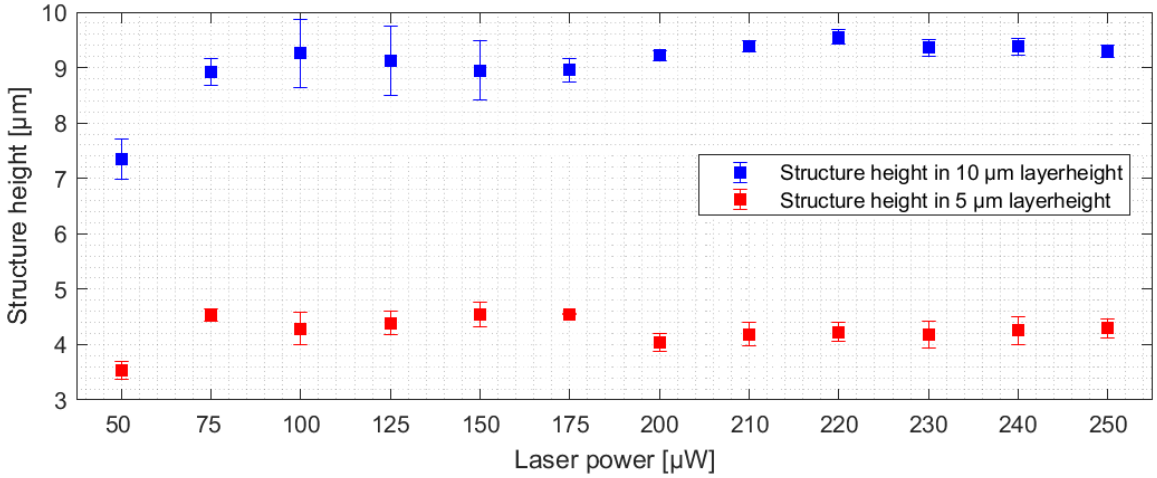

Figure 7.5: Measured structure heights and standard deviation over laser power to determine the minimum necessary laser power for fully cured structures in a 5 and 10 µm layer

The following figure 7.6 shows a cross-section profile generated by averaging the measured values of a line cured with 100 µW laser power in a 10 µm photopolymer layer. When analyzing the width of the structures, it is seen that the structures show a width between 20 and 30 µm. The width significantly thickens towards the substrate though, at the point of adhesion the width of the structures is observed to be in a range between 70 and 80 µm (5 µm layer) and 100-120 µm (10 µm layer). This needs to be considered, especially when it comes to the optical properties of cured structures and when determining the minimum distance between structures to generate individual features presented in the following subchapter 7.2.

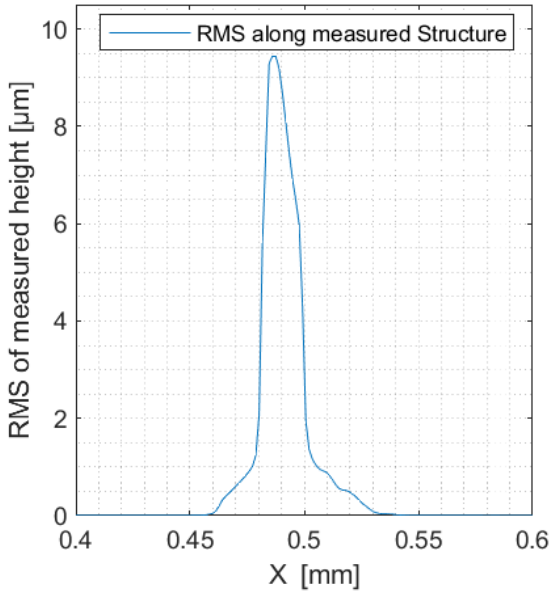

Figure 7.6: Averaged cross section profile for a line geometry cured with 100 µW laser power in a 10 µm layer

In this section the minimum laser power for reliable, complete curing of structures was determined. For the current setup, structures in 5 and 10 µm photopolymer layers cure to their maximum achievable height at a laser power of 75µW and above. To achieve the maximum

possible height with the current setup, a minimum laser power of 100 µW is chosen for the following experiments to ensure maximum layer curing. The measurements presented in this section show that the structures are still not fully cured, the measured structure height shows a deviation of up to 2.5 µm from the layerheight. The hypothesis of insufficient laser power as a reason for incompletely cured layers must be rejected. This means that the deviation of the measured structure height from the layer height most likely comes from a combination of polymerization-induced material shrinkage and residual oxygen in the material. Since the material shrinkage of the photopolymer used cannot be mitigated without significant loss of scanning dynamic and the creation of an oxygen-free working atmosphere would be necessary to completely prevent oxygen inhibition, the height deviation is accepted in this work. This results in an expected structure height of 2.5 to 4.5 µm in 5 µm layers and 7.5 to 9.5 µm in 10 µm layers. The resulting structures show a width between 20 and 30 µm which increases up to 80 µm for 5 µm layers and 120 µm for 10 µm layers at the adhesion area on the substrate. Using the laser power determined in this chapter the the beam diameter for the calculation model of curing parameters from chapter 4.3.2.1 needs to set at 15 µm to fit the results from these section and be used to determine curing parameters.

7.1.4 Results and Conclusion

This subchapter presented the determination of the process parameters for the lithography system to achieve a continuous structure cross section and the smallest possible structure geometry while ensuring a maximum cured layer. To achieve this a minimum voxel resolution of 333 points per millimeter is determined, limiting the maximum scanning velocity to 15 mm/s. The z-position of the substrate with the best possible curing height and the corresponding offset to the identified focus position for planar and convex surfaces is determined. The minimum laser power required to fully cure structures in 5 and 10 µm layers is set to 100 µW. This results in structure heights between 2.5 and 4.5 µm in 5 µm layers and 7.5 to 9.5 µm in 10 µm layers. The deviation from the coated film thickness and large variation within these measurements is suspected to come from the diffusion of oxygen into the material during storage or spin coating and polymerization-induced material shrinkage. Structures cured with these parameters have a width between 20 and 30 µm. At the adhesion surface, however, this width increases significantly up to 120 µm. Using these determined parameters, the following subchapters 7.2 and 7.3 present experimental results of structure curing and process optimization on planar and convex surfaces respectively.

7.2 Curing Structures on Planar Substrates

This subchapter presents the determination of the minimum and maximum line spacing to cure individual structures and homogenous areas respectively as well as evaluating resulting structures cured with the lithography setup to functionalize structures on planar surfaces with layer-

heights of 5 and 10 µm. The next section 7.2.1 presents the experimental determination of the line spacing to fabricate individual structures and fully cured areas.

7.2.1 Resolution for individual Features and homogenous Surfaces

To be able to cure free standing individual structures as well as surface areas, the minimum line spacing for individual structures and the maximum line spacing for homogenous surfaces need to be determined. Thereby, the necessary infill density in the slicer (see chapter 4.2) can be determined and the possible cure resolution with this setup can be characterized. The necessary structure distances are determined by curing a line pattern with decreasing line distances in a defined layer. The following figure 7.7 shows the cross section of a measurement of such a line pattern in a 10 µm layer of PR48 on a microscope slide with line distances between 20 and 200 µm. Here it is seen, that at a distance below 140 µm the structures begin cross-linking at the substrate surface. For the respective measurement in a 5 µm layer, this is only observed at a line distance below 100 µm. If the line spacing is reduced further, the structures grow together more and more into a connected geometry. At a distance below 20 µm the lines are grown together up to at least 80% of their height. To ensure complete structure cross-linking at the surface of the geometry, which results a in homogeneous surface, a maximum line spacing of 10 µm or less is determined. This condition holds for both 5 and 10 µm layers.

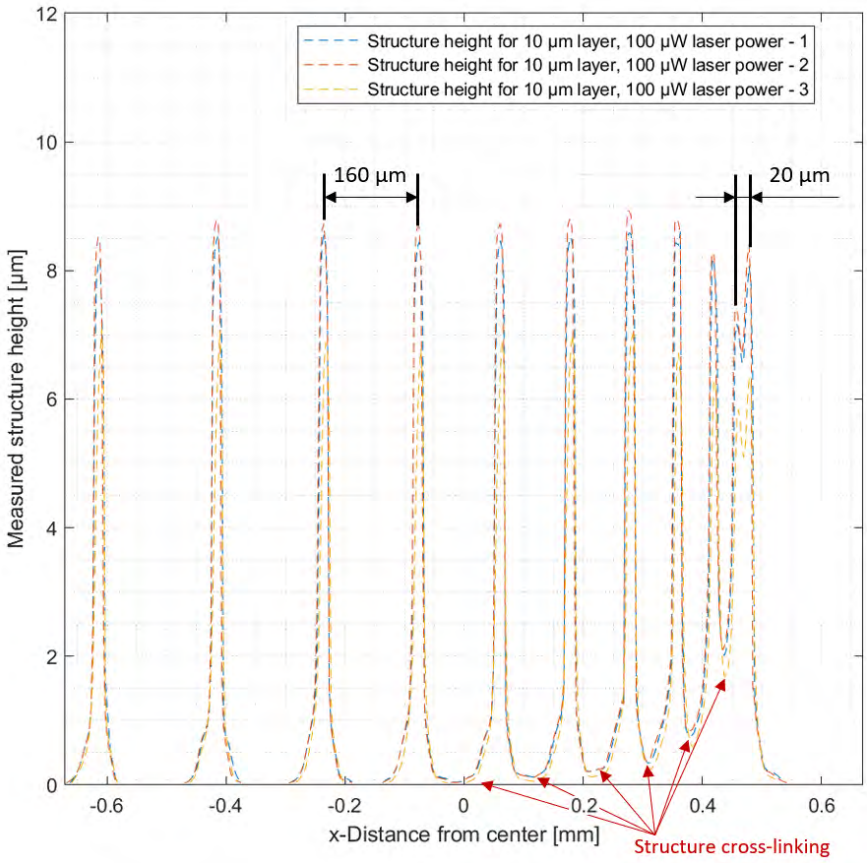

Figure 7.7: Slice through a WLI measurement of a line pattern cured in a 10 µm layer with decreasing line distances to determine minimum and maximum line distance for individual structure and surface curing

With this information the final necessary condition for curing predictable structures in a defined layerheight is determined. The minimum line distance for individual features in 5 and 10 µm photopolymer layers is determined to be 120 and 160 µm respectively. To achieve fully and homogenously cross-linked structures to manufacture wider structures and cure areas, the maximum possible line distance for fully cross-linked structures is set at 10 µm. The next section 7.2.2 presents the curing results for structures on planar surfaces using the layer application method from chapter 5.3 in combination with the curing parameters from the previous section 7.1 and the line spacing determined in this section.

7.2.2 Evaluation of cured Structures

To test the viability of the line distance for individual features and homogenous geometry surfaces determined in the previous section, the determined curing parameters are used to fabricate patterns on microscope slides. The structures discussed in this chapter are line gratings, a set of concentric circles and a fully cured square area. The line grating and the concentric circles are used to verify the distance for individual structures. The line grating is also used as a proof of concept for functionalizing surfaces using the current lithographic setup. The square geometry is used to determine the quality of a surface cured with the current setup and parameters. The following sections present the measurements and evaluation of the curing results with these three structure geometries.

Using the determined minimum structure distance, a line grating is created with a line distance (i.e. grating constant) of 160 µm for a 10 µm layerheight using a python script. The following figure 7.14 shows the measurement of such a grating. Here the reliable separation between individual lines is seen in the top-down view (figure 7.8a) and a slice through the measurement (figure 7.8b) shows that the structures are fully separated even at the point of adhesion on the substrate, verifying the minimum structure distance determined in the previous section. The measured lines show an even height and width throughout the pattern, with an average height of 8.97 µm and an average width of 23.8 µm, which widens to an average adhesion width of 114 µm within the last micrometer towards the substrate surface, resulting in an average slit width of circa 133 µm. The height of individual lines varies within $\pm$ 200 nm around the average measured height, the width ranges within $\pm$ 3 µm around the average width, which shows a good repeatability within a single substrate.

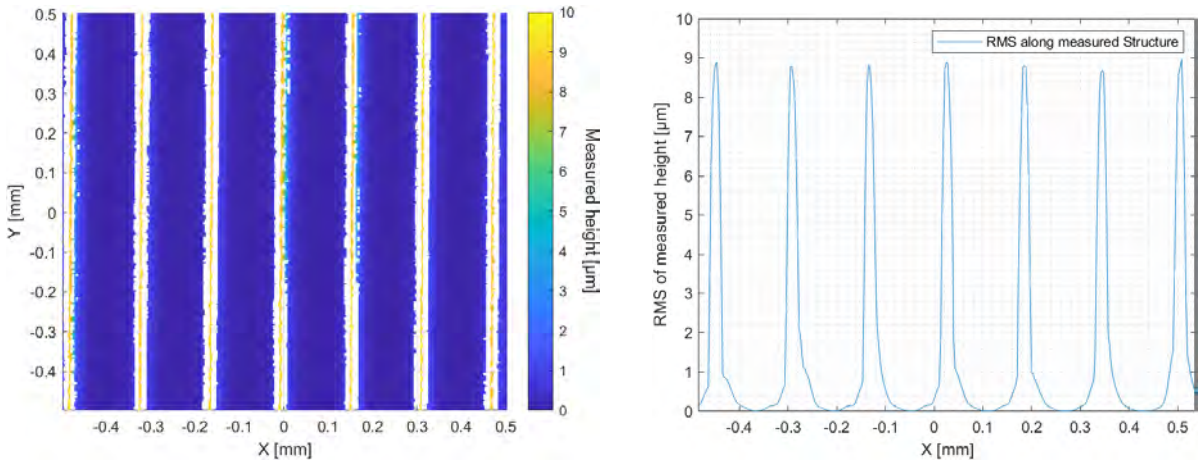

(a) (b)

Figure 7.8: Verification of minimum line distance by curing a line grating with a linedistance of 160 µm in a 10 µm photopolymer layer a) Top down view of the WLI measurement, b) Averaged cross section geometry of line grating

The following figure 7.14 shows a picture of such a line grating (figure 7.9a) and a comparison of the average structure height and width for three gratings cured on individual substrates (figure 7.9b) using a slice through the measured structures. When analyzing the repeatability of the structure geometry on multiple substrates, the measurements show a very good repeatability with the structure- and adhesion width, however as observed in the previous tests, the height of the structures here also varies greatly between different substrates but shows a good repeatability within a single substrate. These measurements of the line gratings show that the height of the cured structures for one measurement drops to as low as 6.9 µm. For this reason, the expectation range of structure heights due to material shrinkage and oxygen inhibition from the previous chapter 7.1 in 10 µm layers is adjusted to 6.9 to 9.5 µm. For structures in 5 µm layers, all measured structure heights stay within the 3.5 to 5 µm range.

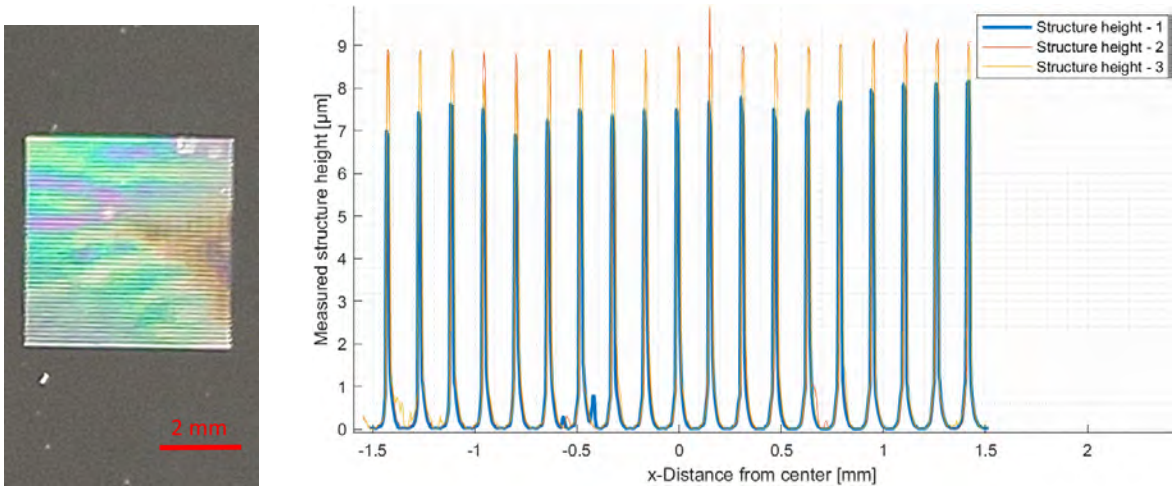

(a) (b)

Figure 7.9: Analysis of repeatability of structure height and width for individual structures in a line grating a) Picture of a 5 x 5 mm line grating cured in a 10 µm layer of PR48, b) Superposition of the measured cross-section geometries for 3 gratings in a 10 µm layer

In the photo (figure 7.9a) above, the grating already shows interference. Using a collimated light source like a laser pointer this line grating is used to create a diffraction pattern. The following figure 7.10 shows a photograph of the diffraction pattern of a grid with 30 slits and a grating constant of 120 µm. Here, a red (633 nm) laser pointer is used to illuminate the grating and project a diffraction pattern on a wall at a 2 m distance. In the picture, the individual diffraction orders can be clearly recognized, here the individual diffraction orders of the grating are observed and a superposition of the diffraction pattern with that of a single slit can be seen. This shows a proof of concept for optically functionalizing surfaces using the lithography setup.

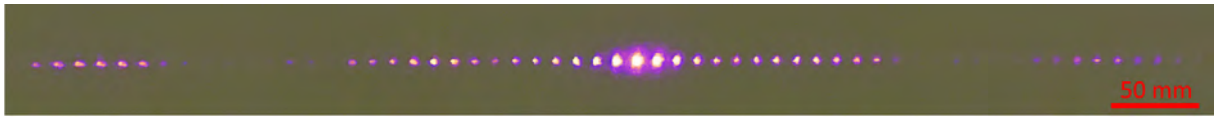

Figure 7.10: Diffraction pattern created with a red laser pointer through a line grating cured in a 10 µm layer of PR48 with a grating constant of 120 µm at a screen distance of 2 m

When comparing the distance of the maxima from the zeroth order in the observed diffraction pattern to the theoretically expected position at a screen distance of 2 m as shown in the following figure 7.11, it is seen that the generated pattern for the position of the first seven orders is very close to the expected position. This shows the successful functionalization of the surface. It is also seen that the deviation of the position of the maxima increases for increasing orders. At the seventh order, a deviation in the position of 4 mm can already be seen. However, this is more likely due to the tilt of the photo from figure 7.10 that was used to determine the distance and cannot be used as a conclusive deviation. This analysis nevertheless shows that it is possible to functionalize surfaces and obtain results that fit the expected values.

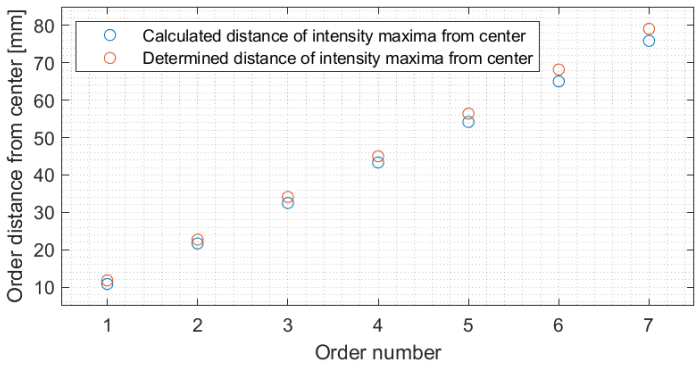

Figure 7.11: Determination of the position of order maxima for a lithographically fabricated line grating and comparison with the theoretically expected maxima positions

To verify the line spacing for non - linear structures in every scanning direction, a pattern of concentric circles is created using a python function to calculate discrete points with the same segment length for each circle. The following figure 7.12 shows a top-down view of a measurement for a pattern of concentric circles with a line distance of 120 µm in a 5 µm layer. The pattern is designed to use the complete field of view of the scan lens up to 10 mm. When creating curved structures such as circles, it is important to choose a sufficient discretization of

the individual points. In the enlarged area of the image, it is seen that the innermost circle is polygon shaped due to the linearization between discrete points by the software. This polygon shape (indicated as red lines in the figure) has not enough sides to sufficiently represent the circular shape, this needs to be accounted for in the creation of patterns. The maximum length of an individual segment for non-linear structures must be below 20 µm to ensure a sufficient representation of the desired shape. Another observation is the irregular line geometry at the outer edge of the cured structure. The outer two circles show a discontinuous shape with larger deviations from the expected circular shape and an inhomogeneous structure width. It is suspected that the distortion at the edge of the field of view of the scan lens is too high to reliably cure homogeneous structures. The maximum structure dimension is therefore set to 9 mm.

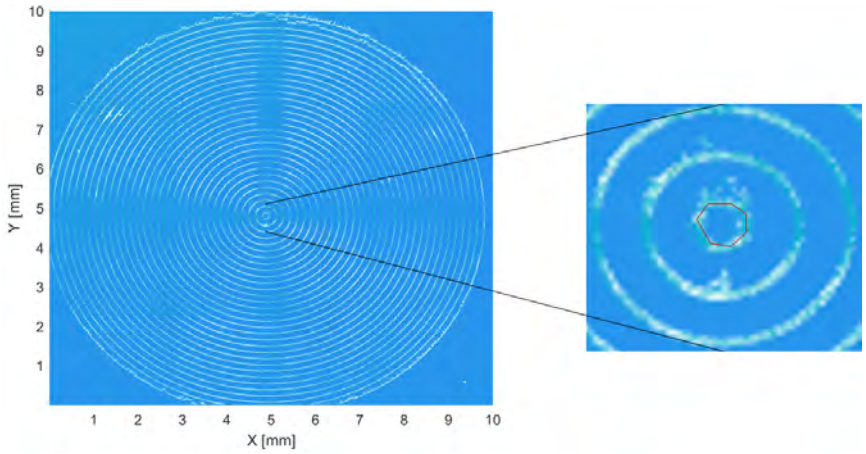

Figure 7.12: WLI measurement of a pattern of concentric circles to evaluate feasibility of line spacing in every curing direction and center segment of the pattern with the observed effect of too little point discretization for non linear structures

The final test geometry that is created, is a filled square geometry. Using a CAD file of a square and appropriate slicer settings in Cura, a .gcode file for a 2.5 x 2.5 mm square with an infill line distance of 10 µm is created. The following figure 7.13 shows the motion paths and orientation calculated by Cura to create a quadratic structure. Since the software is optimized for FDM printing, the outer geometry is first traced twice and then the infill is traced at a 45° angle. Since the edge of the structure is cured twice and is approached again during the production of the infill geometry, this influences the expected shape of the structure edges.

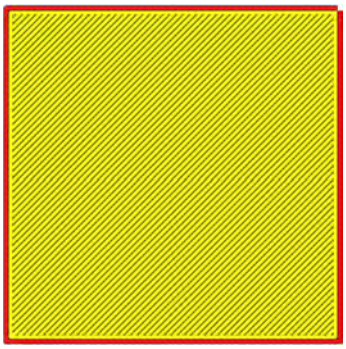

Figure 7.13: Movement path calculated by Cura for a square geometry

The following figure 7.14 shows the measurement and a slice through the center of the measurement for such a square cured in a 10 µm photopolymer layer. These measurements show a complete cure of the square surface with an average surface roughness (S_a) of less than 250 nm and a peak-valley ($P-V$) distance of up to 1.5 µm, which can be attributed to the higher curing at the structure edges, since multiple exposures occur there due to the way the scan path is created in the slicer (see figure 7.13 above). Without the structure borders the $P-V$ distance is below 0.7 µm. Overall, the structure surface shows a fully cured structure, verifying the maximum line distance of 10 µm for curing areas. These geometries still show the effect that structures do not fully polymerize the layer, however, due to the small line spacing, each point on the surface experiences two exposure cycles and the structure polymerizes more evenly and reliably. This leads to a better repeatability within one and throughout multiple substrates. A decrease of the range of measured structure heights to between 8.6 and 9.7 µm in a 10 µm layers and between 3.5 and 4.8 µm in 5 µm layers is seen.

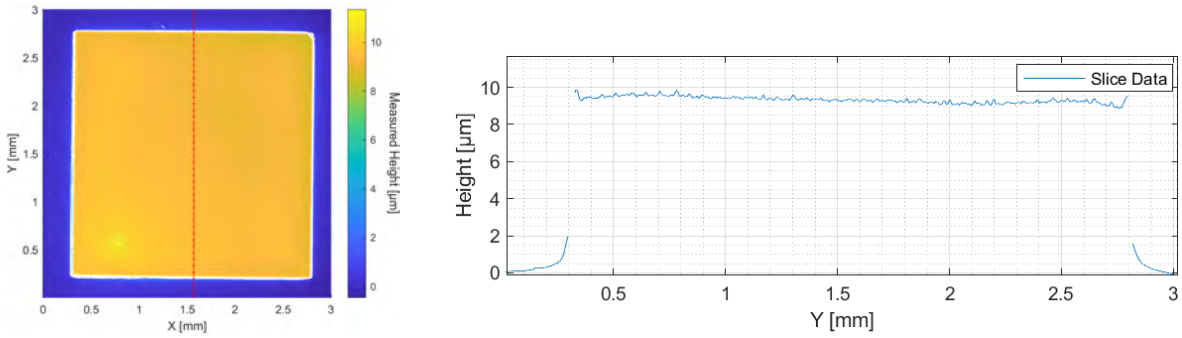

(a) (b)

Figure 7.14: Analysis of curing areas a) Top down view of a WLI measurement of a 2.5 x 2.5 mm square cured with a line distance of 10 µm in a 10 µm layer of PR48

In this section, the previously determined minimum and maximum line distances for individual structures and homogenous areas are verified. The concept of functionalizing surfaces using lithographically cured structures is proven by manufacturing a line grating on a glass slide and creating a diffraction pattern using this sample. For homogenous structures and to mitigate effects of distortion on the borders of the scan lens' field of view, the maximum dimension of a cured geometry is set to be 9 x 9 mm. The cured structures show a repeatable width between 20 and 30 µm and – for area curing – a repeatably good surface quality of S_a below 250 nm. The height variation of the measured structures is seen to be in a range of 2.5 and 4.5 µm for 5 µm layers and 6.9 to 9.5 µm for 10 µm layers. This variation decreases to between 8.6 and 9.7 µm in a 10 µm layers and between 3.5 and 4.8 µm in 5 µm layers for cured areas.

7.2.3 Results and Conclusion

In this subchapter curing results on planar substrates with the determined focal position (chapter 7.1.2) and laser power (chapter 7.1.3) are presented. The minimum and maximum line distance for curing individual structures and curing homogenous surfaces in 5 and 10 µm PR48 pho-

topolymer layers are determined. The minimum line distance for individual features is determined to be 120 µm for 5 µm layers and 160 µm for 10 µm layers. The maximum line distance for homogenous surfaces is determined to be 10 µm for both 5 and 10 µm layers. The maximum dimensions of a structure cured with the current lithography setup is determined to be 9 x 9 mm due to the limited field of view of the scan lens. Using the layer application method presented in chapter 5 and the curing parameters determined in this chapter, it is possible to cure structures with repeatable structure heights between 2.5 – 4.5 µm (5 µm layer) and 6.9 to 9.5 µm (10 µm). Individual structures show a width of 20 to 30 µm, which widens to 70 to 80 µm (5 µm layer) and 100 to 120 µm (10 µm layer) towards the point of adhesion on the substrate. The height of the cured structures varies between individual results up to 2.75 µm but shows good repeatability below 0.5 µm within an individual substrate. This deviation between substrates decreases to around 1.3 µm when curing areas. Using the information, parameters and results presented in this subchapter, a functionalization of a surface using a line grating and the possibility to cure homogenous surfaces with the setup is shown. Using the determined layer application method and determined curing parameters, free form 2.5 D geometries with a defined height and width can be manufactured. The following figure 7.15 shows an example of a free form geometry fabricated with the determined curing process. Here, the logo of the Hochschule Aalen, where this work was conducted, is cured in a 0.5 x 3 mm area in a 5 µm layer of PR48 on a microscope slide. The figure shows a photograph of the substrate with the corresponding WLI measurement of the cured structure. Here it is seen that individual features e.g., the space in the “o” can be reliably distinguished up to a structure distance of 25 µm even though a cross-linking on the substrate surface is observed for structure distances at 100 µm. Another observation here is that for small distances between structures, the movement of the beam to a new point can sometimes result in a slight polymerization of the intermediate space where the laser skips to the new point, this is seen for example in the bottom right space between the circles of the logo. For the polymerization of such free form structures and to improve the curing results, an eventual implementation of an external shut-off mechanism becomes necessary.

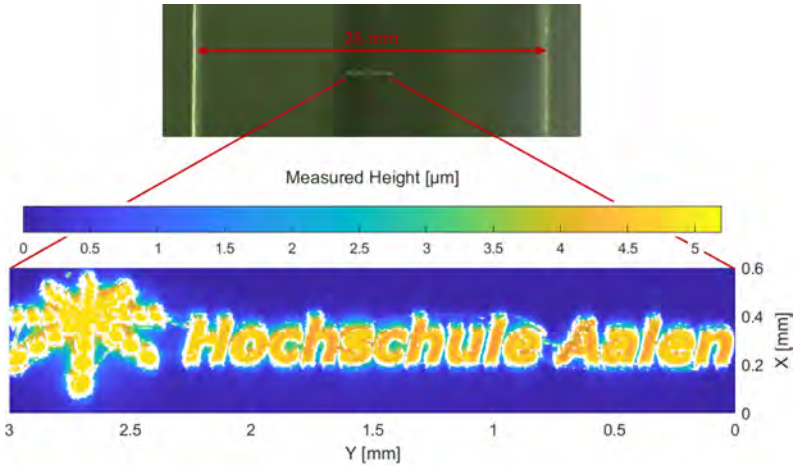

Figure 7.15: Picture and corresponding WLI measurement of the ’Hochschule Aalen’ Logo cured in a field of 3 x 0.5 mm in a 5 µm PR48 layer

In the next subchapter 7.3, the information and parameters from this subsection will be applied to structure curing on convex surfaces. The influence of surface curvature will be analyzed and experimentally evaluated. A way of mitigating the curvature is presented and experimentally validated.

7.3 Curing Structures on Convex Surfaces

This subchapter deals with the implementation of the curing procedure to manufacture structures on convex surfaces. First, the expected influence of the curvature on the exposure, dependent on the distance to the center of curvature is determined. The actual influence of the surface curvature on the curing result is determined experimentally. Finally, a proof of concept for mitigating the effect on curing results due to the substrate curvature using the hexapod to reposition the substrate is presented. The next section 7.3.1 presents the analytical and experimental evaluation of the influence of the substrate curvature on the curing results.

7.3.1 Evaluation of cured Structures

To determine and predict the expected effect of a non-planar substrate on the curing geometry, the following section presents a simulation of the expected intensity distribution at a point of a convex surface at a given distance from the substrate center. The diameter of a a beam with a defined diameter on a convex surface at a defined distance from its center axis can be approximated using the geometrical model shown in the following figure 7.16. The beam diameter on the substrate surface is approximated here as the hypotenuse of a right-angled triangle depending on the initial beam diameter at the incident point.

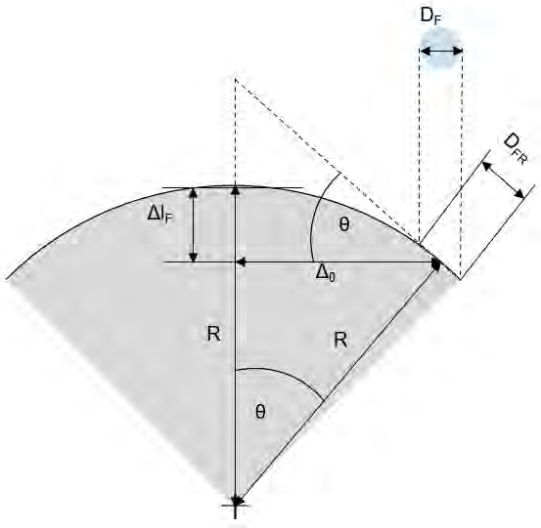

Figure 7.16: Geometric model to approximate beam diameter on convex surfaces (cf. [1])

Using the geometric relationships in the figure above, the beam diameter seen by the substrate can be calculated with the following equation 7.3.1 depending on the distance to the substrate

center and the original beam diameter, if the radius of curvature of the substrate is known.

$$D_{FR}(\Delta_0) = \frac{D_F \cdot R}{\sqrt{R^2 - \Delta_0^2}} \tag{7.3.1}$$

With the initial beam diameter D_F, the radius of curvature R and the distance from the substrate center Δ_0. Using this approximation and the angle θ, the diameter of the beam experienced by the substrate can be determined relative to a defined beam position at a desired distance from the center. By approximating the beam diameter in x- and y- direction individually and creating an ellipse using the approximated diameters, the shape of the beam on the substrate surface can be approximated. Using equation 3.3.4 from chapter 3.3 to calculate the intensity of a focused beam at a given z-position and radial distance from the focus point, the intensity at a given point on the substrate surface within the experienced beam shape can be calculated. Since the intensity of a laser beam is shown to be proportional to the exposure energy experienced by a photosensitive material (see chapter 3.3), this can be used to determine the expected curing shape at a defined point on a convex surface. The following figure 7.17 shows a comparison of the intensity distribution for the substrates used in this work with a radius of curvature of 19.5 mm. The top of the figure (a) shows the expected intensity distribution when the focal position is not adjusted to compensate the substrate sag. A simulated movement of the beam position to the left (compare figure 7.16) by 3, 9 and 15 mm is shown. The bigger the distance from the center, the more the point with the highest intensity is offset against the direction of movement. The beam center at the simulated movement distance is at the intersection of the black lines in the figures. The sag height of the substrate at a given distance from the center causes defocusing of the beam. Since one side of the substrate surface is higher when moving outward from the center, this part of the surface experiences a higher intensity because it is closer to the focal position of the laser beam - the intensity distribution shows an offset from the center point. The lower the radius of curvature and the higher the distance to the substrate center, the more significant this influence becomes. The shape of the cured geometry is expected to follow the intensity distribution. A structure on a convex surface will no longer have a uniform cross-section after a certain distance and the position of the tip of the cured geometry is displaced towards the substrate center. When compensating the defocusing due to the change of the surface shape by refocusing the beam dependent on the distance from the substrate center as seen in the bottom part of the figure (b), the intensity distribution becomes uniform around the point of impact. For both situations, however, the diameter experienced on the substrate surface becomes narrower along the direction of motion as the curvature of the surface increases. This affects the dimensional accuracy and directional repeatability of the curing geometry, since the aspect ratio of the intensity distribution on the surface is dependent on the scanning direction.

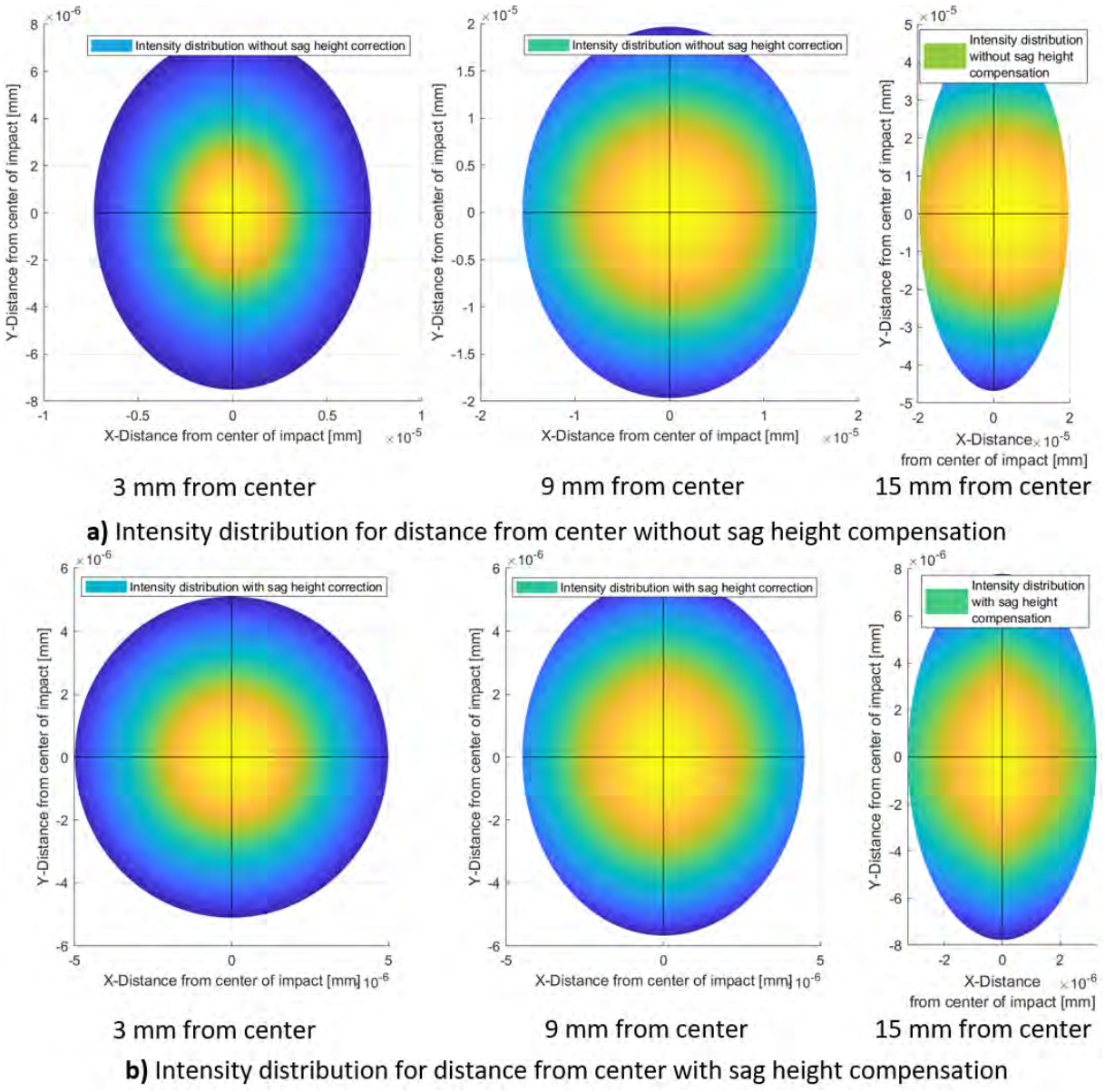

Figure 7.17: Simulation of the intensity distribution of a laser beam focused on the tip of a convex substrate for defined distances from the substrate center a) Without correction of the focal height, b) With correction of the focal height

The simulation shows that the shape of a surface has a big influence on the intensity distribution and therefore the expected shape of a geometry cured on it. Therefore, the focus position and the orientation of the beam towards the surface need to be adjusted. However, as seen in figure 7.17 above, the expected change in the curing shape only becomes significant at a specific shape deviation (i.e., distance from substrate center). To analyze the significance of the error due to the substrate curvature and to determine an acceptable range in which the curing results show repeatable results without compensation of the surface shape, a line pattern and concentric circles are cured in a 9 x 9 mm area around the substrate center without hexapod movement. The following figure 7.18 shows a picture of the structures on the lens after the curing process.

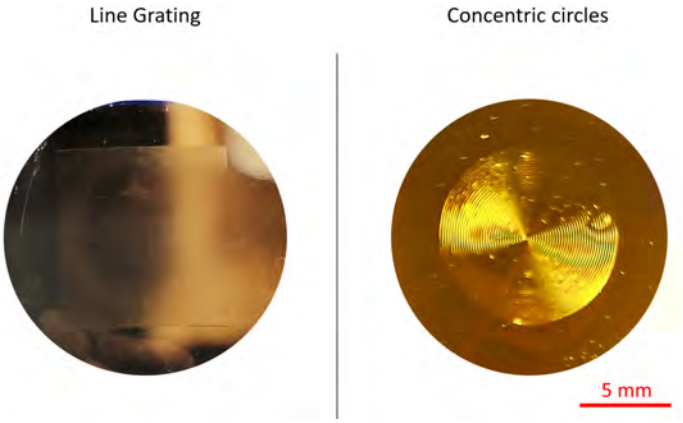

Figure 7.18: Picture of line grating with a grating constant of 160 µm and a pattern with a structure distance of 160 µm a 10 µm PR48 photopolymer layer

When measuring these structures using the WLI it is observed that the result shows an oscillation of the measured height. Datapoints even below the surface of the lens are measured. The following figure 7.19 shows a surface plot of a measured line segment (figure 7.19a) and a plot of the measurement cross section (figure 7.19b) with the expected surface position. To verify the assumed position of the lens surface, a measurement using a chromatic confocal sensor in combination with a linear stage is used to measure the topography. This measurement is shown in figure 7.19b as the orange curve. This shows that the expected surface position is plausible. It is seen that a topography measurement using the chromatic confocal sensor is not feasible since the measurement is very noisy and, due to the spot size of the measurement beam, the structure height is not correctly measured since the measured height is averaged over the spot size.

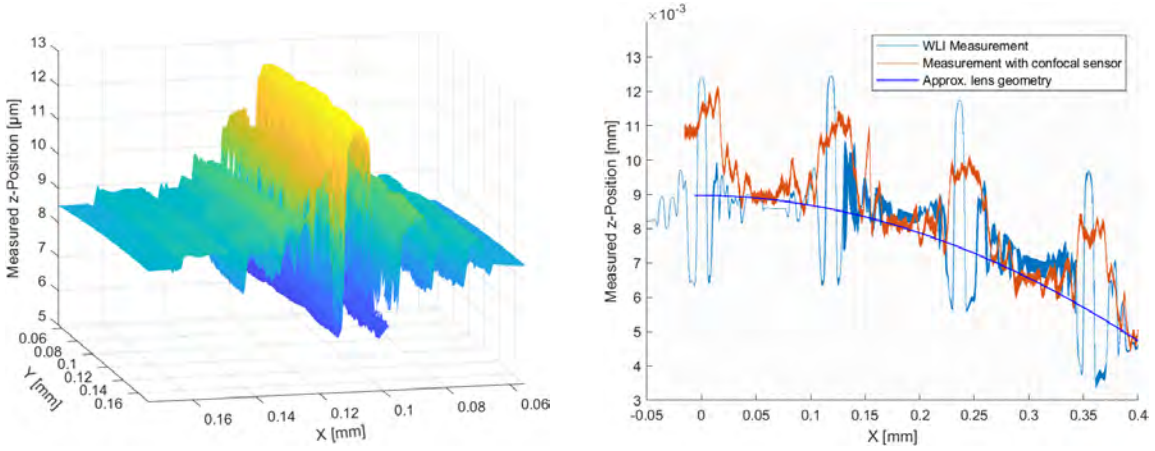

(a) (b)

Figure 7.19: Observation of oscillation phenomenon for WLI measurements of small structures on convex surfaces with anti reflective coating a) Surface plot of a WLI measurement of a line segement cured in a 10 µm layer on the peak of a convex substrate, b) Slice through WLI and confocal measurement of a line pattern on a convex surface

The phenomenon of the oscillation in the WLI measurement is assumed to be due to the anti-reflective (AR) coating for wavelengths between 420 and 760 nm of the used substrates. Since the coating is a different material than the substrate, the WLI fringes are affected due to a

spectral phase change between the AR and substrate material, leading to a nonlinear behavior of the measurement [28, p. 450]. Reflections on both the coating and substrate material can lead to a superposition of the fringes, resulting in a shift of the measured height [66]. Especially for narrow gap sizes, this can lead to a deviation of the measurement from the actual geometry. Therefore, the substrates are replaced by uncoated plano convex lenses with a similar radius of curvature (19.69 mm). The following figure 7.20 shows the resulting cross section of the measured geometries for a line pattern in a 5 µm photopolymer layer on an uncoated substrate without a compensation of focus position or curvature. The oscillation no longer occurs, and the structure geometry and cross section can be determined. In the analyzed segment of the lens, the expected change in the cross section from the simulation (figure 7.17) is observed. It can be seen that the peak of the measured structure moves towards the substrate center as the distance from the center increases, and a steep slope is formed at the right edge of the structures. The central structures show the same shape, height, and width range as for planar surfaces.

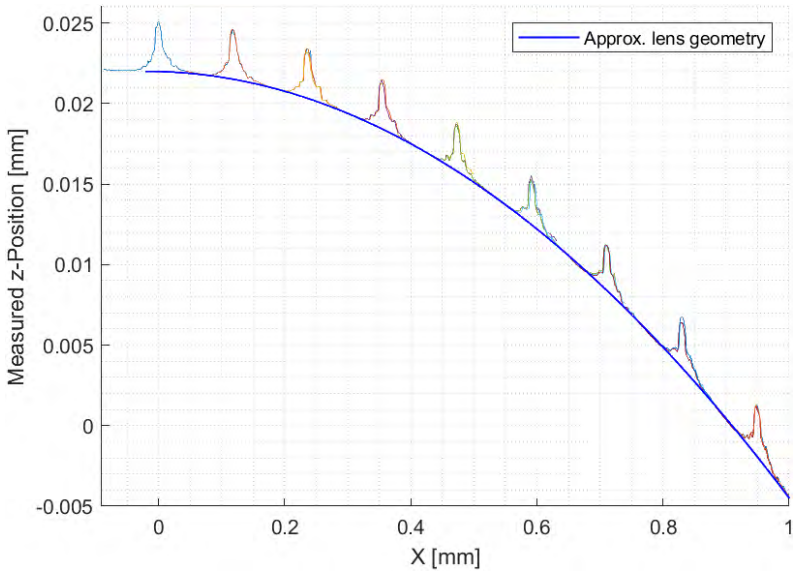

Figure 7.20: Slice through a WLI measurement of a line pattern with a line distance of 120 µm in a 5 µm PR48 layer on a substrate with radius of curvature of 19.69 mm without protective/anti-reflective coating

Based on these measurements, the maximum distance of structures from the substrate center at which the deviation of the curing geometry is still within the acceptable range is set at 0.4 mm for this type of lens. Above this distance, increased flank formation and peak shift are observed, which lead to undesirable results. This allows the substrate surface to be divided into 0.8 x 0.8 mm squares in which structures can be cured uniformly and where the influence of curvature leads to an acceptable shape deviation. To ensure accuracy in every curing direction and allow the possibility of structure curing with defined orientation to the surface to the incident beam, not only the focus position but also the orientation of the substrate to the beam needs to be adjusted. For this reason, the next section 7.3.1.1 presents initial results for the structure curing in 0.8 x 0.8 mm regions using hexapod rotation to cure perpendicular to the substrate surface.

7.3.1.1 Compensating of the Surface Curvature

This section presents the approach and the proof of concept of using the hexapod to cure structures perpendicular to a convex surface. This can be achieved by rotating the substrate around the center of curvature. The following figure 7.21 shows the implementation by shifting the hexapod coordinate system to the center of the radius of curvature. It is important to use the Work coordinate system of the hexapod for this (see chapter 3.9) to create a static point for the center of rotation. Using the geometric relationships in the curing setup with the determined focus position from chapter 7.1.2, the distance of the center point of the lens surface is determined to be 28.35 mm. Since the Work coordinate system is located on the surface of the hexapod carriage by default, a shift of the coordinate system of 8.66 mm is necessary when accounting for the radius of curvature to locate the coordinate system at the center of the radius of curvature. At this point, the substrate can be rotated around any of the three axes of the coordinate system and the surface of the substrate at the angle of rotation comes into focus.

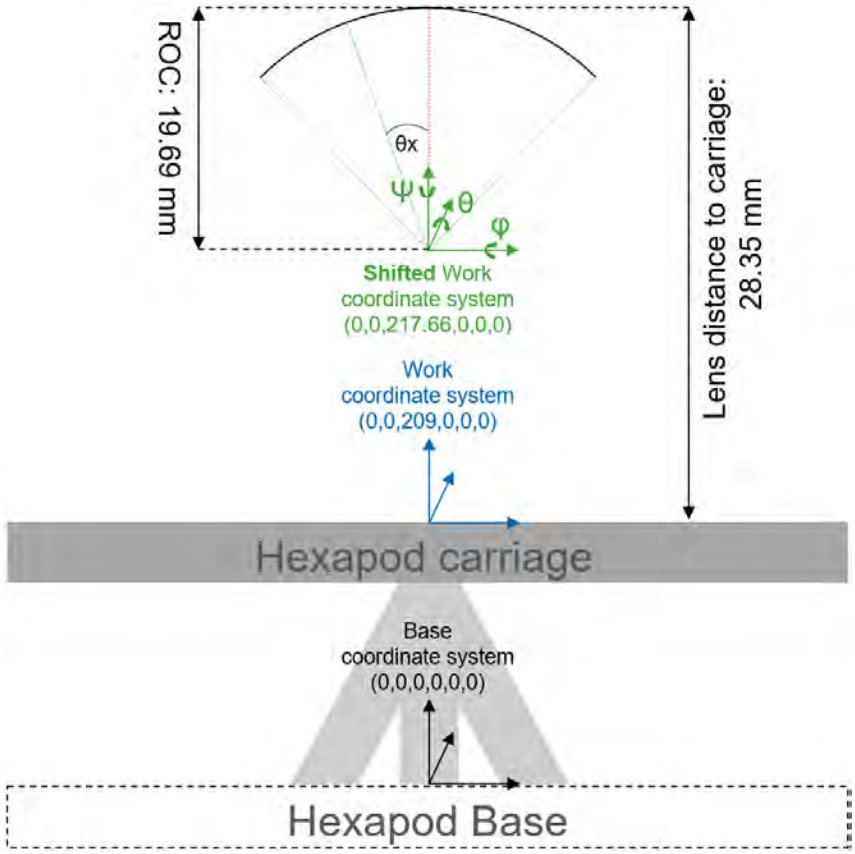

Figure 7.21: Schematic representation of determining the necessary shift of the hexapod coordinate system to rotate Substrates around the center of their radius of curvature (Here: for the used substrates with a radius of curvature of 19.69 mm)

To analyze and validate this approach, line patterns with a size of 0.8 x 0.8 mm are created with line orientations in x and y direction and cured at pitch and roll angles of $\pm 3°$ around the substrate center. This allows to see if the tilt correction using the hexapod is feasible and if the orientation of the structure influences the curing results. The following figure 7.22 shows

a picture of this pattern on a convex lens (Note: Picture is for an area of 2.5 x 2.5 mm for each pattern, to visualize structure orientation) and a top down view of WLI measurements for roll angles of -3, 0 and 3 ° in a 5 µm photopolymer layer. To analyze the quality of the cured structures and compare them to the results on planar surfaces, the spheric shape of the substrate is removed in the post processing software of the WLI. An observation made with this process is, that errors in the coating are a critical factor. It is observed that layers where pinholes form or which are contaminated with particles during handling and curing tend to collapse during the tilting, which can result in layer tearing and rendering the result unusable. The substrate after layer application needs to be handled with care and inspected for errors prior to the curing process to ensure the desired curing results. These measurements indicate a symmetric shape of the the structure cross section and a repeatability within a single pattern.

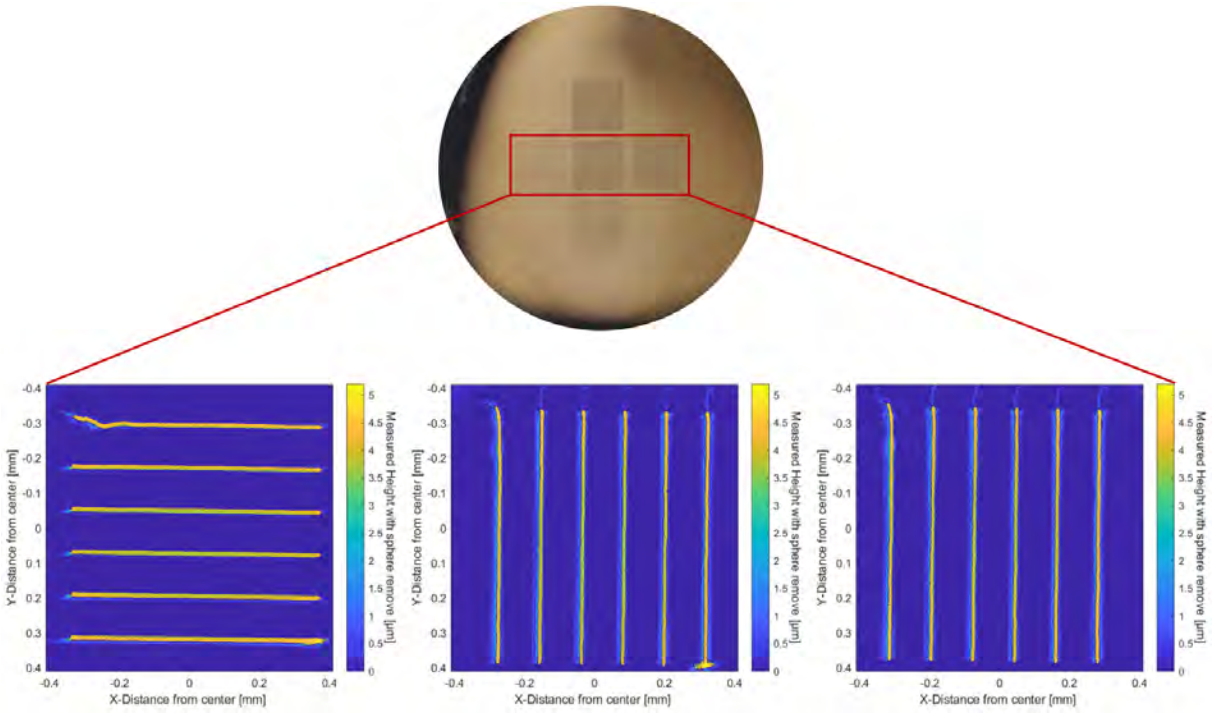

Figure 7.22: Picture of x- and y oriented line patterns on convex lens and WLI measurement of structures at roll angles of -3, 0 and 3°

To determine the feasibility of the tilt correction and determine the curing repeatability, the structure cross section is analyzed. When analyzing the cured structures cross section, it is seen that the cured structures with a tilted convex substrate show a comparable height and width as for curing on planar surfaces. The following figure 7.23 shows the cross section of the geometry for the measurement of the lines at a roll angle of +3 and - 3° in the figure above. Due to the retrograde surface correction, the surface of the substrate cannot be determined exactly, but still sufficiently accurate to get an understanding of the curing geometry. It is seen that the height of the cured structures for these measurements is between 3.55 and 4.2 µm, and the structures show a width between 18 and 26 µm. The repeatability of the structure height within a single substrate is observed to be below 1 µm. This repeatability within a single substrate is expectedly

slightly worse than for structures cured on planar surfaces due to the additional influence of the surface geometry and the repositioning of the substrate, which influences the positional accuracy and presumably leads to an altered material flow on the surface. For all structures within this measurement a range of curing heights between 3.4 and 4.3 µm and widths between 18 and 31 µm are determined, which are comparable to the results on planar surfaces. The influence of the curvature, i.e. the shift of the structure peak and flank formation is largely prevented, although a slight shift with steeper flank can be observed at the outermost lines. It is shown that repeatable and uniform structures can be cured at some distance from the substrate center by rotating the substrate around the center of its radius of curvature.

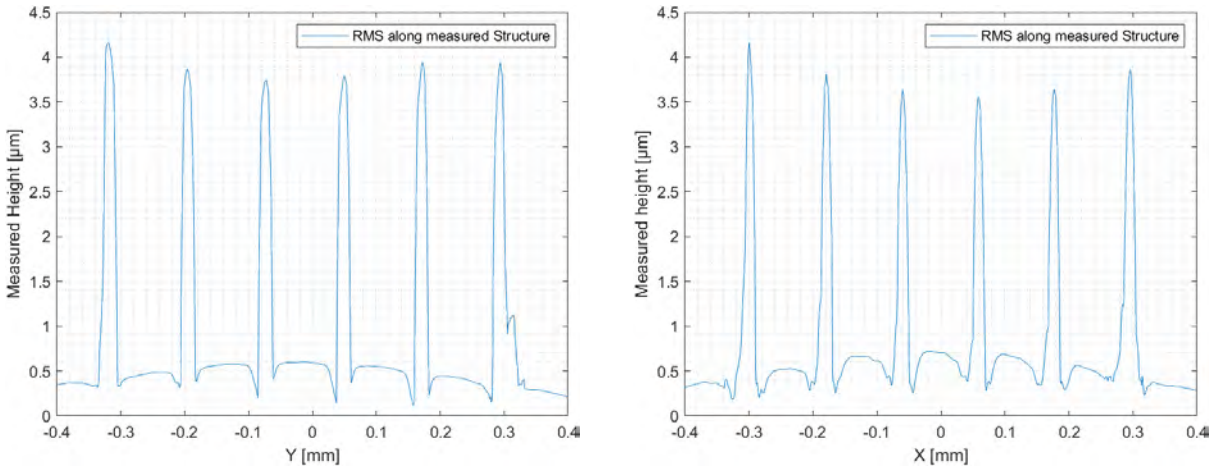

(a) (b)

Figure 7.23: Comparison of structure cross section for hexapod tilt correction of surface shape a) Averaged structure geometry of a sphere-removed WLI measurement for structures cured at a roll angle of -3°, b) Averaged structure geometry of a sphere-removed WLI measurement for structures cured at a roll angle of +3°

The measurements from this verify the effectiveness of correcting the surface shape with the hexapod and serve as a proof of concept for the possibility of curing repeatable geometries on convex surfaces by rotating the substrate around the center of the radius of curvature. Further steps to investigate the curing results and improve and automate the method for the compensation of the substrate geometry and functionalizing structures on convex substrates need to be taken.

7.3.2 Results and Conclusion

This subchapter presented the theoretical and experimental analysis of the influence of the curvature of a convex substrate on the curing results. It is shown that the surface curvature of convex substrates affects the beam shape and its intensity experienced by the substrate surface, if the focus position is not corrected to compensate the substrates sag height. The orientation of the incident laser beam to a surface affects the aspect ratio of the beam diameter experienced by the surface. Experiments show that these phenomena cause the structure peak to shift towards the center of the substrate and form a steep flank at the edge of the cured structures.

Furthermore, the incident angle of the beam to the surface influences the structure geometry depending on the curing direction. It is shown that an anti-reflective coating on the substrate surface can lead to errors in the measurement procedure with the WLI. On uncoated surfaces, for substrates with a radius of curvature of 19.69 mm, a maximum distance from the substrate center of 0.4 mm is determined, up to which the cured structures show acceptable cross-section repeatability and little to no peak shift or shoulder formation. This results in an area of 0.8 x 0.8 mm, in which structures can be cured without focus and orientation correction on the used substrates. The position of the center of the used substrates radius of curvature is determined relative to the hexapod carriage and the origin of the hexapod work coordinate system is set at this position. The substrate can be rotated around the axes of this coordinate system in order to focus on a point at a certain distance from the substrate center (i.e. angle) and to cure structures in an area of 0.8 x 0.8 mm around this point. A proof of concept of structure curing with correction of surface curvature is presented. These structures show comparable results regarding the height and width of the cured structures. However, the repeatability of the structure dimensions within a single substrate is worse due to the remaining influence of the surface curvature and repositioning of the substrate during the curing process. This is the final result in the present work. Further analysis and experiments are necessary, especially for the functionalization of convex surfaces. In the further course of this project an automation of the tilt correction using the hexapod to increase process dynamic and allow for the creation of larger elements is necessary.

7.4 Conclusion

This chapter presented the determination of parameters and analysis of curing results for structures cured in a defined photopolymer layer on planar and convex surfaces. A minimum voxel resolution of 333 points per millimeter to achieve structures with a homogenous cross section is determined, limiting the maximum scanning velocity to 15 mm/s. The best focal position is experimentally determined and correlated to the result from the focusing method (see chapter 6.3) to determine the offset from the expected focus position of the planar and convex substrates used in this work. The minimum necessary laser power, where structures cure to the maximum possible height is determined to be 100 µW for both 5 and 10 µm layers of PR48. It is observed that even with the nitrogen inerting chamber presented in chapter 6.2.1 the cured structures still do not fully polymerize the applied layer. The reason for this is presumably a combination of oxygen already diffused into the material during storage and spin coating and polymerization-induced material shrinkage during curing. This results in a range of structure heights between 2.5 – 4.5 µm (5 µm layer) and 6.9 to 9.5 µm (10 µm). Individual structures show a width of 20 to 30 µm. It is seen that the width of a structure increases significantly on the point of adhesion which can be attributed to the reflection of the impeding light on the surface of the substrate.
A minimum structure distance for individual features and a maximum structure distance for homogenous surface curing are determined. With a laser power of 100 µW the minimum dis-

tance for individual features in a 5 µm layer is determined to be 120 µm, for 10 µm layers this distance increases to 160 µm. With the determined parameters 2.5 D structure curing with predictable curing results on planar surefaces is possible. The repeatability of structure heights within one substrate is observed to be below 0.5 µm on planar surfaces. The functionalization of a surface is proven possible by curing a line grating on a microscope slide and creating a diffraction pattern by exposing this structure to a collimated light source.
The influence of the surface curvature on the expected curing result is analytically analyzed and experimentally verified. It is seen that the curvature of a substrate leads to a shift of the point with the maximum intensity towards the center of a substrate when the sag height is not compensated. In practice, this leads to an asymmetrical shape of the cured structures and the formation of a steep flank. The beam shape experienced by the substrate surface becomes more and more elliptical with increasing distance from the substrate center even with compensation of the sag height, due to orientation of the incident beam to the surface. Since the orientation of this elliptical deformation of the beam shape on the surface is dependent on position of the beam on the substrate, the achievable structure size becomes dependent on the scanning direction. These effects are shown to be significant above a distance of 0.4 mm from the substrate center for the used substrates with a radius of curvature of 19.69 mm. To compensate the influence of the surface curvature, a method for compensating the substrate curvature and orientation of the surface to the incident beam using the hexapod is presented. The curvature of the surface is compensated by rotating the substrates around the center of their radius of curvature. The feasibility of this method is proven experimentally. The resulting structures show comparable dimensions to structures cured on planar surfaces when using the curvature compensation method for 0.8 x 0.8 mm areas on the substrate surface. The dimensional repeatability for structures cured on convex substrates is seen to be slightly worse than for results on planar substrates. The deviation in structure height on a single substrate is shown to be up to 1 µm.

8 Conclusion

In this work, the development and experimental verification of a system for layer application and structure curing on planar and convex surfaces is presented. It is shown that with this system it is possible to cure micronscale structures and functionalize surfaces. This chapter summarizes the most important results and observations from this work.

In order to obtain defined layer heights on substrates, the spin coating process is chosen and evaluated. A measurement method for transparent layers on both planar and convex surfaces with a WLI is developed and verified. With this method it is possible to determine the layerheight in a 3.03 x 3.03 mm area on the surface of a substrate. The spin coating method is analyzed and optimized for use with microscope slides and convex lenses with a radius of curvature of 19.5 mm using the PR48 prototyping photopolymer. A mathematical model of the material distribution on surfaces during spin coating is presented and an optimization of the spin coating parameters is derived. It is shown that for stable coatings which are homogeneously distributed on the surface, substrate surface activation becomes necessary to improve the wettability of the surface and to counteract layer contraction due to surface tension. With the implementation of surface activation using oxygen plasma, defined layerheights between 5 and 30 µm are achieved on planar surfaces with an accuracy below 650 nm and a repeatability of below 800 nm. For convex surfaces it is shown that due to material flow along the curvature (for the used substrate with radius of curvature 19.5 mm) a time unstable layer is created and only layers smaller than 10 µm are possible. Coating parameters for a layerheight of 5 and 10 µm are determined experimentally. The applied layer with these parameters can be used in a defined time window of two minutes at a specific time after the coating process. This makes it possible to apply defined layers on the substrates used, which have an accuracy below 750 nm and a repeatability of 800 nm within a two-minute timeframe that needs to be individually determined for a desired layerheight.

A modular lithography setup is presented, which allows to cure structures as a stand-alone system as well as offering the possibility to integrate a 6 DOF hexapod. The use of the hexapod allows to orient the substrate relative to the incident beam, which is used to compensate the geometry of non-planar substrates. A multifunctional substrate holder is developed to accommodate microscope slides and convex substrates, as well as to enable beam focusing. The substrate holder also serves as a holder for an intertchamber, which allows a volume around the substrate to be flooded with an inert gas, in this case nitrogen, during the curing process to mitigate the influence of oxygen inhibition on the curing results. This allows the oxygen concentration in the inert chamber to be reduced to below 0.5 % within 180 seconds. The determination of the focus point relative to the hexapod z-coordinate by using a photodiode sensor for measuring laser power and a 5 µm pinhole is presented. The determination of the focus position is automated and shows a positional repeatability of less than 160 µm for the focus determination.

The lithography setup is used to cure micronscale structures in defined photopolymer layers. To achieve uniform structure cross sections, a minimum number of voxels per millimeter of 333 is determined, which limits the maximum scan speed of the setup to 15 mm/s due to the sampling rate of the DAQ card. An offset of the optimal focus position for the used substrates to the position determined using the pinhole method is determined. This allows the focus position to be determined for substrates in the substrate holder in any setup configuration, when the system is readjusted, and for arbitrarily positioned hexapod coordinate systems. The necessary laser power to ensure complete structure curing in 5 and 10 µm PR48 layers is determined experimentally to be 100 µW. It is observed that the height of the cured structures is significantly lower than the thickness of the applied photopolymer layer. It is assumed that is due to a combination of oxygen already diffused into the material during storage and spin coating and polymerization-induced material shrinkage during curing. This results in a range of structure heights between 2.5 – 4.5 µm (5 µm layer) and 6.9 to 9.5 µm (10 µm). However, the repeatability within one substrate is observed to be below 0.5 µm. Individual structures show a width between 20 to 30 µm. It is seen that the width of a structure increases significantly on the point of adhesion, which affects the minimum distance between two structures so that no cross-linking occurs between them. For 5 µm layers the minimum distance for individual features is determined to be 120 µm, for 10 µm this distance increases to 160 µm. Experimental results for the structure curing of structures on planar and convex surfaces are presented. Surface functionalization is achieved by curing and evaluating a line grating on a microscope slide. The influence of the surface curvature of convex substrates on the expected curing result is analyzed and experimentally determined. As a result, a range of 0.8 x 0.8 mm is determined in which the influence of the surface curvature is small enough to cure repeatable structures on the substrates used in this work. In this range, structure dimensions comparable to those on planar surfaces are observed. Only the repeatability of the structure height with 1 µm shows larger deviations than on planar surfaces due to the substrate curvature and measurement method. Using the hexapod, a method is presented which allows to compensate the curvature of a convex surface by rotating it around the center of the radius of curvature. It is shown that this method can be used to cure repeatable structures on convex surfaces which are oriented to the incident beam.
With the developed system and the reported methods and results, a possibility for repeatable laser lithographic fabrication of micronscale structures and surface functionalization on planar and convex surfaces in defined photopolymer layers in the range of tens of micrometers is created. The following chapter 9 gives an outline of the further steps necessary in this project to improve and automate the function and precision of the system and to enable functionalization of surfaces with enhanced optical properties and gray scaling by applying multiple layers.

9 Outlook

This chapter describes the next steps towards automated layer application and surface functionalization on planar and non-planar surfaces. For this purpose, necessary optimizations of the setup and the process as well as further experiments that proved to be necessary in the course of the project are presented. To enable more freedom of design and enable the possibility of manufacturing gray scale holographic optical elements, the topic of applying multiple layers needs to be examined and evaluated for the spin coating process. Finally, the necessary steps towards an automated layer application and curing process are presented. The next subchapter describes the optimizations and experiments that have shown to be necessary in the course of this work.

9.1 Improvement of the lithography Setup and Curing Process

The next logical step in the course of this project is the continuation of the investigation and curing of structures on convex surfaces. Since only a proof of concept of the orientation-dependent surface correction was possible due to time constraints, further experiments on the characterization and functionalization of surfaces are required here. For this purpose, a measurement method must be developed to reliably determine the structure geometry and substrate surface, since the method of subsequent sphere removal in chapter 7.3.1 only allows an estimate of the structure height. The structure quality can then be analyzed. Finally, further experiments on curing functionalized surfaces should be carried out and the results need to be evaluated. This requires the integration of the curvature correction into the python software in order to correct the position of the hexapod depending on the substrate geometry. That not only leads to increased system dynamics and therefore to less influence of the material flow on the repeatability of the structures, but also allows to cure continuous structures beyond the maximum dimensional limits of 0.8 x 0.8 mm determined in chapter 7.3.1. In this case, an analysis of the polymer cross-linking at the transition between two differently oriented structures is necessary to analyze the structure continuity.
During the experiments on structure curing in chapter 7, it is shown that the structure height is significantly lower than the applied layerheight. This phenomenon is assumed to be due to a combination of polymerization-induced shrinkage and residual oxygen inhibited in the material. To test this hypothesis and to verify the individual influence of the two phenomena, it would be useful to perform curing and coating tests in an oxygen-free environment (e.g. a glovebox filled with an inert gas). As a result, the influence of oxygen inhibition could be excluded as a factor and the influence of material shrinkage on the curing height can be characterized.

When analyzing cured structures in chapter 7.2, it is noticed that especially in areas with a high intensity density (see 'Hochschule Aalen' structure in figure 7.15) a polymerization is observed along the travel path of the laser beam between non-adjacent points of a cured structure. This is because the photopolymer experiences a low exposure dose when skipping to a new point along the travel path. A combination of this exposure and the exposure by light diffusion into the surrounding material at points where curing occurs can lead to polymerization of the travel path. This affects the quality of the cured structures. To prevent this, an external laser shut off mechanism must be implemented. For example, an acousto-optic modulator (AOM) could be used, which, when integrated into the setup and control software, provides a quick and easy way to position the laser beam outside the input angle of the scan lens and act as a shut off mechanism. As a result, the travel path can be displaced with the Galvo mirrors without exposure of the material to ensure more reliable curing of only the desired geometry. A method using an AOM would also allow for the possibility to modulate the laser power during the curing process.
The final improvement of the setup would be the implementation of an in-situ focusing method. For example, by using a beam splitter in the focused beam path, the reflection intensity of the laser beam on the substrate surface could be continuously monitored using a (CCD) camera chip during the curing process. This offers the possibility to dynamically adjust the position of the focus point, especially on non-planar surfaces, during the curing process and to correct it if necessary. As a result, the reliability of the focus position relative to the substrate or layer surface would be significantly optimized. Furthermore, with this method, the focus position for new substrates does not have to be determined experimentally first, and it is directly possible to use substrates with different shapes, such as concave lenses or even free-form substrates, and cure structures on them.
In order to have more freedom in the creation of functionalized surfaces, the next subchapter presents the necessary steps for the application and curing of multiple photopolymer layers.

9.2 Multilayer Application

In order to be able to cure 3-dimensional structures and to extend the possibilities for surface functionalization, it is necessary to apply multiple layers to already cured structures. This means that not only binary structures can be cured, but also structures with variable optical density can be produced by selective higher curing of structure elements. Therefore, by applying multiple layers, the possibility of gray scale curing is created, which offers a wide range of functionalization options, such as the fabrication of holographic optical elements. Therefore, it is necessary to create a process for the layer application over topographies. When analyzing the theory and results of spin coating over topography it has been shown by Peurrung et. al [55, 56] that the material distribution of a thin photoresist film is expected to follow the underlying geometry of a topography on a planar surface. In their work they present an analytical model for the expected material distribution of a positive photoresist layer over micron scale topographies during the spin coating process. An experimental verification of this model is shown in the

following figure 9.1, where in-situ measurements of the layerheight and shape over time during the spin coating process on square topographies with an edge length of 100 µm (figure 9.1a) and 500 µm (figure 9.1b) are shown. In their work [55] they show that the wider a structure is, the more the material distribution in a layer follows the geometry. Nevertheless, a flank is always formed at the edges due to material flow. It is shown that for structures larger than 500 µm a homogeneous layer can be generated over a large part of the topography. [55, 56]

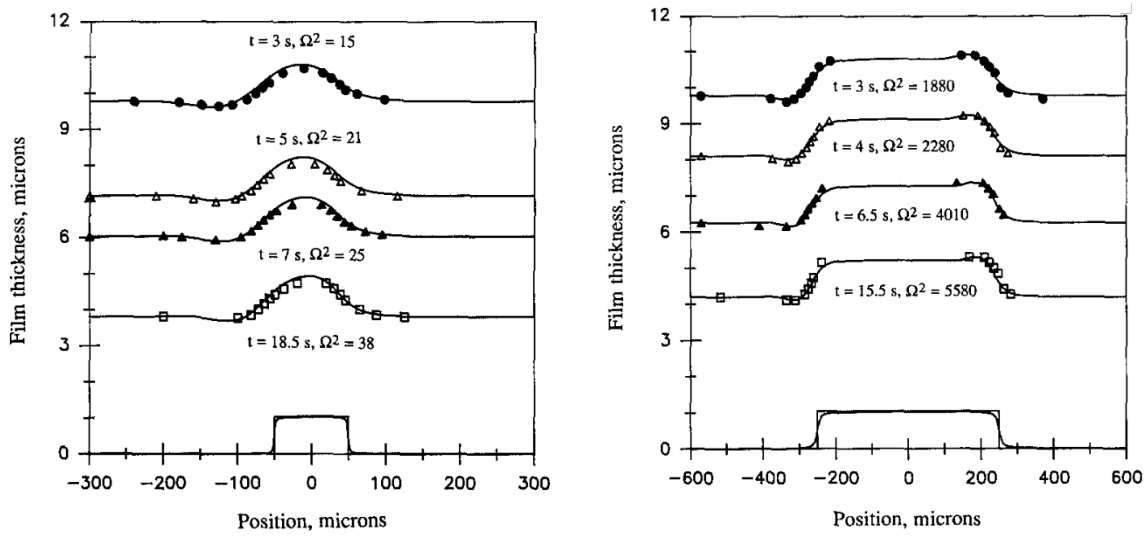

Figure 9.1: Analysis of material distribution over topography during the spin coating process for a positive photoresist [55] a) Cross section of material distribution over a 100 x 100 µm square, a) Cross section of material distribution over a 500 x 500 µm square

Initial coating tests with the PR48 photopolymer used in this work show that for non-drying layers (i.e. negative photoresists), the material flow immediately after the coating process causes the photopolymer to flow off the structure and leave a drop on the structure surface. The following figure 9.2 shows the layer distribution of a PR48 film coated with parameters for a 5 µm layerheight on a 2.5 x 2.5 mm square structure (in red). It is seen that a homogeneous layer has formed outside the structure and a droplet formation can be observed on the topography. This results in a non-uniform layer that is significantly higher than the expected layerheight of 5 µm on top of the square. This observation shows that the feasibility of the spin coating process for the deposition of photopolymer layers over topographies needs to be evaluated. The applicability of the spin coating process needs to be tested, especially for narrow free standing structures.

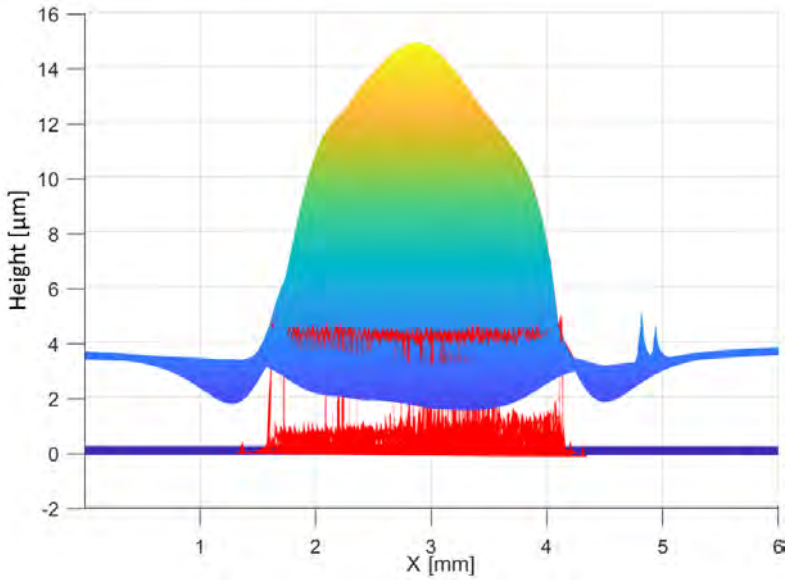

Figure 9.2: Combination of WLI measurements for a 2.5 x 2.5 mm square structure and a PR48 coating, spin coated with parameters for a layerheight of 5 µm

Another observation made during these initial recoating attempts is that the frequency of pinhole errors (see chapter 3.6.4) increases significantly. One reason for this is that surface cleaning of substrates on which structures are cured is difficult to perform. The substrates were cleaned by spinning isopropanol and the treatment with the plasma pen, which is significantly less effective than the cleaning method presented in chapter 4.3. Another important influence on the formation of pinholes is the air turbulence and surface texture of the topography over which the curing is performed. A turbulent flow of air increases the likelihood of air bubbles diffusing into the material and the surface roughness of the topography acts as a nucleation side, where these bubbles attach. The literature (Gupta et. al [21]) shows that this phenomenon can be mitigated by introducing an inert gas flow perpendicular to the surface, which displaces air and leads to laminar flow where it meets the substrate. The following figure 9.3 shows the results of a first experiment where nitrogen is introduced centrally above the surface during spin coating. The figure shows the surface topography of a recoated substrate without nitrogen flow and the result with the introduction of the gas flow. It is seen that this measure leads to a significant reduction in the pinhole density on the entire substrate, but especially in the center where the nitrogen flow is applied. This shows that a method for inert gas introduction during the coating process becomes necessary. The effectiveness of this method for defect-free coating application and the influence of substrate cleaning need to be evaluated.

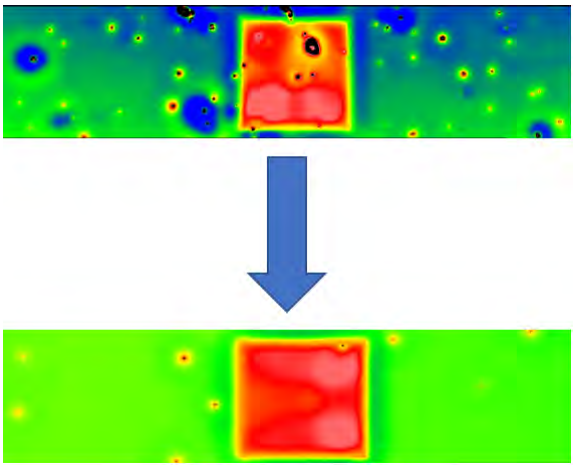

Figure 9.3: Layer topography before and after the introduction of nitrogen purging to mitigate pinhole formation

The literature review and initial experiments on the topic of multilayer application and spin coating over topography indicate that an evaluation of the feasibility of spin coating as a layer application method on topographies is needed and that alternative methods may need to be considered. Especially for free standing and discontinuous structures the spin coating process has to be analyzed. The surface cleaning and its influence on the coating results must be evaluated and a possibility for repeatable inert gas injection during the spin coating process must be created to prevent the formation of pinholes in the layer.
Since the ultimate goal of this project is to develop an automated and user-friendly process for layer application and structure curing on planar and non-planar surfaces, the next subchapter describes necessary steps towards process automation.

9.3 Process Automation

The first step towards an automated curing process is the integration of the hexapod control into the software. Until now, the orientation and focusing with the hexapod is done individually for one substrate and one orientation via the web interface or a Matlab script. The integration into the python software allows, as mentioned above in subchapter 9.1, an automatic positioning and orientation of substrates to the incident beam for curing structures over a larger surface areas, which is necessary for the functionalization of surfaces. Through the integration, a method for automatic coordinate calculation can be developed for individual surface segments depending on the substrate geometry and structure dimensions. Furthermore, the current and future focus method can be integrated into the software. This allows to design a single user interface for the whole curing process and to automate functions like curvature correction, coordinate calculation for curved surfaces and focusing.
Since the ultimate goal of the project is to create a completely automated process for layer application and surface structuring, the final step in process automation is the automation of layer deposition and substrate handling and their integration with the lithography setup. For this

purpose, a modular setup with industrial robots is required to perform the individual steps in an automated way. To have enough space for substrate positioning, the lithography setup must also be integrated with a robot. This not only allows the automation of the layer application and substrate handling with a second robot, but also offers additional freedom in the orientation of the lithography system to the substrate. The following figure 9.4 shows a schematic of the desired setup for automated layer application and structure curing. The main functionalities are numbered from 1 to 3. The first desired functionality (1) of the setup is the defined layer application and substrate positioning using a 6 DOF robot. The second functionality (2) is the orientation of the lithography system to the substrate using a robot. The third part of the setup (3) is the orientation of the curing system to cure perpendicular to the substrate surface and laser focusing using the hexapod.

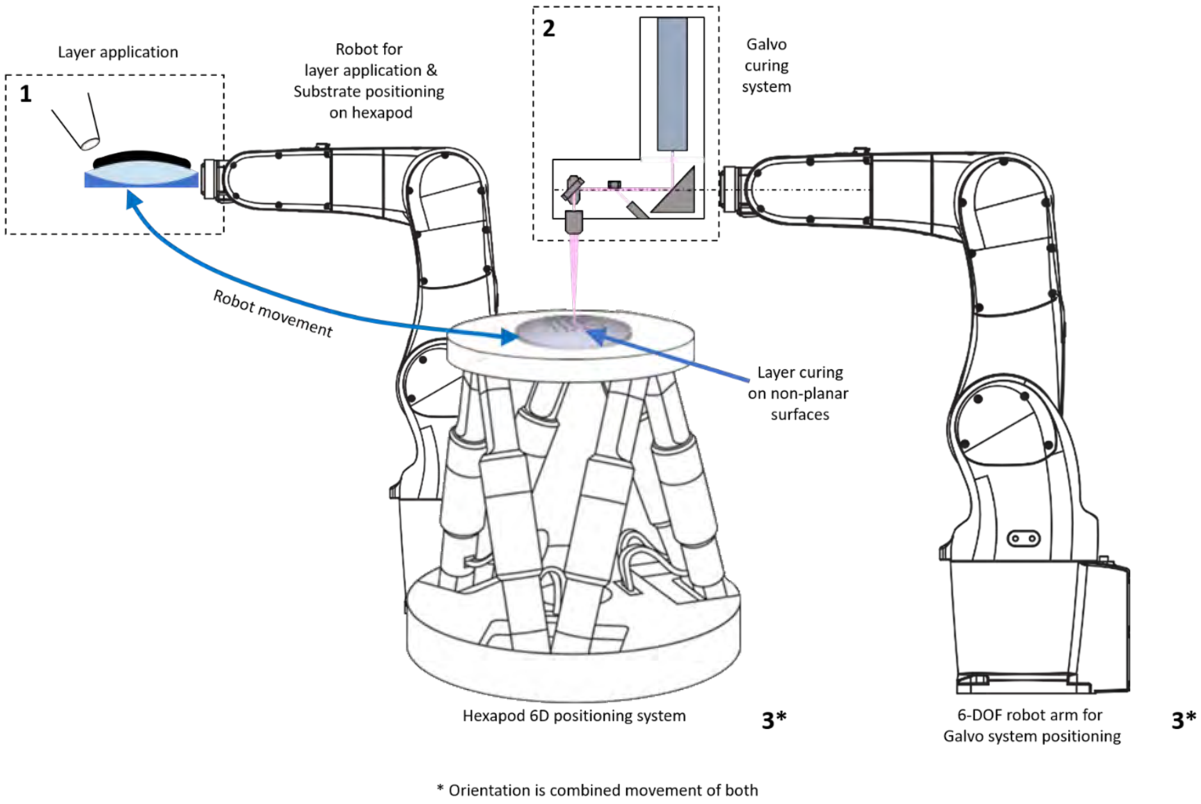

Figure 9.4: Schematic of the desired final curing setup with two 6-axis robots for layer application and positioning of the lithography setup and hexapod for positioning of the substrate

The development of this setup is the final step towards achieving the project goal for an automated process to cure functionalized structures in multiple photopolymer layers on planar and convex surfaces using a laser lithography setup based on a two mirror galvanometer scanning system.

Bibliography

[1] Ai, J., Du, Q., Qin, Z., Liu, J., Zeng, X.: Laser direct-writing lithography equipment system for rapid and mum-precision fabrication on curved surfaces with large sag heights. Optics express **26**(16), 20965–20974 (2018). DOI 10.1364/OE.26.020965

[2] AlQattan, B., Yetisen, A.K., Butt, H.: Direct laser writing of nanophotonic structures on contact lenses. ACS nano **12**(6), 5130–5140 (2018). DOI 10.1021/acsnano.8b00222

[3] Arceneaux, J.A.: Mitigation of oxygen inhibition in uv led, uva, and low intensity uv cure (2015). URL `https://uvebtech.com/articles/2015/mitigation-of-oxygen-inhibition-in-uv-led-uva-and-low-intensity-uv-cure/`

[4] Bauer, W., Weber, M., Chanbai, S.: White light interferometry. In: Q.J. Wang, Y.W. Chung (eds.) Encyclopedia of Tribology, pp. 4115–4127. Springer US, Boston, MA (2013). DOI 10.1007/978-0-387-92897-5{\textunderscore}320

[5] Bibin, J.: Spin coating on a curved surfaces

[6] Boudrioua, A.: An introduction to organic lasers. Elsevier, London, England and Oxford, England (2017). URL `https://ebookcentral.proquest.com/lib/kxp/detail.action?docID=4913721`

[7] Chartoff, R.P.: Linear Shrinkage Of Stereolithography Resins. University of Texas at Austin (1995). DOI 10.15781/T25H7CD0C. URL `https://repositories.lib.utexas.edu/handle/2152/69333`

[8] Chemat Scientific: Spin coating technology (2016). URL `http://www.chematscientific.com/uploadfiles/2016/11/spincoating-introduction.pdf`

[9] Cody, D., Moothanchery, M., Mihaylova, E., Toal, V., Mintova, S., Naydenova, I.: Compositional changes for reduction of polymerisation-induced shrinkage in holographic photopolymers. Advances in Materials Science and Engineering **2016**, 1–11 (2016). DOI 10.1155/2016/8020754

[10] Duclos, A.M., Jézéquel, J.Y., Corbel, S., André, J.C.: Industrial photochemistry xxii. simulation model of the warping of a bar made by laser photopolymerization. Journal of Photochemistry and Photobiology A: Chemistry **78**(1), 85–96 (1994). DOI 10.1016/1010-6030(93)03703-J

[11] Ebnesajjad, S.: Adhesive coating and lamination of polyvinyl fluoride films. In: Polyvinyl Fluoride, pp. 213–249. Elsevier (2013). DOI 10.1016/B978-1-4557-7885-0.00009-0

[12] Edmund Optics: 25.4mm dia. x 38.1mm fl, uncoated, plano-convex lens: Cad zeichnung (-)

[13] Emslie, A.G., Bonner, F.T., Peck, L.G.: Flow of a viscous liquid on a rotating disk. Journal of Applied Physics **29**(5), 858–862 (1958). DOI 10.1063/1.1723300

[14] Feng, X.G., Sun, L.C.: Mathematical model of spin-coated photoresist on a spherical substrate. Optics express **13**(18), 7070–7075 (2005). DOI 10.1364/OPEX.13.007070

[15] Fuerst, M.E., Csencsics, E., Haider, C., Schitter, G.: Confocal chromatic sensor with an actively tilted lens for 3d measurement. Journal of the Optical Society of America. A, Optics, image science, and vision **37**(9), B46–B52 (2020). DOI 10.1364/JOSAA.394212

[16] Gayan Adikari Appuhamillage: New 3d printable polymeric materials for fused filament fabrication (fff) (2018). DOI 10.13140/RG.2.2.31264.43526

[17] Gebhardt, A., Kessler, J., Thurn, L.: 3D Printing: Understanding Additive Manufacturing, 2nd edition edn. Hanser Publications, Cincinnati, Ohio (2018)

[18] Gilson: Guide to pipetting: Third edition (2019). URL `https://de.gilson.com/pub/media/docs/2019_Guide_to_Pipetting_LT800550-F_compressed.pdf`

[19] Glenn Elert: Viscosity. The Physics Hypertextbook (2021). URL `https://physics.info/viscosity/`

[20] Gong, L., Xiang, L., Zhang, J., Chen, J., Zeng, H.: Fundamentals and advances in the adhesion of polymer surfaces and thin films. Langmuir : the ACS journal of surfaces and colloids **35**(48), 15914–15936 (2019). DOI 10.1021/acs.langmuir.9b02123

[21] Gupta, S., Kulbak, M., Cahen, D.: Pin-hole-free, homogeneous, pure cspbbr3 films on flat substrates by simple spin-coating modification. Frontiers in Energy Research **8**, 897 (2020). DOI 10.3389/fenrg.2020.00100

[22] Häfner, M., Pruss, C., Osten, W.: Laser direct writing. Optik & Photonik **6**(4), 40–43 (2011). DOI 10.1002/opph.201190387

[23] Häfner, M., Reichele, R., Pruss, C., Osten, W.: Laser direct writing of diffractive structures on curved surfaces (2012)

[24] Han, S.: Modeling and analysis of extrusion-spin coating : an efficient and deterministic photoresist coating method in microlithography (1972). URL `https://dspace.mit.edu/handle/1721.1/8694`

[25] Hellstrom, S.L.: Basic models of spin coating: (submitted as coursework for physics 210, stanford university, autumn 2007) (2007)

[26] Henreich, P.: Investigation and calculation of the curing results cured with a direct-laser-writing setup (03.2021)

[27] Henreich, P.: Development and verification of a test setup for direct-laser-writing using a two-mirror galvanometer system (11.09.2020)

[28] Ida, N., Meyendorf, N. (eds.): Handbook of advanced nondestructive evaluation. Springer Nature eReference Engineering. Springer, Cham (2019). DOI 10.1007/978-3-319-26553-7

[29] Jacobs, P.F.: Fundamentals of stereolithography (1992). URL https://repositories.lib.utexas.edu/handle/2152/64400

[30] Jones, C.: How sensors work: Comparison of non-contact displacement sensor technologies. URL https://www.sensorland.com/HowPage098.html

[31] Karalekas, D., Aggelopoulos, A.: Study of shrinkage strains in a stereolithography cured acrylic photopolymer resin. Journal of Materials Processing Technology **136**(1-3), 146–150 (2003). DOI 10.1016/S0924-0136(03)00028-1

[32] Karalekas, D., Rapti, D., Gdoutos, E.E., Aggelopoulos, A.: Investigation of shrinkage-induced stresses in stereolithography photo-curable resins. Experimental Mechanics **42**(4), 439–444 (2002). DOI 10.1007/BF02412150

[33] Keyence: Coating & dispensing technology: Shaping the future of automation (2019)

[34] Kim, Y.G., Rhee, H.G., Ghim, Y.S.: Real-time method for fabricating 3d diffractive optical elements on curved surfaces using direct laser lithography. The International Journal of Advanced Manufacturing Technology **114**(5-6), 1497–1504 (2021). DOI 10.1007/s00170-021-06862-5

[35] Korkin, A. (ed.): Nanoelectronics and photonics: From atoms to materials, devices, and architectures ; [tutorial lectures at NGC2007 in Phoenix, Arizona, 2007. Nanostructure science and technology. Springer, New York, NY (2008). URL http://swbplus.bsz-bw.de/bsz278788521cov.htm

[36] Korzec, D., Hoppenthaler, F., Andres, T., Burger, D., Werkmann, A., Nettesheim, S., Puff, M.: piezobrush prz3: Part i: operation principle and characteristics (2020). URL https://www.relyon-plasma.com/wp-content/uploads/2020/11/201024_whitepaper_piezobrush_PZ3_1.pdf

[37] Koseki, K., Sakamaki, H., Jeong, K.M.: In situ measurement of shrinkage behavior of photopolymers. Journal of Photopolymer Science and Technology **26**(4), 567–572 (2013). DOI 10.2494/photopolymer.26.567. URL https://www.jstage.jst.go.jp/article/photopolymer/26/4/26_567/_article/-char/ja/

[38] L. E. Scriven: Physics and applications of dip coating and spin coating. MRS Online Proceedings Library (OPL) **121** (1988). DOI 10.1557/PROC-121-717

[39] Ligon, S.C., Husár, B., Wutzel, H., Holman, R., Liska, R.: Strategies to reduce oxygen inhibition in photoinduced polymerization. Chemical reviews **114**(1), 557–589 (2014). DOI 10.1021/cr3005197

[40] Mendes-Felipe, C., Oliveira, J., Etxebarria, I., Vilas-Vilela, J.L., Lanceros-Mendez, S.: State-of-the-art and future challenges of uv curable polymer-based smart materials for printing technologies. Advanced Materials Technologies **4**(3), 1800618 (2019). DOI 10.1002/admt.201800618

[41] Micro Epsilon: Confocaldt: Confocal chromatic measuring system: Datasheet (-). URL https://www.micro-epsilon.com/download/products/cat-confocal/dax--confocalDT-IFS2405--en-us.html

[42] Montazer, M., Harifi, T.: Nanosurface activation. In: M. Montazer, T. Harifi (eds.) Nanofinishing of Textile Materials, pp. 65–82. Elsevier (2018). DOI 10.1016/B978-0-08-101214-7.00005-4

[43] Mrsic, I., Bäuerle, T., Ulitzsch, S., Lorenz, G., Rebner, K., Kandelbauer, A., Chassé, T.: Oxygen plasma surface treatment of polymer films—pellethane 55de and epr-g-vtms. Applied Surface Science **536**, 147782 (2021). DOI 10.1016/j.apsusc.2020.147782

[44] Mulik, S., Sotiriou-Leventis, L., Leventis, N.: Adhesion enhancement of polymeric films on glass surfaces by a silane derivative of azobisisobutyrinitrile (aibn). Polymer Preprints (2008,49(2)), 498–499 (2008). URL https://core.ac.uk/download/pdf/229032893.pdf

[45] N. Pham, E. Boellard, P. Sarro, J. Burghartz: Spin , spray coating and electrodeposition of photoresist for mems structures – a comparison (2000). URL https://www.semanticscholar.org/paper/Spin-%2C-Spray-coating-and-Electrodeposition-of-for-%E2%80%93-Pham-Boellard/f7a3478abfaaddb64710c364da2efe46cd93a5ce

[46] National Instruments: Specifications ni usb-6001: Low-cost daq usb device (2014). URL https://www.ni.com/pdf/manuals/374369a.pdf

[47] Newport: Motion in 3-d: Newport hexapod coordinate systems: Technical note (2012)

[48] Newport: 6-axis-parallel kinematic positioning systems: Hxp100 hexapods: Datasheet (2018)

[49] Nguyen, D.T.T., Do, M.T., Li, Q., Tong, Q.C., Au, T.H., Lai, N.D.: One-photon absorption-based direct laser writing of three- dimensional photonic crystals. In:

A. Vakhrushev (ed.) Theoretical Foundations and Application of Photonic Crystals. InTech (2018). DOI 10.5772/intechopen.71318

[50] Norrman, K., Ghanbari-Siahkali, A., Larsen, N.B.: 6 studies of spin-coated polymer films. Annual Reports Section "C" (Physical Chemistry) **101**, 174 (2005). DOI 10.1039/b408857n

[51] O'Kane, M.: Solution-processing techniques: a comparison. URL `https://www.ossila.com/pages/solution-processing-techniques-comparison`

[52] Onanuga, T.: Process modeling of two-photon and grayscale laser direct-write lithography. Friedrich-Alexander-Universität Erlangen-Nürnberg (FAU), Erlangen (2019)

[53] OPM: Principle of operation confocal sensor. URL `http://www.opm-messtechnik.de/e_ap-k.htm`

[54] Ossila: Spin coating: complete guide to theory and techniques. URL `https://www.ossila.com/pages/spin-coating`

[55] Peurrung, L.M., Graves, D.B.: Film thickness profiles over topography in spin coating. Journal of The Electrochemical Society **138**(7), 2115–2124 (1991). DOI 10.1149/1.2085935

[56] Peurrung, L.M., Graves, D.B.: Spin coating over topography. IEEE Transactions on Semiconductor Manufacturing **6**(1), 72–76 (1993). DOI 10.1109/66.210660

[57] Pil, A.: Optische precisie op de nanometer. Mechatronica&Machinebouw (7) (2018). URL `https://mechatronicamachinebouw.nl/artikel/optische-precisie-op-de-nanometer/`

[58] Pipette.com: Guide to pipetting: Understanding pipettes (2021). URL `https://www.pipette.com/public/staticpages/guidetopipetting.aspx?menuid=493`

[59] Polos: Faq: Do i need to nitrogen purge

[60] Prabhakaran, P.: An introduction to direct laser writing (dlw) (2017)

[61] Quan, H., Zhang, T., Xu, H., Luo, S., Nie, J., Zhu, X.: Photo-curing 3d printing technique and its challenges. Bioactive materials **5**(1), 110–115 (2020). DOI 10.1016/j.bioactmat.2019.12.003

[62] Radtke, D., Duparré, J., Zeitner, U.D., Tünnermann, A.: Laser lithographic fabrication and characterization of a spherical artificial compound eye. Optics express **15**(6), 3067–3077 (2007). DOI 10.1364/OE.15.003067

[63] Radtke, D., Zeitner, U.D.: Laser-lithography on non-planar surfaces. Optics express **15**(3), 1167–1174 (2007). DOI 10.1364/OE.15.001167

[64] Reicher, H., Petrica, M., Pesendorfer, F.: Effect of surface modification of glass substrates on adhesive strength of copper coatings. International Journal of Surface Science and Engineering **9**(5), 436 (2015). DOI 10.1504/IJSURFSE.2015.072065

[65] relyon plasma: Glossary: Surface treatment (2020)

[66] Roy, M., Cooper, I., Moore, P., Sheppard, C., Hariharan, P.: White-light interference microscopy: effects of multiple reflections within a surface film. Optics express **13**(1), 164–170 (2005). DOI 10.1364/OPEX.13.000164

[67] Sahu, N., Parija, B., Panigrahi, S.: Fundamental understanding and modeling of spin coating process: A review. Indian Journal of Physics **83**(4), 493–502 (2009). DOI 10.1007/s12648-009-0009-z

[68] Saive, R., Bukowsky, C.R., Atwater, H.A.: Three-dimensional nanoimprint lithography using two-photon lithography master samples. URL http://arxiv.org/pdf/1702.04012v1

[69] Selimis, A., Mironov, V., Farsari, M.: Direct laser writing: Principles and materials for scaffold 3d printing. Microelectronic Engineering **132**, 83–89 (2015). DOI 10.1016/j.mee.2014.10.001

[70] Shiratori, S., Kubokawa, T.: Double-peaked edge-bead in drying film of solvent-resin mixtures. Physics of Fluids **27**(10), 102105 (2015). DOI 10.1063/1.4934670

[71] Stöhr, U.: Surface activation of plastics by plasma for adhesion promotion. Womag (Womag 2016/05/15) (2016). URL https://www.wotech-technical-media.de/womag/ausgabe/2016/05/15_stoehr_surface_activation_05j2016/15_stoehr_surface_activation_05j2016.php

[72] Streicher, A.: "spectra-cular" measurements. Optik & Photonik **12**(4), 38–40 (2017). DOI 10.1002/opph.201700023

[73] Thompson, L.F., Willson, C.G., Bowden, M.J. (eds.): Introduction to Microlithography. ACS Symposium Series. AMERICAN CHEMICAL SOCIETY, WASHINGTON, D. C. (1983). DOI 10.1021/symposium

[74] Thorlabs: Scan lenses for laser scanning microscopy. URL https://www.thorlabs.de/newgrouppage9.cfm?objectgroup_id=2910

[75] Thorlabs: Ldm405, ldm635, ldm670, ldm785, ldm850, ldm1550 laser diode modules: User guide (2017). URL https://www.thorlabs.com/newgrouppage9.cfm?objectgroup_id=1219

[76] Thorlabs: Gsm002-ec/m galvo scanning system: User guide (2019). URL https://www.thorlabs.com/newgrouppage9.cfm?objectgroup_id=3770&pn=GVSM002-EC/M

[77] Tyona, M.D.: A theoritical study on spin coating technique. Advances in materials Research **2**(4), 195–208 (2013). DOI 10.12989/amr.2013.2.4.195

[78] Vijay Kumar Singh, Minoru Sasaki, Kazuhiro Hane, Yoshihiko Watanabe, Hirosuke Takamatsu, Masato Kawakita, Hiroki Hayashi: Deposition of thin and uniform photoresist on three-dimensional structures using fast flow in spray coating. Journal of Micromechanics and Microengineering **15**(12), 2339 (2005). DOI 10.1088/0960-1317/15/12/016. URL https://iopscience.iop.org/article/10.1088/0960-1317/15/12/016

[79] Weidner, D.E.: Analysis of the flow of a thin liquid film on the surface of a rotating, curved, axisymmetric substrate. Physics of Fluids **30**(8), 082110 (2018). DOI 10.1063/1.5034359

[80] Weissman, P.: Material and process parameters that affect accuracy in stereolithography. DOI 10.15781/T2J679D77

[81] Xie, Y., Lu, Z., Li, F.: Lithographic fabrication of large curved hologram by laser writer. Optics express **12**(9), 1810–1814 (2004). DOI 10.1364/OPEX.12.001810

[82] Xie, Y., Lu, Z., Li, F., Zhao, J., Weng, Z.: Lithographic fabrication of large diffractive optical elements on a concave lens surface. Optics express **10**(20), 1043–1047 (2002). DOI 10.1364/OE.10.001043

[83] Xie, Y., Zabihi, F., Eslamian, M.: Fabrication of highly reproducible polymer solar cells using ultrasonic substrate vibration posttreatment. Journal of Photonics for Energy **6**(4), 045502 (2016). DOI 10.1117/1.JPE.6.045502

[84] Zeitner, U., Bräuer, A.: Laserlithography on plane and curved surfaces

[85] Zeng, H., Huang, J., Tian, Y., Li, L., Tirrell, M.V., Israelachvili, J.N.: Adhesion and detachment mechanisms between polymer and solid substrate surfaces: Using polystyrene–mica as a model system. Macromolecules **49**(14), 5223–5231 (2016). DOI 10.1021/acs.macromol.6b00949

[86] Zygo: Newview 8300: Specifications (2017)

Appendices

A Specifications of the GSM002-EC/M Galvanometer Scanning System [76, p. 29–30]

Appendix A Specifications and Associated Parts

A.1 Specifications

Parameter	Value
Mirror	
Maximum Beam Diameter	5 mm
Finish	GVS00x: Protected Silver Coated GVS10x: Protected Gold Coated GVS20x: Broadband, E02 GVS30x: Dual Band Hi Power, K13
Damage Threshold*	GVS00x: 3 J/cm^{2}at 1064 nm, 10 ns pulse GVS10x: 2 J/cm^2 at 1064 nm, 10 ns pulse GVS20x: 0.25 J/cm^2 at 532 nm, 10 ns pulse GVS30x: 5 J/cm^2 at 1064 nm, 10 ns pulse
Motor & Position Sensor	
Linearity	99.9%, range ±20°
Scale Drift	40PPM/°C(Max)
Zero Drift	10 µRad/°C(Max)
Repeatability	15 µRad
Resolution With GPS011 Linear PSU With standard switch mode PSU	 0.0008° (15 µRad) 0.004° (70 µRad)
Average Current	1 A
Peak Current	5 A
Load Mirror Aperture	5 mm
Coil Resistance:	2.2 Ω±10%
Coil Inductance:	150µH ±10%
Rotor Inertia:	0.02gm per cm^2
Maximum Scan Angle (Mechanical Angle)	±12.5° (with 0.8V/° scaling factor)
Motor Weight (inc cables, excl bracket)	50 g
Operating Temperature Range	0 ~ 40° C
Optical Position Sensor Output Range	40 to 80 µA

Note

*The way our mirrors are tested is continually updated, please consult www.thorlabs.com for more information.

Drive Electronics

Parameter	Value
Full Scale Bandwidth*	100 Hz Square wave, 250 Hz Sinewave 175 Hz Saw Tooth 175 Hz Triangular
Small Angle (±0.2°) Bandwidth*	Typ. 1kHz with Sinewave
Small Angle Step Response	300 µs
Power Supply	+/-15V to +/-18V dc (1.25 A rms, 5A peak MAX)
Analog Signal Input Resistance	20K±1%Ω (Differential Input)
Position Signal Output Resistance:	1K±1%Ω
Analog Position Signal Input Range	±10V
Mechanical Position Signal Input Scale Factor	switchable: 0.5V/°, 0.8V/° or 1.0V/°
Mechanical Position Signal Output Scale Factor	0.5V/°
Operating Temperature Range	0 ~ 40°C
Servo Board Size (L x W x H)	85 mm × 74 mm × 44 mm (3.35” x 2.9” x 1.73”)

* Using heat sink to keep temp <50°C (see Section 3.2.2.).

A.2 Associated Products

Product Name	Part Number
2D Galvo System - Protected Silver Mirrors	GVS002
1D Galvo System - Protected Silver Mirror	GVS001
2D Galvo System - Protected Gold Mirrors	GVS102
1D Galvo System - Protected Gold Mirror	GVS101
2D Galvo System - Broadband E02 Mirrors	GVS202
1D Galvo System - Broadband E02 Mirror	GVS201
2D Galvo System - Dual Band High Power K13 Mirrors	GVS302
1D Galvo System - Dual Band High Power K13 Mirror	GVS301
Motor Assembly Heatsink	GHS003(/M)
Galvo Power Supply	GPS011
Servo Driver Card Cover	GCE001
1D Galvo Cage System Mount	GCM001
2D Galvo Cage System Mount	GCM002 (/M)
Tip/Tilt Mount Adapter	GTT001

B Specification sheet of the LDM405 Diode Laser Module [75]

Blue Laser Module, 405 nm, 4.0 mW

LDM405

Description

The 405 nm LDM compact laser source has a Ø1.40" by 5.8" housing that contains a laser diode, collimating lens, and automatic power control circuit. The module includes a built in shutter and SM1 internal thread for mounting with an extensive range of optomechanical devices. It can be mounted to an optical table using one of our C1512, C1513, or VC3C V-groove mounts. The module features a remote interlock connection, key-lock power switch, enable/disable toggle switch, a laser on indicator LED, and power adjustment potentiometer.

Specifications

Specification	Value
Wavelength, Typical	405 nm
Wavelength, Min/Max	395 – 415 nm
Beam Diameter[a]	3.0 mm x 5.0 mm
Power, Adjustable[b]	4.0 mW

a. Measured 3 m from module. Beam shape is elliptical.
b. The maximum power is given for an operating temperature of 25 °C. When operated at a temperature other than this, the maximum output will vary.

Specification	Value
Stability, Short-Term (30 min)	0.01 dB
Stability, Long-Term Drift (24 hr)	0.1 dB
Operating Temperature	10 – 40 °C
Storage Temperature	5 – 50 °C
Power Supply @ ±10% (Included)	100 - 240 VAC, 0.48 A 50 – 60 Hz Output: 9 VDC @ 2.2 A

Drawings

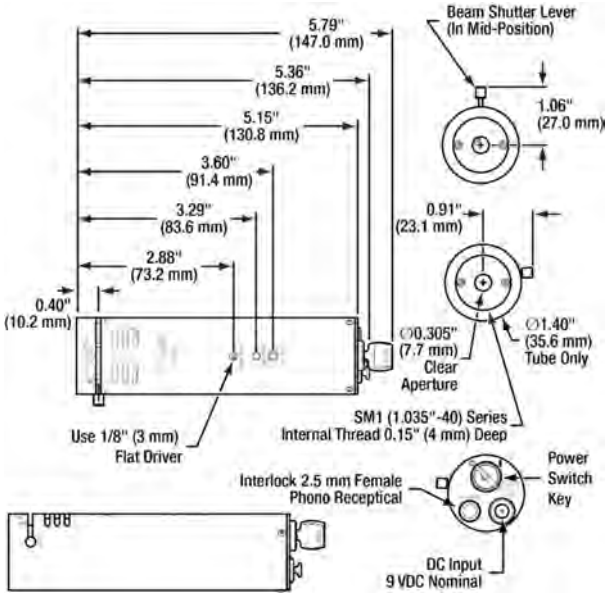

Specifications Subject to Change without Notice

September 26, 2017
11837-S01, Rev C
www.thorlabs.com/contact

C Specifications of the LSM03-VIS Scan Lens [74]

Lenses with Wavelength Ranges Starting Between 400 and 450 nm

Item #		LSM03-VIS
Optical Specifications		
Wavelength Range		400 to 700 nm
Effective Focal Length (EFL)		39 mm
Entrance Pupil Diameter[a]		4 mm
Parfocal Distance		50.7 mm
Lens Working Distance		25.1 mm
Scanning Distance[b]		29.0 mm ± 5 mm
Optical Scan Angle[c] (Single-Axis Scan)	Maximum	±10.6°
	Difffraction Limited	±8.4° (543 nm)
Optical Scan Angle[c] (Two-Axis Scan)	Maximum	±7.5° x ±7.5°
	Diffraction Limited	±5.1° x ±5.1° (543 nm)
Spot Size Plots[a]		Two-Axis Scan:  Single-Axis Scan: 
Field of View[e]	Maximum	10.3 x 10.3 mm^2 (Two-Axis Scan)
	Diffraction Limited	6.9 x 6.9 mm^2
Depth of View[e] (Twice Rayleigh Length)		0.15 mm
F-Theta Distortion[e]		<0.8%
Field Curvature[e]		<0.3 mm
Axial Color		60 µm (400 to 700 nm)
Lateral Color Shift		15 µm (400 to 700 nm)
f/#		9.8
Transmittance		-
Reflectance		
Dimensional Specifications		
Mounting Thread (External)		M25 x 0.75
Thread Length		4.4 mm (0.17")
Barrel Diameter		34 mm (1.35")
Length of Barrel		25.5 mm (1.00")

a. For the LSM03-VIS lens, the beam at the entrance pupil is assumed to be Gaussian, and the entrance pupil is assumed to be the $1/e^2$ diameter of the Gaussian beam. For the CLS-SL and SL50-CLS2 lenses, the beam at the entrance pupil is assumed to have uniform intensity across the entrance pupil. A mirror separation of 10 mm is assumed for the LSM03-VIS lens.
b. Distance from Pupil Position to the Base of the Mounting Threads (See Diagram Below)
c. Defined with Respect to the Optical Axis of the Lens
d. FN: Field Number, Given in mm with Field of View = (FN) / (Lens Magnification)
e. At the Center Wavelength, Unless Noted Otherwise

D Specifications of the NI USB-6001 DAQ card [46, p. 1-6]

SPECIFICATIONS

NI USB-6001

Low-Cost DAQ USB Device

The following specifications are typical at 25 °C, unless otherwise noted. For more information about the NI USB-6001, refer to the *NI USB-6001/6002/6003 User Guide* available at `ni.com/manuals`.

Analog Input

Number of channels

- Differential....4
- Single-ended....8

ADC resolution....14-bit

Maximum sample rate (aggregate)....20 kS/s

Converter type....Successive approximation

AI FIFO....2,047 samples

Trigger sources....Software, PFI 0, PFI 1

Input range.....±10 V

Working voltage.....±10 V

Overvoltage protection

- Powered-on.....±30 V
- Powered-off.....±20 V

Input impedance.....>1 GΩ

Input bias current.....±200 pA

Absolute accuracy

- Typical at full scale.....6 mV
- Maximum over temperature, full scale.....26 mV
- System noise.....0.7 mVrms

DNL.....14-bit, no missing codes

INL.....±0.5 LSB

CMRR.....56 dB (DC to 5 kHz)

Bandwidth.....300 kHz

Analog Output

Analog outputs.....2

DAC resolution.....14-bit

Output range.....±10 V

Maximum update rate.....5 kS/s simultaneous per channel, hardware-timed

AO FIFO.....2,047 samples

Trigger sources.....Software, PFI 0, PFI 1

Output current drive.....±5 mA

Short circuit current.....±11 mA

Slew rate.....3 V/µs

Output impedance.....0.2 Ω

Absolute accuracy (no load)

Typical at full scale.....9.1 mV

Maximum over temperature, full scale.....34 mV

DNL.....14-bit, no missing codes

INL.....±1 LSB

Power-on state.....0 V

Startup glitch.....-7 V for 10 µs

Timebase

Note The following specifications apply to the sampling accuracy for hardware-timed analog input and analog output.

Timebase frequency.....80 MHz

Timebase accuracy.....±100 ppm

Timing resolution.....12.5 ns

Digital I/O

13 digital lines

Port 0.....8 lines

Port 1.....4 lines

Port 2.....1 lines

Function

P0.<0..7>.....Static digital input/output

P1.0.....Static digital input/output

P1.1/PFI 1.....Static digital input/output, counter source or digital trigger

P1.<2..3>.....Static digital input/output
P2.0/PFI 0.....Static digital input/output, counter source or digital trigger

Direction control.....Each channel individually programmable as input or output

Output driver type.....Each channel individually programmable as open collector or active drive

Absolute maximum voltage range.....-0.3 V to 5. 5 V with respect to D GND

Pull-down resistor.....47.5 kΩ to D GND

Power-on state.....Input

Digital Input

Input voltage range (powered on).....0 to 5 V

Input voltage range (powered off).....0 to 3.3 V

Input voltage protection.....±20 V on two lines per port (maximum of five lines for all ports) for up to 24 hours

Caution Do not leave a voltage above 3.3 V connected on any DIO line for extended periods of time when the device is powered off. This may lead to long term reliability issues.

Minimum V_{IH}.....2.3 V

Maximum V_{IL}.....0.8 V

Maximum input leakage current
At 3.3 V.....0.8 mA
At 5 V.....4.5 mA

Digital Output (Active Drive)

Maximum V_{OL} (4 mA).....0.7 V

Maximum V_{OL} (1 mA).....0.2 V

Minimum V_{OH} (4 mA).....2.1 V

Minimum V_{OH} (1 mA).....2.8 V

Maximum V_{OH}.....3.6 V

Maximum output current per line.....±4 mA

Digital Output (Open Collector)

Maximum V_{OL} (4 mA).....0.8 V

Maximum V_{OL} (1 mA).....0.2 V

Note Minimum V_{OH} dependent on user-provided pull-up resistor and voltage source. Recommended pull-up resistor is 1 kΩ.

Using a 1 kΩ pull-up resistor and 5 V voltage source:

- Minimum V_{OH}.....3.5 V
- Typical V_{OH}.....4.5 V

Maximum output (sinking) current per line.....-4 mA

Maximum pull-up voltage.....5 V

Maximum leakage current

- At 3.3 V.....0.8 mA
- At 5 V.....4.5 mA

Counter

Number of counters.....1

Resolution.....32-bit

Counter measurements.....Edge counting, rising or falling

Counter direction.....Count up

Counter source.....PFI 0 or PFI 1

Maximum input frequency.....5 MHz

Minimum high pulse width.....100 ns

Minimum low pulse width.....100 ns

+5 V Power Source

Output voltage.....+5 V, ±3%

Maximum current.....150 mA

Overcurrent protection.....200 mA

Short circuit current.....50 mA

Overvoltage protection.....±20 V

Bus Interface

USB specification.....USB Full Speed

USB bus speed.....12 Mb/s

Physical Characteristics

Dimensions

Without screw terminal connector plugs....75.4 mm × 86.2 mm × 23.6 mm, (2.97 in. × 3.40 in. × 0.93 in.)

With screw terminal connector plugs.....93.2 mm × 86.2 mm × 23.6 mm, (3.67 in. × 3.40 in. × 0.93 in.)

E Specifications of the HXP100P-MECA Hexapod [48, p. 2-4]

The HXP100 design also includes two programmable pivot points, enabling more flexibility to align a sample at a particular point or points of that sample. The Newport Hexapod can not only relocate the pivot point, but through our advanced technology, the entire coordinate system can be relocated. In addition, two user-definable coordinate systems are provided, called tool (moves with the Hexapod) and work (stationary coordinate systems). Incremental displacements are possible in either one of these systems in user-friendly Cartesian coordinates, and positions can be easily calculated from one system to the other by a function call, without the need for complex external coordinate transformations.

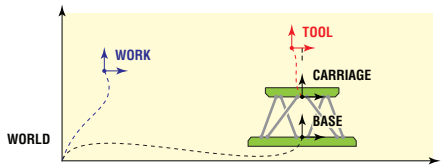

Absolute moves and positions are defined in the work coordinate system. Incremental moves can be done in the tool or in the work coordinate systems.

As a standard feature, the HXP controller allows the user to define a virtual pivot point in space for all rotations

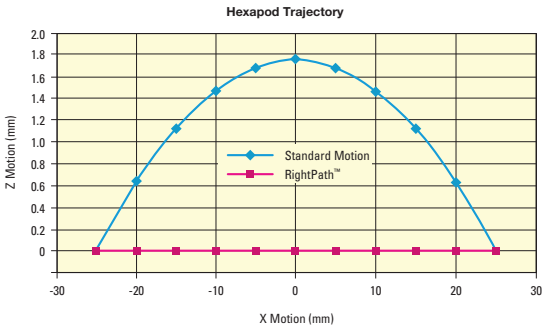

RightPath™ Trajectory Control enables minimal runout in linear and arc trajectories.

Specifications

	HX100-MECA	HXP100HA-MECA	HXP100P-MECA	HXP100PHA-MECA	HXP100V6-MECA
Travel Range X, Y, Z [1]	±27.5, ±25, ±14 mm	±27.5, ±25, ±14 mm	±27.5, ±25, ±14 mm	±27.5, ±25, ±14 mm	±27.5, ±25, ±14 mm
Travel Range ΘX, ΘY,ΘZ	±11.5, ±10.5, ±19 °	±11.5, ±10.5, ±19 °	±11.5, ±10.5, ±19 °	±11.5, ±10.5, ±19 °	±11.5, ±10.5, ±19 °
Minimum Incremental Motion X, Y, Z [2]	0.5, 0.5, 0.25 µm	0.50, 0.50, 0.25 µm	0.10, 0.10, 0.05 µm	0.10, 0.10, 0.05 µm	0.5, 0.5, 0.25 µm
Minimum Incremental Motion ΘX, ΘY, ΘZ	0.25, 0.25, 0.5 mdeg	0.25, 0.25, 0.5 mdeg	0.05, 0.05, 0.10 mdeg	0.05, 0.05, 0.10 mdeg	0.25, 0.25, 0.5 mdeg
Uni-directional Repeatability X, Y, Z, Typical	±0.25, ±0.25, ±0.125 µm	±0.14, ±0.13, ±0.05 µm	±0.10, ±0.10, ±0.05 µm	±0.10, ±0.10, ±0.05 µm	±0.50, ±0.50, ±0.50 µm
Uni-directional Repeatability X, Y, Z, Guaranteed	–	±0.25, ±0.25, ±0.125 µm	–	±0.15, ±0.15, ±0.075 µm	–
Uni-directional Repeatability ΘX, ΘY, ΘZ, Typical	±0.125, ±0.125, ±0.25 mdeg	±0.125, ±0.125, ±0.25 mdeg	±0.05, ±0.05, ±0.10 mdeg	±0.05, ±0.05, ±0.10 mdeg	±0.25, ±0.25, ±0.50 mdeg
Accuracy XYZ, Guaranteed	–	±10, ±10, ±5 µm	–	±5.0, ±5.0, ±2.5 µm	–
Maximum Speed X, Y, Z	2.5, 2, 1 mm/s	2.5, 2, 1 mm/s	12, 10, 5 mm/s	12, 10, 5 mm/s	0.5, 0.5, 0.25 mm/s
Maximum Speed ΘX, ΘY, ΘZ	1.8, 1.7, 3 °/s	1.8, 1.7, 3 °/s	8, 8, 16 °/s	8, 8, 16 °/s	0.2, 0.2, 0.4 °/s
Rigidity X, Y, Z [3]	5, 5, 40 N/µm	5, 5, 40 N/µm	3, 3, 24 N/µm	3, 3, 24 N/µm	5, 5, 40 N/µm
Pitch X, Y, Z, Guaranteed	–	±75, ±75, ±75 µrad	–	±37.5, ±37.5, ±37.5 µrad	–
Yaw X, Y, Z, Guaranteed	–	±75, ±75, ±75 µrad	–	±37, ±37, ±37 µrad	–
Centered Load Capacity (4)	200 N	200 N	60 N	60 N	200 N
Cable Length	1.5 m	1.5m	3 m	3 m	1.5 m
Motor	DC Servo	DC Servo	DC Servo	DC Servo	Stepper motor
Weight	7.2 kg	7.2 kg	7.2 kg	7.2 kg	7.2 kg

[1] Travel ranges are interdependent. The listed values aremax. travels per axis when all other axis are in their centered position.
[2] Open loop values shown.
[3] Stiffness depends on Hexapod position. Values are given for all axis in their centered position.
[4] For Value shown for horizontal base plate. See graphs for maximum payload height and cantilever distance on next page

Max. Cantilever Distance of the Load

HXP100 Horizontal Base Plate

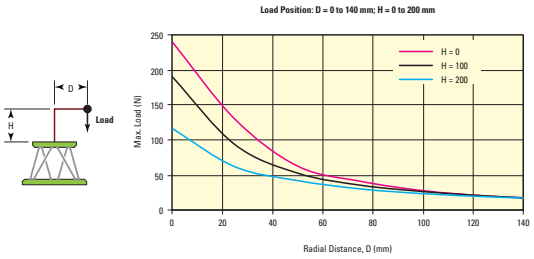

HXP100P Horizontal Base Plate

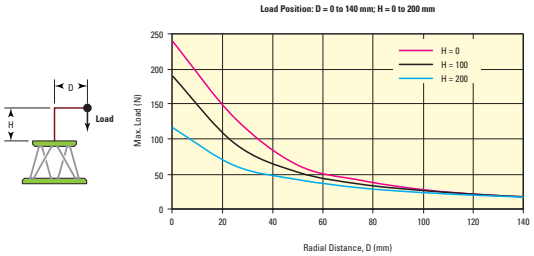

HXP100-MECA and HXP100HA-MECA

Note: Other top plate hole patterns or a center aperture are available upon request.

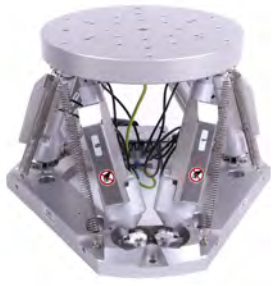

HXP100P-MECA Hexapod

Dimensional Drawings

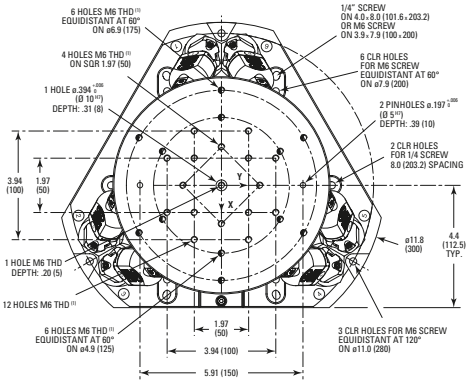

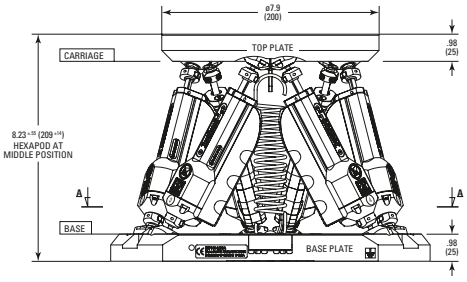

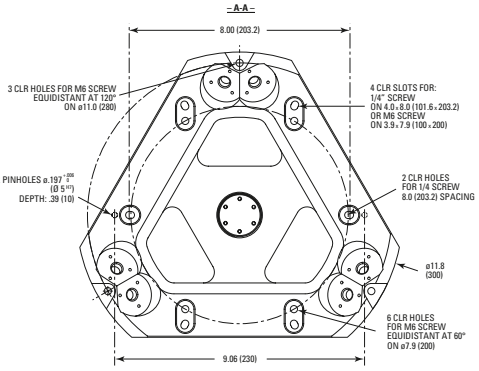

Dimensional Drawings

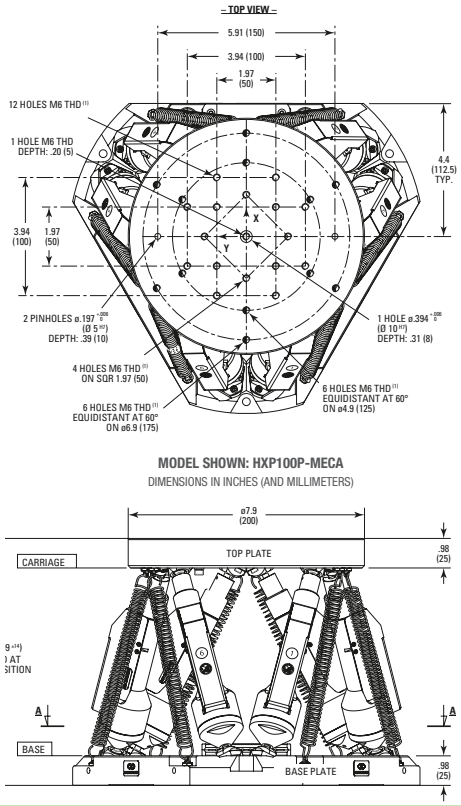

HXP100P-MECA and HXP100P-MECA

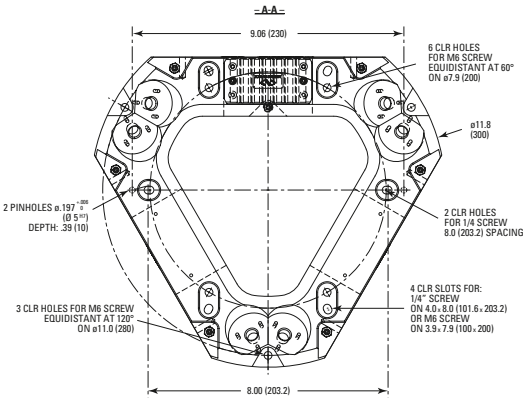

Note: Other top plate hole patterns or a center aperture are available upon request.

Ordering Information

Model	Description
HXP100-MECA	Hexapod, 200 N load capacity
HXP100-ELEC-D[1]	Hexapod controller for HXP100-MECA
HXP100P-MECA	Hexapod Precision, 60 N load capacity
HXP100P-ELEC-D [1]	Hexapod controller for HXP100P-MECA

[1] *Contact Newport for the two additional SingleAxis drive capability*

Model	Description
HXP100HA-MECA	Hexapod with guaranteed specifications, 200 N load capacity
HXP100HA-ELEC-D[1]	Hexapod controller for HXP100HA-MECA
HXP100PHA-MECA	Hexapod Precision with guaranteed specifications, 60 N load capacity
HXP100PHA-ELEC-D [1]	Hexapod controller for HXP100PHA-MECA

[1] *Contact Newport for the two additional SingleAxis drive capability*

Note: Call Newport for quotes on the 10-6 hPa vacuum version.

www.newport.com

DS-102102 HXP100 Datasheet_10/21

F CAD Drawing of Techspec uncoated Plano convex Lens [12]

NOTES:

1. SUBSTRATE:
   GRADE A FINE ANNEALED
   SCHOTT: N-BK7 517/642
2. ROHS COMPLIANT
3. CENTERING TOLERANCE (AT 587.6nm):
   BEAM DEVIATION (HALF ANGLE): <1 ARCMIN
4. COATING (APPLY ACROSS COATING APERTURE)

   S1: NONE
   S2: NONE

5. FINE GRIND SURFACE
6. POWER, IRREGULARITY, AND SURFACE QUALITY SPECIFICATIONS APPLY ACROSS CLEAR APERTURE
7. FOCAL LENGTH (EFL): 38.10mm±1%
   BACK FOCAL LENGTH (BFL): 33.48mm
8. PROTECTIVE BEVEL AS NEEDED
9. DESIGN WAVELENGTH: 587.6nm

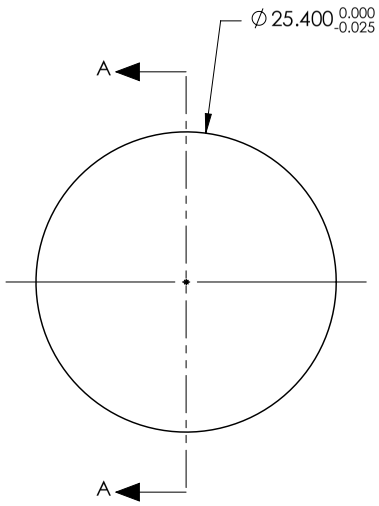

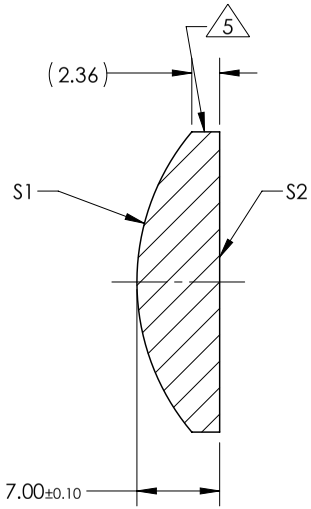

SECTION A-A

FOR INFORMATION ONLY:
DO NOT MANUFACTURE PARTS TO THIS DRAWING

	S1	S2
SHAPE	CONVEX	PLANO
RADIUS	19.69	INFINITY
SURFACE QUALITY	40 - 20	40 - 20
MIN CLEAR APERTURE	∅24.40	∅24.40
MIN COATING APERTURE	N/A	N/A
POWER AT 632.8nm	3.00 RINGS	3.00 RINGS
IRREGULARITY AT 632.8nm	0.50 RINGS	0.50 RINGS

SPECIFICATIONS SUBJECT TO CHANGE WITHOUT NOTICE
DIMENSIONS ARE FOR REFERENCE ONLY

Edmund Optics®

THIRD ANGLE PROJECTION		TITLE	25.4mm Dia. x 38.1mm FL, Uncoated, Plano-Convex Lens
ALL DIMS IN	mm	DWG NO	49848
			SHEET 1 OF 1